Reactive transformation of extraction byproducts: Enhanced production of the antimalarial artemisinin

Dissertation

zur Erlangung des akademischen Grades

Doktoringenieurin
(Dr.-Ing.)

von M.Sc. Susann Triemer
geb. am 09.09.1990 in Chemnitz

genehmigt durch die Fakultät für Verfahrens- und Systemtechnik der
Otto-von-Guericke-Universität Magdeburg

Promotionskommission:
apl. Prof. Dr. rer. nat. Heike Lorenz
Prof. Dr.-Ing. Andreas Seidel-Morgenstern
Ass.-Prof. Dr. Kerry Gilmore
Prof. Dr.-Ing. Ulrike Krewer

eingereicht am 29.09.2022
Promotionskolloquium am 24.03.2023

Susann Triemer
Reactive transformation of extraction byproducts: Enhanced production of the antimalarial artemisinin
Dissertation

Otto-von-Guericke Universität
Lehrstuhl für Chemische Verfahrenstechnik
Institut für Verfahrenstechnik
Fakultät für Verfahrens- und Systemtechnik
Universitätsplatz 2
39106 and Magdeburg

Abstract

The natural product artemisinin is the precursor to the most efficacious antimalarial medications currently available on the market. However, the high artemisinin production cost limits the availability of these treatments for wide parts of the population in developing countries. The main production pathway is the extraction of the plant *Artemisia annua*. In this process, the late-stage biological precursor to artemisinin, Dihydroartemisinic acid (DHAA), is obtained as a major side product. DHAA can be converted to artemisinin via a cascade of photooxygenation and acid-catalyzed cyclization steps. So far, this partial synthesis was only demonstrated with purified reagents exploiting intensified reaction conditions.

During this work, a simple process was developed to convert the former waste product DHAA directly in the extract to artemisinin without requiring additional purification steps. The reaction step could be simplified by using co-extracted chlorophyll as a highly potent, abundant, and non-toxic photocatalyst, eliminating the need for adding and recycling purified photocatalysts.

For the natural DHAA concentration in the extract, the reaction performance is robust regarding reaction temperature, acid concentration, and extraction conditions. In the final suggested process, co-extracted DHAA is converted to artemisinin by treating the extract with $0.0625\,\mathrm{M}$ trifluoroacetic acid, visible light, and pressurized air in $9\,\mathrm{min}$ residence time at ambient temperature. Artemisinin is obtained in a yield ranging from $43\,\%$ to $49\,\%$ with respect to the initial DHAA concentration.

To facilitate optimization of the overall process chain, a semi-mechanistic kinetic model was developed, which considers photon transfer and oxygen mass transfer. The parameterized model reproduces the observed formation of the main intermediate and artemisinin with a relative deviation of $7.5\,\%$ and $14.0\,\%$, respectively. The investigations identified the acid concentration as a key factor affecting both the reaction rates as well as the overall selectivity to artemisinin.

The developed process and the identified model are essential building blocks to increase the artemisinin amount obtainable with the available resources. Therefore, both can contribute to improve the availability of artemisinin-based medications for the large number of people suffering from malaria.

Kurzfassung

Der Naturstoff Artemisinin wird als Vorstufe hochwirksamer Medikamente gegen Malaria benötigt. Durch die hohen Herstellungskosten sind diese Präparate allerdings für die Bevölkerung in Entwicklungsländern nur in eingeschränktem Maß zugänglich. Artemisinin wird primär durch Extraktion aus der Pflanze *Artemisia annua* gewonnen. Dabei fällt als Nebenprodukt Dihydroartemisininsäure (DHAA) an, die biologische Vorstufe zum Artemisinin. DHAA kann über eine Reaktionskaskade aus Photooxygenierung und anschließender säure-katalytischer Zyklisierung zu Artemisinin umgewandelt werden. Allerdings wurde diese Synthese bisher ausschließlich mit aufgereinigten Edukten und Katalysatoren bei starker Kühlung und hohen Sauerstoffdrücken umgesetzt.

In dieser Arbeit wurde ein Verfahren entwickelt, in welchem DHAA ohne vorherige Aufreinigung im vorliegenden Pflanzenextrakt bei milden Bedingungen zu zusätzlichem Artemisinin umgewandelt werden kann. Der Reaktionsschritt konnte stark vereinfacht werden, indem mitextrahiertes Chlorophyll als hochaktiver Photokatalysator genutzt wird und somit den Einsatz und die Rückgewinnung reiner Photokatalysatoren überflüssig macht. So kann extrahiertes DHAA innerhalb von $9\,\mathrm{min}$ Verweilzeit zu Artemisinin umgewandelt werden, in dem das Extrakt mit Druckluft, sichtbarem Licht und $0.0625\,\mathrm{M}$ Trifluoressigsäure bei Raumtemperatur kontaktiert wird. Es werden dabei Ausbeuten an Artemisinin von 43 bis 49 % bezogen auf die Startkonzentration an DHAA erreicht.

Um die modellgestützte Optimierung des gesamten Produktionskette zu ermöglichen, wurde ein semimechanistisches kinetisches Modell für die Partialsynthese entwickelt, das neben der Reaktion auch Photonen- und Sauerstofftransportprozesse berücksichtigt. Das parametrisierte Modell beschreibt die Bildung der Reaktionsprodukte mit einer relativen Abweichung von $7.5\,\%$ für das Hauptzwischenprodukt und von $14.0\,\%$ für Artemisinin. Die Analyse verschiedener abgeleiteter Modellkandidaten ergab dabei, dass die Säurekonzentration mit höherer Ordnung in die effektiven Reaktionsraten eingeht und somit die Artemisininselektivität bestimmt.

Sowohl der entwickelte Prozess als auch das validierte Modell stellen wichtige Bausteine dar, um mit den vorhandenen Ressourcen die Artemisininausbeute erhöhen zu können und somit die Verfügbarkeit an wirksamen Malariamedikamenten zu verbessern.

Collaborations and Research Publications

This Ph.D. project was embedded in a larger research project on optimizing the production of artemisinin within the group for *Physical and Chemical Foundations of Process Engineering research* at the *Max Planck Institute for Dynamics of Complex Technical Systems Magdeburg* and the research group for *Continuous Flow Chemistry* at the *Max Planck Institute of Colloids and Interfaces* in Potsdam/Golm, led by Kerry Gilmore and Peter H. Seeberger. The methods for extraction *A. annua* leaves and analyzing the extract by HPLC were adopted from Truong Giang Vu (MPI Magdeburg). The initial study on the utilization of chlorophyll was performed at research stays at the *Max Planck Institute of Colloids and Interfaces* in Potsdam/Golm. The continuous flow reactor and quantification via qNMR developed in the group for *Continuous Flow Chemistry* were further improved within this Ph.D. project to cover the plant extract as reaction medium.

The kinetic model for the partial synthesis of artemisinin was developed in collaboration with the *Institute of Energy and Process Systems Engineering* (InES) of the *Technische Universität Braunschweig*. Moritz Schulze, a Ph.D. candidate at this institute, performed the model implementation, parameter estimation, model-based design of experiments, and sensitivity analysis. The design of the model equations and simplified reaction networks was joint work. The characterization of the flow reactor setup and the kinetic experiments were performed by the author of this thesis.

Benjamin Wriedt and Dirk Ziegenbalg from the *Institute of Chemical Engineering* at *Ulm University* contributed to developing the photooxygenation model with their expertise in designing and analyzing actinometric measurements and modeling of photon transfer within photoreactors.

This Ph.D. thesis was supported by the *International Max Planck Research School for Advanced Methods in Process Systems Engineering* (IMPRS ProEng).

The research results were published in the following journal articles:

S. Triemer, K. Gilmore, T.G. Vu, P.H. Seeberger, A. Seidel-Morgenstern: "Literally Green Chemical Synthesis of Artemisinin from Plant Extracts". In *Angewandte Chemie*

Int. Edition 57 (2018), pp. 5525–5528.
Ref. [382] - The results are discussed in Chapter 5.

E. Horosanskaia, S. Triemer, A. Seidel-Morgenstern, H. Lorenz: "Purification of Artemisinin from the Product Solution of a Semisynthetic Reaction within a Single Crystallization Step". In: *Organic Process Research & Development* 23 (2019), pp. 2074–2079.
Ref. [215] - The results are introduced in Section 6.6.

S. Triemer, M. Schulze, B. Wriedt, R. Schenkendorf, D. Ziegenbalg, U. Krewer, A. Seidel-Morgenstern: "Kinetic analysis of the partial synthesis of artemisinin: Photooxygenation to the intermediate hydroperoxide”. In: *Journal of Flow Chemistry* 11.3 (2021), pp. 641–659.
Ref. [388] - The results are discussed in Chapter 7.

Glossary

Abbreviations

AA	Artemisinic acid
ACN	Acetonitrile
ACT	Artemisinin-combination therapy
Act	Actinometer
AIC	Akaike information criterion
AICc	AIC with small sample correction
Arte	Artemisinin
Arte H	Arteannuin H
API	Active pharmaceutical ingredient
BP_3	Dihydro-*epi*-deoxyarteannuin B
Chl	Chlorophyll
DAD	Diode-array detector
DCA	9,10-Dicyanoanthracene
DHAA	Dihydroartemisinic acid
DHAEMC	Dihydroartemisinic acid mixed anhydride
DMT	Dimethylterephthalate
DW	Dried weight
ELSD	Evaporative light scattering detector
FEP	Fluorinated ethylene propylene copolymer
FIM	Fisher information matrix
FPP	Farnesyl pyrophosphate
FTIR	Fourier-transform infrared spectroscopy
HPLC	High performance liquid chromatography
HPA	Heteropoly acid
ID	Inner diameter
IR	Infrared
LED	Light-emitting diode
LVRPA	Local volumetric rate of photon absorption
MBDoE	Model-based design of experiments
MPI	Max Planck Institute

NMR	Nuclear magnetic resonance
OD	Outer diameter
Pheo	Pheophytin
RTE	Radiative transfer equation
SMB	Simulated moving bed chromatography
$scCO_2$	Supercritical carbon dioxide
SSE	Sum of squared error
TEA	Triethylamine
TFA	Trifluoroacetic acid
THF	Tetrahydrofuran
TPP	Tetraphenylporphyrine
UV	Ultraviolet
WHO	World Health Organization

Latin symbols

Symbol	**Quantity**	**Unit**
A	Area	m^2
A_λ	Absorbance	-
c	Molar concentration	mol/L
C	Cost	$/kg
C_0	Distribution factor	-
d	Diameter	mm
D	Diffusion coefficient	$cm^2 \, min^{-1}$
f	Absorption factor	-
F_{conc}	Concentration factor	-
g	Spectral distribution	-
GEP	Gross economic profit	$\$/L_{Extract}$
H	Henry constant	bar
Ha	Hatta number	-
I	Radiation intensity	W/sr
j	Mass transfer rate	mol/L/min
J	Molar diffusion flux	mol/L/min
k	Rate constant	
$k_l a$	Mass transfer coefficient	s^{-1}
l	Length	m

Symbol	**Quantity**	**Unit**
$L_{\mathrm{p}}^{\mathrm{a}}$	Local volumetric rate of photon absorption	$\mathrm{mol/L/s}$
l_{opt}	Optical path length	mm
m	Mass	g
M	Molar mass	$\mathrm{g/mol}$
n	Reaction order	-
N	Molar amount	mol
NEP	Net economic profit	$\mathrm{\$/L_{Extract}}$
p	Pressure	bar
$\mathrm{P^C}$	Electrical power	kW
$\mathrm{P_{LED}}$	Relative power setting of LED modules	$\%$
PLL	Profile log-likelihood	
Pr	Price	$\mathrm{\$/kg}$
$\mathrm{q_p^0}$	Incident photon flux	$\mathrm{mol/s}$
r	Reaction rate	$\mathrm{mol\,L^{-1}\,min^{-1}}$
R	Universal gas constant	$8.3145\,\mathrm{kJ/mol/K}$
s	Optical path	mm
S	Signal integral	
SM	Sensitivity matrix	
t	Time	s
T	Temperature	K
V	Volume	mL
$\dot{\mathrm{V}}$	Volumetric flow rate	$\mathrm{mL\,min^{-1}}$
u	Velocity	$\mathrm{m/s}$
X	Conversion	$\%$
y	Number of protons	-
Y	Yield	$\%$
z	Axial reactor coordinate	mm

Greek symbols

Symbol	**Quantity**	**Unit**
α	Gas ratio	-
β	Gas holdup	-
δ	Chemical shift	ppm
ϵ	Decadic absorption coefficient	$\mathrm{L/mol/cm}$

Symbol	**Quantity**	**Unit**
κ	Naperian absorption coefficient	$L/mol/cm$
λ	Wavelength	nm
ν	Stoichiometric coeffient	-
Ω	Direction	sr
Φ	Quantum yield	-
ρ	Density	g/mL
σ	Volumetric scattering coefficient	m^{-1}
τ	Residence time	min

Superscripts

0	Initial value
∞	Equilibrium state
a	Absorption
drift	Drift
OPEX	Operating
s	Superficial
v	Volumetric

Subscripts

2nd	Second reaction line
a	Absorbing
Crude	Crude extract
em	Emitted
g	Gas phase
i	Species i
l	Liquid phase
p	Photon
photo	Photoreactor
R	Entire reactor
r	Reaction
UC	Unit cell
λ	at wavelength λ

Contents

1

Introduction and motivation

Natural products are the basis of more than a third of the active pharmaceutical ingredients (API) approved in the last 40 years [1]. Biological evolution pre-optimized metabolites to bind to biomolecules leading to properties often not covered by conventional medications [2]. These unique structural features are difficult to reproduce by chemical total synthesis and are often accessible only by complicated multiple-step pathways. Natural products are often secondary metabolites formed only in a minor amount in their natural source to protect it from external threats. Producing an API based on its natural origin, thus, requires a stable supply of large amounts of biomass. Therefore, the reliable and cost-efficient production of natural products remains a major challenge, limiting their application as APIs [3].

Artemisinin (in this work also "Arte"), a secondary metabolite of the plant *Artemisia annua*, showcases this general problem related to natural products. The plant has been used as a malaria medication for more than 2000 years in Traditional Chinese medicine [4, 5]. In 1972, the active compound artemisinin was isolated from *Artemisia annua* by the Chinese pharmacologist Youyou Tu, who was granted the Nobel prize in "Physiology or Medicine" in 2015 [6]. The structure of artemisinin (Fig. 1.1a) consists of a sesquiterpene lactone with a reactive 1,2,4-trioxane bridge. This endoperoxide is highly active against the unicellular *Plasmodia* strains [7, 8] that cause malaria and are responsible for more than 600,000 casualties in 2020 [9]. The World Health Organization (WHO) recommends artemisinin-based combination therapies (ACT) as a first-line treatment against the disease [10]. Their high efficacy and weak side effects make ACTs a key in the global effort to fight malaria [11]. Besides the anti-parasitic effect, artemisinin is under investigation as a future drug lead against cancer [12–15], viral infections including SARS-CoV-2 [16–19], and schistosomiasis [20–22].

However, the high ACT price of around 2 $ for a complete treatment limits access to these medications, especially for the people in the sub-Saharan region suffering most of the disease. The cost for the starting material artemisinin accounts for 20 % to 23 % of that price [23]. The total ACT demand is estimated to be 539 million dosages in 2021, corresponding to 218 metric tons of artemisinin [24]. The primary access for artemisinin is extraction from the plant *A. annua* [25]. The artemisinin yield obtained from cultivation depends strongly on the environmental conditions

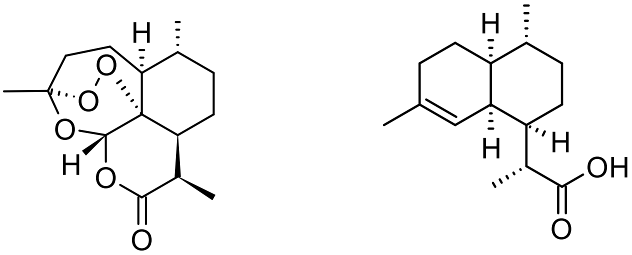

(a) Artemisinin (Arte)

(b) Dihydroartemisinic acid (DHAA)

Fig. 1.1: Chemical structure of artemisinin and its biological precursor dihydroartemisinic acid.

and can vary significantly from year to year. In optimal conditions, the artemisinin content in the leaves reaches up to $1.5\,\mathrm{wt}-\%$ of the dried matter. The volatility of *A. annua* cultivation has led to significant shortages in the artemisinin supply and major price fluctuations from $200\,\$/\mathrm{kg}$ to $1100\,\$/\mathrm{kg}$ in recent years [26].

As an alternative, semi-synthetic processes for artemisinin production were developed [27, 28] and applied in industrial scale [29, 30]. In an initial fermentation step, genetically engineered yeasts produce dihydroartemisinic acid (DHAA), the direct biological precursor to artemisinin. In a second production step, DHAA is converted in a photo- and acid-catalyzed partial synthesis to artemisinin in high yield. The standard price of semi-synthetic artemisinin is $400\,\$/\mathrm{kg}$ [31].

To significantly increase the availability of artemisinin-based medications for the population of malaria-endemic countries, the artemisinin price needs to be reduced to $100\,\$/\mathrm{kg}$ [24, 31]. Therefore, artemisinin production is in need for process optimization to prevent future bottlenecks in artemisinin supply.

This work aims to intensify plant-based production as an established process by utilizing co-extracted DHAA as an additional resource. Depending on the cultivation conditions and the *A. annua* strain, DHAA accumulates in the plant in similar amounts as artemisinin [32]. Converting this byproduct from extraction to additional artemisinin increases the overall yield retrieved from the plant and thereby stabilizes the artemisinin supply without expanding *A. annua* cultivation. In the optimal case, the reaction step from the partial-synthetic pathway can be integrated into the extraction plant without posing additional constraints on the extraction step or affecting the downstream purification (Fig. 1.2). The viable coupling of all three process steps requires an highly selective conversion of DHAA into artemisinin without the need for major purification of the extract prior to the reaction or extensive use of auxiliary materials. This primary goal is related to four different research questions to be answered in this work:

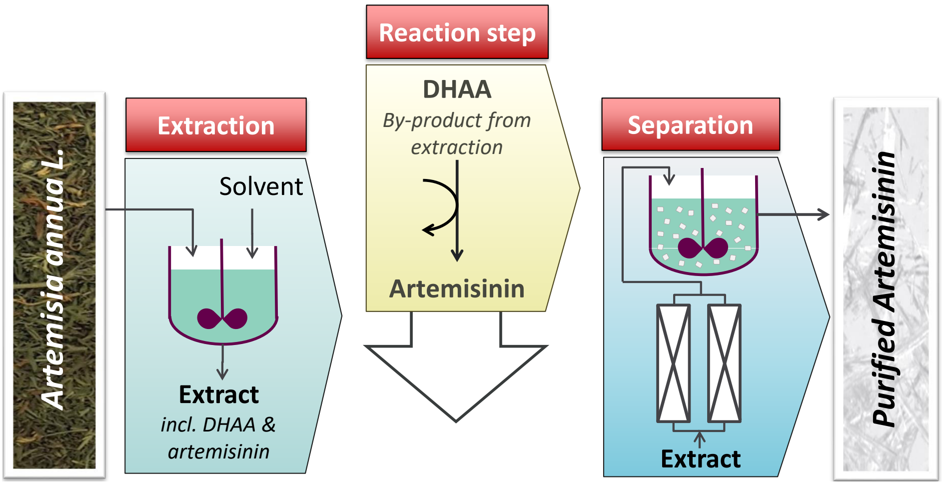

Fig. 1.2: Integration of a reaction step in the plant-based production enables conversion of the extraction byproduct dihydroartemisinic acid to additional artemisinin.

1. How can the known partial synthesis from DHAA to artemisinin be further simplified to facilitate the integration in plant-based production?

2. How can this developed concept be adapted to process impurity-rich extract with a lower DHAA concentration?

3. How can the partial synthesis be described by a simple semi-mechanistic model to facilitate later model-based optimization of the overall process?

4. Which factors limit the viability and applicability of the partial synthesis as an extension of the extraction-based production of artemisinin?

These four questions also reflect the structure of this thesis.
This work is embedded in the research project on optimizing the artemisinin production at the *Max Planck Institute for Dynamics of Complex Technical Systems*, Magdeburg, in cooperation with the *Max Planck Institute of Colloids and Interfaces* in Golm. The main focus of this thesis is the reactive conversion of DHAA to artemisinin. The conditions for the upstream extraction were developed by Truong Giang Vu (MPI Magdeburg). The downstream purification was investigated with Elena Horosanskaia and Steffi Wünsche (MPI Magdeburg) as main contributors.
The process developed in the group of Peter Seeberger on utilizing milliscale reactor systems to synthesize artemisinin served as a starting point. In collaboration with Kerry Gilmore and Peter Seeberger from the *Max Planck Institute of Colloids and Interfaces*, this initial process was further improved regarding the integration in the extraction-based production pathway in this thesis. The development of the kinetic

model was performed in close collaboration with Moritz Schulze, René Schenkendorf, and Ulrike Krewer from *Technische Universität Braunscheig* and *Karlsruhe Institute of Technology*. The characterization of the irradiation conditions by chemical actinometry was supported by Benjamin Wriedt and Dirk Ziegenbalg from *Ulm University*. The specific contributions to the results of this thesis are clearly stated at the beginning of the corresponding chapters.

The following two chapters introduce the available pathways for artemisinin production, the recent developments in the partial synthesis specifically, and the principles of modeling such light-initiated reactions. In Chapter 4, the reactor setup and the experimental procedures are explained, which were applied to study the partial synthesis together with the extraction and to obtain kinetic data on the reaction step. Chapter 5 presents the results for choosing the photocatalyst, the acidic catalyst, and the solvent to enable an easy and efficient coupling with the extraction. In Chapter 6, this developed process setting is then applied to the diluted conditions of crude plant extracts. The specific process conditions are further optimized, and the final process is upscaled to allow for coupling with the extraction and purification at a comparable flow rate range. Chapter 7 comprises the joint work with Moritz Schulze from TU Braunschweig on developing and identifying a kinetic model for the reaction step. The kinetics for the photooxygenation were parametrized with the reactor model as a first part. This model was then used as a building block to identify a suitable model structure for the acid-catalyzed reaction sequence. The final chapter addresses the economics of integrating the partial synthesis as an additional process step in an extraction-based production and identifies main cost factors.

2

Artemisinin production: State-of-the-art

The importance of artemisinin as a precursor to antimalarial medications fostered intensive research on optimizing the extraction process of the plant *A. annua* and developing novel alternatives to plant-based extraction. The following section gives an overview of the recent research approaches and the industrial realization of artemisinin production. The focus is on the extraction of *A. annua* as source for dihydroartemisinic acid as biological precursor and additional resource of artemisinin and the semi-synthetic conversion of DHAA to artemisinin. Total synthetic pathways developed so far are briefly introduced.

2.1 Artemisia annua: Natural source for artemisinin

Artemisia annua (genus of Artemisia, the family of Asteraceae), also known as sweet wormwood or Qinghao, is an aromatic herbal plant with an annual life cycle that grows as a shrub reaching a height of over 2 m [33]. The plant is native in East Asia, from China and Japan to Vietnam, India and southern Siberia [33]. The plant was later introduced in various countries and grows nowadays wild in North and South America and Europe [34].

A. annua has been used in traditional Chinese medicine for more than 2000 years due to its antimalarial activity [5]. It is the only species within the Artemisia genus that forms artemisinin as secondary metabolite in substantial amounts [5]. Artemisinin is mainly located in the glandular trichomes at the outer surface of the leaves [35–38] to protect the plant itself from the phytotoxicity of artemisinin. Significant artemisinin levels can also be found in seeds, flowers, and buds [39–43].

2.1.1 Biosynthesis of artemisinin

The biosynthesis of artemisinin gained major importance as stepping stone for further understanding and optimization of cultivation, metabolic engineering, and biotechnological production. In the following, the main steps and intermediates are

(a) Plant *Artemisia annua L.* [44]

(b) Dried leaves

Fig. 2.1: The natural source of artemisinin: *Artemisia annua L.*

introduced. For more details, the interested reader is referred to reviews published on the topic [39, 45–52] and the references therein.
The pathway can be divided into three phases (Fig. 2.2) [50]:

1. Formation of amorpha-4,11-diene
2. Formation of dihydroartemisinic acid (DHAA)
3. Conversion of DHAA to artemisinin.

Farnesyl pyrophosphate (FPP) is the first major precursor in the artemisinin biosynthesis. FPP is converted to several sesquiterpenes, including amorpha-4,11-diene, in enzyme-catalyzed pathways.

The second phase of the biosynthesis involves modifying the isopropylidene group of amorpha-4,11-diene to artemisinic aldehyde [27, 28]. Artemisinic aldehyde is a key intermediate in the biosynthesis affecting the overall selectivity to artemisinin. Within the pathway to artemisinin, it is first dehydrogenated to dihydroartemisinic aldehyde [53] and second oxidized by the enzyme ALDH1 to DHAA. However, the same enzymatic complex also oxidizes artemisinic aldehyde directly, forming artemisinic acid (AA) [54]. AA and DHAA can both accumulate in the plant in similar magnitudes as artemisinin[32, 55–57]. So far, all steps within the biosynthesis are catalyzed by specific enzymes, which were identified in recent years [27, 28, 51, 53, 54, 58, 59]. Introduction and overexpression of the corresponding genes in tobacco [60], bacteria [54], and yeast (*Saccharomyces cerevisiae*)[27] lead to the formation of the artemisinin precursors within these organisms. Fermentation of engineered yeasts for artemisinic acid production was realized as a starting point for industrial, plant-independent production of artemisinin [27–29] (Sec. 2.3.2).

There is still an ongoing discussion, whether AA or DHAA is the late-stage biological

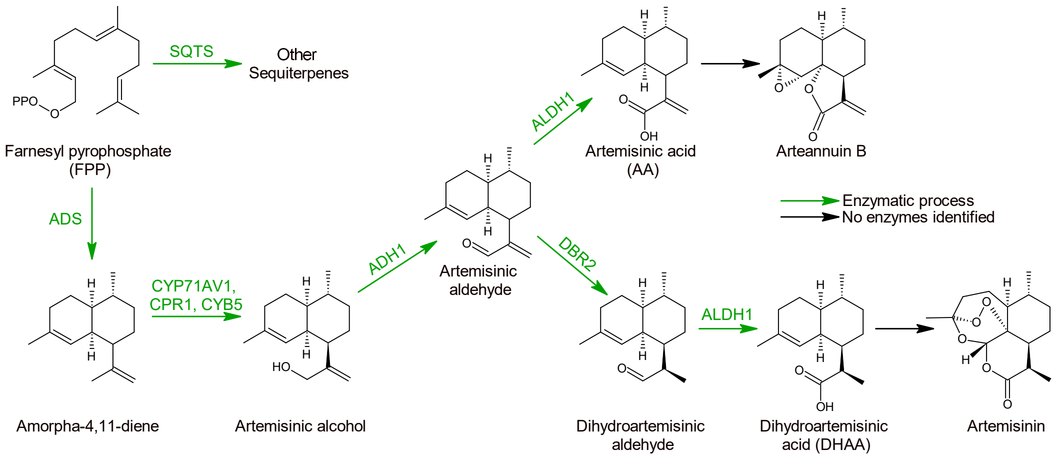

Fig. 2.2: Biosynthetic pathway to artemisinin in *Artemisia annua L.* starting from farnesyl pyrophosphate. Adapted from [51, 64].

precursor of artemisinin [50, 51]. Feeding studies, however, strongly proposed that artemisinin is solely formed by the conversion of DHAA. Artemisinic acid is neither converted to artemisinin nor DHAA [61–64] *in planta* but to arteannuin B [65]. Therefore, AA does not contribute to the formation of artemisinin [65, 66].

In contrast to the previous steps, it is still in question if enzymes are involved in the final conversion of DHAA into artemisinin [67–69]. The conversion was successfully demonstrated via a spontaneous autooxidation process without any enzymes present [70]. The proposed mechanism, derived from these *in vitro* studies, is described in Sec. 2.3.1. Whether plant tissue is tolerant to the harsh conditions required for the spontaneous autoxidation [51, 71] is still in question.

The formation and accumulation of artemisinic acid and dihydroartemisinic acid and their facile conversion *in vitro* to artemisinin made both precursors targets for further optimization of the cultivation and plant processing.

2.1.2 Bio-synthetic precursors as new targets for cultivation and plant processing

A. annua is mainly cultivated in China, India, and Vietnam [23, 39], extending recently to Africa and North America [43, 72, 73]. The content of artemisinin and its precursors in the plant strongly depends on the chosen plant cultivar, the harvest time, and the regional environmental conditions. Traditionally, cultivation focused solely on obtaining plants high in artemisinin content and the overall biomass at harvest time, neglecting AA and DHAA.

The biomass production of plants increases with photoperiods of $13\,\mathrm{h}$ or longer, favoring regions with distinct seasons [43]. In contrast, cultivation in tropical regions favors a high artemisinin content in the plant due to the intense sunlight and warm temperatures.

Depending on the cultivar, the artemisinin content peaks in the late vegetative state or right before flowering [42, 74–76]. With the development of late flowering plants, the growth period was prolonged, yielding higher biomass at the artemisinin peak. Depending on the climatic conditions, the overall cultivation time from planting to harvest takes four to seven months [39]. Exposing the plant to physical stress as short-time drought [77], chilling [55, 78], salinity [79, 80] or intensive irradiation [81–83] enhances artemisinin formation in *A. annua* [84, 85].

While the wild-type contains up to $0.1\,\mathrm{wt}-\%$ artemisinin, the content could be enhanced to $1.5\,\mathrm{wt}-\%$ [39, 43, 85] by genetic engineering [52], selective breeding of the plant [86], and optimization of the cultivation conditions. Depending on the growth conditions, $1\,\mathrm{ha}$ produces $3\,\mathrm{t}$ to $5\,\mathrm{t}$ of dried matter of *Artemisia annua L.* [34, 43], corresponding to a total artemisinin amount of a maximum of $74\,\mathrm{kg}$ [74].

The content of DHAA correlates with the artemisinin levels [32, 55–57, 87]. Many strains, which are high-yielding in artemisinin, contain similar amounts of DHAA of $0.3\,\mathrm{wt}-\%$ to $1.2\,\mathrm{wt}-\%$ [32, 55, 56, 62, 63, 76, 87] (Tab. 2.1). In some cases, even DHAA contents up to $1.8\,\mathrm{wt}-\%$ were reported, almost double the corresponding concentration of artemisinin $(0.95\,\mathrm{wt}-\%)$ [32].

Artemisinic acid can be contained in up to 10-fold concentration than artemisinin [34, 55]. However, plants high in artemisinic acid seem to be low in artemisinin and DHAA, while strains with high artemisinin and DHAA levels exhibit only low concentrations of AA [32, 55, 63, 88]. Due to the joint accumulation with artemisinin, DHAA is the more promising target for further crop breeding.

In addition to cultivation and strain selection, post-harvest treatment by drying intensely affects the plant's artemisinin and dihydroartemisinic acid concentrations [34, 57, 76, 87, 89, 90]. Drying the plant to a moisture content of less than $15\,\%$ supports efficient extraction of the plant material [39, 43]. During the drying process, DHAA contained in the leaves is converted partially to artemisinin. As shown in Tab. 2.1, the drying technique determines the velocity and selectivity of this post-harvest conversion. Drying the leaves in the sun or the shade for several weeks or in an oven for $16\,\mathrm{h}$ leads to almost complete DHAA decomposition [57, 76, 89]. While artemisinin is formed marginally during oven drying, artemisinin contents gain up to $45\,\%$ related to the initial amount by sun-drying [34, 57, 76, 87].

The conversion of DHAA to artemisinin while drying makes the selection based on both artemisinin and DHAA advantageous to raise the overall artemisinin yield obtained from the plant [32, 57]. This step, however, requires leaving the harvested material in the field for several weeks before extraction. Transferring this slow conversion to the intensified and precisely controlled conditions in chemical reactors could achieve an enormously shortened reaction time and improved yield facilitating a more efficient plant-based artemisinin production process.

Tab. 2.1: Contents of artemisinin and dihydroartemisinic acid (DHAA) in the dried weight (DW) and their relative proportion reported for the high-artemisinin-producing chemotype of *Artemisia annua L.*. Drying of the leaves results in partial conversion of DHAA to artemisinin. The studies are ordered according to the measured content of DHAA. [55]

Ref.	Plant material	Content, wt-% DW		[DHAA]/[Arte], %
		DHAA	Artemisinin	
Kær et al.(2013) [91]	Freeze dried	0.02 - 0.20	0.17 - 0.30	10 - 100
Ferreira et al. (2007)[56]	Oven dried	0.10 - 0.20	0.69 - 1.60	12 - 15
Subero et al. (2016)[92]	Dried	0.37 - 0.73	0.80 - 1.30	33 - 66
Larson et al. (2013) [88]	Dried	0.20 - 1.00	0.40 - 1.40	30 - 100
Ferreira et al. (2018) [32]	Oven dried	0.30 - 1.80	0.70 - 1.50	40 - 180
Lommen et al. (2007) [76]	Fresh leaves	0.10 - 0.15	0.10 - 0.15	95 - 105
	Dead leaves	0.03 - 0.05	0.14 - 0.30	20 - 30
Ferreira et al. 2010 [57]	Freeze dried	0.45 - 0.61	0.60 - 0.75	60 - 100
	Oven dried	<0.15	0.80 - 0.90	< 20
	Sun dried		1.00 - 1.10	
	Shade dried		0.90 - 1.10	
Czechowski et al. (2018) [64]	Fresh	< 0.5	0.90	<50
	Dried		1.20	

2.1.3 Further metabolites present in the plant

Besides artemisinin and DHAA, *A. annua* produces a complex spectrum of natural products with over 600 metabolites reported so far [50]. Two of the largest groups are phenolics [50, 64, 93, 94] and terpenes, including sterols and sesquiterpenes. Sesquiterpenes are an exceptionally diverse group in *A. annua* [64], all arising from farnesyl pyrophosphate. More than forty species are connected to the biosynthetic pathway to artemisinin either as precursors or side products (Sec. 2.1.1).
Over 50 phenolic species were isolated from *A. annua* [94]. The most abundant phenolics as artemetin, casticin, eupatin, quercetin, chrysoplenol D, and chrysoplenetin D [95, 96] belong to the class of flavonoids. Flavonoids gained importance due to their synergistic enhancement of artemisinin's antimalarial and anti-cancer activity in whole-plant extracts [90, 94, 97–99]. The richness of *A. annua* with phenolics and their economic value makes the optimization of the production process to obtain both artemisinin and flavonoids a promising option [25, 94]. However, flavonoids also complicate the purification of artemisinin by hindering crystallization [100].

Besides these characteristic species, extraction of the plant also yields waxes and plant dyes as tocopherol, β-carotine and chlorophylls [101]. Due to the complex product spectrum, the separation of artemisinin from the extract is a multi-step process. To ease the downstream processing, an extraction process is required which selectively separates only the target compounds, e.g., artemisinin and DHAA, from the plant tissue [101].

2.1.4 Extraction and purification of artemisinin

The dried leaves are extracted with organic solvents, like hexane, petroleum ether, toluene, and ethanol in batch-wise processing for industrial production. The leaf-solvent mixture is stirred or steeped for up to $12\,\mathrm{h}$ [39] before reaching equilibrium [102–104]. Percolation and Soxhlet-extraction are used less frequently [104]. Processing at elevated temperatures and reflux shortens the extraction time [105]. In this conventional way, $40\,\%$ to $70\,\%$ of the total artemisinin content in the leaves is extracted [39, 103]. The incomplete recovery of artemisinin is mainly attributed to the decrease in the concentration gradient when reaching equilibrium, potential degradation of artemisinin, and insufficient mixing [104].

Recent research focused on substituting the currently used hazardous and explosive solvents to more environmentally benign alternatives [106–109]. A second approach aimed to increase the extraction efficiency by accelerating the mass transfer between leaf and solvent.

In the endeavor to find solvents which combine environmental with extraction efficiency, special attention was paid to the use of refrigerants as R1234yf [25, 92, 110], supercritical carbon dioxide (scCO$_2$) [111–120], deep eutectic solvents [121, 122], hot water [108], ionic liquids [123–125], and other solvents with high-boiling point [106, 126]. So far, none of these mentioned alternatives could substitute conventional hydrocarbon solvents to a substantial part, despite clear benefits in the specificity and efficiency of the extraction [92, 103, 109]. The reasons for this market resistance are the need for either cost-intensive and specialized equipment, e.g., for scCO$_2$ and R1234yf, or the high cost and limited availability of proposed solvent, e.g., for deep eutectic solvents, refrigerants, and ionic liquids.

The second approach to enhance artemisinin extraction focuses on accelerating the mass transfer. Methods to intensify the contact between leaves and solvent are the application of pressure [127, 128], microwave-assisted heating, and ultrasound [109, 129, 130] during extraction. Applying pressure of $35\,\mathrm{MPa}$ [127, 128] and microwave-assisted extraction [131] reduces the required extraction time from previously several hours to less than $30\,\mathrm{min}$ but does not affect the overall amount of

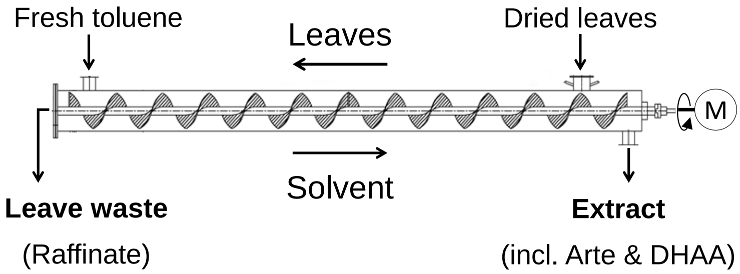

Fig. 2.3: Schematic representation of the counter-current screw extractor developed and implemented by Truong Giang Vu for continuous extraction of *Artemisia annua L.* [137].

artemisinin obtained. Instead, sonication acts in a two-fold manner. It accelerates the mass transfer and disrupts leaf tissue [104]. The latter effect results in an up to $60\,\%$ increase in the recovery of artemisinin [132, 133] but also a less selective extraction due to the enhanced release of other metabolites [104, 134].

A third approach to achieving high mass transfer rates is the optimal exploitation of concentration gradients [135] during extraction by counter-current processing [136]. Troung Giang Vu and colleagues at the *Max Planck Institute for Dynamics of Complex Technical System* recently adapted this approach and developed a continuous extraction process to produce artemisinin based on a counter-current screw extractor (Fig. 2.3). The counter-current direction of solid and liquid streams enables a four-fold increase in productivity compared to batch processing [137].

The effluent stream exiting the extraction constitutes a complex mixture of metabolites of the plant, including artemisinin, DHAA, waxes, plant dyes, and flavonoids (Sec. 2.1.3). The separation of artemisinin from these co-extracted compounds is a complex task that requires coupling of several adsorption, chromatography, and crystallization steps [138, 139].

In industrial production, the extract is first subjected to adsorption, e.g., on silica gel [140] or celite-carbon mixtures [100], before the extract is concentrated by evaporation. The primary separation is achieved by cooling crystallization [104]. The obtained crystals are recrystallized in ethanol to improve the purity further. The presence of co-extracted metabolites as waxes and especially flavonoids [100] hinders the crystallization and causes low yields or low product purity necessitating the initial adsorption step [104].

Recent research focused further on optimizing the purification step either by application of sophisticated chromatographic methods [102, 141–143], selective adsorption of artemisinin on specifically designed polymers [140, 144], selective desorption from a solid support [145], or coupling of chromatography with crystallization [146–149]. A second approach targeted the parallel purification of artemisinin with other co-extracted products of value as its precursor dihydroartemisinic acid [143,

150] or flavonoids [25].
The technical complexity and the corresponding high investment cost of the required equipment limited the industrial application of the previously stated processes. A further challenge is the significant variability in the plant metabolic profile and the corresponding extracts, which complicates the development of a purification method that can be universally applied to all *A. annua* sources.

In summary, the primary resource for the antimalarial artemisinin is still its natural source *Artemisia annua*. The biosynthesis of artemisinin involves a sequence of enzyme-catalyzed and non-enzymatic steps which form various sesquiterpenes, including dihydroartemisinic acid, the late-stage precursor to artemisinin. The cultivation of the plant takes 4 to 7 months. The plant can contain similar or higher contents of DHAA compared to artemisinin. After harvest, the plant material is left in the field for several weeks to dry. In this time, the DHAA is partially converted to artemisinin. The dried plant matter contains up to $1.5\,\mathrm{wt-\%}$ of artemisinin. Extraction of artemisinin from the plant is based on batch-wise processing by stirring the leaves in organic solvents. The obtained extract is a complex mixture of artemisinin and further plant metabolites as residual DHAA, flavonoids, and plant dyes as chlorophyll. Artemisinin is purified by a sequence of adsorption and crystallization steps. The process of plant cultivation, extraction, and purification is well established, even though there is major optimization potential. The disadvantages of plant-based production are the changing area used for the cultivation of *A. annua*, the long cultivation time of the plant, and the volatility in the obtained artemisinin yield. All three factors lead to instability in the artemisinin supply and thus to drastic shortages in antimalarial medications in recent years [26]. Therefore, plant-independent production pathways were developed as an alternative.

2.2 Total syntheses of artemisinin

The total synthesis of artemisinin was investigated intensively soon after isolation of artemisinin [151] due to its potential in ensuring stable artemisinin supply. The first multi-step synthesis was published by Schmid and Hofheinz from Hoffmann-La Roche in 1983, starting from iso-pulegol. The synthesis involves 11 steps yielding less than $5\,\%$ of artemisinin [152]. Soon afterward, several alternative routes were developed, which utilize terpene-based chemicals as starting material [153–161]. The developed syntheses are summarized in Fig. 2.4.

A key intermediate in many developed pathways is dihydroartemisinic acid or one of its derivatives. The final conversion to artemisinin proceeds via a similar

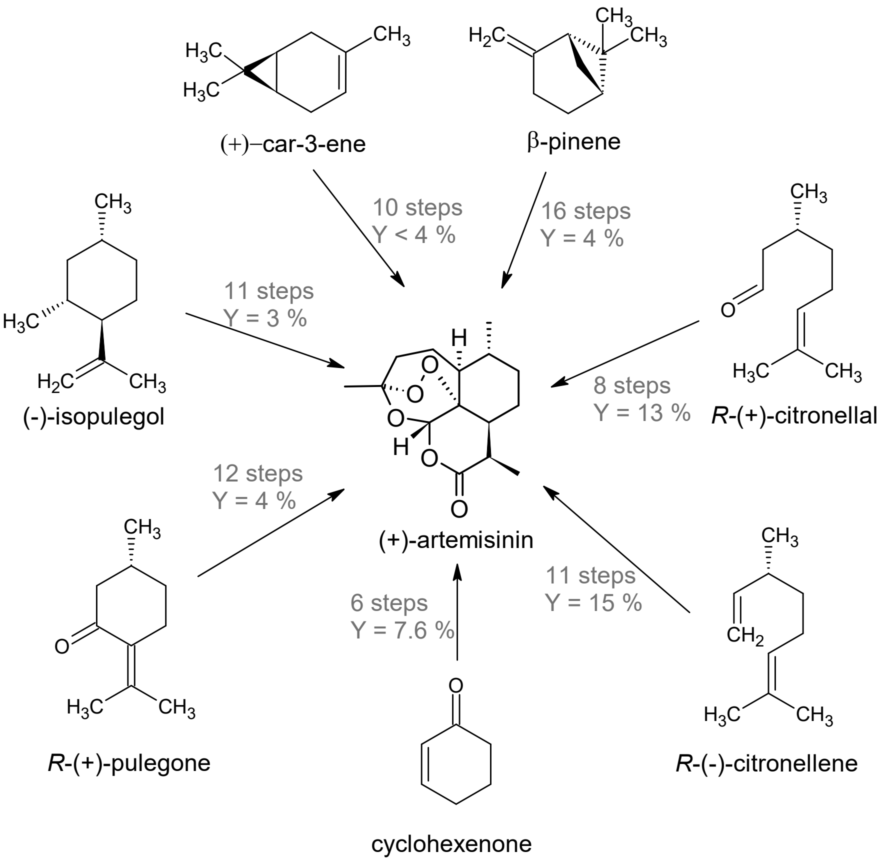

Fig. 2.4: Summary of the total synthesis routes and the obtained yield, Y, of artemisinin sorted by the starting material applied [153–164].

pathway as the partial synthesis involving singlet oxygen and acid-catalyzed ring condensation (Sec. 2.3.1)[152–154, 156, 158–162]. The main difference between the published routes lies within the formation of this DHAA-related intermediate. Inspired by the biosynthesis, Yadav et al. demonstrated that this intermediate can be obtained from the conversion of amorphadienes [160, 161]. New total synthetic approaches focus on optimizing the production of DHAA derivatives from known intermediates of the biosynthesis [165–167].

The total synthesis with the highest total yield of artemisinin with $15\,\%$ was developed by Krieger et al. [161], converting R-citronellene in 11 steps. The use of S-citronellene gives the (-)-artemisinin, the enantiomer of the natural product (+)-artemisinin. The pathway with the minor synthetic steps was demonstrated by Cook et al., starting from the abundant and cost-efficient reactant cyclohexenone [162]. In a 6-step and 5-pot route artemisinin, was obtained in a $7.6\,\%$ yield. The cost for this most efficient total synthesis route, so far, was estimated to be still $500\,\$/\mathrm{kg}$ to $750\,\$/\mathrm{kg}$, excluding the cost for chromatography, reactor time, and labor

[164]. Currently, total synthesis is not a viable alternative to plant-based artemisinin production.

2.3 Semi-synthetic production of artemisinin

The third option to total synthesis and extraction of the target from its natural source is semi-synthetic production. In this approach, the starting point is a direct precursor of the target that is either more abundant or obtained from a different source. This precursor is then transformed into the target compound in feasible chemical synthesis. In the case of artemisinin, such precursors are artemisinic acid and dihydroartemisinic acid. Both are formed within the plant *A. annua* and obtained as byproducts of the extraction (Sec. 2.1.2). Aiming at the independence of artemisinin production from plant supply, Keasling and co-workers [27, 28, 168] developed in cooperation with Amyris a biotechnological process producing artemisinic acid by genetically-engineered yeast.

Starting from artemisinic acid, dihydroartemisinic acid is accessible by hydrogenation. DHAA can then be transformed in an established two-step one-pot synthesis to artemisinin. In this thesis, the term "partial synthesis" exclusively refers to that final conversion of DHAA to artemisinin. The following section introduces the reaction mechanism of the partial synthesis, its industrial realization, and the recent progress in optimizing this reaction step regarding efficiency, safety, and sustainability.

2.3.1 Reaction mechanism of the partial synthesis from dihydroartemisinic acid to artemisinin

The conversion of DHAA to artemisinin is crucial in all production pathways of artemisinin presented so far. Within the biosynthesis *in planta*, DHAA is formed as the late-stage intermediate to artemisinin (Sec. 2.1.1). Many total synthetic pathways and the semi-synthetic method only differ in how to obtain DHAA but use a similar synthetic step from DHAA to artemisinin. The comparison between the conversion of DHAA *in vitro* and *in vivo* inclines a substantial similarity between both processes [50, 66, 70]. Thus, understanding the reaction mechanism of this conversion gives insight into the formation of artemisinin *in planta* and raises optimization potential for both total- and semi-synthetic production.

The conversion of DHAA to artemisinin can be separated into three steps illustrated in Fig. 2.5. The reaction is initiated by the *in situ* formation of singlet oxygen, which

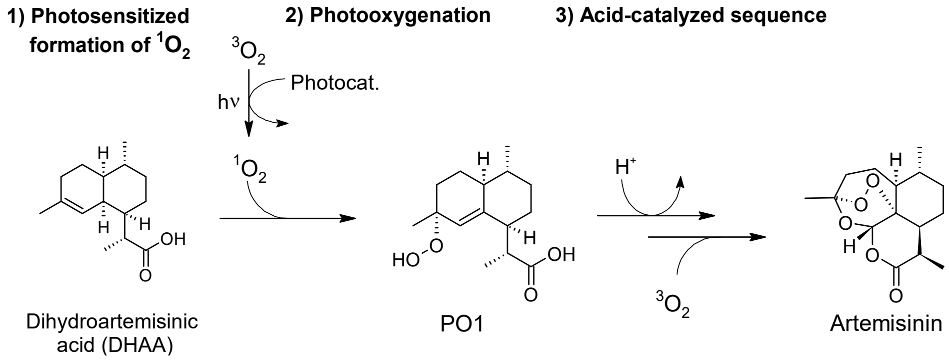

Fig. 2.5: The partial synthesis of artemisinin starting from dihydroartemisinic acid consists of three main reaction steps initiated by the formation of singlet oxygen.

reacts with dihydroartemisinic acid forming a tertiary hydroperoxide as the central intermediate. In the presence of an acidic catalyst, the hydroperoxide undergoes a complex rearrangement sequence, including the incorporation of a second equivalent of oxygen. In the following the three main reaction steps are described in more detail.

2.3.1.1 In-situ formation of singlet oxygen

Two commonly used methods to produce singlet oxygen are photosensitization and molybdate-catalyzed disproportionation of hydrogen peroxide [169–171]. Both methods have been successfully demonstrated for the partial synthesis of artemisinin [172].

The photosensitized production of singlet oxygen requires a photo-active molecule as catalyst, the photosensitizer, which absorbs light of a matching wavelength and transfers this energy to oxygen, forming singlet oxygen [173]. In contrast, the "dark" formation of singlet oxygen utilizes the disproportionation of hydrogen peroxide in the presence of molybdate oxide as the catalyst [28, 170]. Photosensitization is currently the preferred method of singlet oxygen formation for artemisinin partial synthesis due to less reagent consumption and higher selectivity observed [29].

Various chemical species with large delocalized π-systems can be used as photosensitizers [174, 175]. The chemical structures of an artificial and a natural photosensitizer, 9,10-dicyanoantracene (DCA) and chlorophyll A, are shown in Fig. 2.6. 9,10-Dicyanoanthracene is a highly active photosensitizer [174, 176–178] which is stable even in acidic conditions. Both properties make DCA a suitable photosensitizer for the partial synthesis of artemisinin *in vitro* [179]. In the plant, the present chlorophyll species are supposed to initiate the conversion of DHAA [39, 50, 62]. The ability of the chlorophylls to catalyze singlet oxygen formation is often

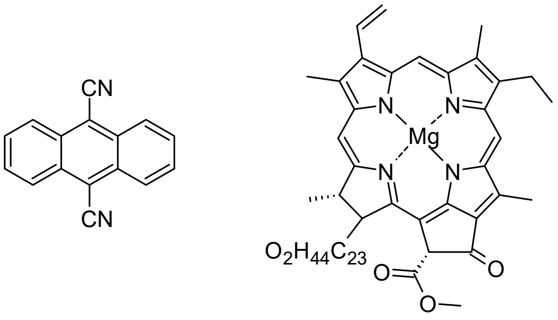

(a) DCA **(b)** Chlorophyll A

Fig. 2.6: Chemical structures of two highly potent photosensitzers applicable for the partial synthesis of artemesinin: a) 9,10-Dicyanoantracene (DCA) and b) Chlorophyll A.

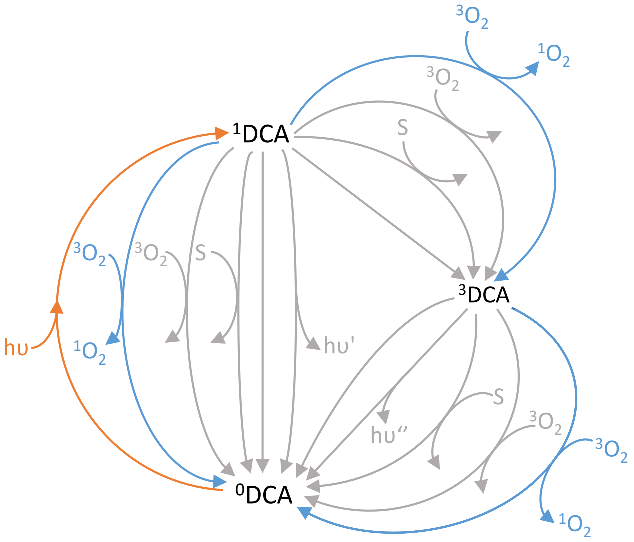

Fig. 2.7: Reaction network of the photosensitized formation of singlet oxygen with 9,10-dicyanoanthracene (DCA) [176, 178, 184–187]

regarded as an undesired side reaction leading to cell death [180–183].

The catalytic cycle of light absorption and energy transfer to oxygen is illustrated in Fig. 2.7 using the example of DCA. After absorption of one photon, DCA is excited to its singlet state ^{1}DCA($276.1\,\mathrm{kJ}$) [185]. ^{1}DCA can now transfer energy to oxygen, forming one molecule of $^1O_2$ ($94.1\,\mathrm{kJ}$) and falling back either to its triplet ^{3}DCA or its ground state ^{0}DCA. This triplet state is still high enough in energy ($105\,\mathrm{kJ}$) to excite another oxygen molecule, producing a second molecule of singlet oxygen [177]. Thus, the absorption of one photon may result in the formation of a maximum of two molecules of $^1O_2$. Besides these desired reaction pathways, however, the excited states of DCA can be quenched by several deactivation mechanisms, including fluorescence, phosphorescence, internal conversion, intersystem crossing, oxygen-induced quenching, and substrate-induced quenching [176, 177, 184–187]. The

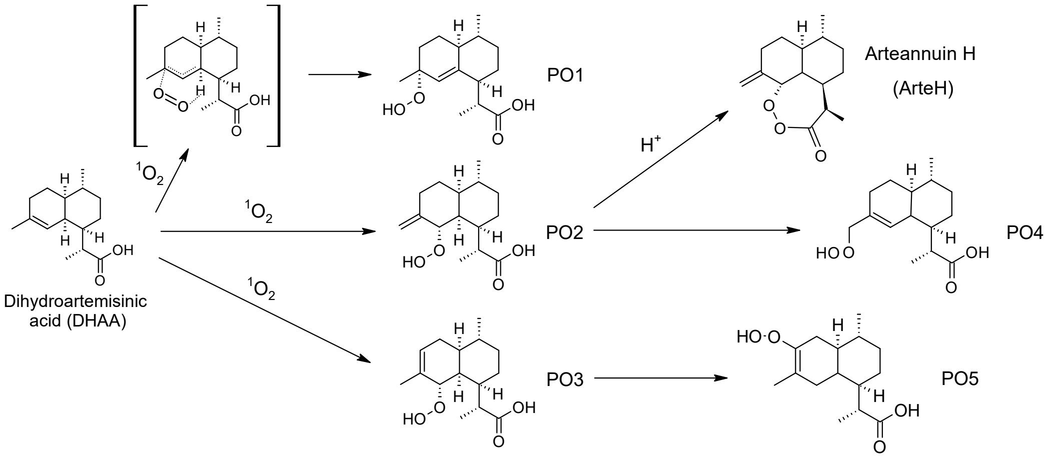

Fig. 2.8: Ene-type reaction of dihydroartemisinic acid (DHAA) forming three different hydroperoxides and their consecutive rearrangement products [197, 198].

contribution of all these reaction steps to the total photosensitization performance depends strongly on the solvent [177, 178, 188], the presence of other quenchers [184, 189], and the reaction conditions, especially the available oxygen concentration and reaction temperature [184, 185, 187]. The primary photon consumption is attributed to quenching of the excited DCA by oxygen leading $^1O_2$ formation and to deactivation by fluorescence [186].

In the case of chlorophyll, excitation of the dye by light absorption results in the maximum of one equivalent of $^1O_2$ produced [180, 181]. The highest rates of singlet oxygen formation were observed with pheophytin, a degradation product of chlorophyll missing the central magnesium ion [190, 191].

Once singlet oxygen is formed, it either reacts with DHAA or is quenched to its triplet state. The lifetime of singlet oxygen is a very solvent-dependent property increasing with decreasing polarity of the solvent [192–194].

2.3.1.2 Ene-type reaction to intermediate hydroperoxides

The reaction between DHAA and singlet oxygen follows an ene-type mechanism also known as Schenk-reaction [195, 196] (Fig. 2.8). The reaction proceeds via a 6-ring transition state leading to a migration of the double-bond and a 1,5-shift of the ene-hydrogen. Since this transition state forms exclusively on the sterically less hindered α-face of the molecule, the conversion of DHAA with $^1O_2$ is enantioselective. Depending on the H-atom, which is shifted, three different hydroperoxides are formed. Due to the cis-effect of the ene-type reaction, the main product is the desired tertiary hydroperoxide PO_1 [199–201]. The secondary hydroperoxide PO_2 is the main byproduct, while PO_3 is only formed in minor quantities [179, 198]. All three species are semi-stable and undergo slow rearrangement to other hydroperoxides (Fig. 2.8) and the endoperoxide Arteannuin H within hours after formation [198]. The total decomposition of the hydroperoxide occurs within weeks of storage [70]. PO_1 is the only species which can react to artemisinin when treated with acid in the presence of oxygen.

2.3.1.3 Acid-catalyzed reaction sequence

While the ene-type reaction of DHAA with singlet oxygen is well understood, the mechanism of the subsequent cleavage and rearrangement to artemisinin is not yet fully elucidated. The reaction mechanism of this transformation was postulated first by Acton et al. [199] and extended by Haynes et al. [202–204], Brown et al. [66, 70, 197, 198], and Varela et al. [205, 206]. The main steps are shown in Fig. 2.9.
The pathway to artemisinin from PO_1 is initiated by the protonation or lewis-acid promoted complexation of the hydroperoxide group at terminal position [197]. Following a Hock-cleavage mechanism [207], the protonation leads to the ejection of water and the formation of a carbenium ion. After a nucleophilic attack of water, the carbenium ion rearranges to a seven-membered hemiacetal. However, this postulated intermediate was not yet observed experimentally [70, 203]. Several groups reported that trace quantities of water are required for the reaction to start [199, 208]. The proximal protonation of the hydroperoxide PO_1 results in the ejection of hydrogen peroxide and the formation of dihydro-*epi*-deoxyarteannuin B BP_3 [199, 205].
The hemiacetal is cleaved to a semi-stable enol [70, 204]. The enol was isolated and characterized at less than $-20\,°C$ [70, 203]. With increasing temperature, the enol reacts to the seco-cadinane. Treating the enol with acid results in the formation of the lactone BP_4 as the main byproduct [70, 203]. BP_4 is stable in acidic conditions and constitutes one endpoint of the reaction network [199].

In the presence of oxygen, the enol reacts with triplet oxygen forming a hydroperoxyl aldehyde, which rearranges to a peroxy-hemiacetal. Both postulated intermediates could be isolated in studies on esterified DHAA [202, 203] but not when DHAA was used as starting material [70]. In the presence of a strong Brønstedt acid [202], the formed peroxy-hemiacetal undergoes further cyclization and water ejection yielding the desired product artemisinin. This final reaction is irreversible. Artemisinin is stable in reaction conditions and only depletes in strongly acidic conditions over several hours [209].
Experiments with labeled compounds support the postulated mechanism via the hemiacetal and the enol [199, 205, 206]. Utilization of labeled $^1O_2$ showed that the

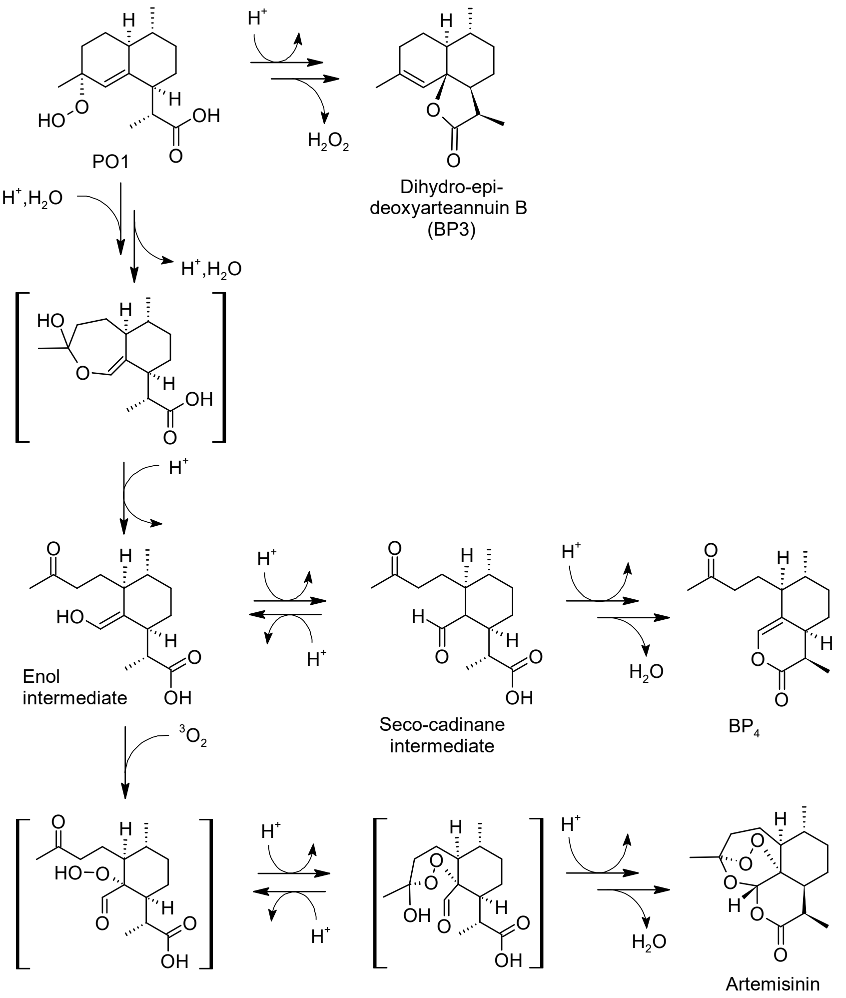

Fig. 2.9: Proposed mechanism for the acid-catalyzed cleavage of PO_1, the incorporation of triplet oxygen, and the subsequent cyclization to artemisinin adapted from [70].

oxygen incorporated in the ene-type reaction is found in the lactone rings in the final artemisinin molecule while O_2 from the second oxidation builds the endoperoxide bridge [199].

The main products evolving from the conversion of dihydroartemisininic acid are artemisinin, dihydro-*epi*-deoxyarteannuin B, the lactone BP_4, and arteannuin H resulting from the acid-catalyzed conversion of PO_2 [30, 70, 179, 198–201, 203, 204, 208]. Depending on the reaction conditions, these four compounds account for up to 80 % of the initially applied amount of DHAA [179, 199]. Apart from those, many other species were isolated and identified as byproducts from the partial synthesis [70] (Fig. 2.9). However, no complete picture of the whole reaction sequence is available so far since none of those studies mentioned above could recover the initial reactant amount entirely in identified products.

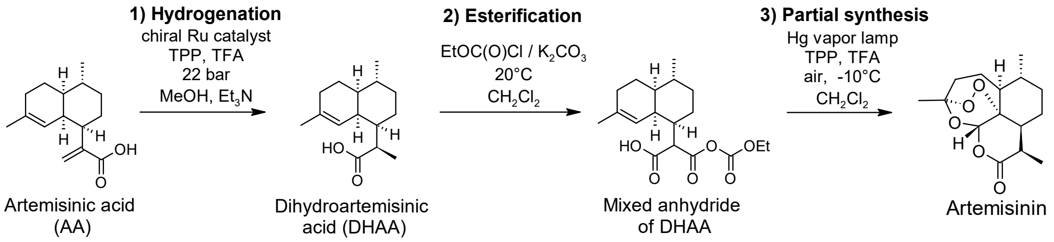

Fig. 2.10: Process path of industrial plant-independent semi-synthetic production of artemisinin starting from artemisinic acid produced by fermentation of genitically engineered yeast. Reproduced from [29].

The strong solvent dependence of the conversion of PO_1 adds a level of complexity. In polar solvents, the formation of artemisinin proceeds very slowly in the presence of Brønstedt acids [201, 208, 210]. However, the addition of Lewis acids accelerates the enol's oxidation resulting in the faster transformation to artemisinin [202, 203]. Best partial synthesis performance is obtained in nonpolar solvents like hexane, toluene, and halogenated solvents as dichloromethane [179, 210, 211]. Despite the complex reaction mechanism, DHAA can be converted enantioselectively to artemisinin in a yield of up to $71\,\%$ [179, 212]. This selective synthesis step facilitated the development of an industrial plant-independent production step for artemisinin. Finding optimal combinations of reaction solvent, a catalyst for singlet oxygen production, an acidic catalyst for artemisinin formation, and reactor concept for efficient, sustainable and safe processing is still a major field of research [213].

2.3.2 Industrial realization of semi-synthetic artemisinin production

In 2013, the pharmaceutical company Sanofi implemented a semi-synthetic, plant-independent production of artemisinin at industrial scale in Garessio, Italy [29]. The pathway is illustrated in Fig. 2.10. The process was based on the work of the Keasling group and Amyris [27, 28], but optimized to meet economic and safety requirements of large-scale production [29, 30].

The starting point of the process is the production of artemisinic acid by large-scale fermentation of *Saccharomyces cerevisiae*. After purification, AA is converted to DHAA by diastereoselective hydrogenation on chiral ruthenium-based catalysts. The hydrogenation is completed after $6\,\mathrm{h}$ at $22\,\mathrm{bar}$ H_2 and $25\,°\mathrm{C}$ achieving a $99\,\%$ yield of DHAA and a selectivity of $95\,\%$ of the desired enantiomer. Before the partial synthesis to artemisinin, DHAA is derivatized to a mixed anhydride (DHAEMC) by esterification with ethyl chloroformate in the presence of potassium carbonate. The activation of DHAA facilitates a higher yield in the final partial synthesis.

The conversion to artemisinin is performed in semi-batch mode in a loop reactor irradiated by a medium pressure mercury lamp and cooled to $-10\,°\mathrm{C}$. The catalysts tetraphenylporphyrine and trifluoroacetic acid are added directly to the DHAEMC containing product solution in dichloromethane. The required oxygen is bubbled through the reaction solution at ambient pressure. No absolute data was given about the duration and yield of this reaction step. After partial synthesis, artemisinin was obtained by anti-solvent crystallization in $55\,\%$ overall yield regarding the starting material artemisinic acid.
With the described process Sanofi could produce $35\,\mathrm{t}$ in 2013 and $60\,\mathrm{t}$ in 2014 with a batch size of $370\,\mathrm{kg}$ each [29]. The plant, however, did not produce any artemisinin in 2015 and was later sold [26]. Production was restarted partly in 2017 [31]. The price from semi-synthetic artemisinin was set to 400 $/kg, attributing both to the high manufacturing cost and a threshold to not undercut prices for plant-based production of artemisinin.

2.3.3 Partial synthesis of artemisinin: Recent developments

The industrial process of semi-synthetic artemisinin production is one of the few examples of photochemical reactions operated at a larger scale [163]. However, the high yields achieved for artemisinin are obtained by utilizing halogenated solvents, homogeneous catalysts, energy-intensive mercury-pressure lamps, labor-intensive semi-batch processing, and long reaction times. Therefore, recent research [213] focused on using

- more efficient light sources,
- less toxic solvents,
- continuous processing,
- new reactor concepts to intensify photon- and mass transfer, and
- heterogeneous catalysts to enable easy recycling.

Extending their work on industrializing the partial synthesis, Burgard et al. from Sanofi [30] substituted the mercury-medium-pressure lamp with light-emitting diode (LED) modules of a matching wavelength ($432\,\mathrm{nm}$, $18\,\mathrm{W}$). The partial synthesis starting from esterified DHAA was performed in a lab-scale loop reactor with trifluoroacetic acid, dichloromethane as the solvent, and the photocatalyst tetraphenylporphyrine (TPP). Illuminating the solution by LEDs, the reaction time could be shortened from $12.5\,\mathrm{h}$ to $8\,\mathrm{h}$ with a final yield of $50\,\%$ artemisinin after purification. Repeating these investigations with DHAA without prior derivatization showed that both reactants are comparable regarding the artemisinin yields ($45\,\%$ to $59\,\%$), reaction time, and safety requirements.

The Seeberger research group [179, 211] pioneered in shortening the residence time of the synthesis by using small-scale tubular reactors operated continuously and in segmented two-phase flow (Sec. 3.1). The small diameter and the specific flow pattern ensured high mass transfer rates and intensive light irradiation in the reactor. In the presence of TPP as photosensitizer, the conversion of DHAA to artemisinin reaches completion after $9\,\mathrm{min}$ residence time in the whole reactor. An artemisinin yield of $39\,\%$ to $46\,\%$ was achieved after purification. The process was optimized by switching from CH_2Cl_2 to toluene as the solvent and substituting TPP with the more chemically stable 9,10-dicyanoantracene [179]. The selectivity of the initial step, the photooxidation, was increased by lowering the reaction temperature to $-20\,°\mathrm{C}$. Coupling the photooxygenation step with the acid-catalyzed reaction sequence resulted in an overall artemisinin yield of $65\,\%$ and a DHAA conversion of $97\,\%$ after a total residence time of $12\,\mathrm{min}$. With the developed reactor setup, $165\,\mathrm{g}$ artemisinin can be produced per day, resulting in a space-time yield of $3500\,\mathrm{kg}\,\mathrm{m}^{-3}\,\mathrm{d}^{-1}$ [179]. The methodology of using milli-structured reactors with intensive mixing for the partial synthesis to artemisinin was later extended by Lee et al. using a continuously operated vortex reactor [210].

The studies on a continuous partial synthesis were complemented by developing a process for the continuous purification of artemisinin [214]. Due to the complex nature of the reactor effluent, the purification demanded simulated moving bed chromatography (SMB) coupled with crystallization. The chromatographic step separated artemisinin from the photocatalyst DCA, which otherwise co-crystallizes with the target in a stand-alone crystallization step, contaminating the product. The coupled process achieves a purity of $99.9\,\%$ with a $61.5\,\%$ yield based on the artemisinin content in the reactor effluent. In a later study, a similar purity was obtained in a single crystallization step [215].

The partial synthesis is often performed in nonpolar solvents due to the decreased selectivity to artemisinin observed for polar solvents [179](Sec. 2.3.1). However, these solvents are often toxic or highly flammable, posing a high risk to the industrial process. Amara et al. [208, 210] developed two process options to reduce the environmental impact of semi-synthetic artemisinin production, changing both the catalyst and solvent system. The first approach uses aqueous solvent mixtures, while the second is based on liquid CO_2 as solvent and a dual-functional heterogeneous catalyst. The first process alternative applies solvent mixtures of ethanol and tetrahydrofuran (THF) with water in combination with water-soluble photocatalysts, as

$[Ru(bpy)_3]Cl_2$. This way, they obtained similar yields of artemisinin of up to $66\,\%$, as observed previously in dichloromethane and toluene. The use of polar solvents also allowed the substitution of trifluoroacetic acid with cheaper inorganic acids, e.g., phosphoric and sulfuric acid, and a simpler separation of artemisinin from the reactor effluent. By evaporating THF or ethanol partially, artemisinin crystallized while the added catalysts stayed in the solution and could be recycled [208].
Another solvent alternative is liquid carbon dioxide blended with toluene [208, 216]. This approach requires operation at an elevated pressure of $18\,\mathrm{MPa}$ but enables a high oxygen solubility. Amara et al. investigated liq. CO_2 together with a dual-functional catalyst, which combines the acidic effect of the base material Amberlyst 15 with the photocatalytic effect of tetraphenylporphyrine. This solvent catalyst combination achieved an artemisinin yield of $50\,\%$.
Other heterogeneous catalysts systems with rose-bengal [217], methylene blue, or porphyrin structures [218] immobilized on polystyrene carrier materials were applied to the photooxidation of DHAA. High yields of $71\,\%$ of artemisinin were obtained with a tailored catalyst consisting of porphyrin metal-organic framework with a large surface area and strong Brønsted acidity incorporated inside the network channels [212]. However, the utilization of heterogeneous catalysts for photoreactions is often difficult due to blocking and shadowing of the light within the reactor resulting in low irradiation efficiency at a larger scale [219].
The partial synthesis of artemisinin serves as a showcase for reactions that either involve limitation by mass and photon transfer or require hazardous solvents, photosensitizers, and acidic catalysts. Various alternatives regarding reactor design, solvent systems, and catalysts were successfully developed for this synthesis. The optimal combination of these options is crucial to achieving a viable overall process.

2.4 Summary

The antimalarial precursor artemisinin is mainly produced from its natural source, the plant *Artemisia annua L.*. The plant's cultivation and subsequent drying takes up to 8 months before the plant material is extracted. The dried matter contains up to $1.5\,\mathrm{wt}-\%$ of artemisinin. Depending on the strain and the cultivation conditions, dihydroartemisinic acid, the late-stage biosynthetic precursor, accumulates up to two-fold compared to the artemisinin content. The dried leaves are extracted batchwise with nonpolar organic solvents while stirred or steeped for several hours. In this way, $70\,\%$ of the artemisinin contained in the leaves is extracted. As an alternative, counter-current continuous extraction can obtain higher recoveries of both artemisinin and DHAA from the plant and achieves a four-fold increased productivity in comparison to batch processing. However, volatile cultivation of *A. annua* has led to shortages in the artemisinin supply in recent years fostering plant-independent production pathways.

Total synthesis of artemisinin is not an economically viable option due to the number of synthesis steps, required intermediate work up, and significant waste production. The partial synthesis starting from dihydroartemisinic acid compromises plant-based production and total-synthesis. DHAA is accessible via fermentation of genetically engineered yeasts producing artemisinic acid and subsequent diastereoselective hydrogenation. The conversion of DHAA to artemisinin is a facile, enantioselective, one-pot synthesis similar to the biosynthesis in the plant. The mechanism is initiated by the photosensitized formation of singlet oxygen, which reacts with DHAA to a hydroperoxide. In the presence of an acidic catalyst, the formed intermediate is cleaved and undergoes a sequence of cyclization reactions and second oxidation yielding artemisinin. Therefore, the synthesis requires the addition of a photocatalyst, an acidic catalyst, and reaction conditions, ensuring a sufficient supply of oxygen and photons.

The industrial process developed for plant-independent artemisinin production utilizes a batch reactor, halogenated solvents, and energy-intensive light sources. Performing the partial synthesis in milli-scaled continuously operated reactors with the accelerated light and mass transfer drastically shortened the reaction time from $12\,\mathrm{h}$ to $15\,\mathrm{min}$. In systematic studies, different combinations of less hazardous solvents, photo- and acidic catalysts were successfully applied, resulting in a wide range of feasible process options.

So far, the partial synthesis was optimized predominantly qualitatively. To obtain an optimal overall process of artemisinin production, the partial synthesis step needs to be designed with respect to all upstream and downstream units. For this task, model-based tools have been proven essential in academia and the pharmaceutical industry. These approaches required predictive but simple models to reduce the computational effort.

The next chapter introduces the methods applied to develop and identify a mathematical model for the partial synthesis of artemisinin.

Kinetics of photoreactions

3

The description of a whole production process constitutes a highly complex mathematical problem with multiple process variables, degrees of freedom and at the same time various constraints, e.g., on product quality and process safety. For each unit within the process, a model is required, which predicts the unit's behavior well but is also simple to enable joint optimization of all involved units [220]. To be predictive and applicable to other systems, the model needs to describe the intrinsic characteristics of the process, e.g., the reaction kinetics, independently of the governing transport phenomena, which are strongly reactor dependent. In the case of the partial synthesis, the decoupling of kinetics and external effects is complicated since the reaction network is complex and masked by photon and oxygen transfer.

Continuous milli- or microstructured reactors are powerful tools to investigate light and mass-transfer-driven reactions since their small dimensions ensure high light absorption rates and accelerated mixing. Quantification of the photon flux incident to the reaction line is crucial to quantify reaction kinetics independent of the reactor geometry or the applied light source. One available approach to measure this quantity is chemical actinometry.

The following chapter introduces the experimental and mathematical tools applied in this thesis to identify a semi-mechanistic model for the partial synthesis from DHAA to artemisinin. First, the main features of continuous milli-scaled reactors are introduced before explaining the basic principles of modeling photooxygenation reactions in this reactor type. The application and limits of chemical actinometry are described specifically for the potassium ferrioxalate actinometer. Finally, the tools applied for the design of experiments and parameter estimation are introduced.

3.1 Flow reactors: A tool for process intensification and investigation of reaction kinetics

The conversion of dihydroartemisinic acid to artemisinin includes light absorption and the incorporation of two equivalents of oxygen. Therefore, the experimental equipment needs to provide high rates of light absorption and a sufficient concentration of oxygen either present in the reaction phase or supplied by fast mass transfer between gas- and liquid phase.

In the recent years, several new reactor concepts [210, 221–238] were developed or adapted to promote the utilization of the unique features of photoreactions [239–242] especially for pharmaceutical industry [243–247]. A reactor type especially suitable for such photooxidation reactions is a continuously operated tubular reactor with a small channel depth, a so-called flow reactor [241, 248]. Reactors with an internal diameter of $\leq 1\,\mathrm{mm}$ are referred to as micro-reactors, while reactors with a larger diameter are called milli-reactors [238].

Several detailed reviews and books [246, 249] summarize the developments in the field of flow chemistry and micro-structured reactors, focusing on best practices in reactor setup and operation [241, 248, 250, 251], chemical synthesis [238, 242, 252–254], process intensification [221, 255–258], photocatalysis in flow [219, 259], solid handling [260], and scale-up [222, 244, 247, 261]. The following section introduces the features of this reactor type as a tool to study the reaction behavior and the kinetics of photon- and mass transfer controlled reactions. For further details, the interested reader is referred to the previously mentioned resources and the references therein.

One essential key feature for applying micro-structured reactors for photoreactions is the short penetration depth, resulting in a more uniform radiation distribution than in batch reactors [238]. The rate of light absorption decreases exponentially with the penetration depth in the absorbing medium. In concentrated solutions, $90\,\%$ of the incident light is absorbed in the reactor's outer $1\,\mathrm{mm}$ to $2\,\mathrm{mm}$ layer [248, 249]. Thus, a large part of the volume in conventional batch reactors is inactive. In contrast, the small channel depth in flow reactors enables 150-fold higher absorption rate densities in milli-scale reactors [262, 263].

The high surface-to-volume ratio also allows fast heat transfer from the environment to the reactor and vice versa [238, 248, 264]. Especially for exothermic reactions, e.g., singlet-oxygen reactions, operation within milli-scale reactors can prevent hotspot formation and enables isothermal conditions [265]. The accelerated heat removal and the overall small holdup of hazardous material in the reactor significantly reduce the safety risks associated with oxidation reactions [265–267].

Another feature of flowreactors is the well-controlled and straightforward multiphase operation [238]. The most common flow pattern of a two-phase flow in these small channel diameters is segmented flow or Taylor flow [268, 269]. As shown in Fig. 3.1a, this flow pattern is characterized by segments of a liquid phase separated by bubbles of an immiscible phase surrounded by thin layer of the liquid phase but otherwise filling the channel diameter entirely [270]. The moving gas

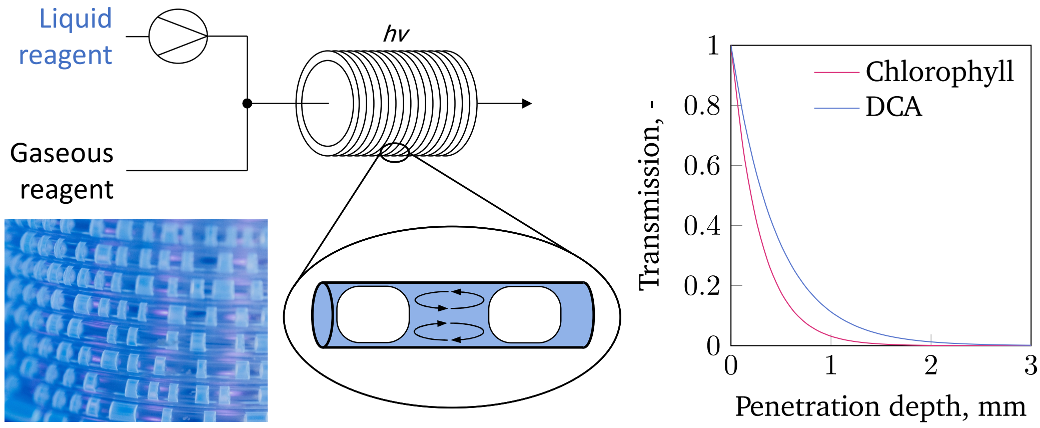

(a) (b)

Fig. 3.1: Process intensification in continuously operated microscale photoreactors: a) Schematic representation of a capillary reactor operated in with two-phase segmented flow (Taylor flow), b) Small diameters of flow reactors enable efficient light absorption in the whole reactor volume.

bubbles induce the formation of internal vortices in the liquid segments [271, 272], achieving intensive mixing. Due to the high surface area between the two phases up to $9000\,\mathrm{m}^2\,\mathrm{m}^{-3}$ [273] and the high mixing rates within the liquid segments, mass transfer rates in milli-scale reactors exceed the rates in conventional multiphase reactors by up to two orders of magnitude [256, 268, 274–276]. Since the liquid slugs do not contact each other directly, back mixing in the axial direction is minimized. Thus, very narrow residence time distributions are obtained in the Taylor flow regime [277].

Besides mixing and mass transfer, the flow pattern also affects photon transfer. The thin films surrounding the gas bubbles contribute significantly to photon absorption and, thus, the formation of reactive species. The absorbed photon flux increases with increasing gas holdup and can exceed photon absorption in single-phase flow by a factor of two [278].

The small dimensions of these reactor systems enable a large flexibility in the specific reactor design [241], which can even be tailored to the specific application case due to rapid prototyping [279] and specifically 3D printing [280–284]. Facile and often used options in photochemistry are coils of transparent tubing from fluorinated polymers [248, 251]. This basic design is easy and cost-efficient to implement, compatible with multiphase flow at elevated pressure, chemical resistant to various solvents, and very flexible in operation [238, 259, 285]. If the range of residence times shifts, the reactor can be adjusted by using tubing of different lengths.

The versatility of possible reactor designs, the accelerated mass and heat transfer, uniform irradiation in the channel, and fast mixing result in improved reaction control and increased selectivities when performing photochemical reactions in multiphase microscale reactors [248, 265, 286]. These features make flow reactors an attractive tool to study the kinetics of reactions that are highly exothermic, involve activation by light, and mass transfer between phases [287–291]. Especially the kinetics of photooxygenations, similar to the initial step of the artemisinin partial synthesis, were successfully investigated using flow reactors [262, 292].

3.2 Modeling of light-induced oxidations in flow reactors

The aim of reaction kinetic studies is the identification of a reliable microkinetic model which can be applied in various contexts independent from the reactor setup where the kinetic measurements were performed. Therefore, modeling the main contributions from reactor-dependent phenomena on the observed reaction performance is essential to allow a conclusion on the target reaction's kinetic constants. This is a particular challenge for photooxygenation reactions since the overall reaction rate is affected by the provision of oxygen and photons, which are both highly dependent on the reactor design. Flow reactors enable high mass and photon transfer rates but also necessitate the consideration of the flow conditions in the reactor line and the spatial distribution of state variables. Fig. 3.2 shows the key elements of the overall process model. The kinetic model requires the absorbed photon flux as an input variable described by the radiation transfer equation. The mass transfer rate depends on the flow rate and distribution of gas and liquid flow in the channel. Balance equations link reaction kinetics and mass transfer.
The following section introduces the general approach to model microkinetics of photoreactions and the reactor model, including photon and mass transfer. In Chapter 7, these concepts are adapted on the specific case of the partial synthesis to artemisinin and the available reactor system.

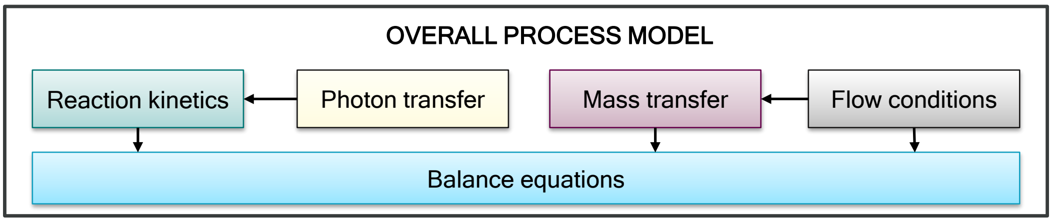

Fig. 3.2: Essential elements of a process model describing light-initiated reactions in flow reactors governed by mass transfer.

3.2.1 Kinetic modeling of photoreactions

For illustration purposes, we consider a chemical reaction from the reactants A and B to the product species C,

$$\nu_{\mathrm{A}}\ \mathrm{A} + \nu_{\mathrm{B}}\ \mathrm{B} \xrightarrow{\mathrm{k}} \nu_{\mathrm{C}}\mathrm{C}. \tag{3.1}$$

The reaction rate r is defined as the number of moles N of a species produced or consumed related to the reaction volume V and time t and its stoichiometric coefficient ν,

$$r = \frac{1}{\nu_A}\left(\frac{dN_A}{d(t \cdot V)}\right). \tag{3.2}$$

According to the power-law approach, the reaction rate can be expressed as the product of the concentrations of the reactants and the rate constant k [293],

$$r = k \cdot [A]^{m_A} \cdot [B]^{m_B}. \tag{3.3}$$

For elementary reactions, the powers m_A and m_B are equal to the stoichiometric coefficients of the reaction considered [293, 294].

In radiation-activated reactions, instead, the reaction rate depends on the absorption of photons [256] and is related to the local volumetric rate of photon absorption (LVRPA) $L_{\mathrm{p}}^{\mathrm{a}}$ [295]. $L_{\mathrm{p}}^{\mathrm{a}}$ is defined as the number of photons absorbed in a specific time interval per volumetric unit of the reactor. The $L_{\mathrm{p}}^{\mathrm{a}}$ results from the present radiation field and varies strongly within the reactor [296]. The radiation field itself depends on the chosen reactor geometry, the light sources, the involved reaction media, and the main absorbing species, including its concentration [297]. The LVRPA can be estimated by solving the radiation transfer equation introduced in the next section.

For single-photon absorption reactions, e.g., photosensitization, the reaction rate r_λ at a emitted wavelength λ is proportional to the local volumetric rate of photon absorption at λ, $L_{\mathrm{p},\lambda}^{\mathrm{a}}$: [296, 298]

$$r_\lambda = \Phi_\lambda L_{\mathrm{p},\lambda}^{\mathrm{a}}. \tag{3.4}$$

The quantum yield Φ describes the efficiency of formation of the respective product related to the number of photons absorbed [299],

$$\Phi = \frac{\text{moles of product formed}}{\text{moles of photons absorbed}}, \tag{3.5}$$

In principle, the quantum yield is defined based on the primary event consisting of absorbing one photon, forming an excited state and the subsequent product formation, or deactivation [300]. The quantum yield of such a primary events is limited from 0 to 1. For practical applications, the definition can be extended to thermal reactions following the primary event compromising the intrinsic quality of the parameter [298]. Values greater than 1 are possible for this efficient quantum yield.

The quantum yield of singlet oxygen is not a constant but depends on the concentration of dissolved oxygen in the reaction medium

$$r_{^1\mathrm{O}_2,\lambda} = \Phi_{^1\mathrm{O}_2,\lambda}([\mathrm{O}_2]) L^{\mathrm{a}}_{\mathrm{p},\lambda}. \tag{3.6}$$

Thus, the modeling of singlet oxygen formation requires an accurate description of the radiation and the mass transfer phenomena in the reactor. Due to the large number of deactivation reactions following the initial excitation of a photosensitizer, the modeling of the photosensitization kinetics requires simplification of the reaction network to obtain identifiable kinetic models [176, 185, 186].

3.2.2 Radiation transfer

The quantification of the LVRPA necessitates the modeling of the radiation field in the reactor line. The radiation intensity I quantifies the radiation energy transmitted [301] relative to the direction Ω, area A, wavelength λ, and time t [256]. The radiation distribution within the reaction line can be determined by the radiation transfer equation (RTE). The RTE describes the change in light intensity along its optical path s by emission, absorption, or scattering [298, 301]. Based on the assumption of steady-state, elastic scattering, and negligible radiation emission, the RTE can be simplified to

$$\frac{dI_\lambda(s,\Omega)}{ds} = \underbrace{-\kappa^v_\lambda(s)\cdot I_\lambda(s,\Omega)}_{\text{Absorption}} - \underbrace{\sigma_\lambda(s) I_\lambda(s,\Omega)}_{\text{Out}-\text{scattering}} + \underbrace{\frac{\sigma_\lambda(s)}{4\pi}\int_{\Omega'=0}^{4\pi} I_\lambda(s,\Omega')p(\Omega' \longrightarrow \Omega)\mathrm{d}\Omega'}_{\text{In}-\text{scattering}}. \tag{3.7}$$

The first term includes attenuation by absorption with κ^v as volumetric absorption coefficient. The second term describes losses by scattering of photons out of the line of propagation with σ as volumetric scattering coefficient. The third term regards the scattering of photons from other directions Ω' into the direction Ω [300, 301]. For complex systems, e.g., heterogeneous photocatalysis, the RTE needs to be solved numerically [302]. Based on the local radiation intensities, the LVRPA at a wavelength λ can be calculated by integration [301]:

$$L^{\mathrm{a}}_{\mathrm{p},\lambda} = \kappa^v_\lambda(s) \int_{\Omega=4\pi} I_{\lambda,\Omega} \mathrm{d}\Omega \tag{3.8}$$

For a detailed derivation of the RTE, the interested reader is referred to the work of Alfano et al. [298, 301]. In the case of a homogeneous medium, the RTE can be simplified by neglecting the effect of scattering [273, 298, 300],

$$\frac{dI_\lambda(s,\Omega)}{ds} = -\kappa^v_\lambda(s) \cdot I_\lambda(s,\Omega). \tag{3.9}$$

Integrating Eq. (3.9) from the path start, $s = 0$, to the total optical pathlength l_{opt} yields the Bouguer-Lambert-Beer relation [303] for one absorbing species,

$$I_\lambda = I^0_\lambda \cdot e^{-\kappa_\lambda \cdot c \cdot l_{\mathrm{opt}}}. \tag{3.10}$$

with c as the concentration of the absorbing species and κ as the molar absorption coefficient. For one-directional light emission, the integration of Eq. (3.10) in Eq. (3.8) and subsequent integration yields a description for the absorbed volumetric photon flux $L^{\mathrm{a}}_{\mathrm{p},\lambda}$ in dependence on the incident volumetric photon flux $L_{\mathrm{p},\lambda}$ [298],

$$L^{\mathrm{a}}_{\mathrm{p},\lambda} = L_{\mathrm{p},\lambda} \cdot \underbrace{\left(1 - e^{-\kappa_\lambda \cdot c \cdot l_{\mathrm{opt}}}\right)}_{f} s. \tag{3.11}$$

The second term represents the fraction of the incident photon which is absorbed by the irradiated medium, also referred to as absorption factor f. $L_{\mathrm{p},\lambda}$ is determined based on the total incident photon flux q^0_p and its spectral distribution g_λ related to the volume of the absorbing medium V^a:

$$L_{\mathrm{p},\lambda} = \frac{q^0_p \cdot g_y}{V^a} \tag{3.12}$$

The connection between the absorbed, incident photon flux and the emitted photon flux from the light source $q_{p,em}$ is illustrated in Fig. 3.3. For polychromatic irradiation,

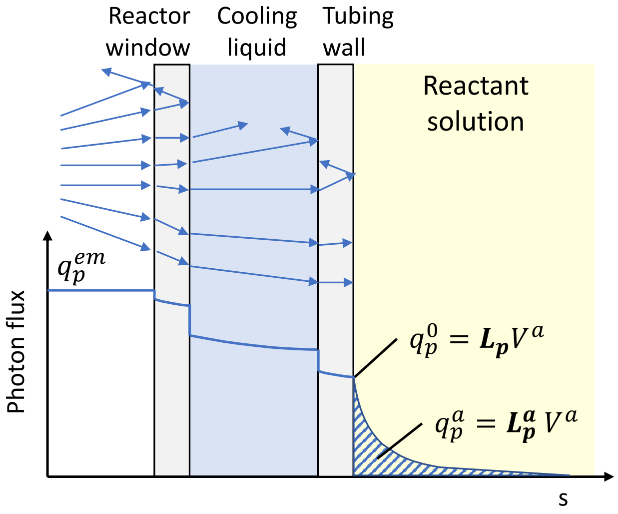

Fig. 3.3: Connection of the emitted photon flux q_p^{em}, the incident photon flux absolute q_p^0 and volumetric $L_{\mathrm{p},\lambda}$, and the local rate of photon absorption $L^{\mathrm{a}}_{\mathrm{p},\lambda}$.

the wavelength specific LVRPA needs to be integrated over the emitted wavelength range,

$$L^{\mathrm{a}}_{\mathrm{p}} = \frac{q_p^0}{V^a} \int_{\lambda_{min}}^{\lambda_{max}} g_\lambda \cdot \left(1 - e^{-\kappa_\lambda \cdot c \cdot l_{\mathrm{opt}}}\right) d\lambda. \tag{3.13}$$

The photon flux incident to the reactor channel is a setup specific quantity, which depends strongly on the applied light source, the reactor materials, and the implemented geometry. Theoretical prediction of q_p^0 from q_p^{em} by solving the radiation transfer equation is only possible for simple reactor geometries. For more complex setups, measurement of the incident photon flux in the specific system is essential to obtain a reliable estimate of the absorbed photon flux [273].

3.2.3 Mass transfer in Taylor Flow

Besides initiation by photon absorption, the photosensitized formation of singlet oxygen requires sufficient supply of dissolved oxygen in the liquid phase. Interfacial mass transfer in chemical reactors is often described based on the two-film model [304]. It relates the mass transfer rate j_i of species i to the difference in concentration at the phase boundary c_i^∞ and in the bulk of the liquid c_i introducing the volumetric transfer coefficient $k_{\mathrm{l}}a$:

$$j_i = k_{\mathrm{l}}a(c_i^\infty - c_i) \tag{3.14}$$

The concentration at the phase boundary is the saturation concentration in the corresponding solvent. The saturation concentration in the liquid phase and the partial pressure in the gas phase are linked by the Henry coefficient H:

$$c_i^{\infty} = \frac{1}{H} p_i \tag{3.15}$$

Generally, the mass transfer between two phases depends strongly on the characteristics of the contacted fluids, the phase distribution, and the specific flow geometry [305]. In Taylor flow (Fig. 3.1a), the film separating the bubble from the channel wall constitutes up to $90\,\%$ of the total interfacial area but is also quickly saturated [270]. Thus, the length of the gas and liquid segments as well as the film thickness surrounding the gas bubble affect the overall mass transfer [268].

These flow characteristics are determined by the applied reactor type, contacting mode, and wetting behavior of the channel wall. With the increasing application of micro-reactors, various empirical correlations were proposed to model the gas-liquid mass transfer in Taylor flow [268, 270, 306–319]. These correlations were determined for specific channel geometries and combinations of fluid-fluid-systems, mainly an aqueous liquid phase and air. The predictions of the available correlations for $k_{\mathrm{l}}a$ vary strongly [268]. Thus, predetermined correlations cannot be transferred to new flow systems without prior validation and adjustment. Alternatives to the empirical approach are CFD simulations or hybrid approaches requiring computationally intensive simulation of the flow [269, 311, 317, 320]. Generally, $k_{\mathrm{l}}a$ values of up to $21\,\mathrm{s}^{-1}$ can be expected in Taylor-flow micro-reactors [312].

One tool to assess whether a chemical reaction is limited by mass transfer is the Hatta number Ha, which compares the diffusion in the film with the reaction rate [256, 321]. For the given reaction in Eq. (3.1), where A is the component transferring from one phase to another and reacts with B, the Hatta number is defined as

$$Ha = \frac{\sqrt{2/(\nu_A + 1) k_r c_{A,i}^{\nu_A - 1} \cdot c_B^{\nu_B} D_A}}{k_L}. \tag{3.16}$$

with k_r as kinetic rate constant and D_A as diffusion coefficient [273]. If the diffusion rate exceeds the reaction rate greatly, the reaction occurs in the bulk of the liquid phase. If the reaction is faster than diffusion, only the film around the phase boundary participates in the reaction. Critical Hatta values are

$Ha \geq 3:$ strong mass transfer limitation,

$Ha \leq 0.3:$ kinetic regime, no limitation by mass transfer.

3.2.4 Consideration of mass, energy, and momentum conservation

The reaction rates and the photon and mass transfer are connected via balance equations. A complete description of the concentration, temperature, and velocity profiles over time and the reactor length requires balances for mass, energy, and momentum [293]. The mass balance can be expressed as a component balance for the species i describing the accumulation of this component over time t in an incremental part of the reactor as a result of convective and diffusive fluxes and the formation or consumption by chemical reactions - the primary sources and sinks

$$\underbrace{\frac{dc_i}{dt}}_{\text{Accumulation}} = \underbrace{-\nabla u c_i}_{\text{Convection}} - \underbrace{\nabla J_i}_{\text{Diffusion}} + \underbrace{R_i}_{\text{Sources \& Sinks}} \tag{3.17}$$

with u as velocity vector, J_i as molar diffusion flux, and r_i as volumetric reaction rate from Eq. (3.2) [300, 322]. The two-phase mass transfer is incorporated in the diffusive flux. The LVRPA is included in the reaction rate (Eq. (3.4)).

In tubular micro-reactors, the flow direction can be considered unidirectional, where axial dispersion is negligible compared to the convective transfer [300, 323]. In addition, Taylor flow enables fast mixing in the liquid segments so that a radial concentration gradient can be neglected. If the reactor has reached a steady state, Eq. (3.17) can be simplified to

$$0 = -\frac{d(uc_i)}{dz} + j_i + R_i. \tag{3.18}$$

where z is the axial reactor coordinate and j_i the diffusive flux across the phase boundary [322].

The temperature field in micro-reactors can be considered uniform even for exothermic reactions due to the small channel width and the high mixing rates [265–267]. This isothermal operation is also an essential requirement for kinetic analysis of experimental data. Thus, the consideration of an energy balance to describe the temperature change is not required.

Determining the precise velocity field in the reaction line necessitates solving the momentum balance. This is especially complex for the diverse nature of multiphase flows. An alternative is the application of simplified model approaches without explicitly assessing the momentum [305]. A well-established method in nuclear reactor technology and the petroleum industry is the two-phase model [324, 325]. Following this approach, the gas and the liquid phase (indices g and l for gas and liquid phase, respectively) are balanced separately. Both balances are then linked by interfacial transfer equations. This approach yields models of moderate complexity and good model-data fits also in milli- and micro-channel reactors [326–330]. The two-fluid model, however, does not explicitly represent the phase interface and describes the interfacial transfer based on isolated compartments limiting its applicability for micro-structured reactors [331, 332].

An essential quantity connecting the gas and liquid phase is the gas fraction α_g, which is defined as the crossectional area covered by the gas phase A_g relative to the total crossectional area A

$$\alpha_{\mathrm{g}} = \alpha = \frac{A_{\mathrm{g}}}{A}, \quad \alpha_{\mathrm{l}} = 1 - \alpha = \frac{A_{\mathrm{l}}}{A}. \tag{3.19}$$

The gas fraction is an intrinsic quantity of the two-phase flow and cannot be known *a priori*. The drift flux model offers a simplified description of α by reducing the momentum and energy balance to one joint equation, compromising the validity regarding other key characteristics of two-phase flow [325]. The drift flux model can be applied to flows with closely coupled dynamics of the two phases, e.g., Taylor flow. The gas-phase velocity is linked to the superficial velocity u^{s} by introducing the distribution factor C_0 and the drift velocity $u_{\mathrm{g}}^{\mathrm{drift}}$ [333]

$$u_{\mathrm{g}} = C_0 u^{\mathrm{s}} + u_{\mathrm{g}}^{\mathrm{drift}}, \text{with} \tag{3.20}$$

$$u^{\mathrm{s}} = \frac{\dot{V}_{\mathrm{l}} + \dot{V}_{\mathrm{g}}}{A}, \tag{3.21}$$

where $\dot{V}$ is the volumetric flow rate. In the case of microreactors, the effect of gravity can be neglected due to the dominating interfacial forces [334]:

$$u_{\mathrm{g}} = C_0 \cdot u^{\mathrm{s}} \tag{3.22}$$

The drift flux model links the unknown gas fraction α with the known gas holdup β

$$\beta = \frac{\dot{V}_{\mathrm{g}}}{\dot{V}_{\mathrm{l}} + \dot{V}_{\mathrm{g}}} \tag{3.23}$$

by

$$\alpha = \frac{1}{C_0} \cdot \beta. \tag{3.24}$$

This relation allows determining the velocities for gas and liquid phase. The distribution factor $\boldsymbol{C_0}$ can either be estimated from correlations or be determined experimentally by flow analysis.

In summary, the overall process model consists of mass balance equations incorporating the model for the reaction kinetics, the mass transfer, and the photon transfer. The model contains several unknown parameters – reaction rate constants, the mass transfer coefficient, the incident photon flux, and the distribution coefficient between gas and liquid phase – that need to be determined based on experiments.

3.3 Quantification of photon emission by chemical actinometry

The provided amount of photons, namely the incident photon flux, is an essential quantity in kinetic models of photoreactions and needs to be estimated accurately to obtain reliable and transferable reaction kinetics [335]. Chemical actinometry is a well-established tool to investigate the incident photon flux in complex reactor geometries, where other methods as radiometry are not readily applicable [336, 337]. This method utilizes a well-characterized photo-induced reaction as a reference, the so-called actinometer [173]. The analysis involves irradiating the actinometer, measuring the conversion, and calculating the incident photon flux based on the known quantum yield for this reaction [336]. Thus, chemical actinometry is an indirect and integral measurement method yielding an average value of the incident photon flux in the reactor [173].

The photodecomposition of potassium ferrioxalate, also known as the Hatchard-Parker-Actinometer [338], is one of the most established chemical actinometers. When irradiated, the Fe(III) of ferrioxalate is reduced to Fe(II) and CO_2 is released.

$$\begin{aligned}
[\mathrm{Fe^{III}(C_2O_4)_3}]^{3-} &\xrightarrow{h\nu} [\mathrm{Fe^{II}(C_2O_4)_2}]^{2-} + (\mathrm{C_2O_4})^{\bullet-} \\
(\mathrm{C_2O_4})^{\bullet-} &\longrightarrow \mathrm{CO_2} + \mathrm{CO_2^{\bullet-}} \\
[\mathrm{Fe^{III}(C_2O_4)_3}]^{3-} + \mathrm{CO_2^{\bullet-}} &\longrightarrow [\mathrm{Fe^{II}(C_2O_4)_2}]^{2-} + \mathrm{CO_2} + (\mathrm{C_2O_4})^{2-}
\end{aligned}$$

By adding phenanthroline to the reacted actinometer solution, the formed Fe(II) is converted to a red ferroin complex, which can be quantified by UV/vis spectroscopy. The primary advantages of the ferrioxalate actinometer are its broad absorption spectrum in the near-UV and blue spectrum [336], the easy preparation, and its extensively characterized reaction mechanism and kinetics [338–347]. The quantum yield of the photodecomposition is independent of temperature and oxygen concentration [336].

The major drawbacks of the ferrioxalate actinometer are its sensitivity to the experimental procedure and its limited linearity [337]. Performing reproducible and reliable measurements requires careful ferrioxalate preparation, irradiation, and sample workup [337, 342, 344, 348–350]. At high actinometer conversions, Fe(III) precipitates and CO_2 bubbles form inside the reaction solution, altering the irradiation conditions in the reactor [351]. Therefore, measurements with ferrioxalate are limited to small conversions of up to $30\,\%$.

Calculation of the photon flux from the actinometer conversion requires modeling of the present irradiation conditions in the reactor, as shown in Sec. 3.2.2 [337]. For monochromatic light irradiation, the change in actinometer conversion X_{Act} over time t can be described as

$$\frac{\mathrm{d}X}{\mathrm{d}t} = \frac{1}{[\text{Act}]^0} \frac{q_p^0}{V^a} \cdot \Phi_\lambda f(X, \lambda) \mathrm{d}\lambda. \tag{3.25}$$

with q_p^0 as total incident photon flux, Φ_λ as the quantum yield (Eq. (3.5)) of the actinometer at emission wavelength λ and f as absorption factor [337, 344]. In batch reactors, the incident photon flux is almost entirely absorbed ($f = 1$). However, in milli-scale photoreactors, this assumption is not anymore valid. Thus, partial absorption must be considered via the Lambert-Beer law (Eq. (3.10)). The irradiation time in flow photoreactors is equal to the residence time τ in the illuminated part of the flow reactor,

$$\frac{\mathrm{d}X}{\mathrm{d}\tau} = \frac{1}{[Act]^0} \frac{q_p^0}{V^a} \cdot \Phi_\lambda \left(1 - e^{\kappa_\lambda [\text{Act}]^0 (1-X) \cdot l_{\text{opt}}}\right) \mathrm{d}\lambda. \tag{3.26}$$

Since the actinometer conversion appears on both sides, Eq. (3.26) needs to be solved numerically.

The ferrioxalate actinometer was developed for batch reactors with low incident photon fluxes. The high photon fluxes, possible in milli-scale photoreactors, restrict the measurement with ferrioxalate to very short residence times to not exceed an actinometer conversion of $30\,\%$ [351]. In addition, recent studies showed that the reaction pathways of the photolysis shift in the presence of high photon fluxes, reducing the effective quantum yield [343, 347, 351]. However, this effect can be overcome by extensive mixing [351].

Alternative actinometers were developed directly for the application in flow reactors at high photon fluxes [352–355]. However, these systems are not yet widely studied and applied. Despite its limitations, the ferrioxalate actinometer is applicable to milli-scaled reactors if the experimental procedure and the reactor operation are carefully adapted to the valid range of the actinometer [262, 292, 337, 344, 351].

3.4 Definition of specific quantities used for performance analysis of the partial synthesis

In this section, important quantities are defined, which are later used to compare and assess the experimental data.

The superficial residence time τ^{s} is defined based on the dosed flow rates of gas and liquid phase, $\dot{V}_{\mathrm{g},0}$ and $\dot{V}_{\mathrm{l}}$, respectively

$$\tau^{\mathrm{s}} = \frac{V_{\mathrm{r}}}{\dot{V}_{\mathrm{l}} + \dot{V}_{\mathrm{g}}} \tag{3.27}$$

with V_{r} as reactor volume. The superficial residence time underestimates the actual residence time in the system. Due to oxygen consumption, the gas flow rate decreases with the increasing conversion of DHAA. Therefore, the real residence time depends not only on the initial flow settings but also on the reaction progress.

For optimization of the experimental conditions, the obtained results are compared in terms of yield Y and conversion X. The yield of a species C formed from the reactant A is defined as

$$Y_C = \frac{[C] - [C]^0}{[A]^0} \cdot 100\,\%. \tag{3.28}$$

The corresponding conversion is

$$X = \frac{[A]}{[A]^0} \cdot 100\,\%. \tag{3.29}$$

If not stated otherwise, the yield and conversion are related to the initial concentration of DHAA in the reaction solution.

To compare the amount of unknown products formed in the partial synthesis, an additional quantity, the recovery, is introduced, which is defined as the ratio of known components of the reaction mixture and the initially added amount of DHAA:

$$Recovery = \frac{[\mathrm{DHAA}] + [\mathrm{PO}_1] + [\mathrm{PO}_2] + [\mathrm{PO}_3] + [\mathrm{BP}_3] + [\mathrm{BP}_4]}{[\mathrm{DHAA}]^0} \cdot 100\,\%. \tag{3.30}$$

3.5 Mathematical tools for the identification of process models

Identifying a reliable kinetic model is a challenging problem for complex reaction networks, where either the model structure is unknown or where many parameters need to be identified [293, 356, 357]. Therefore, a systematic procedure for the planning of experiments, the model evaluation, and the parameter estimation is key to achieving a reliable mathematical model [358, 359].

The model identification for the kinetics of the partial synthesis was performed in cooperation with Moritz Schulze from TU Braunschweig. The following section shortly introduces the tools used for parameter estimation, identifiability assessment, and model-based design of experiments. For more details, the interested reader is referred to the Ph.D. thesis of Moritz Schulze [360].

The maximum likelihood approach aims at obtaining a model with a set of parameter estimates $\hat{\boldsymbol{\theta}}$, which exhibits the highest likelihood to the measured data [361]. Assuming independent and identically distributed Gaussian variables with zero mean value and variance σ^2, the maximum likelihood estimate of the model parameters $\hat{\boldsymbol{\theta}}$ can be determined by minimizing the residual sum of squares RSS [362] between the model predicted results $y_{i,j}(\theta)$ and the measured data $y_{i,j}^{\mathrm{data}}$ [362],

$$\hat{\boldsymbol{\theta}} = \arg\min_{\theta} RSS(\theta) = \arg\min_{\theta} \sum_{i=1}^{n} \sum_{j=1}^{n_y(i)} (y_{i,j}^{\mathrm{data}} - y_{i,j}(\theta))^2, \tag{3.31}$$

with n being the number of samples and $n_y(i)$ being the number of measured quantities in each of the samples. The corresponding log likelihood function is

$$\mathcal{L}(\theta, \sigma^2; y_{1,1}^{\mathrm{data}}, \ldots, y_{n,n_y(n)}^{\mathrm{data}}) = -\frac{N}{2} \ln(2\pi) - \frac{N}{2} \ln(\sigma^2) - \frac{1}{2\sigma^2} RSS(\theta). \tag{3.32}$$

The total number of data points is $N = \sum_{i=1}^{n} \sum_{j=1}^{n_y(i)} 1$.

Direct search algorithms or gradient-based algorithms as Gauß-Newton or Quasi-Newton can be applied to solve the optimization problem in Eq. (3.31). These methods are suitable for non-linear models like reaction kinetics [363, 364]. The optimization can be performed repeatedly with different starting points within the physically plausible range of the model parameters to avoid getting stuck in a single local minimum [365].

Besides a good model-data fit, the model parameters need to be checked whether their estimates can be uniquely determined from the available measurement data. This identifiability is crucial for a reliable interpretation of parameter values [361, 366]. The maximum likelihood approach enables direct assessment of the parameter identifiability and the determination of confidence intervals [367, 368] via profile log-likelihood function PLL [368]:

$$PLL_k(\theta_k) = \max_{\theta_i, \forall i \in \{1,\dots,n_p\} \neq k} \mathcal{L}(\boldsymbol{\theta}) \tag{3.33}$$

If this function exhibits a unique maximum and falls below the confidence threshold on both sides of the maximum, the parameter is considered to be identifiable [367]. In this case, bounded confidence intervals can be determined for the parameter [369].

Often in chemical reaction kinetics, the model structure is not evident but varies based on the level of simplification. Increasing network complexity results in an improved model-data fit but yields more parameters and may result in overfitting and unidentifiability of the parameter set. Thus, model selection aims to balance the goodness of the model-data fit with the number of unknown parameters, favoring simpler models. One criterion for model selection is the Akaike information criterion (AIC) [370]. In the case of the least-squares regression in Eq. (3.31), the AIC criterion can be computed based on the maximum likelihood estimate $\hat{\sigma}^2$ [371]

$$\mathrm{AIC} = -2\log(\hat{\sigma}^2) + 2K \tag{3.34}$$

with

$$\hat{\sigma}^2 = \frac{RSS(\hat{\boldsymbol{\theta}})}{N} \tag{3.35}$$

where K is the number of estimated parameters. If the sample size is small compared to the number of unknown parameters as $N/K < 40$, the second-order AIC variant, AICc, is recommended [371, 372]

$$\mathrm{AICc} = \mathrm{AIC} + \frac{2K(K+1)}{N-K-1}. \tag{3.36}$$

The AICc is a tool to compare model candidates. However, AICc values cannot be interpreted in isolation but only compared relative to each other. The model with the smaller AICc should be preferred.

Model structure discrimination and parameter identification require sufficient experimental data of high informative output. One method to aid in planning such experiments is model-based design of experiments (MBDoE) [373–376]. In the context of identifying process parameters, MBDoE aims at minimizing the uncertainties of the model parameters by maximizing the parameter sensitivities on the measured outputs [361, 377]. MBDoE is based on an iterative strategy of model development, planning and performing optimal experiments, parameter estimation, checking on

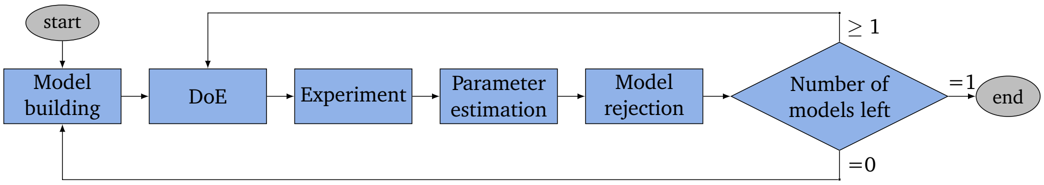

Fig. 3.4: Workflow of model-based design of experiments. Reproduced from [378].

the identifiability of the process parameters, and the repetition of that cycle until all parameters are identifiable. The procedure is illustrated in Fig. 3.4.

The parameter uncertainties can be quantitatively assessed via the parameter covariance matrix $\sum$. According to the limiting case of the Cramér-Rao inequality, $\sum$ can be calculated as the inverse of the Fisher-Information-Matrix $\boldsymbol{FIM}$ [361]:

$$\boldsymbol{\Sigma} = \boldsymbol{FIM}^{-1}. \tag{3.37}$$

The $\boldsymbol{FIM}$ is derived from the log-likelihood function, Eq. (3.32)

$$\boldsymbol{FIM} = - \left. \frac{\partial^2 \mathcal{L}(\boldsymbol{\theta})}{\partial \theta_i \partial \theta_j} \right|_{\hat{\boldsymbol{\theta}}} . \tag{3.38}$$

It can be approximated by the effective information matrix M based on the sensitivity matrix of the model parameters $\boldsymbol{SM}$,

$$M(\boldsymbol{\xi}_1, \dots, \boldsymbol{\xi}_{n_{\text{tot}}}; \hat{\boldsymbol{\theta}}) = \sum_{i=1}^{n_{\text{tot}}} \boldsymbol{SM}_i(\boldsymbol{\xi}_i; \hat{\boldsymbol{\theta}})^\top \boldsymbol{SM}_i(\boldsymbol{\xi}_i; \hat{\boldsymbol{\theta}}). \tag{3.39}$$

Several objective functions were developed based on the Fisher-information matrix to facilitate mathematical optimization [361]. In the D-optimality criterion, the experimental parameters $\boldsymbol{\xi}$ are optimized so that the volume of the parameter covariance matrix, assessed by the determinant, is minimized. This corresponds to a maximization of the determinant of the $\boldsymbol{FIM}$. The D-optimality criterion is most widely used as it is stable against re-parameterizations of the model and its computational efficiency [358, 379]. The DoE optimization problem can then be stated as:

$$\max_{\boldsymbol{\xi}_1, \dots, \boldsymbol{\xi}_{n_{\text{DoE}}}} \quad \det\left(M(\boldsymbol{\xi}_1, \dots, \boldsymbol{\xi}_{n_{\text{DoE}}}, \boldsymbol{\xi}_{n_{\text{tot}}-n+1}, \dots, \boldsymbol{\xi}_{n_{\text{tot}}}; \hat{\boldsymbol{\theta}})\right) \quad , \tag{3.40}$$

where $\boldsymbol{\xi}_{\text{min}}$ and $\boldsymbol{\xi}_{\text{max}}$ are lower and upper bounds of the design vector, respectively. Solving this optimization problem yields a set of optimal conditions for the next experiment, ensuring a high information gain for model identification. Thus, model-based design of experiments significantly reduces the experimental workload while at the same time achieving high parameter accuracy [380].

3.6 Conclusion

The conversion of dihydroartemisinic acid to artemisinin comprises a complex reaction network, including light-induced steps, oxidations, reversible reactions, and byproduct formation. Kinetic analysis of this reaction network necessitates experimental tools, ensuring sufficient supply of oxygen and light and deep system understanding to develop a suitable model structure, and mathematical tools for model selection and parameter estimation.

Continous milli- or microscale reactors are particularly suitable to study light-activated or mass-transfer-governed reactions. The small inner channel depth facilitates uniform irradiation in the channel and straightforward gas-liquid operation. The most common two-phase flow pattern in milli-scale reactors is Taylor flow with regular liquid segments separated by gas bubbles. It is characterized by a large interfacial area, intensive mixing in the liquid slugs, and a narrow residence time distribution.

Modeling the photooxygenation kinetics needs to consider oxygen mass transfer from the gas to the liquid phase, photon transfer, and the specific flow conditions. Strong assumptions and simplified approaches like the two-fluid model are necessary to obtain a model with moderate complexity. The key assumptions are isothermal and steady-state operation, monochromatic light irradiation, and uniform light distribution in the whole reactor.

The photon flux incident to the reactor is a central parameter in the process model. One widely used approach to quantify the incident photon flux in complex reactor geometries is chemical actinometry based on the photolysis of ferrioxalate. However, the application of this method requires careful validation of the measurement conditions to stay within the physical limitations of this reference system.

Estimating the remaining unknown parameters in the model requires a substantial amount of experimental data on the partial synthesis of artemisinin. Here, model-based design of experiments is a tool to minimize the number of necessary experiments while maximizing the accuracy of the obtained parameter set.

A crucial requirement for kinetic studies is that all experimental data is obtained within the validity limits of the submodels used. The following chapter describes how the specific restrictions on the experimental setup and procedure were implemented.

4

Experimental setup and procedures

The partial synthesis to artemisinin was studied with a milli-scaled continuous flow reactor system, which was designed, implemented, and characterized as part of this work. The reaction investigation was performed by continuous steady-state experiments and complemented by experiments utilizing batch equipment. The reactor feed consisted of *A. annua* extract or pure DHAA together with photosensitizers and acidic catalysts. The formation of reaction products was followed by quantitative $^1\mathrm{H-NMR}$ while the extract was characterized by HPLC and UV/Vis analysis.

In the following, the developed reactor setup and its characterization regarding photon flux and two-phase flow are described before introducing the experimental procedures of the extraction and synthesis experiments. The applied analytical methods are described at the end of the chapter.

4.1 Milli-scale photoreactor system for investigating the partial synthesis to artemisinin

The majority of the experimental data in this thesis was obtained with the reactor system designed and implemented at the Max Planck Institute Magdeburg. For initial studies on the utilization of chlorophyll, the experimental setup at the *Max Planck Institute for Colloids and Interfaces* in the group *Biomolecular Systems* in Potsdam-Golm was utilized during several visits. If not stated otherwise, the data shown in this work was collected with the setup at the MPI Magdeburg shown in Fig. 4.1. The components are specified in App. A.1. Details on the setup used at the *Max Planck Institute for Colloids and Interfaces* are given in [381].

The reactor setup consists of two main components, the photoreactor and the reaction module for the acid-catalyzed sequence. These main parts are complemented by a dosing unit, process monitoring, depressurization, and phase separation at the end of the reaction line.

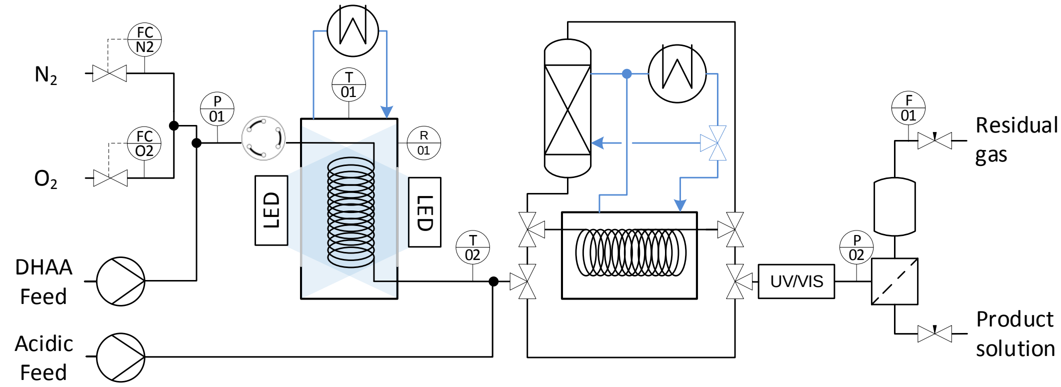

(a) Flow scheme

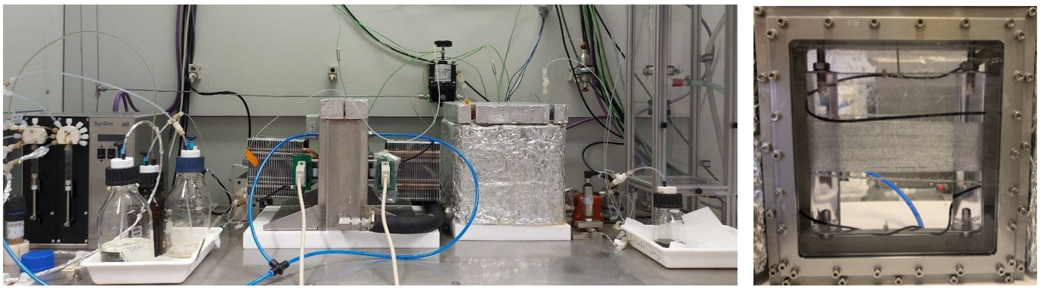

(b) Reactor system

(c) Photoreactor (in the middle in b))

Fig. 4.1: Continuous photo-flow reactor setup applied for the partial synthesis of artemisinin starting from dihydroartemisinic acid (DHAA).

Reactant dosing The liquid feed is pumped by a syringe pump to ensure constant and low-fluctuating flow. The acidic feed can be added separately by a second syringe pump. The gases oxygen and nitrogen were withdrawn from the inhouse gas supply (max. pressure 9 bar) and dosed separately by two mass flow controllers. The gas and liquid stream are contacted in a t-mixer and then pass a pressure sensor and a 6-way-valve used for residence time measurements before entering the reaction line.

The reaction line in the whole reactor setup consists of fluorinated ethylene propylene (FEP) tubing. In standard setting, the inner tubing diameters (ID) in the photoreactor section and in the acid-catalyzed part are $0.8\,\mathrm{mm}$ (OD: $1.6\,\mathrm{mm}$) and $1.6\,\mathrm{mm}$ (OD: $3.2\,\mathrm{mm}$), respectively.

Photoreactor In the photoreactor, the tubing is coiled in a single layer around a polystyrene frame (Fig. 4.1c). The first and the last part were shielded from light with shrink tubing to allow for equilibration of the flow and the definition of a precise starting point. The frame is positioned centrally in a stainless-steel casing with polystyrene windows. A high-intensity LED module is positioned on each side of the casing and attached to stainless steel hoods preventing the light from leaving the reactor and shielding the practitioner from the intense light. During an experiment, the spread between the reactor windows and the hoods is flushed with dried air to prevent moisture from condensation. LED modules with two different wavelengths of $417\,\mathrm{nm}$ and $660\,\mathrm{nm}$ were applied as light sources. The emission spectra are included in App. A.2. Position and size of the frame are designed so that both LED modules irradiate the whole tubing-covered area. The casing is filled with cooling liquid and connected to a thermostat to ensure a constant temperature in the experiment.

Acid-catalyzed section After leaving the photoreactor, the reactant solution either enters another reactor section to offer more residence time or it undergoes direct depressurization and phase split (Fig. 4.1). The acid required to cleave the hydroperoxide is either added directly to the DHAA containing reactor feed, dosed as additional feed to the reaction stream after leaving the photoreactor, or provided as heterogenous catalyst immobilized in a fixed bed.

In case of either of the first two options, the acidified reaction stream enters a second tubing line (ID: $1.6\,\mathrm{mm}$, OD: $3.2\,\mathrm{mm}$). The tubing of a larger diameter was used to limit the pressure drop over the reaction line while offering enough reaction volume for the slower reaction to arteminsinin to complete. This reaction line is wrapped around a stainless steel frame and integrated in a second stainless steel container connected to a second thermostat for temperature control.

When applying a heterogeneous catalyst, the acidic material is packed in a double-walled glass column with an inner diameter of $1.5\,\mathrm{cm}$. The column is connected directly to the photoreactor and positioned within a casing for safety. A thermostat controls the temperature within the column.

Depressurization and reaction monitoring Before collecting the effluent stream, the reaction solution passes a flow cell for tracer detection. The flow cell consists of FEP tubing (ID: $1.6\,\mathrm{mm}$) and a fiber probe. A surrounding T-piece fixes the probe in a perpendicular position directly at the outer face of the tubing. The probe is connected to a UV/Vis spectrometer and measures in reflection mode.

The two-phase stream leaving the flow cell is first split in a membrane phase separator and then depressurized in a diaphragm-back-pressure regulator. The non-converted gas stream is quantified in a mass flow meter. The gas stream passes a stainless steel cylinder serving as a second phase separator before entering the mass flow meter. A spring-back-pressure regulator sets the pressure on the gas side. Pressure sensors measure the system pressure inline after the feed pump, after contacting gas and liquid stream, and in front of the phase separator. The maximum system pressure is $8\,\mathrm{bar}$. Thermocouples measure the temperature within the photoreactor, the casing of the second reaction line, and inline between both sections. The process control system (WinCC, Siemens) operates all sensors, the dosing of the gas and liquid feed, the position of the six-way valve, emission intensity and emission duration of the LED modules, and temperature of the photoreactor.

4.2 Characterization of flow and irradiation conditions

Mass and photon transfer are essential phenomena governing the performance of the partial synthesis. Quantifaction of the incident photon flux and the slip between gas and liquid phase is crucial for the kinetic investigations and for the transferability of the obtained results to other reactor setups. The irradiation inside the reactor was investigated by chemical actinometry (Sec. 3.3) and the flow conditions by residence time measurements.

4.2.1 Residence time measurement with tracer injection

The residence time of the liquid phase was measured by tracer injection and online detection with UV/Vis spectroscopy. All measurements were performed at room temperature and a system pressure of $7\,\mathrm{bar}$ absolute. Toluene was dosed as liquid phase and nitrogen as gas phase. The total flow rate was varied from $1\,\mathrm{mL/min}$ to $2\,\mathrm{mL/min}$ and the gas holdup between 0.4 – 0.9 (vol/vol) (Eq. (3.23)). The tracer, Sudan Red G dissolved in toluene, is injected as pulse by a six-way injection valve (Fig. 4.1). After leaving the corresponding reactor section, the tracer is detected by the UV/Vis spectrometer attached at the end of the reaction line. For each setting, the tracer injection was repeated three times.
Tracer experiments were also applied to measure the residence time of the liquid phase when passing the packed bed reactors. In this case, 9,10-dicyanoantracene was used as tracer with a step injection. The time at which the tracer was detected in the effluent stream was defined as endpoint. Thus, the stated residence times are minimal estimates.

4.2.2 Measurement of the incident photon flux by actinometry

Chemical actinometry as a tool to characterize the number of photons reaching the reactor is introduced in Sec. 3.3. Potassium ferrioxalate – also known as the Hatchard-Parker-Actinometer [338] – was used as an actinometer, because of its broad absorption in the visible spectrum, and established procedure for preparation and handling (Sec. 3.3). The procedure of actinometer preparation, measurement, and analysis was adapted from Wriedt et al. [337, 344]. The method is shortly introduced in the following. Further details are given in App. F.

Preparation of the actinometer solution The materials used in the actinometric measurements are specified in App. A.3. All chemicals were used without further purification. A fresh solution of $0.15\,\mathrm{M}$ ferrioxalate was prepared daily by adding $0.075\,\mathrm{mol}$ $FeCl_3$ and $0.225\,\mathrm{mol}$ $K_2C2O_4\cdot$ H_2O to $500\,\mathrm{mL}$ of $0.05\,\mathrm{M}$ sulfuric acid. The mixture was stirred for $30\,\mathrm{min}$ in a dark room to complete the formation of the ferrioxalate complex. The quality of the obtained solution was checked with a reference irradiation device before using it for the measurements (App. F.2).

Measurement procedure The actinometric experiments were performed in three different flow modes: 1) Stop flow 2) Continuous single-phase flow, and 3) Two-phase flow.

In the first option, the actinometer solution was pumped into the photoreactor. When the reactor line was filled completely, the pump was stopped and the actinometer solution irradiated by turning the LED modules automatically on and of for the set irradiation time from $3\,\mathrm{s}$ to $12\,\mathrm{s}$. Longer irradiation times resulted in actinometer conversions exceeding the linear region of ferrioxalate [336, 337]. The reacted solution was purged out of the reactor with nitrogen and collected completely as one sample. This method allowed for measurements in all used reactor lines but provided no mixing of the reaction solution during irradiation.

In the continuous measurement settings (2 & 3), the actinometer solution was pumped continuously through the irradiated reactor at $7\,\mathrm{bar}$ system pressure, either as single-phase or with nitrogen as an inert phase in slug flow pattern. In the latter case, the gas holdup β was 0.8 (vol/vol) in all experiments – equal to the flow conditions in the photooxidation experiments. The slug flow pattern enabled fast mixing in the reaction line during the measurement. Due to the limited flow rate range of the used dosing system, however, the required short residence times could only be achieved for the shortest reaction line of $2\,\mathrm{m}$ length. The single or two-phase-flow was pumped at a total flow rate of $5\,\mathrm{mL\,min^{-1}}$ to $10\,\mathrm{mL\,min^{-1}}$ through the photoreactor resulting in a residence time of $6\,\mathrm{s}$ to $12\,\mathrm{s}$ in the irradiated section. After keeping stable flow conditions for at least $5\,\mathrm{min}$, three samples of the liquid effluent stream were collected.

In addition, samples of the reactor effluent without irradiation were collected in all measurement methods and processed along with the irradiated samples to determine actinometer conversion due to ambient light irradiation during sample workup.

The stop-flow method was applied to compare the irradiation conditions in the photoreactors with varied tubing lengths. Measurements in two-phase flow continuous conditions were then performed only in the shortest reactor. The obtained results are then transferred to the longer reactors based on the initial comparison.

Determination of the actinometer conversion The collected sample was diluted 25-fold with $0.05\,\mathrm{M}$ sulfuric acid, before adding a buffered solution of $0.1\,\%$ phenanthroline solution in $0.05\,\mathrm{M}$ sulfuric acid with $0.06\,\mathrm{M}$ sodium acetate. The mixture was kept for $30\,\mathrm{min}$ in a dark room before measuring the absorption at $510\,\mathrm{nm}$ with a UV/Vis spectrometer (Genesys 6, Thermo Fisher).

The concentration of Fe(II) formed in the actinometric experiment is determined based on the calibration with iron(II) sulfate following the procedure in [338] (App. F.1) and corrected by the dilution steps during sample workup. The actinometer conversion results from the concentration of formed Fe(II) in the irradiated sample corrected by the concentration of Fe(II) measured in blind samples related to the initial concentration of ferrioxalate $[\mathrm{Act}]^0$.

$$X^{Act} = \frac{[\mathrm{Fe}^{\mathrm{II}}_{\mathrm{sample}}] - [\mathrm{Fe}^{\mathrm{II}}_{\mathrm{blind}}]}{[\mathrm{Act}]^0} \tag{4.1}$$

Numerical determination of the incident photon flux The incident volumetric photon flux L_{p} was determined based on the actinometric model developed in [344] and introduced in Sec. 3.3. Estimating the incident photon flux requires the measured actinometer conversion and the corresponding irradiation time as input parameters (Eq. (3.26)). The latter is calculated as residence time in the irradiated section assuming ideal plug flow conditions (Eq.(3.27)). The incident photon flux can only be obtained by solving Eq. (3.26) numerically due to the dependence of absorption on the actinometer conversion. The model was implemented in Matlab.2018b and solved as least-squares minimization for each measured value of actinometer concentration separately. The predefined function *fminsearch*, which is based on a Simplex algorithm, was used for the optimization.

4.3 Experimental procedures for the investigation of the partial synthesis

The partial synthesis was mainly investigated in the previously introduced reactor setup. The feed solution either consisted of extract obtained from contacting *A. annua* with toluene or a solution of pure DHAA and the photocatalyst 9,10-dicyanoanthracene (DCA) in toluene. The two main reaction steps of the partial synthesis, the photooxygenation of DHAA and the subsequent acid-catalyzed rearrangement, were studied mainly together by adding trifluoroacetic acid (TFA) to the feed. Alternatively, the reaction steps can be investigated individually by separating the DHAA feed containing the photosensitizer from the provision of the acid. One tested option was to connect a packed bed reactor filled with solid acids to the photoreactor as an alternative to the addition of TFA. Batch experiments were used as a complement for screening applicable solid acids and to studying the reaction kinetics of the acid-catalyzed cleavage of the intermediate hydroperoxides.

The used materials are specified in App. A.3. All chemicals were used as purchased without any prior purification.

4.3.1 Extraction of *A. annua* to provide for the synthesis feed

Dried leaves of *Artemisia annua* from two different sources were used for the extraction (more details in Sec. 6.1). The majority of the experiments were performed with plant material supplied by Mediplant and grown in Switzerland. To compare the reaction performance in different extracts, leaves from ArtemiFlow, grown in Kentucky, USA, were used. If not stated explicitly, the data given in this work relates to leaves from Mediplant.

Before extraction, the dried leaves were ground in a centrifugal mill (Retsch ZM 200, $1.5\,\mathrm{mm}$ sieve, $12.000\,\mathrm{rpm}$). The resulting main particle size fraction ($85\,\mathrm{wt}-\%$) is in the range of $0.06\,\mathrm{mm}$ to $0.4\,\mathrm{mm}$ [382]. All plant material was stored in a fridge in cool and dark conditions.

For batch extraction, the solvent was stirred in a double-walled glass vessel, which was connected to a thermostat (Lauda Ecoline E 100) for temperature control. The flask was loosely closed by a plastic stopper to prevent extensive evaporation of the solvent. When the extraction temperature was reached, ground leaves were added to the solvent. In the case of extraction studies on chlorophyll, the extract was sampled in regular time intervals through the closed stopper with a syringe and a cannula. Directly after sample collection, the extract was filtered with a $0.2\,\mu\mathrm{m}$

syringe filter. After extraction for the time set, the extract was separated from the residual leaves by filtration with glass frits.

Alternatively, extract from continuous extraction at room temperature was used for the investigations. The extract was supplied by Truong Giang Vu using the counter-current screw extractor implemented at the *Max Planck Institute for Dynamics of Complex Technical Systems*, Magdeburg. The mass flow rate of the leaves and toluene were $1.3\,\mathrm{g\,L^{-1}}$ and $11.7\,\mathrm{g\,L^{-1}}$, respectively.

The concentration of artemisinin (Arte) and dihydroartemisinic acid (DHAA) in the extract were determined by HPLC (Sec. 4.4.1). The chlorophyll concentration was quantified by UV/Vis spectroscopy (Sec. 4.4.3)).

4.3.2 Preparation of the heterogeneous acidic catalyst

Solid acids were investigated as an alternative to trifluoroacetic acid as a catalyst. The specification and manufacturer of the applied materials are listed in App. D.1.

4.3.2.1 Pretreatment of solid acids

The catalyst materials were heated in a vacuum oven or muffle furnace for several hours to remove adsorbed water. The pretreatment temperature ranged between $70\,°\mathrm{C}$ to $500\,°\mathrm{C}$ depending on the thermal stability of the catalytic material. The zeolites H-ZSM5(Si/Al=25) and H-Y(Si/Al=5) were unavailable with H^+ as a counterion. Therefore, both materials were first stirred in a $1\,\mathrm{M}$ NH_4Cl solution for $2\,\mathrm{h}$ before calcination at $500\,°\mathrm{C}$ overnight to obtain the desired change in the counterion. The pretreatment for each material is summarized in App. D.1.

4.3.2.2 Preparation of the packed-bed reactors

Two types of reactors were used as a container for the packed bed of solid acids: 1) A double-walled glass column (YMC, ECO SR, ID: $1.5\,\mathrm{mm}$ with adjustable frits for variable bed length and 2) FEP tubing (ID: $1.6\,\mathrm{mm}$, OD: $3.2\,\mathrm{mm}$). For the preparation of the packed-bed in the glass column, the column was filled partially with toluene, and sea sand was poured slowly into the column up to a layer of $1\,\mathrm{cm}$. The pretreated solid catalyst was dispersed in toluene and poured into the column. The bed was repeatedly compressed at a pressure of $10\,\mathrm{bar}$ and topped up by additional catalyst until a stable catalyst packing with a length of $20\,\mathrm{cm}$ to $30\,\mathrm{cm}$ is obtained. The bed was completed by a $1\,\mathrm{cm}$ thick layer of sea sand. In case of the beta-zeolite, the material was mixed with sea sand in a 50/50 ratio (v/v) to reduce the pressure drop of the packing. The composition, dimension, and the resulting back-pressure of the used columns are listed in App. D.1.

In the case of the milli-scale fixed-bed reactor, the tubing was connected to a vacuum pump with a preceding cold trap and immersed in an ultrasonic bath. The catalyst particles dispersed in toluene were sought into the tubing by the draft of the vacuum pump. The end of the used tubing line was blocked with cotton to prevent the catalyst from exiting the tubing section.

4.3.3 Continuous synthesis experiments in the photoreactor system

The partial synthesis of DHAA to artemisinin was studied based on continuous steady-state experiments utilizing the previously introduced photo-flow reactor setup in four different modes (Fig. 4.2). If no acid is added, the reaction stops at the hydroperoxide and allows investigation of the photooxygenation. TFA as the homogeneous catalyst can either be (a) added directly to the DHAA containing feed or (b) dosed as a separate feed stream. The first option was used to optimize the reaction conditions using the extract as a feed source, while the second option was preferred for kinetic studies due to the distinct decoupling of both reaction steps. A second reaction line of varied lengths could be connected to the photoreactor as an additional residence time module in both modes (c). A packed-bed reactor filled with a heterogeneous acid is directly connected to the photoreactor in option d.

The reactor feed was prepared fresh on the day of the experiment and kept in containers of brown glass to prevent conversion by ambient light. For extract-based feed, the leaf extract was kept at $-20\,^{\circ}\mathrm{C}$ overnight to freeze out waxes and other components, which otherwise would clog the reactor. Depending on the set experimental conditions, purified dihydroartemisininic acid (DHAA) is added to the extract to better observe the reaction progress. To prepare the feed from only pure substances, DHAA and 9,10-dicyanoanthracene (DCA) were dissolved in the reaction solvent. The mixture was kept for $10\,\mathrm{min}$ in an ultrasonic bath. If required by the experimental setting, trifluoroacetic acid was added directly before the start of the experiment.

In preparation for the experiment, the whole system is rinsed with toluene and nitrogen, and the photoreactor is cooled down to reaction temperature. Once the reactor system reaches the desired temperature, the feed solution is connected to the reactor system, the gas phase is switched to the desired gas phase composition, and the acid dosing is started. The total flow rate was varied in a tight range of $0.5\,\mathrm{mL\,min^{-1}}$ to $2\,\mathrm{mL\,min^{-1}}$ to ensure comparable Taylor flow conditions in all

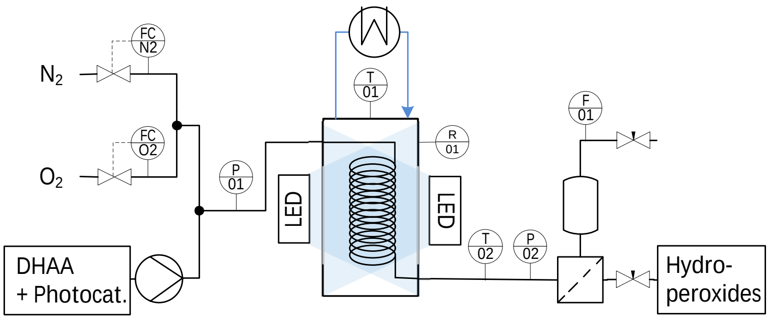

(a) Photooxygenation setting.

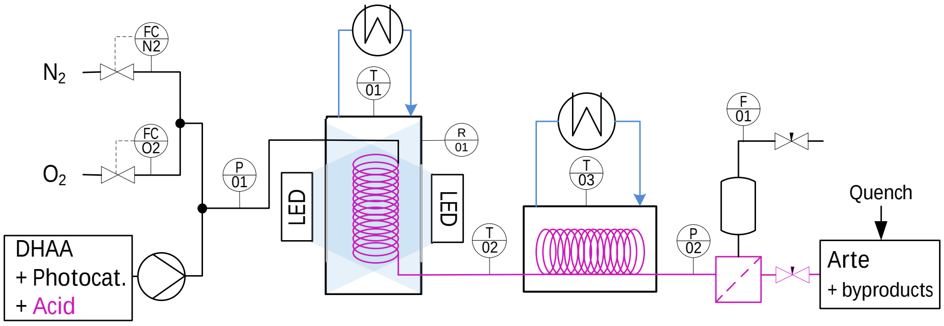

(b) Complete partial synthesis homogeneously catalyzed.

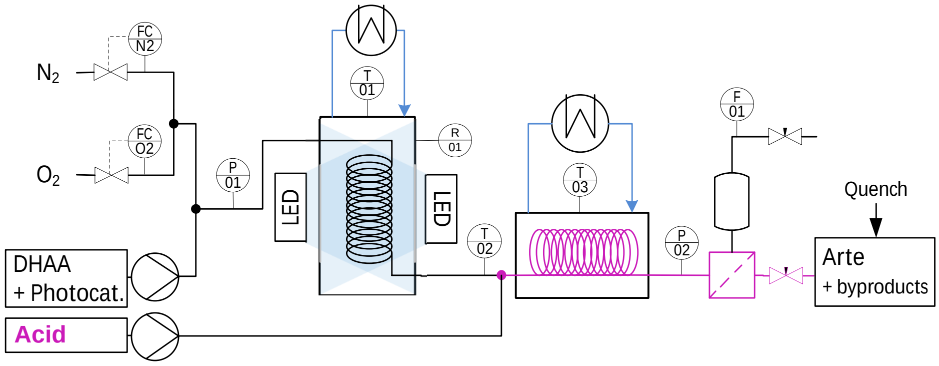

(c) Complete partial synthesis with separate photooxygenation and homogenously acid-catalyzed section.

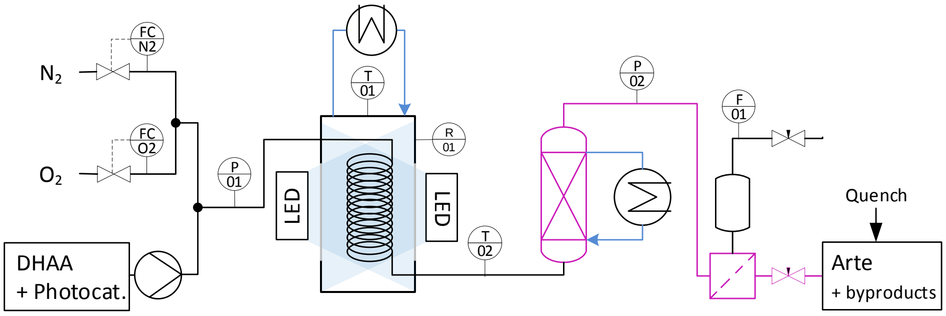

(d) Complete partial synthesis with solid-acid catalyzed formation of artemisinin.

Fig. 4.2: Experimental settings for the investigation of the photooxygenation and acid-catalyzed sequence, either separately or in combination. The pink marked lines highlight the reactor section where the acid-catalyzed reaction sequence is active.

experiments. The gas holdup ratio was kept constant at $\beta = 0.8$. If acid was dosed separately, the liquid flow rate consisted of a DHAA and a TFA containing stream in the ratio of 9:1 (v/v). When a stable system pressure of $7\,\mathrm{bar}$ was reached, the LED modules were turned on, and the experiment started.

Samples of the reactor effluent were collected when the whole system was in a steady state. If acid was present during the experiments, the samples were quenched with triethylamine, if not stated otherwise. To ensure the stationarity of the system, the samples of the reactor effluent were collected after the reactor showed constant conditions for at least four-fold of the theoretical residence time (Eq. (3.27)) in the whole system. When packed-bed reactors were used, the reactor effluent was sampled every $30\,\mathrm{min}$ for several hours. At least two samples were collected for each experimental setting. The samples were analyzed offline by HPLC and $^1\mathrm{H{-}NMR}$ depending on the product concentration and the experiment's aim. After sampling, the experimental conditions were changed to a new set, and a second experiment started. So each data point of the continuous experiments represents a single experiment.

4.3.4 Batch experiments for investigating the acid-catalyzed reaction sequence

Batch experiments were performed only in the context of the acid-catalyzed reaction sequence with two specific aims:

1. Identification of suitable heterogeneous catalysts
2. Kinetic investigation of the acid-catalyzed conversion of the intermediate hydroperoxide PO_1

The significant advantage of batch experiments is the amount of time-dependent data gained from one experiment. However, the lower surface area between gas and liquid phase in the available setup and the resulting slow mass transfer [256] limits the applicability to experimental settings where oxygen supply is not critical. Therefore, batch experiments are only suitable for performing a qualitative comparison of material combinations where all settings are equally affected by mass transfer limitation (application 1) or studying reaction pathways that do not involve oxygen at all (application 2).

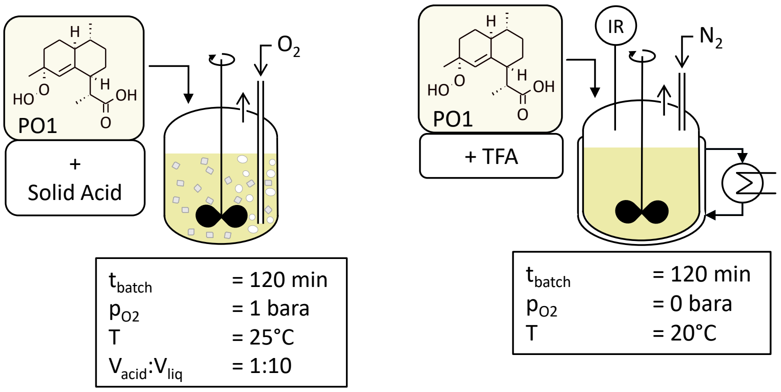

(a) Setup for screening solid acid materials

(b) Setup for kinetic studies on the acid-catalyzed cleavage of PO_1

Fig. 4.3: Experimental setup and condtions used for batch experiments regarding a) the utilization of with solid acids or b) the kinetics of non-oxygen controlled reaction pathways within the partial synthesis to artemisinin.

4.3.4.1 Preparation of the PO_1 containing reactant solution

The reactant PO_1 was produced on the day before the batch experiment using the continuous setup with the standard photooxygenation procedure (Sec. 4.3.3). The reactor feed consisted of $0.25\,\mathrm{M}$ DHAA and $2.5\,\mathrm{mM}$ DCA in toluene. The feed was pumped through the photoreactor together with pure oxygen with a total flow rate of $2\,\mathrm{mL\,min^{-1}}$ so that a residence time of $2.5\,\mathrm{min}$ in the irradiated section was obtained. The photoreactor was operated at $-20\,°\mathrm{C}$. The reactor effluent was collected after depressurization in a brown flask and stored overnight in a fridge at $4\,°\mathrm{C}$. The obtained solution was used directly as the feed solution for the batch experiments without further workup. Using this procedure, an initial concentration of $0.2\,\mathrm{M}$ PO_1 was obtained.

4.3.4.2 Setup and procedure

Two different batch setups were used for testing solid acidic catalysts and for investigating the reaction kinetics, as depicted in Fig. 4.3. The tests on solid acids were performed in a $100\,\mathrm{mL}$ glass flask stirred by a magnetic stirrer and closed with a rubber stopper as shown in Fig. 4.3a. Oxygen from the inhouse gas supply was bubbled through $30\,\mathrm{mL}$ reactant solution containing PO_1 at ambient conditions.

The experiment was started by adding $3\,\mathrm{mL}$ of the corresponding solid acid. In regular time intervals, $0.4\,\mathrm{mL}$ samples of the reaction solution were withdrawn with a syringe, separated from the solid acid with a syringe filter (cellulose, $0.20\,\mu\mathrm{m}$) and quenched with triethylamine (TEA).

For the kinetic experiments, precise temperature control and reaction monitoring was applied to obtain reliable kinetic data. Therefore, the equipment was improved by using a double-walled glass reactor attached to a cooling thermostat keeping the temperature within the reactor at constant $20\,^{\circ}\mathrm{C}$ (Fig. 4.3b). For temperature and reaction monitoring, a FTIR probe was integrated into the setup. The reactor was rinsed with nitrogen to prevent oxygen from diffusing into the reactant solution. The glass reactor was again stirred by a magnetic stirrer and closed with a rubber stopper.

For the experiment, $30\,\mathrm{mL}$ reactant solution were given in the reactor and stirred for $30\,\mathrm{min}$ while rinsed with nitrogen to remove all oxygen from the flask. The experiment was started by adding TFA dissolved in $1\,\mathrm{mL}$ toluene. The samples were collected through the rubber stopper with a syringe and directly quenched with TEA dissolved in $0.4\,\mathrm{mL}$ toluene. The collected samples of both types of batch experiments were analyzed by $^{1}\mathrm{H-NMR}$ (Sec. 4.4.2).

4.4 Analytical Methods

The product solutions of extraction and partial synthesis were characterized using high-performance liquid chromatography (HPLC), nuclear magnetic resonance spectroscopy (NMR), and UV/Visible spectroscopy (UV/Vis). HPLC was applied to quantify the content of the reactant dihydroartemisinic acid (DHAA) and the product artemisinin in the extract. However, most of the reaction intermediates and byproducts are not available in pure form or are not stable enough to be purified as a standard, which is required for calibration of the detector. Therefore, $^{1}\mathrm{H-NMR}$ complemented the HPLC analysis and was mainly used for highly concentrated solutions. The concentration of the chlorophyll species was determined by UV/Vis spectroscopy.

4.4.1 HPLC analysis for quantifying artemisinin and DHAA in the extract

The analysis is performed on an analytical HPLC unit (Agilent 1100 Series, Agilent Technologies Germany GmbH). The system consists of an autosampler, a four-channel pump, a column oven, and an evaporative light scattering (ELS) detector (Agilent Infinity II ELSD). DHAA and artemisinin are weak chromophores exhibiting only low absorbance in the far UV spectrum. The sample solvent toluene, however,

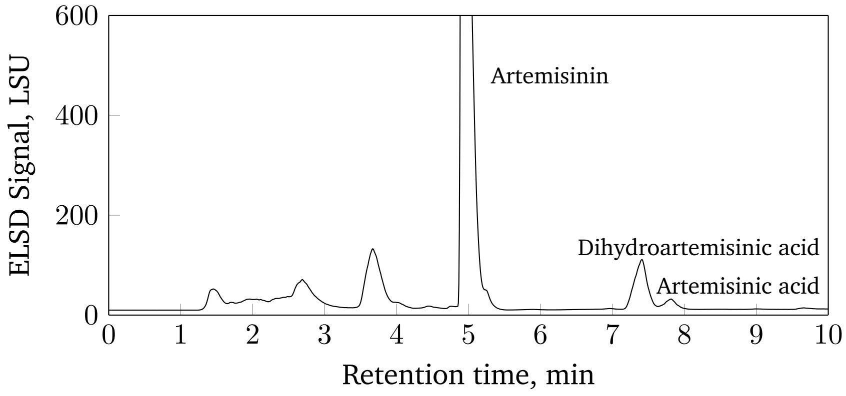

Fig. 4.4: HPLC-Chromatogram of the extract of *A. annua* in toluene using an evaporative light-scattering detector (ELSD) for quantification.

shows a strong absorption at $\lambda \ln 284\,\mathrm{nm}$ and masks the artemisinin signal in a diode-array detector (DAD) due to their similar retention times. The ELSD enables the quantification of artemisinin in the presence of toluene by evaporating all volatile components and analyzing the light scattering at the formed particles of the non-volatile analytes.

The separation of the extract was achieved with a reversed-phase column (KINETEX C18, 250 mm × 4.6 mm; 5 μm, Phenomenex GmbH, Germany) and acetonitrile (ACN) water mixtures as mobile phase. The sample preparation and measurement conditions of the applied gradient method are given in App. B.1. An exemplary chromatogram of the extract is shown in Fig. 4.4.

The measurement accuracy for the applied analysis is in the range of $15\,\%$ relative to the absolute results. The measurement variance arises mainly from the lower accuracy of the applied ELSD detector compared to absorption-based methods.

4.4.2 NMR analysis for quantifying the products of the partial synthesis

Nuclear magnetic resonance spectroscopy facilitates the quantification of analytes without the requirement of a pure reference for quantification. The ^{1}H spectrum is used exclusively in this work to quantify the reaction products of the artemisinin partial synthesis. Each signal in the ^{1}H spectrum contains three types of information representing a group of hydrogen nuclei exposed to the same chemical environment within a molecule. The chemical shift δ gives information on the electronegative and inductive effect of the surrounding groups. The form or multiplicity of a signal shows how many magnetic nuclei are in close proximity and couple with each other. The integral of the signal contains the number of nuclei in the same chemical environment, contributing to that considered signal. All three types of information are equipment-independent and can be accessed for already identified and assigned compounds in literature and databases. The research group of Brown et al. provided a library of NMR spectra assigned to 33 species related to the artemisinin partial synthesis [70, 197, 198].

The proportionality of a signal's integral to the number of nuclei enables quantification of an analyte related to an added internal reference with known concentration. In this work, mesitylene and dimethyl terephthalate (DMT) were used as internal standards to quantify the reaction products of the artemisinin partial synthesis. The samples were analyzed in the NMR laboratory of the *Otto-von-Guericke University*. Details on the sample preparation and quantification are given in App. B.2.1 and B.2.2.

Fig. 4.5 shows a $^1\mathrm{H{-}NMR}$ spectrum of the product solution after the partial synthesis. In the region $\delta \leq 3\,\mathrm{ppm}$ the signals strongly overlap, preventing a clear distinction and quantification of the separate species. Therefore, the signals within the region of $4.5\,\mathrm{ppm}$ to $6.5\,\mathrm{ppm}$ were used to calculate the concentration of the formed species. A list of all regarded reaction products and their NMR signals is included in App. B.2.2.

With the applied method, the analyte was determined with a relative measurement error of $\pm\,5\,\%$.

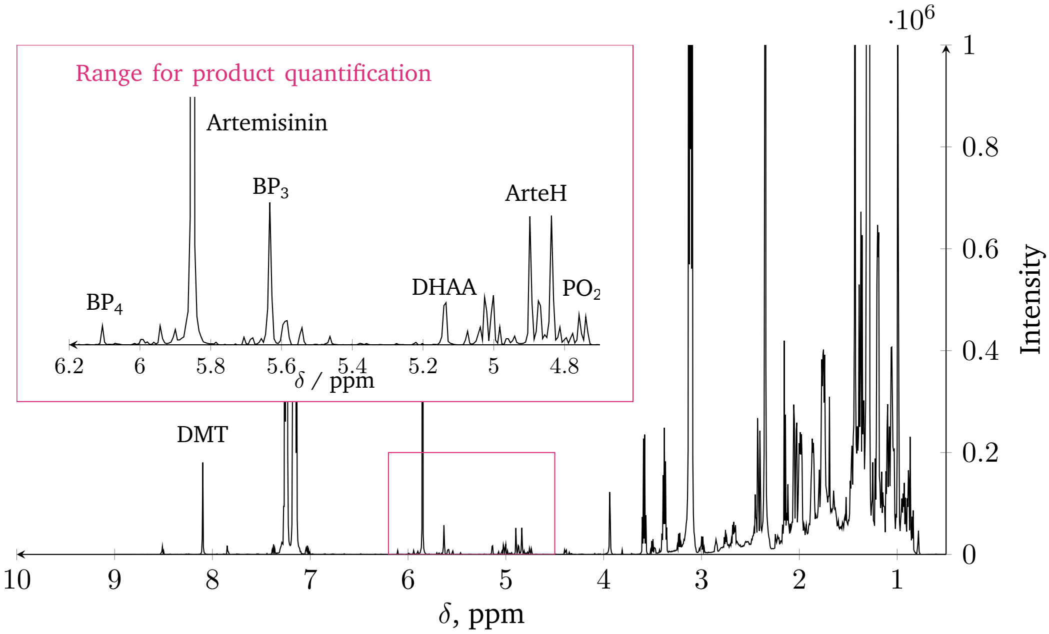

Fig. 4.5: ^{1}H spectrum of the product solution from the partial synthesis starting from dihydroartemisinic acid (DHAA). Dimethylterephthalate (DMT) is used as internal reference for quantification.

4.4.3 UV/Vis analysis for quantifying chlorophylls

The concentration of the present chlorophyll species in the extract was determined based on UV/Vis spectroscopy following the method of Lichtenthaler et al. [383]. All UV/Vis spectra in this work were measured with the spectrophotometers Genesys 6 by Thermo Electron Corporation and UVmini-1240 by Shimadzu in the region of $350\,\mathrm{nm}$ to $750\,\mathrm{nm}$. If necessary, the samples were diluted to keep the absorption in the region of $600\,\mathrm{nm}$ to $700\,\mathrm{nm}$ between $0.3\,\mathrm{A}$ to $1.5\,\mathrm{A}$.

The absorption of the extract was determined at the wavelength with maximum absorption of chlorophyll A (ChlA), chlorophyll B (ChlB), and the degradation product pheophytin A (PheoA). The concentration of the chlorophyll species were obtained by solving a system of linear equations based on the Lambert-Beer-law (App. B.3.2) The required absorption coefficients at the absorption maxima of the different chlorophyll species were determined with the pure pigments dissolved in the corresponding solvent (App. B.3).

4.5 Summary

The partial synthesis of artemisinin starting from dihydroartemisinic acid was studied based on a continuous photo-flow reactor system with a thin channel diameter of less than $2\,\mathrm{mm}$ utilizing Taylor flow conditions. The photoreactor system is versatile so that the photooxygenation and the acid-catalyzed reaction sequence can be studied separately or in combination using either trifluoroacetic acid as homogeneous catalyst or solid acids as heterogeneous alternatives. The provided photon flux within the reactor channel was estimated with chemical actinometry using the established potassium ferrioxalate actinometer.

The reactor feed of the experiments on the partial synthesis consisted of either pure reactants including 9,10-dicyanoanthracene as photocatalyst or crude extract obtained from the extraction of ground and dried leaves of *A. annua* in toluene as standard solvent. The continuous experiments in the photo-flow reactor were complemented with batch experiments studying reaction pathways where oxygen mass transfer is not crucial. The *A. annua* extracts and the product solution of the partial synthesis are characterized by HPLC analysis for the quantification of DHAA and artemisinin, in combination with quantitative ^{1}H-NMR analysis for byproducts and intermediates and UV/Vis spectroscopy to estimate the chlorophyll concentration.

5

Selection of photocatalyst, solvent, and acidic catalyst for the partial synthesis of artemisinin

The central aim of this thesis is to investigate whether dihydroartemisinic acid (DHAA) obtained as a side-product from the extraction can be utilized in a safe and economically viable process as a source for additional artemisinin. The chemical conversion of DHAA to artemisinin, referred to as partial synthesis, requires a photosensitizer for the formation of singlet oxygen and an acidic catalyst (Sec. 2.3.1). In the best case, both catalysts are nontoxic, easily recyclable, and highly active in the chosen solvent. The solvent itself should enable high selectivity in the extraction and the reaction step. Therefore, the choice of catalysts in combination with the solvent is crucial to achieving a cost-efficient reaction step complementing the overall extraction-based production process.

As introduced in Sec. 2.3.3, several different reaction systems were proposed for the partial synthesis in pure and precisely controlled conditions. In the following, these concepts are investigated regarding their applicability on plant extracts. In addition, new candidates as catalysts and solvents are proposed, derived from the specific combination of extraction and reaction. Specifically, co-extracted chlorophyll is tested as a natural and abundant photosensitizer. In the next step, solvents are investigated to enable extraction and synthesis with high efficiency. Finally, heterogeneous acidic catalysts are studied to eliminate the need for catalyst recycling.

All concepts are investigated in highly concentrated solutions regarding DHAA before transferring the most promising alternatives to extracts with natural DHAA content in the following chapter. The comparison of process options focuses on achieving a simple, safe, and efficient production process.

The study on chlorophyll as alternative photosensitizer was performed in close cooperation with Peter Seeberger and Kerry Gilmore from the *Max Planck Institute of Colloids and Interfaces*, Potsdam/Golm. The flow reactor system developed and implemented in the Group for *Flow Chemistry* was applied for the synthesis experiments on using chlorophyll as photosensitizer. The contribution of the author of this

thesis was adapting the experimental setup to handle plant extract and designing, performing, and analyzing the continuous flow experiments. The work on the utilization of chlorophyll was published in [381]:
S. Triemer, K. Gilmore, T.G. Vu, P.H. Seeberger, A. Seidel-Morgenstern: "Literally Green Chemical Synthesis of Artemisinin from Plant Extracts". In *Angewandte Chemie Int. edition* 57 (2018), pp. 5525–5528.

5.1 Co-extracted chlorophyll as a cost-efficient alternative to currently applied photosensitizers

The initial step in the artemisinin partial synthesis requires the *in situ* formation of singlet oxygen, which either is produced by molybdate mediated consumption of hydrogen peroxide or photosensitized formation (Sec. 2.3.1.1). Both methods require the addition of catalysts which later need to be recycled and potentially contaminate the purified product [214].
In toluene, the chemical conversion of DHAA to artemisinin proceeds in $69\,\%$ yield in twelve minutes when singlet oxygen is produced in the presence of 9,10-dicyanoanthracene (DCA) [179, 211].
Apart from artemisinin and DHAA, the extract of *A. annua* also contains various other plant metabolites including the chlorophylls. The chemical structures of chlorophyll species present in plants and their absorption spectrum are shown in Fig. 5.1. Besides their essential function in photosyntheis, chlorophylls are known to sensitize the formation of singlet oxygen within the plant [181, 182, 191, 384]. This process is the probable source for $^1O_2$ required for the biosynthesis of artemisinin [62, 71]. For chemical synthesis, chlorophyll was already successfully applied as photosensitizer in the production of ascaridol [385, 386]. Due to its abundance and its broad absorption in the visible spectrum, chlorophyll is a potential alternative to conventional, often toxic photosensitizers.
The approach was to exploit the co-extracted chlorophyll as a photosensitizer for the conversion of co-extracted DHAA. The questions to be answered were

1. Is the activity and concentration of chlorophyll in the *A. annua* extract sufficient to initiate the photooxygenation?

2. Do other co-extracted impurities affect the overall selectivity to artemisinin?

First, the extraction of *A. annua* regarding chlorophyll in toluene was investigated. Then these extracts were used as feed for the photooxygenation. In the last step, the

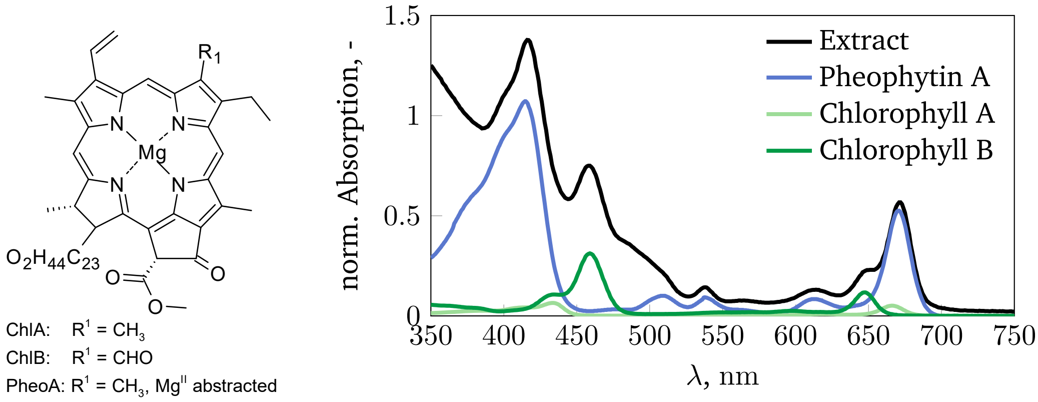

(a) **(b)**

Fig. 5.1: Three different chlorophyll species are present in the extract of *A. annua* in toluene: a) Chemical structure of chlorophyll A (ChlA), chlorophyll B (ChlB) and the decomposition product pheophytin A (PheoA); b) Absorption spectrum of the pure chlorophyll species and the crude extract obtained after 10 min extraction in toluene at 50 °C.

acid was added to the extract-based feed to study the complete reaction pathway to artemisinin.

5.1.1 Chlorophyll as byproduct of the extraction

The extraction of chlorophyll, DHAA, and artemisinin (Arte) was investigated by batch extraction at varied extraction temperatures. The concentration of artemisinin and DHAA were determined by HPLC analysis and the chlorophyll concentration by UV/Vis analysis (Sec. 4.4).

The obtained concentration profiles are shown in Fig. 5.2. The extraction of DHAA and Arte proceeds fast, reaching a constant concentration after 10 min. In all *A. annua* extracts examined, the DHAA concentration was only approximately one quarter of that of artemisinin. In contrast to DHAA and Arte, the extraction of chlorophylls shows a strong dependence on extraction temperature and time, reaching equilibrium after 24 h.

A high extraction temperature of 50 °C was chosen to obtain a high chlorophyll content for the initial studies on chlorophyll as photocatalyst. The extraction time was set to 10 min. In later studies, the batch extraction was performed at room temperature to simulate the conditions of the continuous extraction (Sec. 4.3.1).

The absorption spectrum of the extract obtained from extraction at 50 °C is shown in Fig. 5.1. The extract broadly absorbs visible light with maxima at 416 nm and

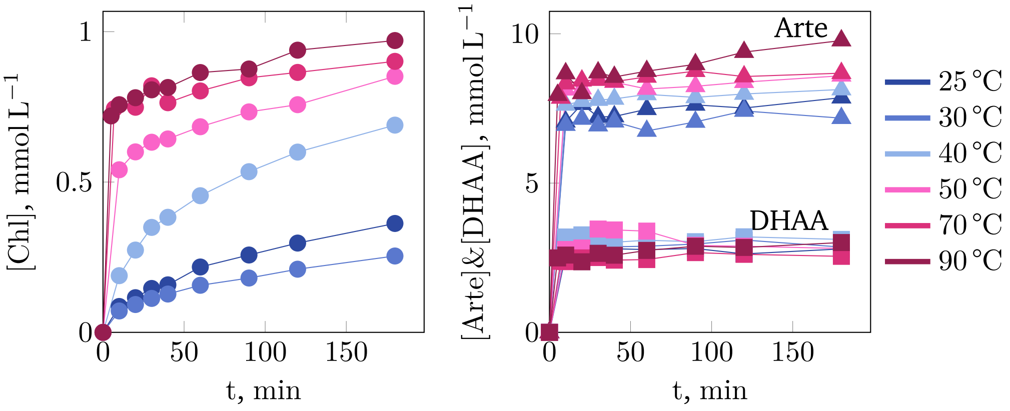

(a) Chlorophylls

(b) Arte & DHAA

Fig. 5.2: Extraction of chlorophyll species, DHAA, and artemisinin from *A. annua* with toluene at varied extraction time and temperature. Conditions: Batch extraction, $m_{leaves}/m_{solvent} = 1{:}5$.

672 nm such that a wide range of light sources can be used to excite the contained chlorophyll. The main chlorophyll species present in the extract is pheophytin A, a decomposition product of chlorophyll A, lacking the central magnesium ion. Chlorophyll A and B are observed only to a minor extent. The mean total concentration of all chlorophyll species in the extract obtained at 50 °C is 0.42 mM.

5.1.2 Photooxygenation performance of chlorophyll

In the first step, the extract was investigated regarding its performance in the photooxygenation. The crude toluene extract was spiked with additional pure DHAA (0.5 M) to facilitate observation of the reaction progress. The reaction conditions for the photooxygenation were chosen based on the work by Kopetzki et al. [179]. The experiments were performed using the flow reactor setup implemented at the Group for *Flow chemistry* of the *Max Planck Institute of Colloids and Interfaces* in Potsdam/Golm. Details on the applied reactor system are included in [387]. The extract was fed together with oxygen into the photoreactor for irradiation with blue (420 nm) or red LED light (660 nm) at −20 °C.

The yield of the key intermediate PO_1 is shown in Fig. 5.3. With DCA as the photosensitizer, DHAA is completely converted after two minutes of irradiation with blue light yielding 91 % of PO_1. The obtained results confirmed the previous findings of Kopetzki et al. using the same photosensitizer [179]. Similar yields were obtained when irradiating the extract for three minutes with red light (87 %) or for five minutes with blue light (88 %). The yield of the byproducts, the secondary

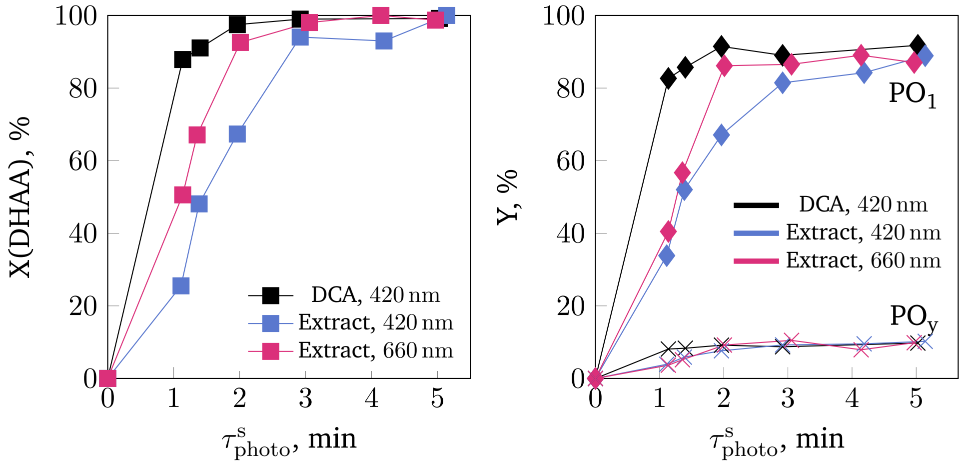

(a) (b)

Fig. 5.3: Performance of co-extracted chlorophyll as photosensitizer in comparison to 2.5 mM 9,10-dicyanoanthracene (DCA) in pure toluene: a) Conversion of DHAA and b) Formation of the main intermediate PO_1 and the byproduct PO_2 in dependence on the residence time and the irradiation wavelength. Reaction conditions: $[DHAA]^0$=0.5 M, T_{Photo}=−20 °C, β = 0.8 (v/v), p_{O_2}=7 bar.

hydroperoxides compiled in the species PO_y, are also similar for the crude extract and DCA in pure toluene. In these experiments, the chlorophyll concentration in the crude extract is six-fold lower than the DCA concentration.

In the next step, the activity of the extract was directly compared with the isolated chlorophyll A, its decomposition product pheophytin A, and DCA at an equal photosensitizer concentration of 30 mM, which is equivalent to the chlorophyll concentration in tenfold diluted extract (Fig. 5.4). With both chlorophyll species, high conversions of DHAA of $\geq$ 90 % were achieved after 7 min residence time, while only 26 % were obtained with DCA. The crude extract performs even better, with full conversion of DHAA and up to 90 % yield of PO_1 after seven minutes.

An increase of the reaction temperature from −20 °C from to ambient conditions results in a 10 % decline of PO_1 yield to 81 % for blue and 83 % for red light. Despite the moderate loss in selectivity to the desired hydroperoxide, room temperature might be economically viable due to the simplicity of the reactor setup and operation. In conclusion, chlorophyll co-extracted from the plant is a potent photosensitizer that exhibits a broad absorption in the visible spectrum. Irradiation of the extract enables fast photooxygenation of DHAA, which can even exceed the performance of conventional photosensitizers as DCA in pure conditions. The other components of the extract neither affect the selectivity to the desired intermediate PO_1 nor the main byproducts.

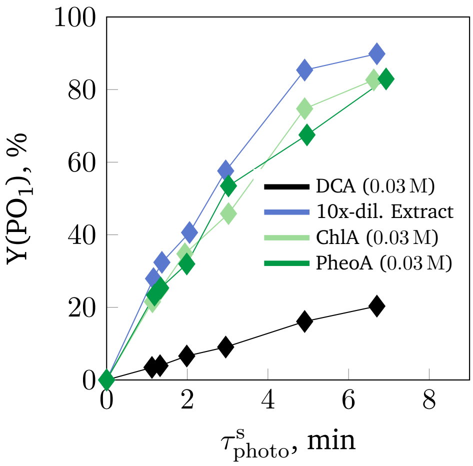

Fig. 5.4: Comparison of the photosensitizing activity of the extract with pure chlorophyll A (ChlA), its decomposition product pheophytin A (PheoA) and 9,10-dicyanoantracene (DCA), and 10-fold diluted extract, which equals a photosensitizer concentration of 0.3 mM. Reaction conditions: [DHAA]=0.5 M, $T_{Photo}=-20\,°C$,g/l=4/1 (v/v), $p_{O_2}=7$ bar.

5.1.3 Coupling of the photooxygenation and the acid-promoted sequence in crude extract

The conditions from the photooxygenation step were now transferred to the complete reaction pathways to artemisinin. In the presence of a strong acid, the intermediate PO_1 is cleaved and undergoes a complex reaction sequence of cyclization reactions yielding artemisinin as the main product. Following the work of Kopetzki et al. [179], trifluoroacetic acid was used as catalyst. The acid was directly added to the feed, initiating the conversion directly after the hydroperoxide formation. A second reaction line connected to the photoreactor (ID: 1.6 mm) served as an additional residence time module.

The length of added tubing section and the acid-concentration in the reactor feed were varied to optimize the obtained artemisinin yield (App. C.2). An additional 10 min residence time in 5 m reaction line were sufficient to reach completion of the partial synthesis. The addition of 0.375 M TFA helped to protonate any basic residues present in the crude extract.

The final process is depicted in Fig. 5.5. DHAA is dissolved in acidified crude extract and converted within 15 min to artemisinin with a final yield of 67 %, which is equal to the yields obtained with pure reagents. When red light is applied, the reaction time can be shortened to 14 min while obtaining a yield of 64 %. The known byproducts from the partial synthesis dihydro-*epi*-deoxyarteannuin B (BP_3) and arteannuin H (ArteH) are only formed to a minor extent of less than 10 %.

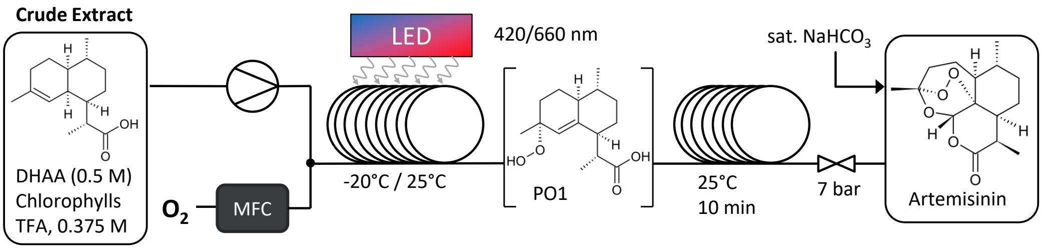

(a)

	T_{photo} °C	λ nm	τ^{s}_{photo} min	[TFA] $mol\,L^{-1}$	X, % DHAA	Y, % Arte	 BP_3	 ArteH
DCA in toluene	-20	420	2	0.25	100	**67**		
Extract	-20	420	5	0.375	100	**67**	3	4
Extract	-20	660	4	0.375	100	**64**	4	4
Extract	25	420	5	0.375	100	52	6	6
Extract	25	660	4	0.375	100	44	6	5

(b)

Fig. 5.5: Utilization of crude extract as reaction medium for the partial synthesis to artemisinin. Co-extracted chlorophylls serve as a natural photosensitizer in the initial photooxygenation: a) Optimized reaction conditions of the continuous photo-flow process b) Obtained artemisinin yield in comparison with the process using pure reagents and ambient temperature in the photooxygenation section.

When operating the photoreactor at room temperature instead of $-20\,°C$, the yield decreases by $15\,\%$ to $20\,\%$. This observation confirms the strong temperature effect observed for the partial synthesis with pure starting materials [70, 179, 203]. Photooxygenation experiments at elevated temperatures (App. C.1) showed that the drop in selectivity to artemisinin is only partly attributed to a less selective photooxygenation. The main decrease in selectivity arises from enhanced decomposition of the hydroperoxide PO_1 in acidic-conditions at higher temperatures.

The simplified photo-flow process with the plant extract as feed produces artemisinin as efficiently as state-of-the-art techniques that use purified reagents. The increased amount of impurities present during the reaction does not affect the selectivity to artemisinin. The addition and later recycling of purified photosensitizers as 9,10-dicyanoantracene are not required anymore. Therefore, the further investigations to optimize the utilization of DHAA are based on using chlorophyll as the photocatalyst and the extract as reaction medium.

5.2 Solvent selection for the combination of extraction and partial synthesis

The applied solvent for both extraction and partial synthesis is crucial for operating the coupled process in a viable, safe, and efficient manner. Toluene exhibits a high solubility of artemisinin [215] but poses high risk for the production process due to its tendency of forming explosive mixtures with air, and its toxicity against aquatic environments and humans [388]. Therefore, substituting toluene with safer and more environmentally benign alternatives is recommended [389, 390].

Liquid CO_2 and aqueous ethanol mixtures were already successfully applied for for the conversion of DHAA to artemisinin [208, 210]. The first option, however, requires sophisticated process equipment for the operation at high pressures, and the second is not recommended for the coupling with the extraction due to the low extraction performance of ethanol [103].

In the following, further solvent alternatives were tested qualitatively regarding their applicability for the partial synthesis. The critical requirements for the preselection were stability in strongly oxidative and acidic conditions, commercial availability, and improved environmental friendliness, and process safety compared to toluene. The final set of tested solvents includes butanol as alcohol, cyclohexanone, acetone and butanone as ketones, cumene and p-cymene as aromatic compounds, and anisol as a stable ether.

The selected solvents were first tested regarding the extraction of chlorophyll and their photooxygenation behaviour. The data is included in App. C. All solvents co-extracted chlorophylls in significant concentrations. The extraction times were adjusted to obtain comparable chlorophyll concentrations for each solvent. Photooxygenation experiments in pure solutions with DCA as the catalyst and in the obtained extracts showed that $0.01\,\mathrm{M}$ DHAA was converted entirely in all tested solvents within $5\,\mathrm{min}$, yielding $63\,\%$ to $74\,\%$ of the desired hydroperoxide PO_1.

The results for the complete partial synthesis of artemisinin with TFA as catalyst are shown in Fig. 5.6. Artemisinin yields comparable to the performance in toluene were only obtained in anisol, cumene, and p-cymene. All three solvents are similar in structure and polarity to toluene. The acid-catalyzed sequence proceeds much slower in the polar solvents butanone, cyclohexanone, and butanol, leading to residual hydroperoxide after $7.5\,\mathrm{min}$ residence time. Thus, the acid-catalyzed reaction sequence is very sensitive to the chemical structure of the applied solvent. This observation also confirms previous studies, which reported a lower yield of artemisinin with increasing polarity of the solvent [179, 201, 210].

Within the tested conditions, anisol, cumene, and p-cymene are the only solvents

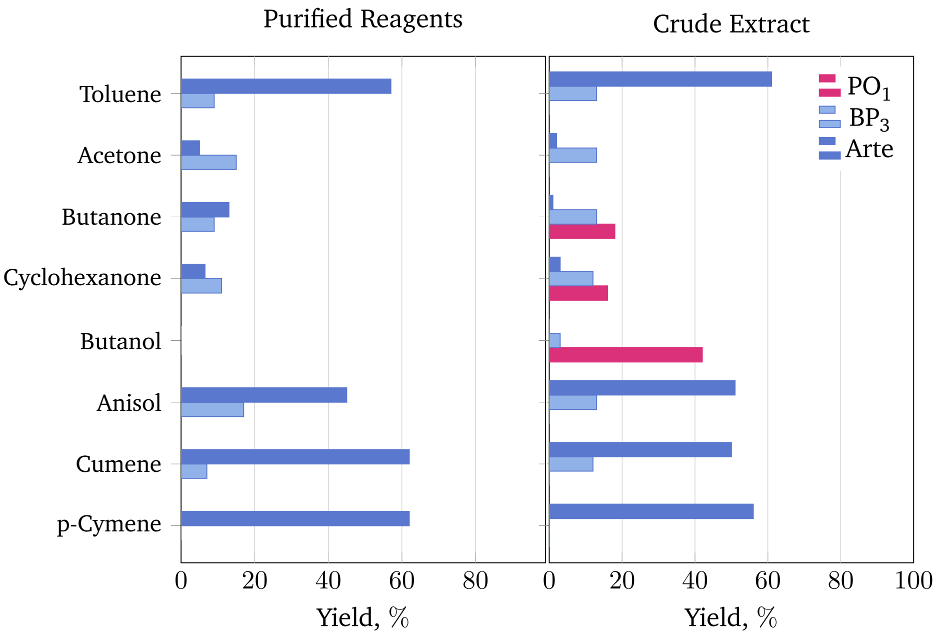

Fig. 5.6: Effect of the reaction solvent on the formation of artemisinin, the intermediate PO_1 and its main byproduct BP_3 in the partial synthesis. The reactor feed consisted either of the pure solvent with DCA as photocatalyst ($0.3\,\mathrm{mM}$) or the extract obtained by contacting *A. annua* with the corresponding solvent. DHAA was converted completely in all experiments. Reaction conditions: $T_{\mathrm{photo}} = -10\,°\mathrm{C}$, $\beta = 0.8$, $p_{O_2} = 7\,\mathrm{bar}$, TEA as quench, Pure conditions: [DHAA] $= 0.01\,\mathrm{M}$, [TFA] $= 0.09\,\mathrm{M}$, Extract-based feed source: [DHAA] $= 0.05\,\mathrm{M}$, [TFA] $= 0.35\,\mathrm{M}$.

that offer equal reaction performance of the partial synthesis as toluene. Cumene and p-cymene exhibit higher flame points than toluene but are similar in toxicity. However, the advantage of reduced flammability is counterbalanced by the benefits of toluene being an established solvent, e.g., the broad experience in operating plants safely, the large amount of available safety data, its high availability, and low price. Anisol is less toxic than toluene, cumene, and p-cymene but also less stable in highly oxidative conditions resulting in an increased explosion risk due to peroxide formation [391]. Therefore, toluene is not substituted by any of these three candidates. Cumene, p-cymene, and anisol are potential alternatives but require further detailed assessment of the process safety before applying them on a larger scale.

5.3 Potential of solid acids as alternative to trifluoroacetic acid

Similar to toluene, trifluoroacetic acid is recommended to be substituted by alternatives due to its related safety hazards and the difficult recycle and waste management [392]. Utilization of heterogeneous acidic catalysts is especially advantageous due to the simple separation of the catalyst from the product solution and therefore the easier reuse [393].

So far mono- and bifunctional catalysts based on ion-exchange resins as DOWEX [28] or amberlyst 15 [208] and metal-organic frameworks [212] could be successfully applied for the partial synthesis of artemisinin achieving comparable yields or even higher yields as observed with homogeneous acids (Sec. 2.3.3).

To explore the potential of solid acids as alternative to TFA in toluene as solvent, candidates from different classes of solid acids were screened in pure conditions in batch equipment. The high-yielding candidates were again tested in a continuous setting before applying the extract as feed source.

5.3.1 Scanning for suitable acidic candidates for the partial synthesis of artemisinin

The spectrum of acidic solids, which are used in chemical synthesis, is very broad [394]. The preselection of solid acids focused on obtaining a set of species with varied functional groups that are commercially available. Further advantageous properties were a high surface area, large pore size and a strong acidity. Based on these criteria, 23 different materials were tested, which belong to six different functional groups of solid acids. The selected materials are grouped in Fig. 5.7 and the specification of each material is included in App. D.1. The zeolite structures were tested with different silica to alumina ratios to observe the effect of a varied acidity on the selectivity.

The screening experiments were performed in batch mode with oxygen dosing at atmospheric conditions (Sec. 4.3.4). The obtained conversion of PO_1, the yield of artemisinin and known byproducts BP_3 and BP_4 at the end of the batch experiments after $120\,\mathrm{min}$ are shown in Fig. 5.8. The concentration profiles for selected materials are depicted in Fig. 5.9. The complete data for all other tested acids is included in App. D.2 .

The results from the heterogeneous acids were compared to the experimental data obtained with TFA ($0.25\,\mathrm{M}$) as homogeneous catalyst serving as a reference case.

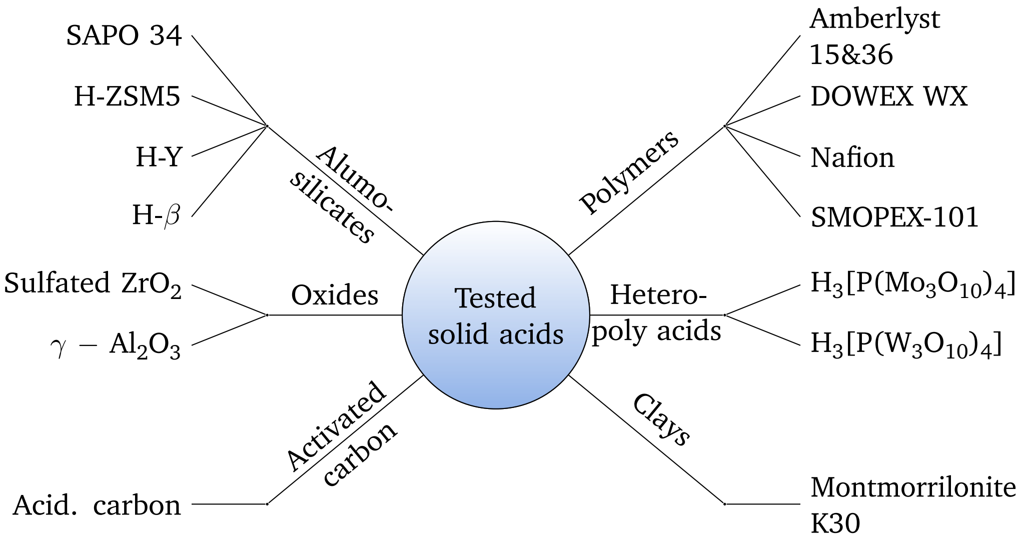

Fig. 5.7: Set of acidic materials tested as catalysts for the conversion of PO_1 to artemisinin in toluene.

After adding TFA, PO_1 is completely converted within $5\,\mathrm{min}$ (Fig. 5.9a). Artemisinin is formed at a slower rate reaching a stable concentration after $30\,\mathrm{min}$ of reaction time (Fig. 5.9b). Due to the lesser oxygen availability, the final yield of artemisinin dropped to $33\,\%$, which is half the yield observed with continuous processing in milli-scale conditions.

Higher artemisinin yields than in the homogenous case could be achieved with the ion-exchange resins DOWEX-50WX8, Amberlyst 15 & 36, SMOPEX-101, a β-zeolite with high silica to alumina ratio, sulfated zirconia, and the heteropoly acid (HPA) $H_3[P(W_3O_{10})_4]$. The reaction catalyzed by Amberlyst 15 exhibited a concentration profile most similar to the homogeneous case with TFA. All other materials showed slower rates of artemisinin formation.

The best performing materials are all strongly acidic. When catalysts with a weak acidity as alumina, SAPO34, and zeolites with low silica to alumina ratios were applied, no considerable conversion of PO_1 was observed. These results confirm that a high acidity is required to promote the cleavage of PO_1.

All tested ion exchange resins, namely the Amberlyst and DOWEX species, were strongly acidic, explaining their overall high activity in converting PO_1 to artemisinin. A critical property for zeolites is the pore size within the network which increases from ZSM5, Y, to β zeolite with a maximum pore size of $6\,\text{Å}$ [394]. The H-ZSM5 zeolite (Si/Al=200) offers a high selectivity to artemisinin. Due to the small pore size of the material, however, only the outer surface is accessible, and therefore the overall reaction is slow (App. D.2). The best performing zeolite, H-β (Si/Al=360), yielded $46\,\%$ of artemisinin after $2\,\mathrm{h}$ of reaction time.

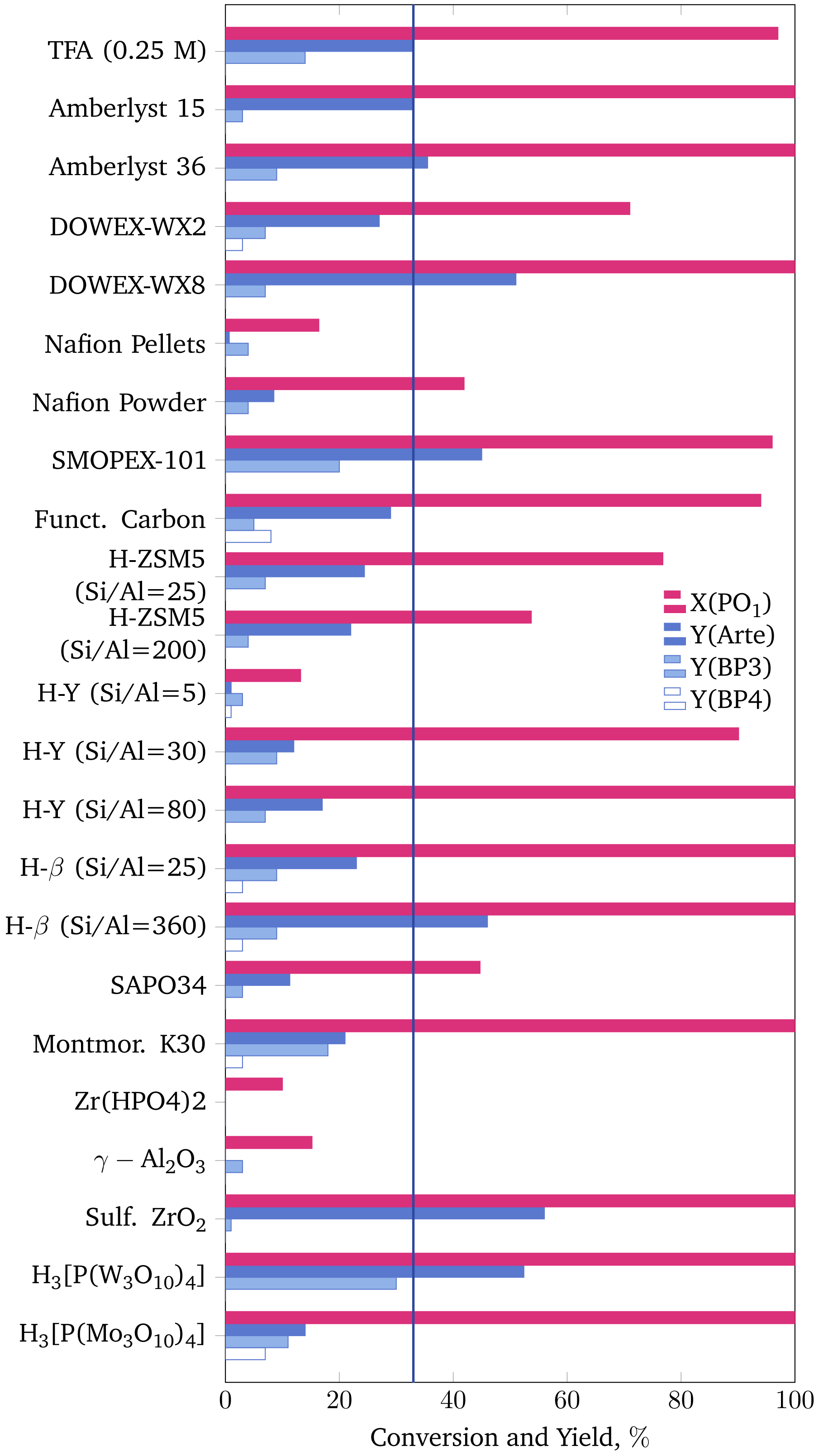

Fig. 5.8: Performance of heterogeneous acidic catalysts in the conversion of the hydroperoxide PO_1 to artemisinin (Arte) and its byproducts BP_3 and BP_4. The vertical line indicates the reference yield of artemisinin obtained with $0.25\,\mathrm{M}$ trifluoroacetic acid (TFA). Conditions: A PO_1 containing feed solution ($[PO_1] = 0.3\,\mathrm{M}$) was stirred with dispersed solid acid ($V_{\mathrm{acid}}/V_{\mathrm{liq}} = 1:10$), and contacted with oxygen at $1\,\mathrm{bara}$ and $25\,^{\circ}\mathrm{C}$ for $120\,\mathrm{min}$.

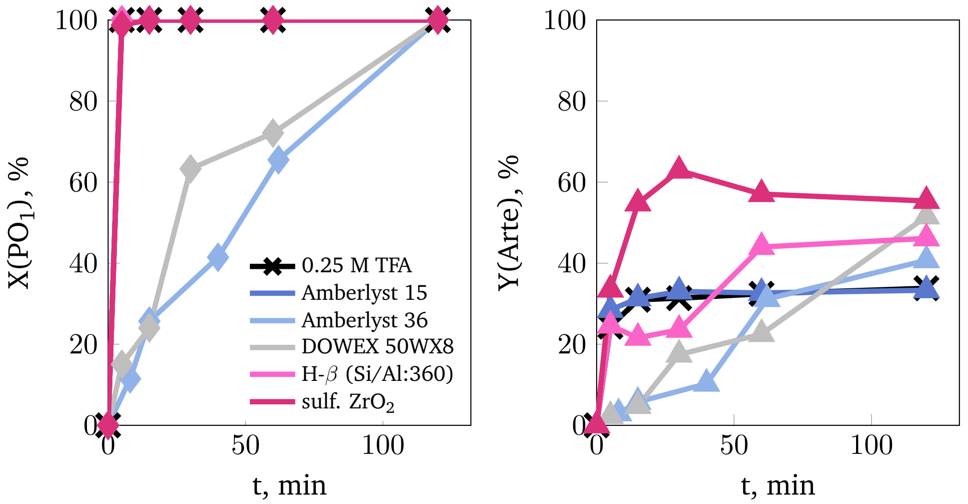

(a) Conversion of PO_1. (b) Yield of artemisinin.

Fig. 5.9: Reaction progress of the acid-catalyzed cleavage of the intermediate PO_1 (a) and formation of artemisinin in presence of five different solid acids (b). TFA serves as reference for the homogeneous catalyzed reaction. Condtions: Batch operation, $[PO_1] = 0.3\,\mathrm{M}$, $V_{acid}/V_{liq} = 1:10$, p_{O_2} =1 bara, T= 25 °C.

The highest yield of artemisinin, with 56 %, was achieved with sulfated zirconia and the heteropolyacid wolframatophosphoric acid. However, $H_3[P(W_3O_{10})_4]$ showed changes in color and visible decomposition of the material during the experiments. Since the heteropolyacids were used directly in their pure form without further stabilization on a support, the observed decomposition may result from the partial dissolution of the material.

The selection of the solid acids also affected the observed spectrum of byproducts. The low artemisinin forming substances, as $\gamma - Al_2O_3$, H-Y (Si/Al=5), and nafion pellets, even produced more BP_3 than artemisinin. The lowest production of known byproducts in comparison to the formed artemisinin concentration is obtained with sulfated zirconia.

These results show that the utilization of heterogeneous catalysts enables equal or even increased selectivity to artemisinin in comparison with the homogeneous case in batch processing. Four candidates were selected from the set of seven high performing materials identified in the batch experiments to be tested in continuous experiments: Amberlyst 36, DOWEX 50WX8, β-Zeolite (Si/Al=360) and sulfated Zirconia. SMOPEX-101 was excluded due to its toxicity. $H_3[P(W_3O_{10})_4]$ could not be used due to its low stability in the pure form. Amberlyst 15 was not further tested because it strongly adsorbs artemisinin which is disadvantageous in combination with the extract and its low artemisinin concentration.

It is essential to highlight that the performed batch experiments only allow for qualitative assessment of the activity of the tested materials. The quantitative comparison of the material is difficult due to the different properties of the used material, e.g., particle size and surface area. Based on the experimental data, only substances with weak acidic centers, e.g., alumina, can be generally classified as unsuitable catalysts for the partial synthesis.

5.3.2 Continuous coupling of the photooxygenation with the solid-acid promoted formation of artemisinin

In the next step, the solid-acid catalyzed reaction step was transferred to continuous operation by applying the four materials as packed beds and connecting them inline with the photoreactor (Sec. 4.3.2.2 and Sec. 4.3.3). The solid acids were packed in a glass column with an inner diameter of $15\,\mathrm{mm}$ for the standard configuration. The column was either fed from the top or the bottom. As an alternative, Amberlyst 36 was applied as a milli-scale flow reactor by immobilizing the particles as a long chain in FEP tubing (ID$=1.6\,\mathrm{mm}$). This reactor setup was not feasible for the other materials due to their smaller particle size and the resulting higher pressure drop. The applied configurations and obtained results are given in Fig. 5.10 and Tab. 5.1.

In the first set the bed was fed from above the column so that the liquid phase streamed along the catalyst particles down and the major part of the column was filled with gas phase. Contacting of the effluent stream from the photooxygenation with the packed beds resulted in almost complete conversion of the hydroperoxide PO_1 for all tested materials. The performance of Amberlyst 36 was equal between downward and upward flow and only slightly increased to $25\,\%$ of artemisinin formed when using the milli-scale flow reactor with a flow pattern comparable to the Taylor conditions in the photooxygenation section. The low yields even in these intensified flow conditions imply that the mass transfer of oxygen from gas to the liquid phase is not the limiting factor in this conversion.

The best performing catalysts were β-zeolite and DOWEX 50WX8 with a maximum yield of $39\,\%$ after passing the bed with an overall residence time of $30\,\mathrm{min}$ and $60\,\mathrm{min}$, respectively. The reaction regime could be extended by either adding a second tubular reaction line after the photoreactor, e.g., H-β or by sampling the reactor effluent without quenching (settings 5 & 8 in Tab. 5.1). Both options, however, could not raise the overall achieved artemisinin yield above $40\,\%$. The continued formation of artemisinin even after leaving the packed-bed reactor shows that H^+ is not contained in the column and needs regular regeneration.

The homogeneously catalyzed process achieves a $67\,\%$ yield when trifluoroacetic acid is already present during irradiation. The obtained yield decreased to $55\,\%$ when the

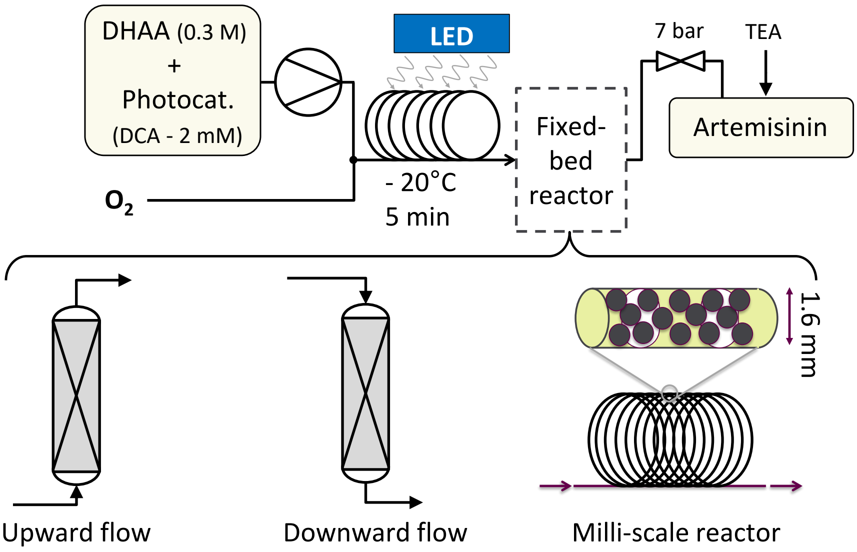

Fig. 5.10: Reaction conditions and tested flow schemes for coupling the photooxygenation with continuous solid acid catalysis.

Tab. 5.1: Obtained partial synthesis performance when coupling the photooxygenation with continous solid acid catalysis in dependence of the acidic material, the flow scheme, and the residence time.

ID	Catalyst	Downward flow			Upward flow			Milli-scale reactor		
		τ	Y, %		τ	Y, %		τ	Y, %	
		min	Arte	PO_1	min	Arte	PO_1	min	Arte	PO_1
1	Amberlyst 36	34	15	0	29	15	0	15	25	0
2		68	17	0	56	19	0	38	25	0
3	DOWEX 50WX8	30	17	0	30	23	0			
4		60	20	0	60	39	0			
5		60^{a}	38	0						
6	H-β (Si/Al=360)	16	31	0	20	20	3			
7		32	39	0	40	26	3			
8					45^{b}	39	5			
9	Sulfated ZrO_2	10^{c}	12	27						
10		20^{c}	20	10						

a: unquenched reactor outlet

b: A tubular reaction coil was connected downstream to the packed-bed reactor: $\tau^{\mathrm{s}}_{\mathrm{2ndline}}=5\,\mathrm{min}$

c: The PO_1 feed was produced the day before and then fed directly into the ZrO_2 column, $[PO_1]=0.22\,\mathrm{M}$

acid is added as a separate feed stream after the photoreactor (Sec. 7.2.1.1). Thus, the decoupling of the photooxygenation and the acid-catalyzed sequence already results in a drop in selectivity to artemisinin. Potential causes for the additional loss when applying solid acids in the tested conditions are limiting mass transfer between the liquid and solid phase and within the particles, enhanced byproduct formation, and reduction of the active acidic sites during operation. Optimization of the reactor type, the contacting of all three phases, reaction temperature, and the catalyst properties including surface area, particle size, chemical composition, and structure has great potential to achieve competitive yields to the homogeneously catalyzed partial synthesis in toluene. This optimization, however, requires further understanding of the reaction mechanism, the adsorption of the reactant and all product species, and the occurring mass transfer phenomena.

The goal of these investigations was to identify promising materials, which can be applied directly with the extract as feedstock to estimate the effect of the present impurities and the lower DHAA concentration on the overall process performance (Sec. 6.2.4). In this context, DOWEX 50WX8 and the β-zeolite were selected since both materials showed the best performance in the batch and continuous experiments out of the tested set of commercially available solid acids.

5.4 Conclusion

The viability of the partial synthesis as complement of the extraction-based production of artemisinin is determined by the choice of the solvent, the photosensitizer, and the acidic catalyst.

The extract of *A. annua* contains various plant metabolites, including the natural photosensitizer chlorophyll. It was demonstrated that chlorophyll is co-extracted in sufficient concentration to catalyze the first step of the partial synthesis, the photooxygenation, at equal rates as solutions with purified DCA. Performing the complete partial synthesis in the crude extract produces equal yields as obtained in purified conditions. Thus, utilizing chlorophyll enormously simplifies the partial synthesis because it eliminates the need for adding and recycling 9,10-dicyanoanthracene as photocatalyst. Crude chlorophyll is also an attractive photosensitizer for other reactions, which involve the formation of singlet oxygen, due to its wide availability, high reactivity and strong absorption in the visible light spectrum.

The scanning of alternative solvents showed that the acid-catalyzed conversion of the hydroperoxide is very sensitive to the selected solvent. Anisol, cumene, and p-cymene were the only tested solvents that achieved a comparable selectivity of artemisinin as in toluene. Due to the comparable toxicity of p-cymene and cumene and the increased explosive hazard of anisol in oxidative conditions, toluene was kept as the solvent for the partial synthesis.

The investigation of solid acids as an alternative to trifluoroacetic acid demonstrated that strongly acidic heterogeneous catalysts can achieve artemisinin yields equal or even higher than obtained with trifluoroacetic acid in batch operation. However, the application as a fixed bed in continuous operation resulted in significantly reduced artemisinin yields compared to TFA. Based on the batch and the continuous experiments, DOWEX 50WX8 and the H-β-zeolite with high silica to alumina ratio of 360:1 were identified as the most promising alternatives to TFA.

The identified set of toluene as process solvent, crude chlorophyll as photosensitizer, and TFA as acidic catalyst is now adapted for the partial synthesis using natural DHAA concentrations contained in the extract of *A. annua*.

6

Utilization of co-extracted DHAA as a source for additional artemisinin

The aim of integrating the partial synthesis into the extraction-based artemisinin production is to utilize co-extracted dihydroartemisinic acid as an additional source for artemisinin. In the best case, the extract can be subjected to the reaction unit directly after extraction without further separation or enrichment of DHAA. The results shown in the previous chapter were obtained at DHAA concentration levels which exceed the natural content in the extract up to 100-fold. Thus, the partial synthesis process has to cope with this lesser concentration of DHAA and, at the same time, an increased ratio of impurities in comparison to the reactant. In the following, the results of the previous chapter using highly concentrated solutions are transferred to extracts exhibiting natural concentrations of DHAA. Reaction conditions for both the photooxygenation and the acid-catalyzed step are optimized concerning the simplicity and economic viability of the process. Finally, the main parameters limiting the applicability of the process are discussed.

6.1 Sources and composition of the used extracts

The partial synthesis was investigated in extracts from two different leaf sources obtained either by batch or counter-current continuous extraction. The specification of the applied leaf sources and the obtained extracts are given in Tab. 6.1.

The batch extract from *A. annua* grown by Mediplant (Switzerland) was used as a standard case for adjusting the process settings to the extract-based feed solutions. Once the reaction conditions were set, the optimized synthesis was tested on the product solution from continuous extraction and on batch extracts from leaves grown in Kentucky, USA (ArtemiFlow). The conditions of the batch extraction (Sec. 4.3.1) were chosen to match the standard conditions of continuous counter-current extraction developed and implemented by Truong Giang Vu [137].

Both leaf sorts are high in artemisinin but low in the DHAA content. The conversion of DHAA to artemisinin during the prior drying process [57] and storage of the

Tab. 6.1: Composition of the used *A. annua* leaf material and the corresponding extracts either obtained by batch or continuous extraction in toluene.

Source		Mediplant (Switzerland)		ArtemiFlow (Kentucky, USA)
Content in dried leaves, wt-%	DHAA	0.1		< 0.1 [a]
	Arte	1.3		1.5 [a]
Extraction method		Batch	Continuous	Batch
Dosage: Leaves/solvent		1:10		1:10
Temperature		25 °C	RT	25 °C
Time		30 min	15 min	30 min
Concentration mM	Arte	4.0	6.3	4.1
	DHAA	0.95	1.3	0.5
	Chl	0.030	0.031	0.038
Solid matter, $\mathrm{g\,L^{-1}}$		5.7	5.9	5.9

[a] Three-year average content: Artemisinin 1.09 %, DHAA 0.3 % (dried weight) [395]

plant material (Sec. 2.1.2) may have caused the low DHAA content, also explaining the increased artemisinin content in Kentucky leaves compared to the three-year average value.

Both sources yield batch extracts with similar artemisinin, chlorophyll, and total solids concentration despite the different origins. The total solids content served as a measure to quantify the amount of impurities in the extract. The composition of these co-extracts was not further analyzed. Due to the low content of DHAA in the leaves, the extracted concentration in all tested extracts was also small. Thus, the potential to enrich the extract with additional artemisinin through partial synthesis is low with the two available leaf sources. The counter-current operation results in a higher concentration of the target compounds DHAA and artemisinin but also in an increased amount of total solids.

6.2 Optimization of reactions conditions

The small natural concentration of DHAA in the extract limited the investigation of the partial synthesis as an extension of the overall extraction-based production process. Studies on *A. annua* cultivation, however, showed that DHAA can be obtained to up to twice the amount of artemisinin (Sec. 2.1.2) [32, 43, 57]. So it was necessary to simulate these DHAA rich extracts by adding additional DHAA to the extracts obtained from the two available leaf sources. The DHAA content was adjusted to $8\,\mathrm{mmol\,L^{-1}}$ (equal to $2\,\mathrm{g\,L^{-1}}$), which is twice the natural artemisinin concentration in the extract. This initial concentration of DHAA represents an upper limit of the viability of the process. Even after DHAA addition, the obtained solutions were 50-fold more diluted than the feed solutions applied in the previous chapter. The total amount of co-extracted impurities exceeded the amount of DHAA by a factor of 2. This DHAA-enriched extract was applied to optimize the experimental conditions. Later in Sec. 6.4 the effect of the initial concentration on the overall reaction performance is investigated.

6.2.1 Irradiation duration, intensity and wavelength

The diluted state of the extract required revision of the residence time in the photoreactor. Therefore, the photooxygenation was studied first before investigating the whole reaction to artemisinin. All experiments were performed in the continuous milli-scale reactor system (Sec. 4.1). The obtained conversion of DHAA and the yields of PO_1 are depicted in Fig. 6.1 in dependence on the residence time, the irradiation intensity, and the emission wavelength.

The overall reaction time to achieve complete conversion of $0.08\,\mathrm{M}$ DHAA in the extract is $4\,\mathrm{min}$ to $5\,\mathrm{min}$, which is equal to the time needed to convert $0.5\,\mathrm{M}$ DHAA (Sec. 5.1.2). Switching from blue to red light slows down the conversion of DHAA, which is contrary to the results previously seen at high DHAA concentrations (Sec. 5.1.2). This reduced performance may be caused by the lower extraction temperature and, thus, the resulting 10-fold lower chlorophyll concentration, or the slightly different light emission wavelength of $660\,\mathrm{nm}$ used in these experiments instead of $666\,\mathrm{nm}$ in Sec. 5.1. The absorption spectrum of chlorophyll in the red range is steep so that small changes in the light source can lead to significantly different absorption rates.

The observed yield of the hydroperoxyl intermediate PO_1 fluctuated strongly in the range of $0\,\%$ to $40\,\%$, independent of reaction time and the experimental conditions set. At these low concentrations, decomposition of PO_1, accelerated by other co-extracted components, e.g., fatty acids [197], during NMR sample preparation, may result in enhanced measurement uncertainties.

For the further investigations with the available setup, a residence time of $4\,\mathrm{min}$ in the photoreactor irradiated with $417\,\mathrm{nm}$ LED light at maximum intensity was chosen as experimental conditions for the photooxygenation step.

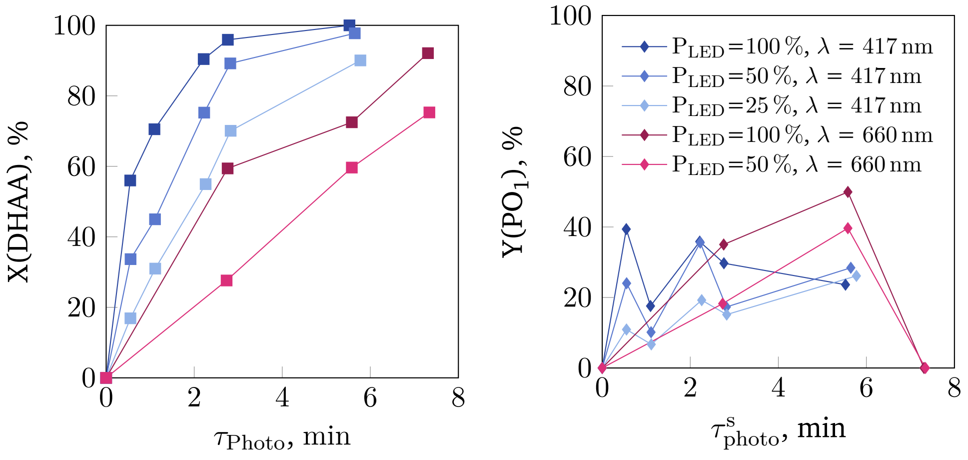

(a) Conversion of DHAA.

(b) Yield of PO_1.

Fig. 6.1: Photooxygenation using the extract with $[DHAA]^0 = 8\,mM$ in dependence on the residence time τ^{s}_{photo}, the emission wavelength and the irradiation intensity. Conditions: Batch extract of Mediplant leaves, no prior solvent removal, $T_{photo}=-20\,°C$, $p = 7\,bara$, $x_{O_2}=1$, $g/l=4/1$ (v/v).

6.2.2 Acid concentration and residence time

In the next step, the required concentration of trifluoroacetic acid and the residence time in acidic conditions was revisited. The acid was added directly to the reactor feed so that the acid-catalyzed sequence starts already in the photoreactor. The residence time was studied by varying the reactor length.

As shown in Fig. 6.2a, a residence time of $4\,min$ in the photoreactor and additional $2\,min$ until quenching is sufficient to reach completion of the partial synthesis with a DHAA conversion of $100\,\%$ and an artemisinin yield of $40\,\%$ to $45\,\%$. This residence time corresponds to passing the photoreactor and the necessary downstream section, including phase separator, and pressure control without any additional second reaction line integrated. Increasing the reactor volume and residence time did not result in increased artemisinin yields. However, the overall yields of artemisinin are $20\,\%$ lower than obtained with extracts highly enriched with DHAA.

Variation of the TFA concentration did also not further raise the obtained artemisinin yield (Fig. 6.2b). A concentration of $0.0625\,M$ is sufficient to drive the reaction to completion within $6\,min$ residence time in the entire reactor system. The obtained yield of maximum $45\,\%$ is still $22\,\%$ lower than observed previously for high DHAA concentrations (Sec. 5.1.3). However, the identified reaction conditions are also equal to a six-fold decrease in the required amount of acid and an almost two-fold reduction in total residence time.

Fig. 6.2b highlights the uncertainty and variability of the obtained reaction per-

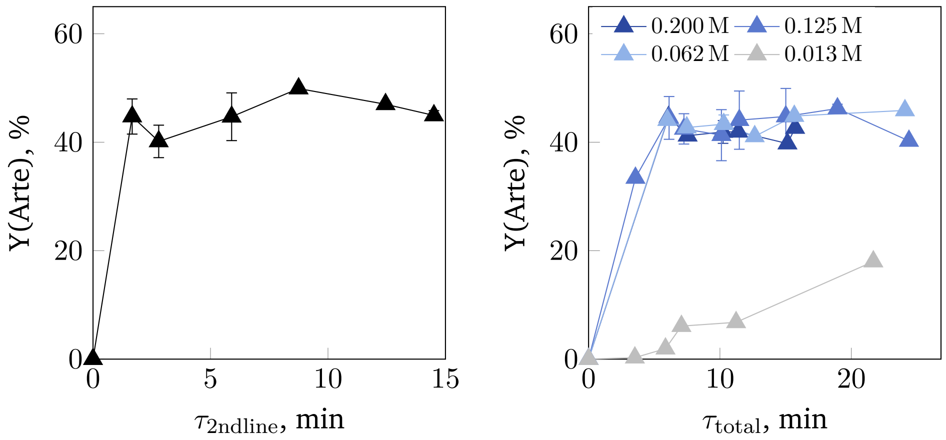

(a) Effect of the residence time on the artemisinin yield, [TFA]= 0.125 M

(b) Effect of the TFA concentration on the artemisinin yield

Fig. 6.2: Short residence times and low concentrations of acid are sufficient to complete the transformation of co-extracted amounts of DHAA to artemisinin: a) Dependence of the artemisinin yield on the residence time in the reactor section between the photoreactor and the outlet; b) Dependence of the artemisinin yield on the concentration of trifluoroacetic acid (TFA) contained in the reactor feed. Conditions: Batch extract of Mediplant leaves, no prior solvent removal, $T_{\text{photo}}=-20\,°C$, p = 7 bara, $x_{O_2}=1$, g/l=4/1 (v/v).

formance. Data obtained at equal acid conditions of 0.125 M but with different extract batches lies within 40 % to 48 % yield of artemisinin. The uncertainty of each data point accumulates from the single deviation for each batch of extract and the measurement uncertainty of the applied HPLC method with 10 % (Sec. 4.4.1).

6.2.3 Reactor temperature and gas phase composition

At a high concentration of DHAA, the selectivity of artemisinin increases with lowering the reactor temperature during photooxygenation (Sec. 5.1.3). That is why all investigations so far have been performed at −20 °C in the photoreactor. Experiments with the extract and an acid concentration of 0.125 M (Fig. 6.3a) showed that similar yields of 38 % to 42 % artemisinin were obtained at ambient temperature as at −20 °C. Complete conversion of DHAA was observed in all experiments. The switch from pure oxygen to pressurized air as gas-phase did also not result in a drop in the process performance.

The viability of these milder conditions was confirmed by performing the partial synthesis at ambient conditions with the lowest feasible acid concentration previously identified of 0.0625 M. The results are shown in dependence on the residence time

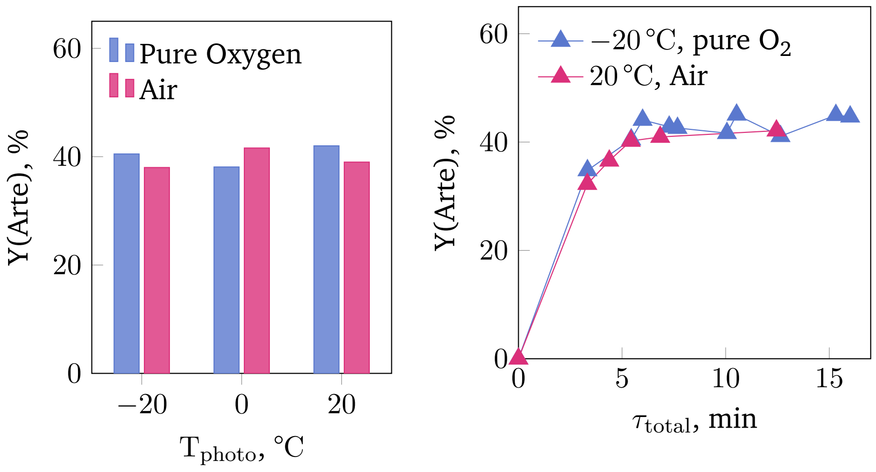

(a) Effect of photoreactor temperature and gas phase composition, ([TFA]=0.125 M).

(b) Comparison of operation at mild and intensified conditions, [TFA]=0.0625 M.

Fig. 6.3: Operation of the partial synthesis at mild reaction conditions: a) Effect of temperature increase and the use of pressurized air ([TFA] $= 0.125\,\mathrm{M}$, $\tau^{s}_{total} = 6\,\mathrm{min}$), b) Artemisinin yields obtained with intensified and mild reaction conditions ([TFA] $= 0.0625\,\mathrm{M}$). Conditions: crude batch extract, source: Mediplant, $[\mathrm{DHAA}]^0 = 8.5\,\mathrm{mM}$, p=7 bar.

in Fig. 6.3b. The data confirmed that a total residence time in the reactor of $6\,\mathrm{min}$ is sufficient to achieve completion of the partial synthesis. With milder reaction conditions, artemisinin yields of $40\,\%$ were obtained, while operation at intensified conditions resulted in $43\,\%$ of yield. This slight decline lies within the experimental uncertainty related to using natural material as feedstock. Even if the drop in artemisinin yield is systematic, it is counteracted by the improved simplicity in process equipment and reduced operational costs since no cooling is required anymore.

6.2.4 Application of heterogeneous acids as acidic catalysts

In the previous chapter, the ion change resin DOWEX 50WX8 and the zeolite H-β (Si/Al=360:1) were identified as potential heterogeneous alternatives to trifluoroacetic acid to catalyze the transformation of PO_1 to artemisinin in toluene (Sec. 5.3). The disadvantage of separating the photooxygenation step and acid-catalyzed step in a packed-bed reactor is the accumulation of hydroperoxides in the reaction line, which can pose a significant safety hazard due to their explosion potential [30]. This risk is reduced when working with the lower DHAA concentration in the extract.

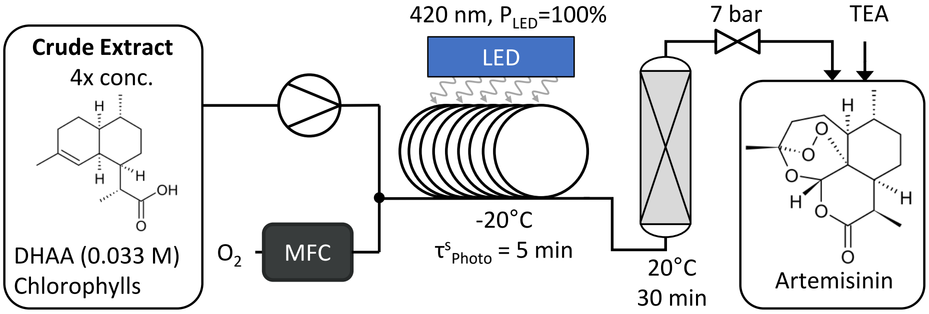

Acidic catalyst	$\tau^{s}_{\text{Fixedbed}}$ min	X, % DHAA	Y, % PO_1	Arte	BP_3
DOWEX 50WX8	30	100	0	11	22
Hβ-Zeolite (Si/Al=1:360)	15	100	0	24	7
Hβ-Zeolite (Si/Al=1:360)	20^{a}	100	0	32	8
Hβ-Zeolite (Si/Al=1:360)	$20^{a,b}$	100	0	36	8

a: A reaction coil was connected downstream of the packed-bed reactor: $\tau^s = 5\,\text{min}$.

b: The reactor effluent was not quenched

Fig. 6.4: Substitution of TFA in the reactor feed by by DOWEX WX8 and Hβ-Zeolite as heterogenous acids: Experimental conditions and obtained yields of artemisinin, its precursor PO_1, and the byproduct BP_3.

The packed-bed reactors of DOWEX 50WX8 and the zeolite H-β (Si/Al=360=1) were prepared as described in Sec. 4.3.2.2. The specifications of the used beds are included in App. D.1. The packed-bed reactors were directly connected to the photoreactor and were operated in upward flow mode. The experimental conditions are illustrated in Fig. 6.4 together with the obtained yields of artemisinin, its precursor PO_1, and the main byproduct BP_3.

A residence time of $30\,\text{min}$ in the presence of DOWEX 50WX8 is sufficient to entirely convert the hydroperoxide PO_1 formed previously in the photoreactor. Artemisinin is produced only to a minor extent while the formation of the byproduct BP_3 is enhanced. The Hβ-zeolite achieves higher yields for artemisinin while forming equal yields of BP_3 as in the homogeneously catalyzed partial synthesis. Complete conversion of PO_1 requires $15\,\text{min}$ residence time in the packed bed reactor. The formation of artemisinin proceeds even after leaving the packed-bed reactor resulting in an artemisinin yield of $36\,\%$ in the unquenched reactor effluent. Thus, the applied beta-zeolite with a high silica to alumina ratio of 1:360 almost equals the results obtained with trifluoroacetic acid in the homogenous case.

Applying a heterogeneous catalyst also adds an additional layer of complexity to the process operation and optimization. The chosen β-zeolite exhibits a significant adsorption capacity for artemisinin, its reactants, byproducts, and all plant dyes. At the tested conditions with a liquid flow rate of $0.2\,\text{mL}\,\text{min}^{-1}$, the first elution of artemisinin and other extract components was detected after 2 h of operation. However, during operation, H^+ is constantly leached out of the column. This effect resulted in reduced artemisinin formation after 4 h of continuous processing. To further optimize the process, the adsorption of the extract components and the leaching of acidic activity need to be quantified and included in the reactor design. Due to this complexity, further investigation on converting co-extracted DHAA to artemisinin focuses on the homogeneous case using trifluoroacetic acid as the catalyst.

6.3 Robustness with respect to leaf source, extraction conditions and extract pretreatment

The broad application of the partial synthesis as a complement of the extraction process requires a reaction step with a robust performance independent of the available leaf source, the extraction mode, or deviations in the extract composition. Therefore, the developed process at mild reaction conditions was extended to batch extracts of the leaves supplied by ArtemiFlow and extracts obtained by continuous extraction of Mediplant leaves. Furthermore, the feed composition was varied by concentrating the extract through evaporation of the solvent prior to the reaction step. This concentration step offers an additional degree of freedom to raise the overall productivity of the reaction step. The experimental results obtained with the different extracts are summarized in Tab. 6.2.

For non-concentrated extracts from Mediplant leaves, equal artemisinin yields of 41 % are obtained with the batch and the continuous extract. The leaves from ArtemiFlow enabled slightly increased yields of up to 48 %. Similar performance is obtained in all three extracts when concentrating the solution up to one-quarter of the initial volume. Due to the higher chlorophyll concentration, the increased initial concentration of DHAA could be converted to artemisinin, while keeping the same residence times as used for the non-concentrated extract.

Only when concentrating the continuous extract and the ArtemiFlow batch extract 8-fold, the conversion of DHAA drops to 70 % to 80 %, and artemisinin is only formed to 10 % yield in the partial synthesis step. The drop in the conversion may be caused by the high chlorophyll concentration, resulting in total absorption of the light and shadowing effects within the reactor setup. In addition, formed $^1O_2$ might be trapped by other co-extracted compounds slowing down the photooxygenation of DHAA. In the 8-fold concentrated batch extract of Mediplant leaves, however, total conversion was achieved, yielding 30 % of artemisinin. This reduced artemisinin

Tab. 6.2: Performance of the partial synthesis using extracts from different leaf sources and extraction modes. The extract was concentrated by toluene evaporation to varied extent. Conditions: $[\text{DHAA}]^0 = 8.5\,\text{mM}$ prior to the concentration, $[\text{TFA}]=0.0625\,\text{M}$, $p=7\,\text{bar}$ pressurized air, $T_{\text{Photo}}=20\,°\text{C}$.

Source			Mediplant				ArtemiFlow	
Extraction mode			Batch		Continuous		Batch	
[Chl] prior conc., mmol/L			0.035		0.038		0.038	
Extract conc.	τ, min τ^{s}_{photo}	$\tau^{s}_{\text{2ndline}}$	X, % DHAA	Y, % Arte	X, % DHAA	Y, % Arte	X, % DHAA	Y, % Arte
-	5	1.8	100	41	100	41	100	47
		5.8	100	42	100	42	100	48
2-fold	5	1.8	100	54	94	43	100	49
		5.8	100	48	100	44	100	49
4-fold	5	1.8	100	40	92	43	100	44
		5.8	100	44	92	45	100	50
8-fold	5	1.8	100	31	75	8	79	10
		5.8	100	34	71	9	75	10

formation implies that the co-extracted compounds also interfere with the acid-catalyzed sequence.

In the experiments with highly concentrated extracts, frequent clogging of the photoreactor by highly viscous, gel-like material was observed. Since the extracts were stored at $-20\,°\text{C}$ and filtered before use, these particles must have formed inside the reactor due to light-induced reactions of co-extracted impurities. For later large-scale operation, this practical issue needs to be solved by applying reactor concepts that are more robust to solids.

In conclusion, the partial synthesis outcome shows great stability on the leaf source and the operation mode used for the extraction. The developed reaction conditions ensure a stable reactor performance if the extract is not too highly concentrated.

6.4 Dependence of the reaction performance on the DHAA concentration

After optimizing the reaction conditions, the artemisinin yield obtained with the extract is $45\,\%$ to $50\,\%$. The initial concentration of DHAA in the extract was enriched to $0.0085\,\text{M}$, which corresponds to $0.033\,\text{M}$ in a four-fold concentrated extract. This

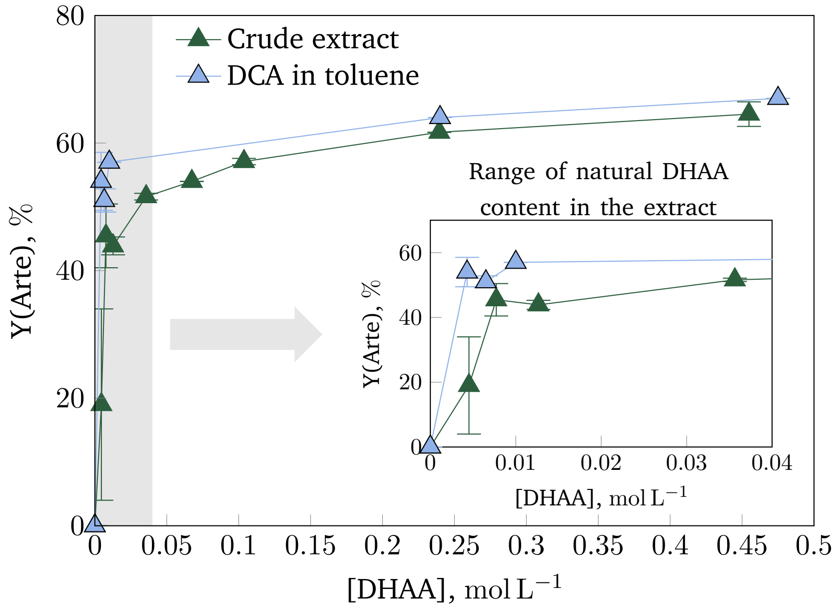

Fig. 6.5: The effect of the initial DHAA concentration present in the extract on the selectivity of artemisinin obtained from the partial synthesis: Conditions: $-20\,^{\circ}\mathrm{C}$, 7 bar O_2; Extract feed: Batch extract, 4-fold concentrated, source: Mediplant, [TFA]=0.375 M; Pure feed: [DCA]= 0.85 mM, [TFA]=0.25 M.

concentration exceeded the artemisinin content two-fold and was defined as the maximal DHAA concentration that can be co-extracted from DHAA-rich plant material. The previous chapter shows that artemisinin yields of up to 67 % are possible in non-concentrated extract when starting from a more than 10-fold increased initial concentration of DHAA.

A better understanding of the effect of the DHAA concentration on the reaction performance is essential to estimate the potential of the partial synthesis, especially for extracts that contain less than 0.0085 M DHAA. Therefore, the added amount of DHAA was varied in the reactor feed from 0.45 M, which is the reference case of Sec. 5.1, to 0.0045 M, the natural DHAA concentration in 4-fold concentrated extract. To differentiate the effect of the DHAA concentration from the influence of the co-extracts, experiments were performed in 4-fold concentrated extract and pure conditions with 0.85 mM DCA as the photocatalyst. The results are shown in Fig. 6.5.

The high yields of artemisinin of 63 % to 66 % observed with non-concentrated extract could be reproduced in the four-fold concentrated extract at DHAA concentrations higher than 0.25 M. At lower concentrations, the selectivity to artemisinin decreases slowly down to 51 % at a DHAA content of 0.035 M, the maximal DHAA concentration expected from natural sources. In the range of lower concentrations, the obtained artemisinin yield drops down to 25 % at 0.0045 M, the natural content co-extracted from the Mediplant leaves without any DHAA addition. However, the data obtained at this lowest concentration deviates widely.

In pure toluene, the selectivity also decreases slowly but achieves a value of $54\,\%$ at the lowest tested concentration of $0.0045\,\mathrm{M}$. Thus, the observed drop in artemisinin yield is partly attributed to a shift in the active reaction pathways at low artemisinin concentration and partly to co-extracts interfering with the reaction. In the concentration range present in the extract, the effect of the co-extracts is enhanced. Therefore, the DHAA content in leaves represents a critical parameter for the viability of the partial synthesis as an additional step in the plant-based extraction of artemisinin.

6.5 Increasing the amount of crude extract processed

The counter-current extraction process developed by Troung Giang Vu operates at an extract flowrate of $10\,\mathrm{mL\,min^{-1}}$[382]. This throughtput is 50-fold higher than the current flowrate range of $0.2\,\mathrm{mL\,min^{-1}}$ to $0.4\,\mathrm{mL\,min^{-1}}$ of extract pumped through the photoreactor system. To allow for a coupling of both processes at equal scale, the reaction step was adapted to maximize the amount of crude extract treatable with the existing reactor setup. The throughput of crude extract $\dot{V}_{Crude}$ is defined as liquid flowrate dosed in the reactor system $\dot{V}_l$ multiplied by extract feed concentration f_{conc} through toluene evaporation prior to the reaction step:

$$\dot{V}_{Crude} = \dot{V}_l \cdot F_{conc} \tag{6.1}$$

The made changes and the achieved throughput of crude extract $\dot{V}_{Crude}$ are illustrated in Fig. 6.6.

As introduced in Sec. 6.3, the extract can be concentrated to one fourth of its initial volume while still ensuring a stable artemisinin yield of $40\,\%$ (entry 2 in Fig. 6.6). Using 4-fold concentrated extract, the oxygen flow rate was reduced and the liquid flow rate increased keeping a total flow rate of $1\,\mathrm{mL\,min^{-1}}$ (entries 3 & 4). An oxygen-to-liquid ratio of $0.43 : 1$ was found sufficient to still reach completion of the partial synthesis. This ratio corresponds to an almost four-fold excess of oxygen related to the dosed DHAA concentration of $8\,\mathrm{g/L}$ in four-fold concentrated extract. The most significant jump in the liquid throughput was achieved by doubling the tubing diameter in the photoreactor section from $0.8\,\mathrm{mm}$ to $1.6\,\mathrm{mm}$ (entry 5 - 10). This change enabled to integrate a reaction volume of first $10\,\mathrm{mL}$ and later $30\,\mathrm{mL}$ in the existing photoreactor. Thus, the liquid flowrate could be increased to $3.5\,\mathrm{mL\,min^{-1}}$ ensuring a low pressure drop of less than $1\,\mathrm{bar}$ and an artemisinin yield of $39\,\%$

ID	F_{conc}	g/l (v/v)	d_{photo}, in	V_{photo} ml	V_{2nd} ml	$\dot{V}$ ml/min
1[1]	1	4/1	1/16	5	1.6	1
2[1]	4	4/1	1/16	5	1.6	1
3[1]	4	1/1	1/16	5	1.6	1
4[1]	4	0.43/1	1/16	5	1.6	1
5[1]	4	0.43/1	1/8	10	4.6	1
6[1]	4	0.43/1	1/8	10	4.6	1.3
7[1]	4	0.43/1	1/8	10	4.6	1.7
8[1]	4	0.43/1	1/8	10	4.6	2
9[1]	4	0.43/1	1/8	30	4.6	4
10[1]	4	0.43/1	1/8	30	4.6	5
11[1]	4	0.43/1	1/8	30	32	5
12[1]	4	0.43/1	1/8	30	32	7.5
13[2]	4	0.43/1	1/8	30	32	7.5
14[3]	4	0.43/1	1/8	30	32	7.5

[1] Storage at −20 °C and subsequent filtration

[2] Storage at −20 °C and subsequent centrifugation

[3] No pretreatment of the extract

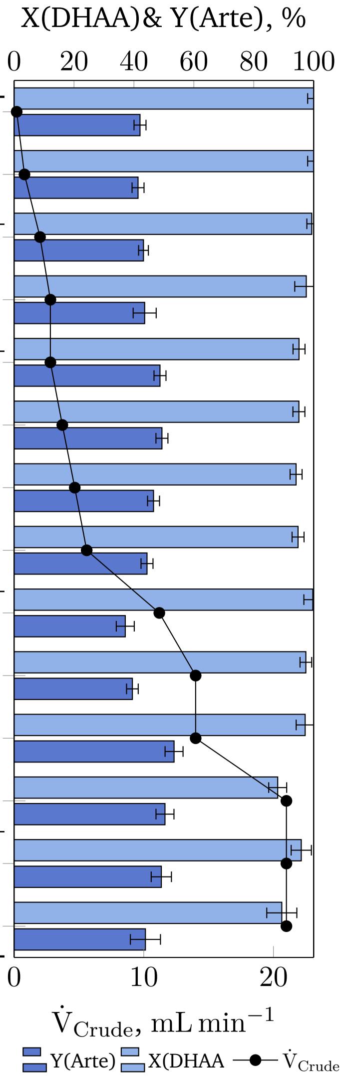

Fig. 6.6: Upscaling of the existing reactor setup regarding the throughput of crude extract $\dot{V}_{Crude}$ by extract concentration, reduction of the dosed gas phase, increase of the reactor volume and simplification of the extract pretreatment. Conditions: [TFA]=0.0625 M, p=7 bar, T= RT, x_{O_2}=1.

(entry 10). Both the liquid flowrate and the artemisinin yield could be increased by extending the second reaction line and offering more residence time for the partial synthesis to reach completion (entries 11 & 12).

In this process of upscaling, clogging of the reaction line became a major issue. Gel-like material formed during irradiation in the reaction line and clogged the narrow parts downstream of the photoreactor. This solid formation was observed in all experiments although the extracts were kept at −20 °C overnight and filtered directly afterwards to remove waxes. These gel-like substances are presumably reaction products of plant metabolites with singlet oxygen or other light-induced processes.

Stable operation of the reactor was achieved by immersing the back-pressure regulator in an ultrasonic bath. For further upscaling, new reactor concepts robust to solids are required. For the current application case, however, the combination of larger tubing and Taylor flow with its internal vortices [260] was sufficient to conduct the reaction for several hours.

In the final setting, $5.25\,\mathrm{mL\,min^{-1}}$ of four-fold concentrated extract containing $0.0625\,\mathrm{M}$ TFA is dosed together with $2.25\,\mathrm{mL\,min^{-1}}$ of oxygen through a total of $32\,\mathrm{m}$ reaction line with an inner diameter of $1.6\,\mathrm{mm}$ resulting in an overall residence time of $9\,\mathrm{min}$ (entry 12). These process conditions achieve an artemisinin yield of $43\,\%$ to $49\,\%$ independent on the pretreatment of the extract (entries 13 & 14). Deep freezing of the extract is not anymore crucial to obtain a stable process. In that way, $1.2\,\mathrm{L\,h^{-1}}$ of effluent from the extraction can be processed which is two-orders of magnitude higher than the starting point of the upscaling without major reworking of the reactor setup.

6.6 Coupling of the partial synthesis with the purification of artemisinin

The purification of artemisinin from product solutions of the partial synthesis and from the extraction was investigated primarily by Elena Horosanskaia and Steffi Wünsche, respectively. The work on separating artemisinin from highly enriched product solutions of the partial synthesis was published in [215]:

E. Horosanskaia, S. Triemer, A. Seidel-Morgenstern, H. Lorenz: "Purification of Artemisinin from the Product Solution of a Semisynthetic Reaction within a Single Crystallization Step". In: *Organic Process Research & Development* 23 (2019), pp. 2074–2079.

The simplified partial synthesis step enables a direct coupling with the crystallization-based purification of artemisinin. At high initial DHAA concentrations of $0.5\,\mathrm{M}$ in the feed for the partial synthesis, artemisinin could be obtained from the product solution of the reaction step in a single cooling crystallization step in the toluene-based extract with a purity exceeding $99\,\%$.

When reducing the DHAA concentration in the extract and thus the artemisinin concentration in the reactor effluent to the natural level, impurities in the plant extract, such as flavinoids [100], prevent artemisinin crystallization. An additional adsorption step using alumina as an adsorbent removes these components and facilitates crystallization [396]. The integration of the partial synthesis does not complicate the adsorption and subsequent crystallization in comparison to purifying artemisinin directly after extraction. In contrast, the higher artemisinin concentration after the reaction benefits the crystallization performance regarding the achieved purity [396].

6.7 Conclusion

The utilization of chlorophyll as an abundant photosensitizer and the robustness of the reaction regarding changes in temperature and gas-phase composition facilitate a synthesis step that is simple in the required process equipment and operation. In the final optimized process, co-extracted DHAA is converted in a $40\,\%$ yield to additional artemisinin within $6\,\mathrm{min}$ by treating the crude toluene-based extract with pressurized air, blue light, and $0.0625\,\mathrm{M}$ trifluoroacetic acid at ambient temperature. The substitution of TFA with an H-β-zeolite offers further simplification of the process but requires additional optimization and system understanding to yield similar process performance as the homogeneously catalyzed case.

The developed process achieves stable artemisinin production even when using the extract from a different leaf source or produced in counter-current continuous extraction. The reaction step could be upscaled to process $1.2\,\mathrm{L_{Extract}/h}$ in the existing experimental setup.

The reduced artemisinin yield compared to the process with high initial DHAA content is attributed partly to a change in the active reaction pathways of the artemisinin formation, which was also observed in pure conditions. In addition, co-extracted impurities cause a substantial decrease in the selectivity to artemisinin at very low DHAA content. Therefore, coupling the partial synthesis with the extraction is attractive only for leaf sources high in DHAA.

7

Semi-mechanistic kinetic model for the partial synthesis of artemisinin starting from DHAA

The following identification of a kinetic model for the partial synthesis of artemisinin was performed in close cooperation with Moritz Schulze from *Technische Universität Braunschweig*. The author of this thesis performed the reactor characterization and the kinetic experiments on the photooxygenation and the acid-catalyzed reaction sequence. Moritz Schulze and the author of this thesis contributed equally to the development of the model equations. Moritz Schulze implemented the model and performed the parameter estimation, design of experiments, and sensitivity analysis. Benjamin Wriedt and Dirk Ziegenbalg from the *Institute for Chemical Engineering* at *Ulm University* supported the model development for the photooxygenation with their expertise on modeling photon transfer and measurement of incident photon fluxes by chemical actinometry. The results on the identified model for the photooxygenation of DHAA were published in:
[387] S. Triemer, M. Schulze, B. Wriedt, R. Schenkendorf, D. Ziegenbalg, U. Krewer, A. Seidel-Morgenstern: "Kinetic analysis of the partial synthesis of artemisinin: Photooxygenation to the intermediate hydroperoxide". In: *Journal of Flow Chemistry* 11.3 (2021), pp. 641–659.

The previous chapters showed that co-extracted DHAA can be utilized to increase the overall amount of artemisinin retrieved from the plant. In this case, the reaction step is integrated in the production process between the initial extraction and the final purification step. Ensuring optimal operation conditions necessitates joint optimization of the overall process. For this task, model-based tools have been proven essential in the pharmaceutical industry to facilitate system understanding and control [397]. The aim of the following investigations was to develop a quantitative model for the formation of artemisinin starting from dihydroartemisinic acid. So far a comprehensive description considering the whole reaction sequence is not available [398].
The kinetic investigations were conducted with purified reagents using 9,10-dicyano-

antracene as photosensitizer and trifluoroacetic acid as acidic catalyst. The aim of this approach was to obtain kinetic parameters for the partial synthesis unaffected by co-extracted impurities. The obtained model can be used in future studies to quantify the effect of extract-based feed sources on the reaction performance.

The challenge in modeling the partial synthesis lies within the strong interconnection of external factors as photon- and oxygen mass transfer with the intrinsic reaction kinetics. The complexity of the reaction network from DHAA to artemisinin was handled by decoupling the photooxygenation and the acid-catalyzed reaction sequence. In the first step, a separate model for the photooxygenation including photon- and mass transfer was developed and fully parametrized. This model was then used as a fixed building block to investigate the whole reaction sequence from DHAA to artemisinin. The challenging identification of the model structure and the kinetic parameters was supported by an iterative strategy applying model-based experimental design (Sec. 3.5) to ensure large parameter sensitivities and reduce the experimental workload [399].

In the following, the first building block including the reactor model and photooxygenation kinetics is introduced. The second part of the chapter focuses on selecting a suitable model describing the acid-catalyzed reaction sequence. In the end, conclusions are drawn on characteristics of the partial synthesis, which are missing in the developed models and need further study.

7.1 Identification of the photooxygenation and reactor model

The basis for obtaining a reliable kinetic model for the photooxygenation is an accurate description of the preceding photon and mass transfer processes. Two-phase flow and photon absorption in chemical reactors, however, are 3D phenomena described either based on first principles yielding complex models or by reducing the complexity with simplifications limiting the model applicability [272, 296, 298, 320]. The approach chosen in this work was to simplify the kinetic network and the occurring physical phenomena to obtain a model which is low in complexity.

The developed model equations were parameterized by three different sets of experiments: The gas-liquid flow was characterized by residence time measurements (Sec. 4.2.1). Actinometeric measurements with ferrioxalate (Sec. 2.3.1.3 and 4.2.2) were performed to quantify the incident photon flux in the reactor. The parameters from the reaction kinetics and the mass transfer coefficient were estimated by steady-state photooxygenation experiments (Sec. 4.3.3). The planning of the photooxygenation experiments was supported by model-based design of experiments.

7.1.1 Development of the model equations

The used approach for model development in flow reactors was introduced in Sec. 3.2. In the following, these principles are applied to the specific case of the DHAA photooxygenation. Accordingly, the identified process model is assembled from two main parts. The kinetic model describes the (photo-induced) chemical reactions and is independent of the process setup. The reactor model, instead, reproduces the fluid dynamics of the two-phase flow, including the interfacial transfer equations, and is dependent on the photo-flow reactor system used.

7.1.1.1 Kinetic description of the photooxygenation

The kinetic description of the conversion of DHAA to the intermediate hydroperoxides needs to include both the photooxygenation itself and the photosensitized formation of singlet oxygen (Sec. 2.3.1.1 and 2.3.1.2). DHAA is converted to three different hydroperoxides, depending on the transition state. $\mathrm{PO_1}$ is the main product of the ene-type reaction and the intermediate in the later conversion to artemisinin. The two byproduct species $\mathrm{PO_2}$ and $\mathrm{PO_3}$ were lumped together to the species $\mathrm{PO_y}$ to simplify the reaction network:

$$\begin{aligned} \mathrm{DHAA} + {}^1\mathrm{O_2} &\xrightarrow{k_{\mathrm{PO_1}}} \mathrm{PO_1}, \\ \mathrm{DHAA} + {}^1\mathrm{O_2} &\xrightarrow{k_{\mathrm{PO_y}}} \mathrm{PO_y}, \end{aligned} \tag{7.1}$$

with the kinetic rate constants k_i, $i \in \{\mathrm{PO_1}, \mathrm{PO_y}\}$.
Both species make up to $95\,\%$ of the total amount of reacted DHAA in the reactor effluent after photooxygenation. The remaining matter could not be identified and was attributed to decomposition products of the formed hydroperoxides during sample workup for NMR analysis. To cover this effect and close the component mass balances, an additional species $\mathrm{PO_x}$ was introduced which is fed from both hydroperoxide species with the same rate.

$$\begin{aligned} \mathrm{PO_1} &\xrightarrow{k_{\mathrm{PO_x}}} \mathrm{PO_x}, \\ \mathrm{PO_y} &\xrightarrow{k_{\mathrm{PO_x}}} \mathrm{PO_x}. \end{aligned} \tag{7.2}$$

The corresponding reaction rates are formulated based on the Power-law-approach in Eq. (3.3):

$$r_{\mathrm{PO_1}} = k_{\mathrm{PO_1}}[\mathrm{DHAA}][{}^1\mathrm{O_2}], \tag{7.3a}$$

$$r_{\mathrm{PO_y}} = k_{\mathrm{PO_y}}[\mathrm{DHAA}][{}^1\mathrm{O_2}], \tag{7.3b}$$

$$r_{\mathrm{PO_x}} = k_{\mathrm{PO_x}}([\mathrm{PO_1}] + [\mathrm{PO_y}]). \tag{7.3c}$$

Singlet oxygen is formed by photosensitization with the dye 9,10-dicyanoanthracene. The reaction network of photosensitization with DCA was introduced in Section 2.3.1.1. After irradiation with light in the blue range, DCA is excited and undergoes a complex cascade of quenching reactions to its triplet and its ground state. Both states can transfer enough energy to form singlet oxygen. Once it is formed, $^1O_2$ either reacts with DHAA or falls back to its triplet state.

$$^0\mathrm{DCA} \xrightarrow{\mathrm{h}\nu} {}^1\mathrm{DCA}, \tag{7.4}$$

$$^1\mathrm{DCA} + \mathrm{O_2} \longrightarrow {}^1\mathrm{O_2} + {}^3\mathrm{DCA}, \tag{7.5}$$

$$^3\mathrm{DCA} + \mathrm{O_2} \longrightarrow {}^1\mathrm{O_2} + {}^0\mathrm{DCA}, \tag{7.6}$$

$$^1\mathrm{O_2} \xrightarrow{1/\tau_\Delta} {}^3\mathrm{O_2}. \tag{7.7}$$

The life time of singlet oxygen in toluene τ_Δ is $33.2\,\mu\mathrm{s}$ at $-20\,°\mathrm{C}$ [192].
The rate of oxygen formation can be expressed based on the quantum yield of singlet oxygen $\Phi_{^1\mathrm{O_2}}$ and the local volumetric rate of photon absorption L_p^a

$$r_{^1\mathrm{O_2}} = \Phi_{^1\mathrm{O_2}} L_\mathrm{p}^\mathrm{a}. \tag{7.8}$$

Assuming that excited DCA is solely quenched by oxygen, the quantum yield of singlet oxygen can be formulated as

$$\Phi_{^1\mathrm{O_2}} = \frac{[\mathrm{O_2}]}{k_{11}[\mathrm{O_2}] + k_{12}}. \tag{7.9}$$

k_{11} and k_{12} are lumped kinetic parameters that combine diverse rate constants [185]. The concentration of triplet oxygen concentration in Eq. (7.9) was replaced by the concentration of dissolved oxygen as singlet oxygen occurs merely in trace quantities [292, 296].
Due to the high reactivity and the short lifetime of singlet oxygen, the steady-state-assumption is applied,

$$\frac{\mathrm{d}[{}^1\mathrm{O_2}]}{\mathrm{d}z} \overset{!}{\cong} 0 \cong r_{^1\mathrm{O_2}} - (k_{\mathrm{PO_1}} + k_{\mathrm{PO_y}})[\mathrm{DHAA}][{}^1\mathrm{O_2}] - \frac{1}{\tau_\Delta}[{}^1\mathrm{O_2}]. \tag{7.10}$$

Combining Eqs. (7.3) and (7.10) yields

$$r_{\mathrm{DHAA}} = r_{1_{\mathrm{O_2}}}^{\mathrm{form}} \frac{-(\tilde{k}_{\mathrm{PO_1}} + \tilde{k}_{\mathrm{PO_y}})[DHAA]}{1 + (\tilde{k}_{\mathrm{PO_1}} + \tilde{k}_{\mathrm{PO_y}})[DHAA]} \tag{7.11a}$$

$$r_{\mathrm{PO_1}} = r_{1_{\mathrm{O_2}}} \frac{\tilde{k}_{\mathrm{PO_1}}[DHAA]}{1 + (\tilde{k}_{\mathrm{PO_1}} + \tilde{k}_{\mathrm{PO_y}})[DHAA]}, \tag{7.11b}$$

$$r_{\mathrm{PO_y}} = r_{1_{\mathrm{O_2}}} \frac{\tilde{k}_{\mathrm{PO_y}}[DHAA]}{1 + (\tilde{k}_{\mathrm{PO_1}} + \tilde{k}_{\mathrm{PO_y}})[DHAA]}, \tag{7.11c}$$

$$r_{\mathrm{PO_x}} = k_{\mathrm{PO_x}}([\mathrm{PO_1}] + [\mathrm{PO_y}]), \tag{7.11d}$$

with the kinetic constants normalized to the lifetime of singlet oxygen

$$\tilde{k}_i = k_i \tau_\Delta, i \in \{\mathrm{PO_1}, \mathrm{PO_y}\}. \tag{7.12}$$

7.1.1.2 Reactor model for gas-liquid flow

The reactor model connects the reaction rates from the kinetic model of the photooxygenation with the external factors as light emission, oxygen supply and two-phase flow. The principles of modeling photoflow reactors were introduced in Sections 3.2.2 to 3.2.4. All experiments were performed in isothermal conditions with only a small pressure drop over the reaction line. Therefore, both the energy and the momentum balance were neglected [326].

Following the simplifications stated in Tab. 7.1, the concentration c of a species i along the reactor coordinate z can be described as

$$\frac{\mathrm{d}c_i}{\mathrm{d}z} = \frac{1}{u_\mathrm{l}}(r_i + \delta_i j_{\mathrm{O_2}}), \quad \delta_i = \begin{cases} 1, & i = \mathrm{O_2} \\ 0, & \text{else} \end{cases}. \tag{7.13}$$

u_l is the liquid phase velocity, r_i is the net rate of reaction and $j_{\mathrm{O_2}}$ is the rate of oxygen mass transfer between the liquid and the gas phase. The delta function δ_i ensures that the oxygen transfer is solely active in the balance for dissolved oxygen. For the gas phase, the consumption of oxygen needs to be considered in terms of a decreasing molar fraction $x_{\mathrm{O_2}}$ and a declining total gas flow rate $\dot{V}_\mathrm{g}$. The change in the molar rate $\dot{n}_\mathrm{g}$ is equal to the loss by mass transfer into the liquid phase. The mass transfer rate $j_{\mathrm{O_2}}$ is referred to the liquid phase and needs to be corrected by the cross-sectional area occupied by the liquid phase A_l.

$$\frac{\mathrm{d}\dot{n}_\mathrm{g}}{\mathrm{d}z} = -A_l j_{\mathrm{O_2}}. \tag{7.14}$$

Tab. 7.1: Summary of key assumptions applied to describe the reactor behavior.

The relative pressure drop over the reactor is small ($0.1\,\mathrm{bar}$ to $0.5\,\mathrm{bar}$ at $7\,\mathrm{bar}$ operating pressure). Consequently, the momentum balance is neglected [326].
Due to the isothermal operation of the reactor, there are no internal temperature gradients. Thus, energy balances are not considered.
The flow is one-dimensional (z axis). Hence, ideal mixing in radial direction is assumed [272, 331].
Diffusion is not considered.
The operation of the setup is in steady-state.
The liquid phase is incompressible. The density is calculated by a simple mixture density of the solvent plus the excess volume caused by the addition of DHAA.
Material exchange between the phases is based on the linear approach to mass transfer.
The gas phase can be described by an ideal gas mixture, i.e., the Taylor bubbles are well mixed.
The dissolved oxygen concentration is derived from Henry's law.

Based on the gas fraction defined in Eq. (3.19), the velocity of each phase can be determined as

$$u_\mathrm{g} = \frac{\dot{V}_\mathrm{g}}{A_\mathrm{g}} = \frac{\dot{V}_\mathrm{g}}{\alpha A}, \quad u_\mathrm{l} = \frac{\dot{V}_\mathrm{l}}{A_\mathrm{l}} = \frac{\dot{V}_\mathrm{l}}{(1-\alpha)A}. \tag{7.15}$$

The drift flux model (Sec. 3.2.4) relates the gas fraction to the known gas holdup β via an proportionality factor, the distribution factor C_0:

$$\alpha = \frac{1}{C_0}\beta, \tag{7.16}$$

The physical properties of the gas phase are described based on the ideal-gas equation [400], which links the amount of substance with the pressure p, the temperature T, and its volume V via the universal gas constant R. The pressure and the temperature are assumed to be constant.

$$N = \frac{pV}{RT} \tag{7.17}$$

Including Eqs. (3.19),(7.16) and (7.17) into Eq. (7.14) gives the material balance over the total gas flow

$$\frac{\mathrm{d}\dot{V}_\mathrm{g}}{\mathrm{d}z} = -\frac{RT}{p}\left(1 - \frac{\beta}{C_0}\right) A j_{\mathrm{O}_2}. \tag{7.18}$$

Correspondingly, the decline in the molar fraction of oxygen x_{O_2} can be described as

$$\frac{\mathrm{d}x_{O_2}}{\mathrm{d}z} = -\frac{RT}{p\dot{V}_g}\left(1-\frac{\beta}{C_0}\right) A j_{O_2}(1-x_{O_2}). \tag{7.19}$$

A detailed derivation of the material balances for the gas and the liquid phase can be found in [387].

Photon absorption In light-activated processes photons must be considered as a reagent, quantified by the local volumetric rate of photon absorption L_p^a. The L_p^a can be determined based on the radiative transfer equation (Sec. 3.2.2). In the regarded reaction system, the photosensitizer DCA is the only species which absorbs radiation in the emitted blue region of visible light. Since no reactants or products absorb the emitted light, the reaction kinetics and the radiation transfer equation can be solved independently, Assuming constant, monochromatic light emission, and negligible scattering simplifies the radiation transfer equation to

$$L_p^a = L_p\left(1 - e^{[-\kappa \; c_{DCA} \; l_{opt}]}\right), \tag{7.20}$$

with κ as the napierian absorption coefficient of the absorbing species DCA.
Eq. (7.20) introduces two parameters which need to be quantified for the available reactor system: The optical pathlength l_{opt} and the local volumetric incident photon flux L_p. The most established method to estimate these quantities in complex reactor geometries is chemical actinometry (Sec. 3.3).
The utilization of Eq. (7.20) for the estimation of L_p^a in the applied reactor system is based on three further simplifications. L_p^a, L_p and l_{opt} represent average values of each quantity and are regarded as constant within the reactor. Including the distribution of L_p^a would require a 3D derivation of the RTE and sophisticated analytical tools to measure the distribution within the reaction line. Thus, the assumption of homogeneous illumination is commonly made in microreactor modeling, and leads to good model-data fits [401]. In conclusion, all reaction rates are related to a constant average volumetric rate of photon absorption.
The second simplification in Eq. (7.20) regards the geometry of the applied reactor setup. The irradiation from two sides is not explicitly included. However, due to the symmetric configuration of the capillary reactor, the superposition of the light emission from two sides is implicitly alleviated in L_p.
Thirdly, the concentration of DCA c_{DCA}, known for its stability, was assumed to be constant during irradiation, neglecting photobleaching processes.

Interfacial oxygen transfer The mass transfer of oxygen was described using the two-film model and Henry's law (Sec. 3.2.3) introducing the volumetric mass transfer coefficient $k_\mathrm{l}a$

$$j_{\mathrm{O_2}} = k_\mathrm{l}a([\mathrm{O_2}]^\infty - [\mathrm{O_2}]), \tag{7.21}$$

with

$$c^\infty_{\mathrm{O_2}} = \frac{1}{H} p_{\mathrm{O_2}}. \tag{7.22}$$

The Henry coeffcient H of oxygen in toluene was adapted from literature [402].

$$\ln\left(H_\mathrm{x}\right) = \frac{A}{T} + B, \quad A = 400.426, \; B = 3.393 \tag{7.23}$$

$$H = \frac{M_\mathrm{solv}}{\rho_\mathrm{solv}} H_\mathrm{x} \tag{7.24}$$

where the temperature T is in Kelvin. The correlation was developed for conditions ranging from 1 to $10\,\mathrm{bar}$ and from 20 to $110\,°\mathrm{C}$ and needed to be extrapolated to $-20\,°\mathrm{C}$, the temperature in the photoreactor. The Henry constant H_x is based on the molar fraction with unit MPa and needs to be converted to the concentration-based Henry constant H based on the molar mass M_solv and the density of the solvent ρ_solv.

The rate of mass transfer is strongly dependent on the flow conditions prevalent during the experiment. In Taylor flow, mass transfer through the liquid film between reactor wall and gas bubble exceeds the contribution of the bubble caps [403]. In addition, the flow velocity affects the rate of mixing within the liquid and also influences the mass transfer coefficient [268]. Thus, the mass transfer was often correlated to the superficial gas phase velocity u^s_g and the length of unit cell l_UC, which consists of a gas bubble and a liquid slug, as in the correlation by Vandu et al. [404]:

$$k_\mathrm{l}a \propto \sqrt{D_{\mathrm{O_2}} u^\mathrm{s}_\mathrm{g} / l_\mathrm{UC}} / d \tag{7.25}$$

with the diffusion coefficient of oxygen $D_{\mathrm{O_2}}$. Since no precise information about the length of the unit cell is readily available, only the dependence of the mass transfer coefficient on the superficial gas velocity was considered:

$$k_\mathrm{l}a = \widetilde{k_\mathrm{l}a} \sqrt{u^\mathrm{s}_\mathrm{g}}, \tag{7.26}$$

introducing a constant $\widetilde{k_\mathrm{l}a}$. The effect of the unit cell length is estimated together with influence of the toluene-gas system in this lumped parameter.

7.1.1.3 The process model: Combining the kinetics with the reactor model

The integration of the chemical kinetics, the photon and mass transfer into the material balances Eqs. (7.13), (7.19), and (7.18) finally provides the complete set of equations of the process model for both the liquid and the gas phase [387]:

$$
\begin{aligned}
\frac{\mathrm{d}[\mathrm{DHAA}]}{\mathrm{d}z} &= \frac{\left(1-\frac{\beta}{C_0}\right)A}{\dot{V}_\mathrm{l}}\Bigg(-\frac{[\mathrm{O_2}]}{k_{\mathrm{l}1}[\mathrm{O_2}]+k_{\mathrm{l}2}}\frac{(\tilde{k}_{\mathrm{PO_1}}+\tilde{k}_{\mathrm{PO_y}})[DHAA]}{1+(\tilde{k}_{\mathrm{PO_1}}+\tilde{k}_{\mathrm{PO_y}})[DHAA]} \\
&\qquad L_\mathrm{p}(1-\exp\left[-\kappa c_{\mathrm{DCA}} l_{\mathrm{opt}}\right])\Bigg), \\
\frac{\mathrm{d}[\mathrm{PO_1}]}{\mathrm{d}z} &= \frac{\left(1-\frac{\beta}{C_0}\right)A}{\dot{V}_\mathrm{l}}\Bigg(\frac{[\mathrm{O_2}]}{k_{\mathrm{l}1}[\mathrm{O_2}]+k_{\mathrm{l}2}}\frac{\tilde{k}_{\mathrm{PO_1}}[DHAA]}{1+(\tilde{k}_{\mathrm{PO_1}}+\tilde{k}_{\mathrm{PO_y}})[DHAA]} \\
&\qquad L_\mathrm{p}(1-\exp\left[-\kappa c_{\mathrm{DCA}} l_{\mathrm{opt}}\right]) - k_{\mathrm{PO_x}}[\mathrm{PO_1}]\Bigg), \\
\frac{\mathrm{d}[\mathrm{PO_y}]}{\mathrm{d}z} &= \frac{\left(1-\frac{\beta}{C_0}\right)A}{\dot{V}_\mathrm{l}}\Bigg(\frac{[\mathrm{O_2}]}{k_{\mathrm{l}1}[\mathrm{O_2}]+k_{\mathrm{l}2}}\frac{\tilde{k}_{\mathrm{PO_y}}[DHAA]}{1+(\tilde{k}_{\mathrm{PO_1}}+\tilde{k}_{\mathrm{PO_y}})[DHAA]} \\
&\qquad L_\mathrm{p}(1-\exp\left[-\kappa c_{\mathrm{DCA}} l_{\mathrm{opt}}\right]) - k_{\mathrm{PO_x}}[\mathrm{PO_y}]\Bigg), \\
\frac{\mathrm{d}[\mathrm{PO_x}]}{\mathrm{d}z} &= \frac{\left(1-\frac{\beta}{C_0}\right)A}{\dot{V}_\mathrm{l}} k_{\mathrm{PO_x}}([\mathrm{PO_1}]+[\mathrm{PO_y}]), \\
\frac{\mathrm{d}[\mathrm{O_2}]}{\mathrm{d}z} &= \frac{\left(1-\frac{\beta}{C_0}\right)A}{\dot{V}_\mathrm{l}}\Bigg(-\frac{[\mathrm{O_2}]}{k_{\mathrm{l}1}[\mathrm{O_2}]+k_{\mathrm{l}2}}\frac{(\tilde{k}_{\mathrm{PO_1}}+\tilde{k}_{\mathrm{PO_y}})[DHAA]}{1+(\tilde{k}_{\mathrm{PO_1}}+\tilde{k}_{\mathrm{PO_y}})[DHAA]} \\
&\qquad L_\mathrm{p}(1-\exp\left[-\kappa c_{\mathrm{DCA}} l_{\mathrm{opt}}\right]) + \widetilde{k_\mathrm{l}a}\sqrt{u_\mathrm{g}^\mathrm{s}}([\mathrm{O_2}]^\infty-[\mathrm{O_2}])\Bigg), \\
\frac{\mathrm{d}x_{\mathrm{O_2}}}{\mathrm{d}z} &= \frac{T}{p\dot{V}_\mathrm{g}}\left(-R\frac{\beta}{C_0}A\widetilde{k_\mathrm{l}a}\sqrt{u_\mathrm{g}^\mathrm{s}}([\mathrm{O_2}]^\infty-[\mathrm{O_2}]) - \frac{p}{T}x_{\mathrm{O_2}}\frac{\mathrm{d}\dot{V}_\mathrm{g}}{\mathrm{d}z}\right), \\
\frac{\mathrm{d}\dot{V}_\mathrm{g}}{\mathrm{d}z} &= -\frac{T}{p}R\frac{\beta}{C_0}A\widetilde{k_\mathrm{l}a}\sqrt{u_\mathrm{g}^\mathrm{s}}([\mathrm{O_2}]^\infty-[\mathrm{O_2}]),
\end{aligned}
\tag{7.27}
$$

with initial conditions

$$
\begin{aligned}
&([\mathrm{DHAA}], [\mathrm{PO_1}], [\mathrm{PO_y}], [\mathrm{PO_x}], [\mathrm{O_2}], [x_{\mathrm{O_2}}], [\dot{V}_\mathrm{g}])^\top(0) \\
&\qquad = ([\mathrm{DHAA}]_0, 0, 0, 0, [\mathrm{O_2}]^\infty, x_{\mathrm{O_2},0}, \dot{V}_{\mathrm{g},0})^\top .
\end{aligned}
$$

The process model includes seven unknown parameters that need to be estimated by experimental data of the photooxygenation.

$$(\widetilde{k_{\mathrm{l}}a}, k_{\mathrm{l1}}, k_{\mathrm{l2}}, \tilde{k}_{\mathrm{PO_1}}, \tilde{k}_{\mathrm{PO_y}}, k_{\mathrm{PO_x}}, l_{\mathrm{opt}})^{\top}. \tag{7.28}$$

In addition to this set, the two other unknown parameters, the distribution factor between liquid and gas phase and the incident photon flux, can be estimated by residence time and actinometric measurements. The determination of C_0 is included in App. E.

7.1.2 Determination of the incident volumetric photon flux by chemical actinometry

Chemical actinometry is a widely used approach to characterize the irradiation in chemical reactors, since the method is applicable to complex reactor geometries and requires only standard lab equipment (Sec. 3.3). In this work, the potassium ferrioxalate actinometer was applied due to its easy preparation, strong absorption at $417\,\mathrm{nm}$, and well-known quantum yield. The validation and adaptation of the published methods to the available milli-scale photoreactor system are included in App. F.4. The developed experimental procedure and method data analysis were explained in Sec. 4.2.2.

The actinometric measurements were performed in Taylor flow conditions as the later presented photooxygenation experiments. The obtained actinometer conversions are depicted in Fig. 7.1a. The experimental operation window of LED settings and residence time in the irradiated section was limited to a narrow range of $6\,\mathrm{s}$ to $12\,\mathrm{s}$ and $10\,\%\mathrm{LED}$ to $25\,\%\mathrm{LED}$ by physical and technical constraints [351]. Precipitation occurred in all samples obtained at LED settings higher than $25\,\%\mathrm{LED}$. Therefore, these data were excluded from further analysis. The conversions obtained without precipitation showed an expected linear dependence on the residence times. Based on the known quantum yield of ferrioxalate, the volumetric incident photon flux (L_{p}) was determined separately for each data point based on Eq. (3.26). In this analysis, the optical path length was set to be equal to the channel diameter of $0.8\,\mathrm{mm}$. The average values of L_{p} for each LED setting are shown in Fig. 7.1b.

The incident photon flux shows a strong linear dependence on the LED power at lower values. The measured incident photon fluxes deviate from that dependence due to the aforementioned observed precipitation during the experiment. The linear behavior is a known property of LEDs and was also confirmed with the irradiation sensor positioned next to reactor casing (Sec. 7.1.1.1). Therefore, the volumetric

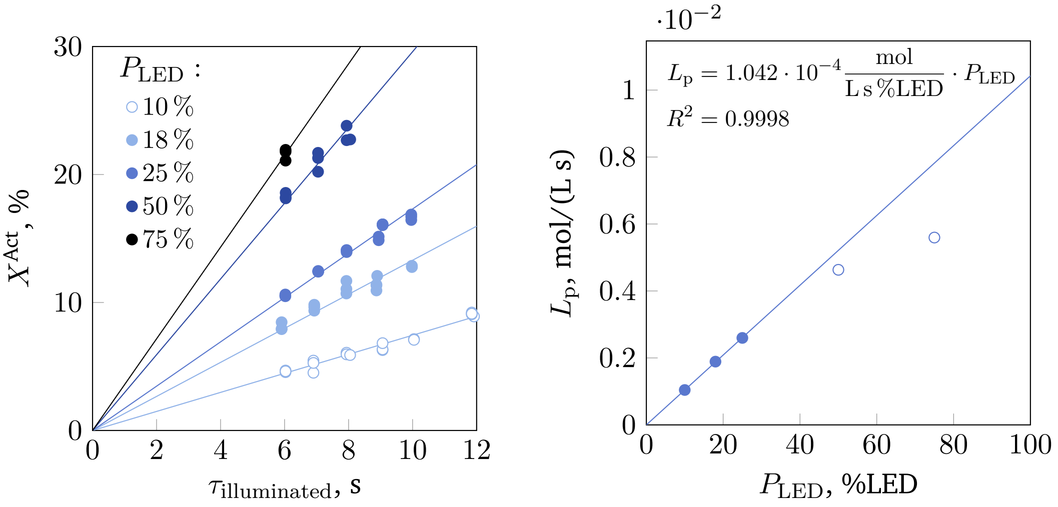

(a) Linearity of actinometer conversion on irradiation time.

(b) Linearity of L_{p} on LED Power.

Fig. 7.1: Quantification of the incident photon flux by ferrioxalate actinometry in two-phase slug flow conditions ($l_{photo} = 2\,\mathrm{m}$): a) Actinometer conversion in dependence on LED power P_{LED} and residence time in the irradiated section of the photoreactor, b) Volumetric incident photon flux L_{p} determined based on measured actinometer conversion ($l_{\mathrm{opt}} = 0.8\,\mathrm{mm}$).

incident photon flux was connected with a linear relation to the LED-power. The relation constitutes an additional model equation introducing $\tilde{L}_{\mathrm{p}}$ as proportionality factor,

$$L_{\mathrm{p}} = \tilde{L}_{\mathrm{p}} \cdot P_{\mathrm{LED}}. \tag{7.29}$$

The determination of the incident photon flux from actinometric experiments requires either conditions of total absorption ($L_{\mathrm{p}}^{\mathrm{a}} = L_{\mathrm{p}}$) or - in the case of partial adsorption Eq. 7.20 - exact knowledge of the optical pathlength [336]. Due to the small dimensions, total absorption cannot be ensured in micro- and milli-scaled channels. Thus, the optical pathlength l_{opt} needs to be either measured or estimated. Based on the actinometric data shown above, it was not possible to resolve both required quantities, the incident photon flux and the optical path length. For any set value of the optical path length, corresponding values for the incident photon fluxes and proportionality factor $\tilde{L}_{\mathrm{p}}$ could be found, which fit the experimental actinometric data equally well (Fig. 7.2). However, the complex irradiation geometry of the applied reactor also makes it difficult to predict the path length from theoretical considerations due to the combination of a wide emission angle of the LED modules, illumination from two sides, reflection within the photoreactor casing and Taylor flow conditions. Actinometric experiments at varied initial concentration of ferrioxalate following the approach of Roibu et al. [278] did also not show a sensitivity high

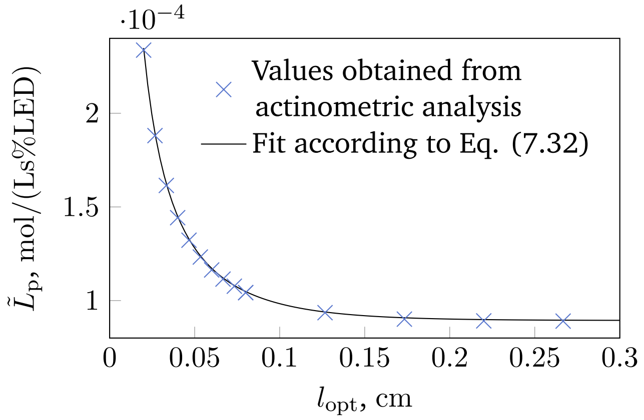

Fig. 7.2: Dependence of the proportionality factor $\tilde{L}_\mathrm{p}$ (Eq. (7.29)) and the optical pathlength l_opt used for the numerical calculations. For each l_opt value chosen a value of $\tilde{L}_\mathrm{p}$ is obtained fitting the actinometric data equally well.

enough to quantify the optical pathlength (App. F.5).

As an alternative approach, the optical path length was set as an additional parameter to be estimated based on the photooxygenation experiments. For that, a relation between the incident photon flux and path length is required which can be used as additional model equation in the identification of the photooxygenation model.

To obtain this relation, the data in Fig. 7.2 was fitted with Eq. (7.31). The structure of Eq. (7.31) is derived from the linear relationship of LED setting and observed incident photon flux (Eq. (7.29)) and the Beer-Lambert law as link between incident and absorbed photon flux (Eq. (3.10)).

$$L_\mathrm{p}^\mathrm{a} = \underbrace{\tilde{L}_\mathrm{p}(1 - e^{-\kappa_{Act}[\overline{Act}]l_\mathrm{opt}})}_{\tilde{L}_\mathrm{p}^a} \cdot P_\mathrm{LED} \tag{7.30}$$

$$\tilde{L}_\mathrm{p} = \frac{\tilde{L}_\mathrm{p}^a}{1 - e^{-\kappa_{Act}[\overline{Act}]l_\mathrm{opt}}} \tag{7.31}$$

Both introduced quantities $[\overline{Act}]$ and $\tilde{L}_\mathrm{p}^a$ are primarily empirical parameters to describe the exponential dependency. Interpreted physically, $\tilde{L}_\mathrm{p}^\mathrm{a}$ can be seen as the proportionality factor between the absorbed volumetric photon flux and the set LED power. [$\overline{\mathrm{Act}}$] represents an average concentration of the ferrioxalate during irradiation. The numerical fit of the values of $\tilde{L}_\mathrm{p}$, obtained for each set pathlength with with Eq. (7.31) as shown in Fig. 7.2, yields

$$\tilde{L}_\mathrm{p} = \frac{8.893 \cdot 10^{-5} \frac{\mathrm{mol}}{\mathrm{L\,s\,\%LED}}}{1 - e^{-\kappa_{Act} 0.1408 \frac{\mathrm{mol}}{\mathrm{L}} l_\mathrm{opt}}} = \frac{8.893 \cdot 10^{-5} \frac{\mathrm{mol}}{\mathrm{L\,s\,\%LED}}}{1 - e^{-23.935 \mathrm{cm}^{-1} \cdot l_\mathrm{opt}}} \tag{7.32}$$

as parameterized relation for the proportionality factor $\tilde{L}_\mathrm{p}$ providing a good description of the observed behavior. In the model for the photooxygenation, Eq. (7.32) serves as link between the knowledge gained from the actinometric measurements and the photooxygenation experiments.

7.1.3 Assessment of the reaction behavior of the photooxygenation

The characterization of the photon flux and the slip between the gas and the liquid phase yielded two paramters of the process model. The remaining set of unknown parameters including five kinetic parameters, the optical path length and the mass transfer coefficient were identified based on experimental data of the photooxygenation.

All data was collected in steady-state experiments using the continuous photoreactor system introduced in Section 4.1. The reactor feed consisted of pure dihydroartemisinic acid (DHAA) as reactant and 9,10-dicyanoanthracene (DCA) as photosensitizer dissolved in toluene. The reactor effluent was characterized by $^1\mathrm{H{-}NMR}$ (Sec. 4.4.2). The experimental conditions were derived from model-based design of experiments (Sec. 3.5), which ensures high sensitivity of the kinetic parameters in the measurements. In this way, 658 data points were obtained as foundation for the parameter identification. Each point represents the concentration of a species or the residual O_2 flow after a separate steady-state experiment.

A subset of the experimental data is shown in Figs. 7.3 and 7.4 to give a first impression on the reaction performance and the main factors of influence. Due to the applied MBDoE, the experimental conditions change between the subplots of Fig. 7.4. The concentration profiles are compared based on the recovery and the superficial residence time, which are both defined in Sec. 3.4. The recovery describes how much of the initially used reactant can be attributed to known products of the reaction.

In the photon-rich conditions of the applied milli-scale photoreactor system, DHAA is photooxygenated fast reaching full conversion in less than $5\,\mathrm{min}$ residence time (Fig. 7.3). The main product of this reaction is the desired tertiary hydroperoxide PO_1 with a final yield of $85\,\%$. The main side products are the two secondary hydroperoxides, which were combined in the byproduct species PO_y. PO_y is obtained in a yield of $8\,\%$. Similar performance of the photooxygenation was observed also in previous studies reporting yields of PO_1 up to $90\,\%$ after $2\,\mathrm{min}$ irradiation [179, 381]. In total, $92\,\%$ of the reactant could be recovered in known products at the end of the reaction. The observed difference is caused by decomposition and rearrangement of the semi-stable hydroperoxides to further byproducts [70, 197, 198]. To close the

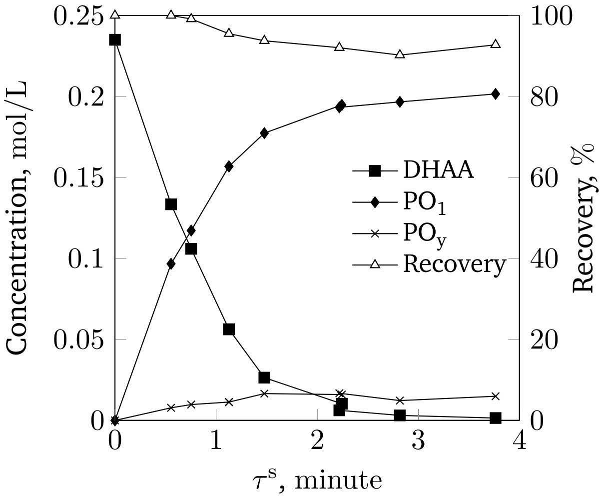

Fig. 7.3: Progress of the photooxygenation of DHAA to the desired hydroperoxides PO$_1$ and its byproduct PO$_y$ with increasing residence time in the irradiated reactor section. Experimental conditions: $[\text{DHAA}]_0 = 0.235\,\text{M}$, $[\text{DCA}] = 0.85\,\text{mM}$, $x_{\text{O}_2,0} = 1$, $P_{\text{LED}} = 50\,\%\text{LED}$.

overall mass balances, these species were lumped to an additional species PO$_x$ (Sec. 7.1.1.1). The shape of the concentration profiles over time (Fig. 7.3) correspond to a mixed zero and first-order reaction, which is expected from the model development and also known from other photochemical reactions [296].

The reaction rates of PO$_1$ and PO$_y$ formation depend directly on the concentration of oxygen in the liquid phase and the rate of photon absorption. The influence of the latter was studied by varying the LED intensity (Fig. 7.4a) and by changing of the photosensitizer concentration (Fig. 7.4b). Fig. 7.4b also shows the effect of a decreased oxygen content in gas phase on the reaction performance. The light intensity, catalyst concentration, and gas phase composition solely affect the reaction rate, while the final yields and the recovery stay constant. This observation agrees with the assumption that all three parameters only influence the formation of singlet oxygen but neither the selectivity of PO$_1$ formation nor the consecutive rearrangement of PO$_1$ and PO$_y$. Correspondingly, the ratio of the reaction rates of PO$_1$ and PO$_y$ is constant and equal to the ratio of the rate constants k_{PO_1} and k_{PO_y}.

The dependence of the reaction rate of PO$_1$ formation is supposed to be linear in respect to amount of photons absorbed and thus on the photon flux emitted from the LED lamps. A two-fold increase in the LED power from $50\,\%$ to $100\,\%$, however, leads only to a 1.5 fold change of the observed initial rate of PO$_1$ formation (from $0.174\,\text{mol}\,\text{L}^{-1}\,\text{min}^{-1}$ to $0.257\,\text{mol}\,\text{L}^{-1}\,\text{min}^{-1}$ at $\tau^{s} = 0.55\,\text{min}$). This observed non-linearity may be arise from a slower oxygen mass transfer between gas and liquid phase, which becomes limiting at high irradiation intensities.

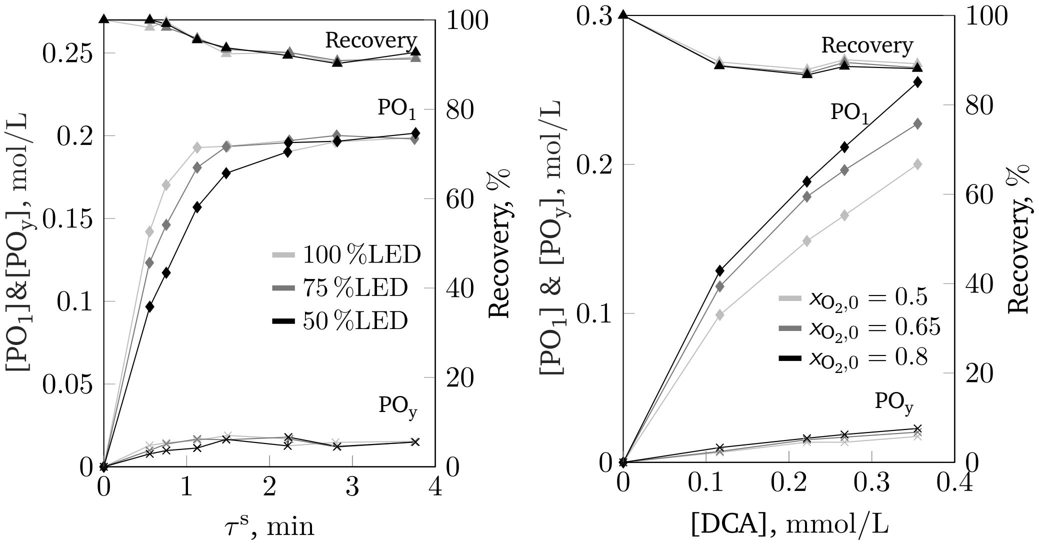

(a) Dependence on LED Power Setting ([DHAA] = 0.235 M, [DCA]= 0.85 mM, $x_{O_2,0} = 1$)

(b) Dependence on x_{O_2} and DCA concentration $\tau^s = 1.2\,\text{min}$, $[\text{DHAA}]_0 = 0.44\,\text{M}$, $P_{\text{LED}} = 100\,\%\text{LED}$

Fig. 7.4: Effect of the experimental conditions on the reaction rate of the photooxygenation: a) Variation of the emitted light intensity and the superficial residence time b) Variation of photosensitizer concentration and gas phase composition at constant superficial residence time.

Likewise to the LED power, changing the photocatalyst concentration shows a smaller effect on the reaction rate (Fig. 7.4b) as expected from modeling. Assuming an optical pathlength equal to the channel diameter, a 3-fold increase of the DCA concentration should result in a 3-fold rise in light absorption and, thus, in the reaction rate. In the experiments, however, only a 2-fold increase in the PO_1 concentration was observed at tripled DCA concentration. Besides a limitation of the oxygen mass transfer, this low sensitivity of the reaction rate on the catalyst concentration may also be the result of a significantly longer pathlength within the reactor leading to high absorption rates even at low catalyst concentrations.

The reduction of the oxygen content in the gas phase results also in a slower formation of PO_1. The observed decrease in yield results from the lower equilibrium concentration of O_2 in liquid phase. It leads not only to slower mass transfer rates but lessens the ${}^1O_2$ quantum yield and therefore directly affects the reaction kinetics. In summary, the key experimental parameters, light intensity, catalyst concentration and gas phase composition, do only affect the reaction rate but not the final yields of the desired hydroperoxide PO_1 and the byproducts. The effect on the reaction rate is less distinct than expected from the kinetic model. Based on the experimental data, it can not be concluded whether the limitation arises from the photon- or oxygen mass transfer. For this conclusion, the quantitative analysis based on a parameterized and validated model of the photooxygenation is required.

7.1.4 Identification of the process model parameters and assessment of the model-data fit

The process model for the photooxygenation contains seven unknown parameters, which need to be identified with experimental data, Eq. (7.28). Two parameters, the mass transfer coefficient $\widetilde{k_\mathrm{l}a}$ and the optical path length l_opt, are characteristics of the experimental setup, while five are kinetic rate constants independent on reactor design.

The identification process showed that the kinetic parameters for formation of the hydroperoxides, $\tilde{k}_{\mathrm{PO}_1}$ and $\tilde{k}_{\mathrm{PO}_\mathrm{y}}$, are strongly correlated with the parameter $k_{\mathrm{l}1}$ describing the quantum yield of oxygen (Eq. (7.9)). It was observed that different combinations of parameter values describe the experimental results equally well. Although the parameter set is theoretically identifiable, it was not possible to disentangle this correlation by MBDoE due to the inherent measurement uncertainty. Therefore, the unknown quantum yield parameters were set to literature values reported for DCA in benzene [185]: $k_{\mathrm{l}1} = 0.641$ and $k_{\mathrm{l}2} = 0.0119\,\mathrm{mol/L}$.

The estimation results for the remaining five parameters are given in in Tab. 7.2. The model-data fit is visualized in the parity plots in Fig. 7.5. The data is colored according to their theoretical residence time.

The identified model provides a good match with the experimental data over the whole range of investigated residence times. Likewise, no systematic model discrepancy was observed over the range of initial DHAA concentration, the LED light power, the photosensitizer concentration, and the molar fraction of oxygen (App. G.1). In total, a relative deviation between the predicted and measured data of $7.09\,\%$ is obtained for the key intermediate PO_1.

In contrast to PO_1, the prediction for PO_y fits the measurement data less. One reason is the decreased measurement accuracy at such small concentrations. The other reason is the tendency of the optimizer to favor high concentration due to the definition of the objective function. All estimated parameters were found to be identifiable based the profile likelihood approach. The confidence intervals show acceptable spreads for each parameter value. However, the kinetic constants have larger confidence intervals and are less certain in their estimates than the setup related properties as the mass transfer coefficient and the optical path length.

Tab. 7.2: Estimated parameter values including their confidence intervals and the obtained goodness of fit for the developed process model describing the photooxygenation, Eq. (7.27).

Model-data fit

Symbol	unit	value	description
SSE	$\mathrm{mol^2/L^2}$	0.1799	sum of squared errors
$\hat{\sigma}^2$	$\mathrm{mol^2/L^2}$	$2.73 \cdot 10^{-4}$	measurement error variance
	%	7.09	mean relative deviation of $\mathrm{PO_1}$†

Estimated parameters

Symbol	unit	value	COD	CI_{95}^{-}	CI_{95}^{+}
$\widetilde{k_la}$	$\sqrt{1/\mathrm{cm\,min}}$	1.094	0.093	1.046	1.148
$\tilde{k}_{\mathrm{PO_1}}$	$\mathrm{L\,mol^{-1}}$	7.130	0.173	6.555	7.790
$\tilde{k}_{\mathrm{PO_y}}$	$\mathrm{L\,mol^{-1}}$	0.644	0.306	0.550	0.747
$k_{\mathrm{PO_x}}$	1/min	0.0249	0.369	0.0204	0.0296
l_{opt}	cm	0.178	0.107	0.169	0.188

Fixed parameters (quantum yield, Eq. 7.9)

Symbol	unit	value	reference
k_{l1}	–	0.641	DCA in benzene [185]
k_{l2}	$\mathrm{mol\,L^{-1}}$	0.0119	DCA in benzene [185]
κ	$\mathrm{L\,mol^{-1}\,cm^{-1}}$	12841.98	see App. B.3
C_0	–	1.02	App. E

†: $\left(\sum_i^{n_{\mathrm{PO_1}}} \left|(y^{\mathrm{data}}_{\mathrm{PO_1},i} - y_{\mathrm{PO_1},i})\right| / y_{\mathrm{PO_1},i}\right) / n_{\mathrm{PO_1}}$

COD: coefficient of dispersion, $COD = (CI_{95}^{+} - CI_{95}^{-})/\hat{\theta}$, $\hat{\theta}$: estimated value

$CI_{95}^{+/-}$: ±95 % confidence interval

The normed reaction constants (Eq. (7.12)) can be converted to the absolute rate constants for the reactions of DHAA with $^1O_2$:

$$k_{\mathrm{PO_1}} = 2.15 \cdot 10^5 \mathrm{L\,mol^{-1}\,s^{-1}},$$
$$k_{\mathrm{PO_y}} = 0.19 \cdot 10^5 \mathrm{L\,mol^{-1}\,s^{-1}}.$$

Both values are in a similar range as rate constants for other ene-type reactions reported previously [292, 405, 406]. The reaction to $\mathrm{PO_1}$ is about 10-fold faster than the formation of the byproducts, which corresponds the high $\mathrm{PO_1}$ selectivity observed in the measurements.

The parameter value for $\widetilde{k_la}$ corresponds to volumetric mass transfer coefficients from $12\,\mathrm{min^{-1}}$ to $20\,\mathrm{min^{-1}}$ in the investigated range of superficial velocities (Eq. (7.26)). These values lie within the upper range of k_la values estimated from correlations reported in the literature for Taylor flow [268].

The estimated length of $0.178\,\mathrm{cm}$ for the optical path length is greater than twice the tubing diameter of $0.08\,\mathrm{cm}$. In the considered photoreactor, two light sources are installed in a closed box of stainless steel, resulting in reflection of the light beam back to the reactor. Furthermore, as the reactor itself is symmetric leaving light beams on one side can re-enter the reactor tubing on the other side. These two effects together with the tube convolutions around the poles and the emission angle of the light sources make optical path lengths exceeding twice the tube diameter very plausible.

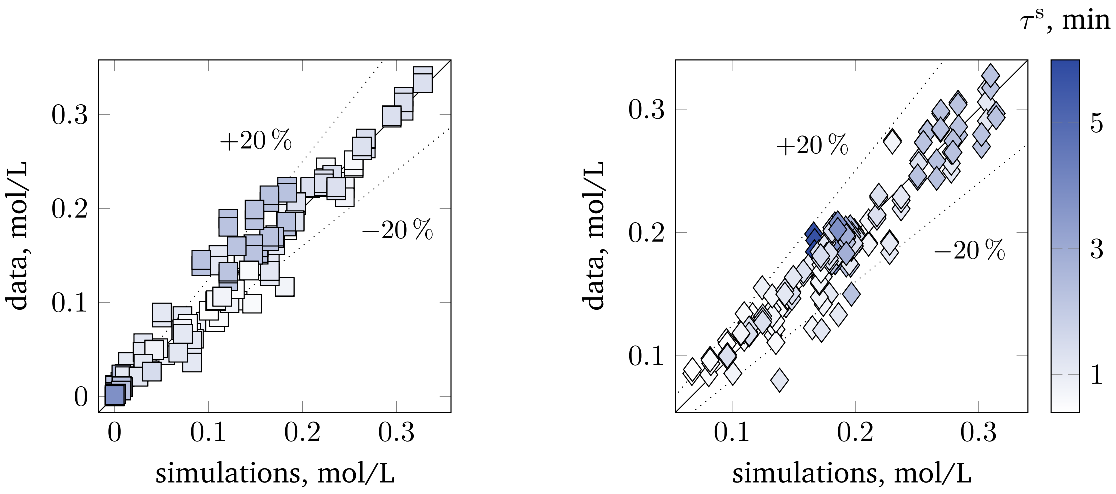

(a) DHAA

(b) PO_1

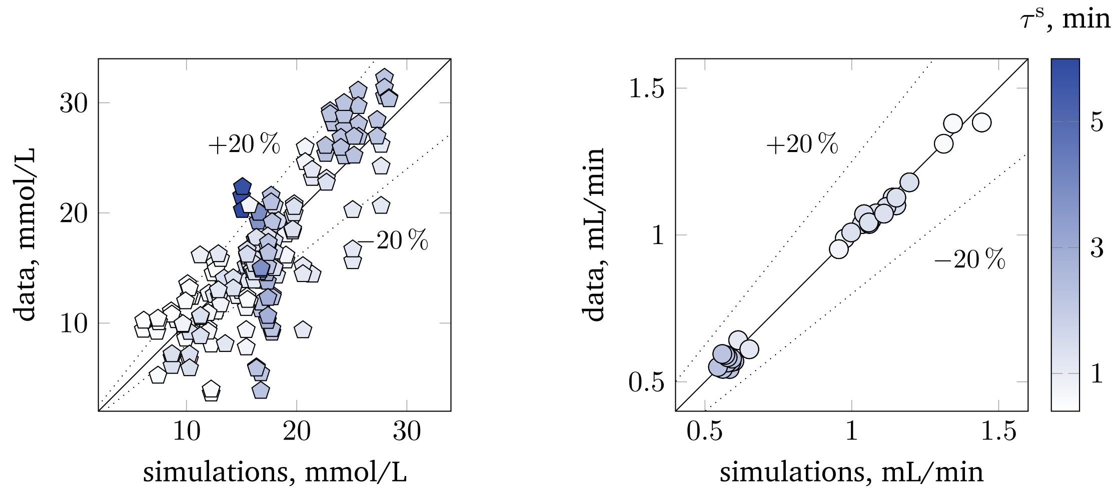

(c) PO_y

(d) Gas flow

Fig. 7.5: Fit of the simulated results obtained with the parametrized process model of the photooxygenation with the experimental data measured at the reactor outlet. The blue scale illustrates the superficial residence time in the photoreactor of each data point.

In conclusion, the model parametrized provides a good description for the photooxygenation of DHAA. All model parameters are identifiable and their estimates are in plausible ranges. The strong simplifications required to obtain a simple model structure, however, need to be taken into account to reliably use the model obtained. Firstly, all parameter values are only valid for a temperature of $-20\,^{\circ}\mathrm{C}$. The temperature affects all physical and chemical phenomena, from mass transfer to flow conditions and the reaction rates. The modeling of this temperature effect requires further studies on all these levels. Secondly, a global sensitivity analysis revealed that the obtained model is very sensitive to the distribution parameter C_0, which links the motion of gas and liquid phase. Therefore, exact determination of C_0 is essential to obtain reliable simulation results. Finally and most important, the assumption of a constant local volumetric rate of photon absorption poses a strong simplification of the real absorption conditions within the reactor. The absorbed photon flux is governed by the gas holdup in the system and photosensitizer concentration. Both quantities, however, are not constant but decrease with reaction progress due to oxygen consumption and photobleaching, respectively. The non-uniform absorption within the reactor channel might lead to a gradient in the rate of singlet oxygen formation within the liquid slug and a potential diffusion limitation of the overall reaction rate. The extension of the model to include these effect necessitates a two-dimensional description of the whole reactor and simulation of the fluid dynamics within the channel.

7.1.5 Using the process model to evaluate the process behavior

The developed model can now be applied to analyze the reaction behaviour during the photooxygenation and to identify optimal operation windows. In the following, the dynamic behaviour of two experiments is shown where either mass transfer or light irradiation was limiting the overall reaction rate. The kinetically controlled regime without further limitation does not occur under the investigated conditions. Figs. 7.6 and 7.7 illustrate the course of the product concentrations, gas flow rate and gas phase composition over the reactor length. The experimental data is plotted at sampling position. The discontinuities in the curves at the photoreactor exit (vertical line) are induced by a temperature jump to ambient temperature and the slow down of the medium due to a diameter change of the tubing. The hydroperoxides are formed fast within in the photoreactor and slowly decompose after leaving the cooled conditions due to the consecutive loss reactions, Eq. (7.2). The volumetric gas flow decreases along the reaction line in the photoreactor as result of the consumption of oxygen during photooxygenation, Fig. 7.6b. Because of

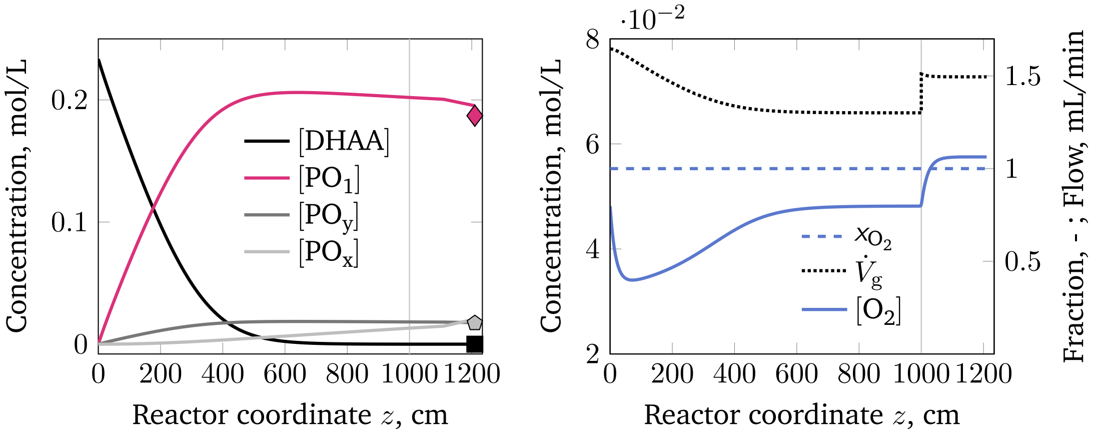

(a) Reaction species

(b) Oxygen mass transfer

Fig. 7.6: Dynamic process behaviour of concentrations, oxygen molar fraction and gas flow along the reactor coordinate in the light and substrate limited regime. The marks illustrate the measurment data and the thin vertical line the reactor outlet. Conditions: $[\mathrm{DHAA}]_0 = 0.23\,\mathrm{mol\,L^{-1}}$, $[\mathrm{DCA}] = 0.85\,\mathrm{mmol\,L^{-1}}$, $P_{\mathrm{LED}} = 100\,\%\mathrm{LED}$, $\mathrm{x}_{\mathrm{O}_2,0} = 1$.

the high initial reaction rates, dissolved oxygen is rapidly consumed after reaction start (Fig. 7.6b) and regained once the reaction slows down. The overall reaction rate is not substantially limited by mass transfer. Instead, the absorbed amount of photons hinders the reaction progress leading to a pseudo-zero order shape of the concentration profiles at the beginning of the reaction (Fig. 7.6a). Following the analysis in [296], the reaction rate in the light-limiting regime is

$$(\tilde{k}_{\mathrm{PO}_1} + \tilde{k}_{\mathrm{PO}_\mathrm{y}})[\mathrm{DHAA}] \gg 1: \quad r_{\mathrm{PO}} = \Phi_{^1\mathrm{O}_2} L_\mathrm{p}^\mathrm{a} = r_{\mathrm{PO}}^{\max}. \tag{7.33}$$

Once DHAA is consumed to a substantial extent, the availability of substrate becomes limiting and the reaction switches to first-order.

$$(\tilde{k}_{\mathrm{PO}_1} + \tilde{k}_{\mathrm{PO}_\mathrm{y}})[\mathrm{DHAA}] \ll 1: \quad r_{\mathrm{PO}} = \Phi_{^1\mathrm{O}_2} L_\mathrm{p}^\mathrm{a} (\tilde{k}_{\mathrm{PO}_1} + \tilde{k}_{\mathrm{PO}_\mathrm{y}})[\mathrm{DHAA}]. \tag{7.34}$$

This pseudo-inflection point between both regimes is defined as the half-maximum kinetic reaction rate [296], which corresponds to $[\mathrm{DHAA}] \approx 0.129\,\mathrm{mol/L}$.

A different process behaviour is shown in Fig. 7.7. The gas phase consists of both oxygen and nitrogen (Fig. 7.7b). Dissolved oxygen is consumed right at the start of the reaction and settles to an equilibrium stage that continuously decreases as the molar fraction of oxygen in the gas phase drops and thus the solubility in the liquid phase (Fig. 7.7b). The lower solubility slows down mass transfer between both phases and results in a decreased quantum yield of singlet oxygen production, Eq. (7.9). Along the whole reaction line, the DHAA concentration does not fall

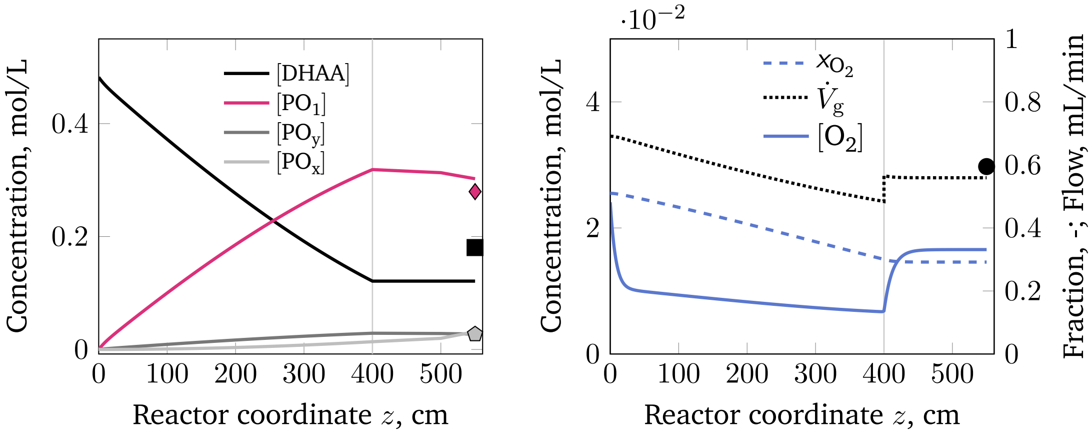

(a) Reaction species

(b) Oxygen mass transfer

Fig. 7.7: Dynamic process behaviour of the concentrations, oxygen molar fraction and gas flow along the reactor coordinate showing mass transfer limitation. The marks illustrate the measurement data and the thin vertical line the reactor outlet. Conditions: $[\mathrm{DHAA}]_0 = 0.48\,\mathrm{mol\,L^{-1}}$, $[\mathrm{DCA}] = 0.60\,\mathrm{mmol\,L^{-1}}$, $P_{\mathrm{LED}} = 100\,\%\mathrm{LED}$, $x_{O_2,0} = 0.51$.

below the inflection point Fig. (7.7a). The combination of pseudo-zero kinetics, less singlet oxygen production, and partially limiting mass transfer lead to the observed reduction in the overall reaction rate preventing a more efficient DHAA conversion. The gained insight in the photooxygenation of DHAA can now be used to complement the model by the acid-catalyzed conversion of PO_1 to artemisinin. The identified model for the photooxygenation kinetics, the photon and mass transfer in the reactor serves as a building block to be extended by the reaction kinetics for the acid-catalyzed cascade.

7.2 Acid-catalyzed reaction sequence

In presence of a strong acid, the formed hydroperoxides undergo a complex network of rearrangements, condensations and oxidations (Sec. 2.3.1.3). The network is characterized by sequences of reversible acid-catalyzed reactions and irreversible reactions eliminating water or hydrogen peroxide. Due to the number of reactions, simplifications on the reaction network are crucial to obtain a kinetic model with an identifiable amount of parameters. Before introducing the assumptions made, first the experimental data is shown to qualitatively illustrate the behavior of the acid-catalyzed sequence and the main products obtained in the product solution.

7.2.1 Qualitative assessment of the experimental data

The reaction kinetics of the acid-catalyzed sequence were investigated by two experimental approaches

1. in continuous operation in the presence of oxygen (Sec. 4.3.3)
2. in batch operation under N_2 atmosphere (Sec. 4.3.4).

In both, trifluoroacetic acid (TFA) was used as acidic catalyst. The continuous experiments were performed in the milli-scale flow reactor extended by an additional second reaction line of varied length kept at room temperature. TFA was either added to the DHAA containing feed or dosed separately as a second liquid feed after the photoreactor. The end of the reaction was defined by quenching the reaction solution with triethylamine at the reactor outlet.
First, the observed product spectrum is exemplified on the data from the continuous experiments with TFA present during photooxgenation. Later, the reaction kinetics are illustrated by the results with separate acid dosing and from the batch experiments.

7.2.1.1 Product spectrum of the acid-catalyzed reaction sequence

Fig. 7.8 shows the obtained yields of artemisinin and its main byproducts, when TFA was dosed together with DHAA. In this case, PO_1 is directly converted after formation in the photoreactor. Therefore, PO_1 is not detected at the end of the reactor line despite full conversion of DHAA and short total residence times of less than $5\,\mathrm{min}$. Artemisinin is formed with a much lower rate reaching its final yield of $66\,\%$ after a total residence time of $22\,\mathrm{min}$. As main byproducts dihydro-*epi*-deoxyarteannuin B (BP_3), and arteannuin H (ArteH) are obtained. Both were also reported as major byproducts in previous studies on the partial synthesis [30, 70, 179, 198–201, 203, 208]. According to the postulated reaction mechanism in Sec. 2.3.1.3, BP_3 evolves directly from PO_1, while arteannuin H results from the conversion of the secondary hydroperoxide PO_2 in the presence of acid. BP_3 forms rapidly within $2.5\,\mathrm{min}$ residence time, while ArteH does not reach a constant concentration before $10\,\mathrm{min}$ residence time. Both species are obtained in a maximum yield of $3\,\%$ to $5\,\%$. The formation of another major byproduct, the lactone BP_4, was not observed as side product in this oxygen-rich conditions.

The sum of all three main reaction products - artemisinin, BP_3, and ArteH - accounts of $76\,\%$ of the total amount of DHAA fed into the reactor. At short residence

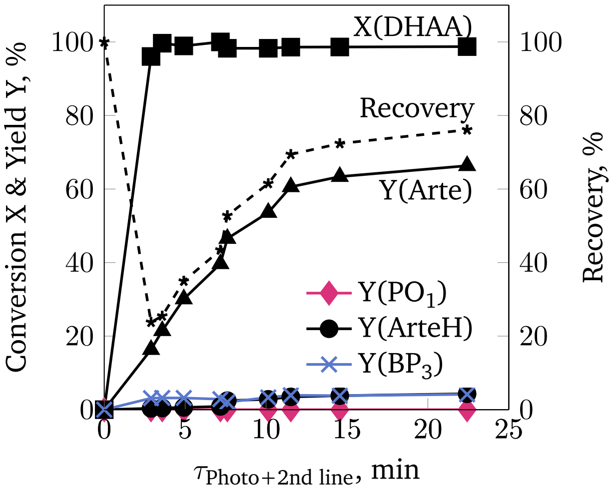

Fig. 7.8: Formation of the quantifiable reaction products and intermediates from the partial synthesis to artemisinin starting from dihydroartemisinic acid with trifluoroacetic acid present during photooxygenation. Conditions: $[\text{DHAA}]^0 = 0.25\,\text{M}$, $[\text{TFA}]=0.125\,\text{M}$ $[\text{DCA}]=0.85\,\text{mM}$, $\text{P}_{\text{LED}}=100\,\%$, $\text{x}_{\text{O}_2}=1$.

times with full conversion of DHAA and low formation of artemisinin, the recovery of product mass (Sec. 3.4) drops down to $24\,\%$. This behavior implies that the conversion of PO$_1$ not only yields unknown side products but also forms intermediate species, which slowly react to artemisinin. None of the species previously reported by Brown et al. [66, 70, 197, 198] could be identified as a major reaction product. 2D-NMR analysis of the reactor effluent suggests that the unknown intermediate does not consist of one or two single species but a pool of various different structures (App. G.2). For complete elucidation of the reaction mechanism and the involved product species, analytical studies including labelling of starting material, online analysis, product separation, and mass spectrometry are required [205, 206]. In this work, the challenge of unknown intermediate and product species is approached by simplifying the reaction network and applying mathematical tools for model identification (Sec. 3.5). The following analysis focuses on the products arising from PO$_1$. The formation of arteannuin H was not studied in detail, since it does not contribute to the production of the target artmisinin.

7.2.1.2 Continuous experiments with separate acid dosing

The separate addition of a TFA-containing feed after the photoreactor allows for a precise definition of the starting point of the acid-catalyzed reaction sequence. In this way, both reaction steps, the formation and the conversion of PO$_1$, and their different temperature regimes at $-20\,°\text{C}$ and $20\,°\text{C}$ can be decoupled. The

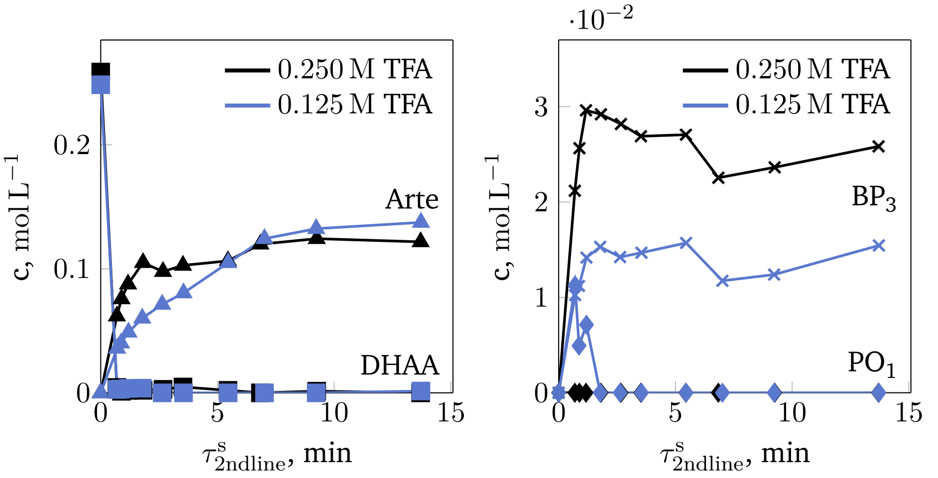

(a) Artemisinin & DHAA (b) PO$_1$ & BP$_3$

Fig. 7.9: Concentration profiles measured at the reactor outlet after photooxygenation and separate acid-catalyzed sequence in dependence on the residence time in the presence of acid. Conditions: $[DHAA]^0 = 0.25\,M$, $[DCA]{=}0.85\,mM$, $P_{LED}{=}100\,\%$, $x_{O_2}{=}1$.

later model selection and parameter estimation uses only data from continuous experiments with separate TFA dosing. Fig. 7.9 shows a subset of the this data.

All experiments were designed so that DHAA is completely converted in the photooxygenation step. After acid addition of $0.125\,M$ inline, the produced PO$_1$ is completely cleaved in less than $2\,min$ (Fig. 7.9b). Likewise, the direct byproduct of this conversion, BP$_3$, is formed in the first $2\,min$. The two-fold concentration of acid in the reaction line results in an almost doubled formation of BP$_3$ reaching a yield of $11\,\%$. In comparison to the experiments with TFA present in the photoreactor with less than $6\,\%$ BP$_3$ yield, BP$_3$ formation is enhanced when the intermediate hydroperoxide is allowed to accumulate before acid is added.

The formation of artemisinin is slower than PO$_1$ conversion and BP$_3$ formation. The final artemisinin yields are $55\,\%$ and $47\,\%$ for $0.125\,M$ and $0.25\,M$ TFA, respectively. The lower arteminsinin yield at a higher TFA concentration results from the enhanced BP$_3$ formation at these conditions. The observed yields are up to $15\,\%$ lower when TFA is dosed separately in comparison to TFA dosage together with DHAA. This large difference indicates that the formation of unknown byproducts is also pronounced, when PO$_1$ is present in high concentrations before acid is added.

7.2.1.3 Batch experiments excluding oxygen

An exact description of the cleavage PO$_1$ is essential to obtain reliable reaction kinetics for the overall synthesis. To resolve this first step, the continuous experiments were complemented by batch experiments using the product solution from photooxygenation as reactant (Sec. 4.3.4). The experiments were performed in nitrogen atmosphere at ambient pressure to exclude oxygen mass transfer from affecting the reaction progress.

A comparison of the results from batch and continuous experiments at similar acid concentration is included in App. G.3. Despite the differences in the used feed and the operation mode, both experimental setups yield similar concentrations for PO_1 and BP_3 at equal initial conditions. Thus, both settings differ mainly in the supply of oxygen as reagent.

Six batch experiments at four different concentrations of TFA were performed. The obtained concentration profiles over reaction time are shown in Fig. 7.10 for each species separately. Different data sets, which were obtained at equal acid

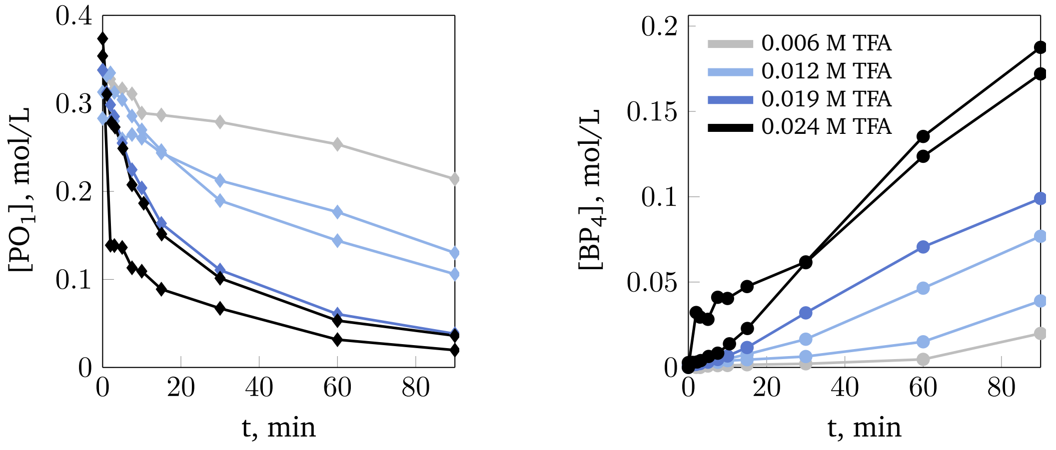

(a) PO_1 **(b)** BP_4

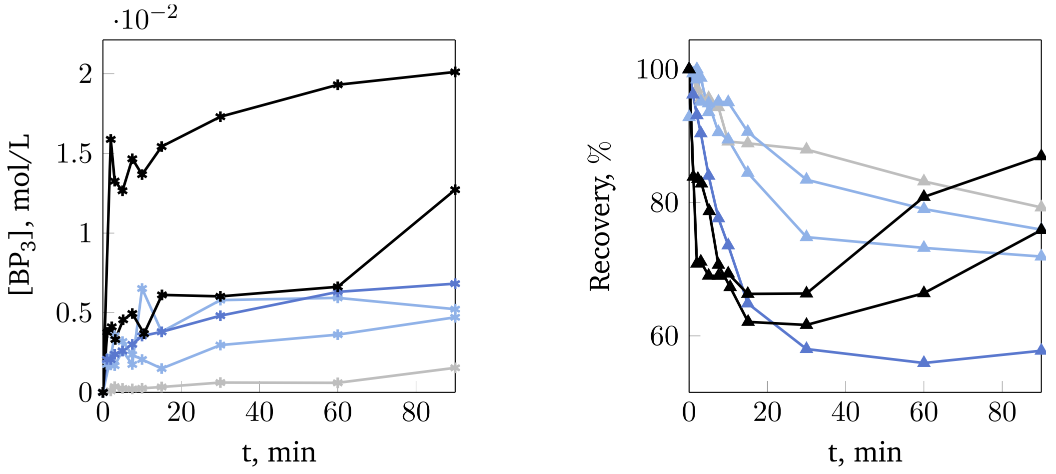

(c) BP_3 **(d)** Recovery

Fig. 7.10: Concentration profiles obtained by adding TFA to the PO_1 containing product solution from photooxygenation in N_2 atmosphere and batch operation.

concentration, are depicted in the same color.

The cleavage of PO_1 takes more $90\,\mathrm{min}$ to reach completion at acid concentrations of $0.024\,\mathrm{M}$ and lower. In absence of oxygen, the main product of the acid-catalyzed sequence is the lactone BP_4 (Fig. 7.10b). Its formation starts with a delay and is also not completed within $90\,\mathrm{min}$ reaction time at all tested acid concentrations.

The recovery follows a similar trend as in the oxygen-rich conditions of the continuous experiments. With progressing consumption of PO_1 the recovery drops down to less than $60\,\%$. Once BP_4 formation sets in, the recovery rises again reaching up to $87\,\%$ after $90\,\mathrm{min}$ of reaction time. So similar to artemisinin, the formation of BP_4 proceeds via one or several intermediate species accumulating during the reaction. Lowering the acid concentration slows the cleavage of PO_1 and correspondingly the formation of BP_4. In contrast to the data from the continuous experiments, the dependence of the BP_3 formation on the acid concentration is less evident (Fig. 7.10c).

The concentration profiles obtained at equal acid concentration show large systematic deviations reaching up to $100\,\%$ of relative error for the PO_1 concentration measured in presence of $0.024\,\mathrm{M}$ TFA. Potential reasons for this observed sensitivity are deviations in the addition of the acid and an initial temperature rise due to the exothermic nature of the reaction. All obtained data sets were included in the following model selection and parameter identification.

7.2.2 Model discrimination

The challenge in the model development for the acid-catalyzed sequence is the complex nature of the overall reaction mechanism (Sec. 7.1.1.1) and the incomplete set of known and quantifiable products. This missing information prevents an entirely mechanistic kinetic model for the acid-catalyzed sequence. Instead, the current knowledge of the reaction mechanism is used to derive simplified reaction networks and develop kinetic models based on these structures. The model candidates were tested regarding their fit with the experimental data from both continuous and batch experiments. The model discrimination was performed in an iterative manner by adding more complexity to the proposed network or revising initial assumptions.

The goodness of the fit was compared based on the Sum of Squared Errors (SSE) and the AICc value (Sec. 3.5). The first quantifies the overall deviation of the simulated from the experimental data. The latter is a quantifier for both the overall fit quality and the model complexity. The aim is to obtain models with low AICc and SSE values.

This way, more than 60 model candidates were tested regarding their potential to describe the observed experimental trends. The simplified reaction networks and the corresponding kinetic models were developed in close cooperation with Moritz Schulze from TU Braunschweig. He performed the parameter estimation, model assessment, and identifiability analysis. Details on the applied methods and the results of all tested model candidates can be found in his Ph.D. thesis [360]. The presentation of the results in the following section focuses on the identified critical aspects of the model structure, which affect the model-data fit most significantly. These are

- Non-linear dependence of the reaction rate for the PO_1 conversion on the dosed acid concentration,
- Introduction of a lumped byproduct species in the reaction path to artemisinin,
- Decoupling of the reaction pathways to BP_4 and artemisinin.

First, the applied simplifications on the reaction network and the resulting base network, starting point of the model discrimination, are introduced.

7.2.2.1 Simplification of the reaction network

The starting point of the reaction network development was the reaction mechanism of the conversion of PO_1 to artemisinin, introduced in Sec. 7.1.1.1. All tested networks are based on the following assumptions:

- The formation of artemisinin, BP_3, BP_4, and BP_5 is irreversible
- Artemisinin, BP_3, BP_4, and BP_5 are stable in the reaction conditions and do not decompose.
- Hydrogen peroxide, formed during the formation of BP_3, does not affect the reaction kinetics.
- The carboxyl group of PO_1 does not contribute to the overall acidity of the system

Fig. 7.11 depicts the base network for the acid-catalyzed sequence together with the extensions added later.

In the simplest network considered, PO_1 is assumed to be irreversibly converted in an acid-catalyzed step to either the byproduct BP_3 or the intermediate IM_2. The kinetics in both pathways are reduced to one step, where the protonation is rate-limiting. The formation of several intermediate species observed in the 2D-NMR data is simplified by introducing one lumped species, IM_2. IM_2 represents the central

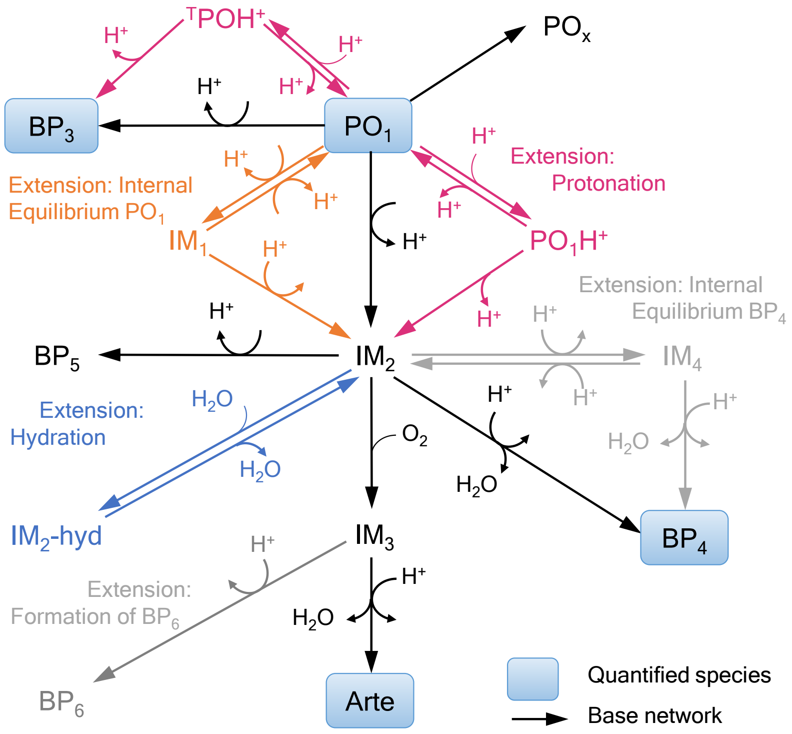

Fig. 7.11: Simplified reaction networks for the acid-catalyzed reaction sequence to artemisinin. The base network is shown in black. The colored extensions were tested as alternatives.

enol intermediate, the starting point of the final artemisinin and the BP_4 formation. The reaction to BP_4 is assumed to be governed by a single acid-catalyzed rate-determining step, which eliminates water. To attribute for the low recovery at the reaction end, a second species BP_5 is introduced, which originates from IM_2 and lumps all unknown byproducts of the acid-catalyzed sequence. IM_2 reacts with oxygen irreversibly to the intermediate IM_3, which is converted to artemisinin in a second, acid-catalyzed step eliminating one equivalent of water. The made simplifications correspond to a reaction mechanism, where the addition of oxygen is rate-determining and the water abstraction is irreversible. This base network assumes that the formed water does not affect the reaction kinetics and that the acid concentration is constant throughout the reaction.

Inspired by the postulated reaction mechanism, the base network was extended by additional reaction pathways taking into account reversible reactions and other side reactions. The cleavage of PO_1 was extended by including a reversible reaction step. In acid-catalyzed reactions, either the initial protonation is rate-determining or the rearrangement following the protonation [407]. The first case is included in the base network. The protonation extension describes the second option. Here PO_1 is reversibly protonated either on the internal or the external oxygen of the

hydroperoxyl group giving the ^{T}POH$^+$ and PO$_1$H$^+$, respectively. Both species are further transformed in an irreversible reaction to IM$_2$, releasing the previously bound proton. As a further alternative, the initial equilibrium step was proposed to progress without the consumption of H$^+$ forming the intermediate IM$_1$.
In a third extension, an internal equilibrium step was added to the reaction network by introducing the intermediate IM$_4$, which is reversibly formed from IM$_2$ and reacts further irreversibly to BP$_5$. Physically interpreted, IM$_3$ corresponds to the seco-cadinane species (Sec. 7.1.1.1), which was also observed as a major byproduct in previous studies [70, 203]. The fourth extension considers the effect of water on the reactivity of intermediates by hydration. For the network development, it was assumed that only the central intermediate IM$_2$ representing the enol species is hydrated. The hydration binds water reversibly and forms the species IM$_2$$-\mathrm{hyd}$ having no reactivity towards IM$_3$. With increasing reaction progress, the concentration of water increases, shifting the hydration equilibrium to the inactive IM$_2$$-\mathrm{hyd}$, which results in slower rates of both BP$_4$ and artemisinin formation at the end of the reaction.

7.2.2.2 Performance of the base network

The developed model candidates were now fit to the experimental data from batch and continuous experiments. The initial photooxygenation step is described by the identified model for forming PO$_1$ and PO$_\mathrm{y}$. $k_{\mathrm{PO}_\mathrm{x}}$ and the initial concentrations in the batch experiments were regarded as additional parameters to be estimated with the acid-catalyzed data due to the composition during storage overnight. The assessment of the model candidates started with the base network. The fitting results for the base network are shown in Fig. 7.12 with the parameter values given in Tab. 7.3. The first species in the parameter subscript states the reactant and the second the product of the regarded reaction. The simple model structure could describe none of the measured species well over the whole concentration range. The experimental data is well matched at the reaction start with high PO$_1$ concentrations, and at the reaction end with high concentrations of artemisinin or BP$_4$. However, systematic deviations are observed in the middle section, where PO$_1$ is already substantially converted, but artemisinin and BP$_4$ are not yet formed.

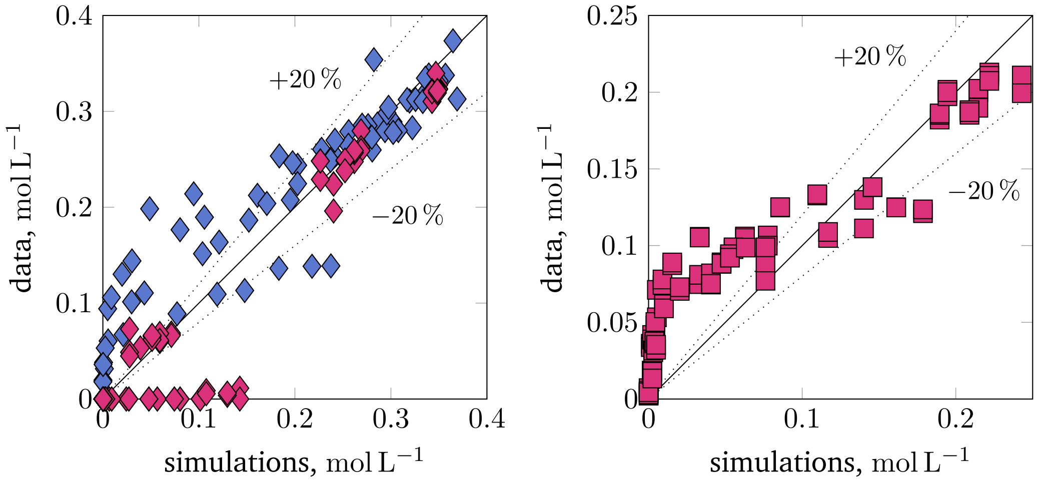

(a) PO_1 **(b)** Artemisinin

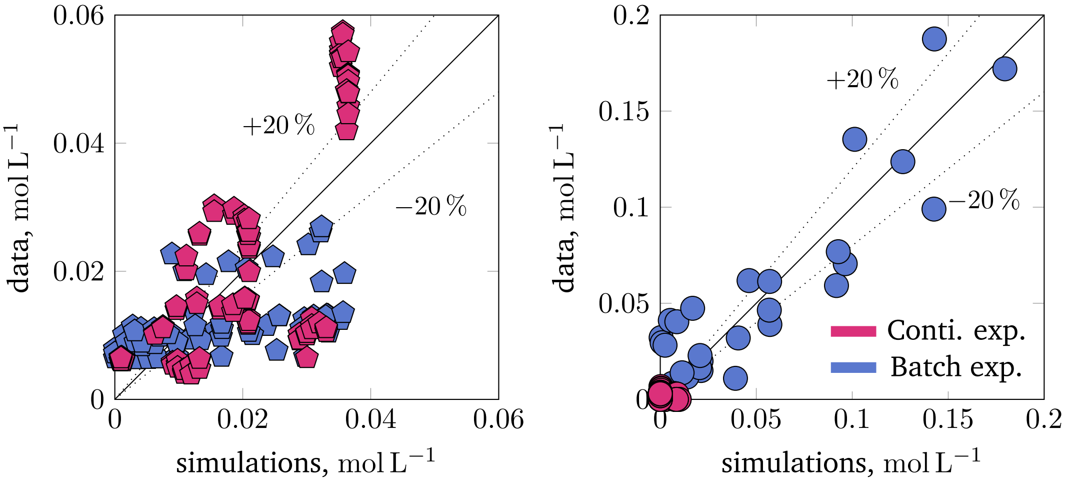

(c) BP_3 **(d)** BP_4

Fig. 7.12: Fit between the experimental data and the parameterized base network (Fig. 7.11) for all measured species. Blue and red points indicate data from the batch and continuous experiments, respectively.

Tab. 7.3: Kinetic parameters identified for the base network (Fig. 7.11) and the corresponding confidence intervals. The first subscript states the reactant and the second the product of the corresponding reaction. The parameters for the photooxygenation and reactor model are taken from Tab. 7.2.

	k_{PO_x}	k_{PO_1,BP_3}	k_{PO_1,IM_2}	k_{IM_2,BP_4}	k_{IM_2,BP_5}	k_{IM_2,IM_3}	$k_{IM_3,Arte}$
Unit	min^{-1}	L mol^{-1} min^{-1}	L mol^{-1} min^{-1}	L mol^{-1} min^{-1}	L mol^{-1} min^{-1}	L mol^{-1} min^{-1}	L mol^{-1} min^{-1}
Value	**6.14 e-4**	**0.349**	**3.17**	**0.441**	**0**	**204.96**	**0.598**
CI_{95}^{-}	0	0.028	2.945	0.368	-	95.63	0.538
CI_{95}^{+}	23.86 e-4	0.419	3.415	0.524	-	1429.74	0.666

7.2.2.3 Description of the acid-catalyzed conversion of PO_1

An accurate description of the conversion of PO_1, the initial step of the acid-catalyzed sequence, is crucial to obtaining a good model-data fit for the final reaction products artemisinin and BP_4. However, with the linear dependence of the reaction rate on the acid concentration, the base model could not reproduce the large spread of PO_1 conversion rates observed at the differing acid concentrations used in continuous and batch experiments (Fig. 7.12a).

The base case neglects the dissociation of the acid on the availability of H^+. Thus, two model extensions were proposed in Tab. 7.4, including a dissociation equilibrium of TFA either affected solely by the solvent (Model B) or a protonatable species such as PO_1 (Model C). In both corrections, the dissociation equilibrium is assumed to be fast with respect to the reaction kinetics of PO_1 conversion, allowing the calculation of the H^+ concentration by the mass action law.

Tab. 7.4: Consideration of the dissociation equilibrium of trifluoroacetic acid on the H^+ concentration based on the mass action law.

Model ID	Calculation of H^+
A	$\mathrm{HTFA} \longrightarrow \mathrm{TFA}^- + \mathrm{H}^+$ $[\mathrm{H}^+] = [\mathrm{TFA}]^0$
B	$\mathrm{HTFA} \rightleftharpoons \mathrm{TFA}^- + \mathrm{H}^+$ $[\mathrm{H}^+] = -\frac{K_A}{2} + \sqrt{\frac{K_A^2}{4} + K_A[\mathrm{TFA}]^0}$
C	$\mathrm{HTFA} + \mathrm{S} \rightleftharpoons \mathrm{TFA}^- + \mathrm{SH}^+$ $[\mathrm{S}] = [\mathrm{DHAA}]^0, [\mathrm{H}^+] = [\mathrm{SH}^+]$ $[\mathrm{H}^+] = \frac{K_A[\mathrm{DHAA}]^0}{2} + \sqrt{\frac{(K_A[\mathrm{DHAA}]^0)^2}{4} + K_A[\mathrm{TFA}]^0[\mathrm{DHAA}]^0}$

Tab. 7.5: Variation of the reaction order of TFA for the description of the PO_1 conversion.

Model equations	$PO_1 \xrightarrow{H^+} IM_2$ $PO_1 \xrightarrow{H^+} BP_3$	$r_{PO_1,IM_2} = k_{PO_1,IM_2}[H^+]^{n_{IM_2}}[PO_1]$ $r_{PO_1,BP_3} = k_{PO_1,BP_3}[H^+]^{n_{BP_3}}[PO_1]$
Model ID	n_{IM_2}	n_{BP_3}
I	1	1
II	2	1
III	variable	1
IV	variable	$n_{IM_2}+1$
V	variable	variable

Tab. 7.6: Comparison of the model-data fit obtained with the simplified reaction networks introduced in Fig. 7.11, Tab. 7.4, and Tab. 7.5. N_p^{kin} is the number of unknown kinetic parameters. The goodness of the fit is assessed based on the Akaike information criterion (AICc) and the sum of squared errors (SSE) (Sec. 3.5). The font color of the extension correspond to Fig. 7.11. The blue color indicates the goodness of the fit. The grey color marks the best model candidate within this set.

	Model Specification [1]				N_p^{kin}, [2]	AICc		SSE	
							Conti.	Batch	Total
1	Base-A-I				7	-4230	0.302	0.212	0.51
2	Base-B-I				8	-4228	0.302	0.212	0.51
3	Base-C-I				8	-4228	0.302	0.212	0.51
4	Base-A-II				7	-4307	0.254	0.198	0.45
5	Base-A-III				8	-4515	0.232	0.087	0.32
6	Base-A-IV				8	-4773	0.121	0.086	0.21
7	Base-A-V				9	-4771	0.121	0.086	0.21
8	Base-A-I	+ Prot			11	-4509	0.131	0.175	0.31
9	Base-A-I	+ EqPO			11	-4415	0.210	0.161	0.37
10	Base-A-I	+ EqBP4			9	-4223	0.282	0.213	0.49
11	Base-A-I	+ Hyd			9	-4308	0.45	0.225	0.45
12	Base-A-I	+ Prot	+ EqBP4		13	-4571	0.118	0.097	0.29
13	Base-A-I	+ Prot	+ Hyd		13	-4789	0.123	0.076	0.20
14	Base-A-I	+ EqBP4	+ Hyd		11	-4287	0.24	0.22	0.46
15	Base-A-I	+ Prot	+ EqBP4	+ Hyd	15	-4607	0.15	0.12	0.27
16	Base-A-IV	+ EqBP4			10	-4769	0.121	0.086	0.21
17	Base-A-IV	+ Hyd			10	-4769	0.121	0.086	0.21
18	Base-A-V	+ Hyd			11	-4741	0.121	0.086	0.21
19	Base-A-V	+ EqBP4			11	-4767	0.121	0.086	0.21
20	Base-A-V	+ Hyd	+ EqBP4		13	-4618	0.121	0.132	0.23
21	Base-A-IV	+BP_6[3]			8	-4895	0.081	0.088	0.17
22	Base-A-V	+BP_6[3]			9	-4895	0.081	0.088	0.17
23	Base-A-V	+BP_6[3]	+ EqBP4	+ Hyd	13	-4887	0.080	0.089	0.17
24	Base-B-IV	+BP_6[3]			9	-4896	0.081	0.087	0.17
25	Base-C-IV	+BP_6[3]			9	-4893	0.081	0.088	0.17

[1] $\widetilde{k_l a} = 1.094\sqrt{1/\mathrm{cm\,min}}$

[2] $[PO_1]^0$ and $[BP_3]^0$ in the batch experiments are additional estimation parameters (N=12)

[3] The formation of BP_6 starting from IM_3 substituted the formation of BP_5 from IM_2, Fig. 7.11

As an alternative extension, the reaction order of the present proton concentration n was set as an additional parameter. A reaction order exceeding one relates to a reaction mechanism where several protonations are required to initiate the final product formation. In this step, the reaction order was varied exclusively for the reactions of PO_1 to IM_2 and BP_3. The tested model extensions are summarized in Tab. 7.5.

The goodness of the model-data fit obtained by adjusting the effect of the acidic catalyst on the PO_1 conversion is given in Tab. 7.6. The results of the base model

(Model 1) serve as a reference point with an SSE of $0.51\,\mathrm{mol}^2\,\mathrm{L}^{-2}$.

Considering a dissociation equilibrium promoted by toluene (Tab. 7.4, Model 2) or by the reactant itself (Model 3) did not significantly improve the model-data fit. In both cases, the value of the equilibrium constant was estimated at the upper bound of the set range so that the effective H^+ concentration equaled the added TFA concentration resembling Model A.

Instead, variation of the reaction orders of TFA achieved a significant improvement of the model-data fit (Model 4, 5, 6 & 7). Model 6 with the coupled reaction orders gives a similar model-data-fit as model 7, where both reaction orders were estimated independently. Both models reproduce the conversion of PO_1 and the formation of BP_3 and BP_4 well, while the artemisinin concentration is described with a systematic deviation comparable to the base model (App. G.4.2). In model candidates 6 and 7, TFA reaction orders exceeding two were obtained. These high values may result from a sequence of rate-limiting acid-catalyzed steps, e.g., multiple protonations, which are lumped together in this simplified model. Another explanation is that these high reaction orders compensate for other physical or chemical phenomena such as hydration by water or additional intermediates formed, which are not covered by the model structure.

A more mechanism-oriented approach to cover the strong acid-dependency offers the protonation extension (Extension Prot, Model 8) introduced in Fig. 7.11. Including an initial protonation step with a temporary binding of H^+ on the pathways to IM_2 and BP_3 achieved a significant improvement of the model-data fit compared to the base model. The key aspect resulting in the improved fit is the variability in the acid concentration throughout the reaction. Model 8 predicts almost complete temporary H^+ depletion in the batch experiments, while the acid concentration in the continuous experiments is not significantly affected due to the higher TFA initial concentration (App. G.4.2). Formulating this initial equilibrium step without binding H^+ (EqPO, Model 9) could not reproduce the experimental data as good as Model 8.

The results of Models 10 and 11 exemplify the importance of modeling the influence of the acidic catalyst on the reaction kinetics. In both models, the reaction networks are extended exclusively downstream of IM_2 without adjusting the linear dependence of PO_1 conversion on the acid concentration. Considering an equilibrium step between the central IM_2 intermediate and BP_4 (Extension EqBP4, Model 10) or the hydration of IM_2 (Extension Hyd, Model 11) resulted in a similar model-data fit as the base model despite the higher complexity of the network and the increased number of parameters.

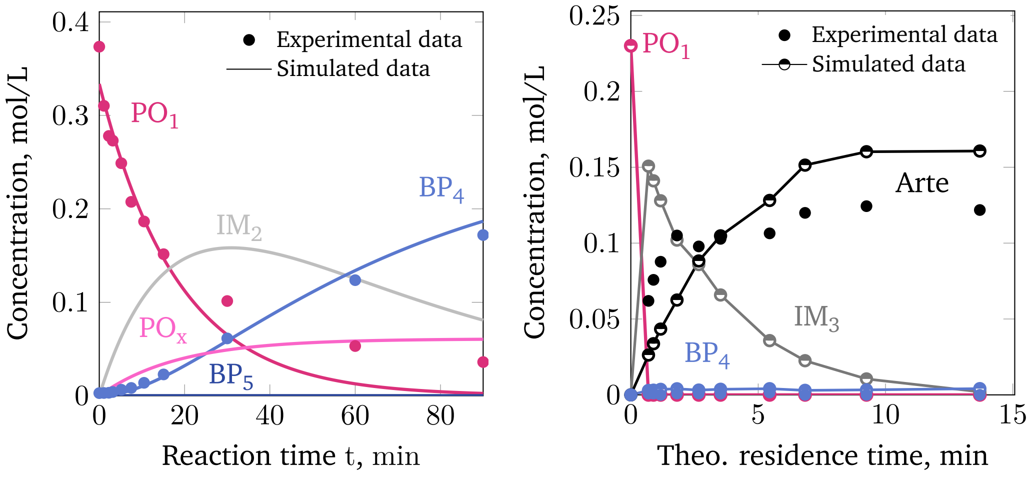

(a) Batch experiment [TFA] = 0.024 M (b) Continuous experiment [TFA] = 0.25 M

Fig. 7.13: Illustration of the concentration profiles of the main products obtained with Model 6 (Tab. 7.6) of (a) a batch experiment and (b) a continuous experiment.

7.2.2.4 Formation of a lumped byproduct species BP_6 in the reaction path to artemisinin

In the next step, the concepts for modulating the acid influence were coupled with the extensions affecting the conversion of the postulated key intermediate IM_2, Fig. 7.11. The performance of those model candidates is included in Tab. 7.6.

Extending the model with explicit consideration of the protonation of PO_1 with the hydration (Model 13) yielded a significantly improved description of the experimental data in comparison to the protonation alone (Model 8). However, the obtained Model 13 performs only slightly better than the simpler Models 6 and 7 with variable TFA reaction orders. Considering an internal equilibrium step of IM_2 in addition to the protonation, Models 12, 14, and 15 showed no beneficial effect on the model-data fit. In contrast to the candidates with protonation, coupling the models with variable TFA reaction orders, Models 6 and 7, with the hydration, Models 17, 18, and 20, or the internal equilibrium, Models 16, 19, and 20, did not improve the process description further.

In all well-performing models, the conversion of IM_2 to IM_3 was estimated to be very fast, while the formation of the lumped byproduct species BP_5 starting from IM_2 was estimated to be negligible. The resulting behavior in a continuous and a batch experiment is exemplified with Model 6 in Fig. 7.13. In the batch experiment at a TFA concentration of 0.024 M (Fig. 7.13a) PO_1 is converted slowly to IM_2. This allows for PO_x to be formed as the main byproduct. Without oxygen, IM_2 cannot react to IM_3 and is slowly converted to BP_4. Due to the significant amounts of PO_x, closing the mass balances for all known species does not require introducing another lumped byproduct species BP_5.

In a continuous experiment (Fig. 7.13b) with a 10-times higher TFA concentration of $0.25\,\mathrm{M}$, PO_1 is rapidly converted to IM_2. In the presence of oxygen, IM_2 reacts almost instantly to IM_3, which accumulates as the main intermediate and slowly forms artemisinin. According to Model 6, PO_1 and IM_2 are present only for a short time, so no significant amounts of byproduct form. Once IM_3 is formed, it must react to artemisinin resulting in higher Arte yields than observed. The fast conversion of IM_2 to IM_3 is crucial to prevent the formation of higher concentrations of BP_4 in the continuous experiment.

As a result of this analysis, BP_6 was introduced as byproduct species formed from IM_3 on the pathway to artemisinin, extension BP_6 in Fig. 7.11 and Tab. 7.6. The formation of BP_6 substituted the reaction of IM_2 to BP_5.

Including the byproduct formation from IM_2 – after oxidation – in the kinetic model enabled a better description of the continuous experiments, Model 21. Model 21 achieved a low AICc value and reproduced the experimental data best with eight kinetic parameters. A further model extension by introducing hydration in Model 23 or the TFA dissociation in Models 24 and 25 did not describe the experimental data significantly better.

7.2.2.5 Discrimination between the reaction paths to artemisinin and BP_4

The best performing model so far, Model 21, contains one unidentifiable parameter, the rate constant for oxidizing IM_2 to IM_3, estimated at the set upper boundary. The rapid conversion of IM_2 in the continuous experiments is crucial to reproduce the low BP_4 formation observed in the experimental data.

In the next step of the model discrimination, the model candidates were further varied to describe this distinction between both main reaction paths with an identifiable parameter set. The tested networks are illustrated in Fig. 7.14. The obtained model-data fits are given in Tab. 7.7.

The continuous experiments differed from the batch experiments in two main aspects affecting the reaction kinetics: The presence of oxygen and an increased acid concentration. The model candidates shown so far only allowed for a distinction of the main active reaction path by the presence of oxygen. This model structure resulted in a high reaction rate estimated for the oxidation, which was limited solely by the mass transfer of oxygen into the liquid phase. The mass transfer coefficient could be increased to physically unrealistic numbers in Model 26, and still, the model-data fit improved. With the reaction network of Model 21, the experimental

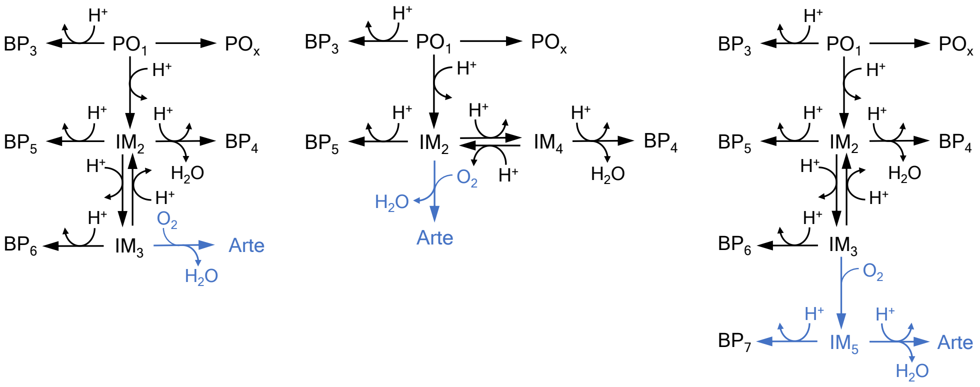

(a) Network B (b) Network C (c) Network D

Fig. 7.14: Extensions of the kinetic networks describing the conversion of IM_2 to achieve an identifiable discrimation between the pathway to BP_4 and Arte.

Tab. 7.7: Comparison of the model-data fits obtained with the adjusted network structures shown in Fig. 7.14 and varied reaction orders for TFA in the conversion of IM_2. The final model candidate is highlighted in grey and described in Fig. 7.15.

		TFA reaction order					SSE ,$mol^2\,L^{-2}$		
ID	Model specification	$IM_2 \rightarrow BP_4$	$IM_2 \rightarrow IM_{3/4}$	$IM_{3/4} \rightarrow IM_2$	N_p^{kin}	AIcc	Conti.	Batch	Total
1	Base	1	-	-	7	-4230	0.302	0.212	0.51
21	Base-A-IV+BP_6	1	-	-	8	-4895	0.081	0.088	0.17
26	Base-A-IV+BP_6 + $\widetilde{k_l a}$	1	-	-	9	-4905	0.073	0.086	0.159
27	Network B-IV	Var.	Var.	-	11	-4695	0.107	0.117	0.224
28	Network B-IV	1	1	0	9	-4634	0.134	0.115	0.249
29	Network C-IV	1	1	1	9	-4265	0.223	0.237	0.460
30	Network C-IV	1	Var.	Var.	11	-4847	0.081	0.093	0.174
31	Network D-IV	1	1	1	11	-4860	0.081	0.088	0.170
32	Network D-IV	Var.	1	1	13	-4892	0.074	0.086	0.160
33	Network D-IV	1	1	0	12	-4891	0.074	0.087	0.161
34	Separate sub-models	1	-	-	8	-4928	0.075	0.085	0.160

data were best described when IM_2 is instantaneously converted to IM_3 once oxygen is present, neglecting any mass transfer limitation.

As a consequence, the reaction network downstream of IM_2 was adjusted with the aim that the active reaction path is not only controlled by the presence of oxygen but also by the acid concentration (Fig. 7.14). The main changes were

- Introduction of a reversible reaction between IM_2 and IM_3 in Network B and D
- Setting the oxidation as the last step of the artemisinin formation in Network B and C
- Variation of the TFA reaction order of either the BP_4 formation or the reversible reaction of IM_2 to IM_3 in Network B and D or IM_4 in Network C.

The position of the oxidation in Network B and C added a significant constraint to the parameter estimation since the measured artemisinin concentration directly determined the oxidation rate. This direct coupling fixed the oxygen consumption to realistic rates. The added flexibility by a reversible conversion of IM_2 and varied reaction orders of TFA in the reactions converting IM_2 could not balance this initial constraint. The model-data fit was lower than obtained with the reference Model 21 for all tested model candidates with direct oxidation to artemisinin (27-30 in Tab. 7.7). Again, at least one parameter was unidentifiable in all tested model candidates of Network B and C.

Network D included a reversible conversion of IM_2 and another intermediate IM_5, which serves as a buffer between oxidation and artemisinin formation. The offered flexibility in the reaction network, together with a variable TFA reaction order in the BP_4 formation, improved the model-data fit for the Model candidate 31. An almost similar increase in the SSE was obtained by defining exclusively the forward reaction as acid-catalyzed but not the backward reaction to IM_2 in Model 33. However, both models could not describe the conversion of IM_2 with an identifiable set of parameters.

So far, the model candidates achieved the best description of the experimental data when the model structure allowed the formation of different intermediates in the presence and absence of oxygen. As a consequence of this observation, the kinetic model for the acid-catalyzed sequence starting from PO_1 was split into two separate sub-models describing either the batch experiments in the absence of oxygen or the continuous experiments in the presence of oxygen. The corresponding Model 34 achieves an equal model-data fit as Model 26 with neglected mass transfer limitation, and Model 32, which includes more parameters. Thus, it was selected as the final kinetic model and is explained in more detail in the following section.

7.2.3 Selected model candidate for the acid-catalyzed reaction sequence to artemisinin

The model selection showed that the differing formation rates of BP_4 in the batch and the continuous experiments could not be described by one joint model without compromising the constraints of the set parameter ranges. As a result, the kinetic model was split into two separate sub-models, as illustrated in Fig. 7.15. The two sub-models are only valid for either an oxygen-pure atmosphere (x_{O_2}=1) or oxygen-free conditions (x_{O_2}=0). Both models are equal in the description of the PO_1 decomposition, including variable reaction orders for TFA. If oxygen is present, the first model is applicable, which includes the reaction of the intermediate $IM_2^{O_2}$ to

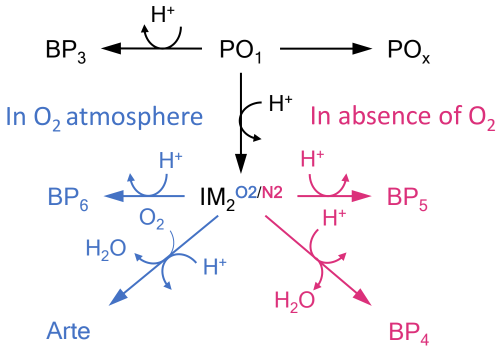

Fig. 7.15: Reaction network of the identified model for the acid-catalyzed reaction sequence starting from PO_1 to artemsinin. The model consists of two sub-models: The blue and red indicated paths are active in oxygen atmosphere (x_{O_2}=1) or in oxygen-free (x_{O_2}=0) atmosphere, respectively.

Tab. 7.8: Kinetic model for the acid-catalyzed sequence to artemisinin corresponding to the reactin network depicted in Fig. 7.15.

In the presence of O_2 $x_{O_2} = 1$	In the absence of O_2 $x_{O_2} = 0$
$[H^+] =$	$[\mathrm{TFA}]^0$
$r_{PO_x} =$	$k_{PO_x}[PO_1]$
$r_{PO_1,BP_3} =$	$k_{PO_1,BP_3}[H^+]^{n+1}[PO_1]$
$r_{PO_1,IM_2{}^{O_2}} = k_{PO_1,IM_2}[H^+]^n[PO_1]$	$r_{PO_1,IM_2{}^{N_2}} = k_{PO_1,IM_2}[H^+]^n[PO_1]$
$r_{IM_2{}^{O_2},Arte} = k_{IM_2{}^{O_2},Arte}[O_2][H^+][IM_2{}^{O_2}]$	$r_{IM_2{}^{N_2},BP_4} = k_{IM_2{}^{N_2},BP_4}[H^+][IM_2{}^{N_2}]$
$r_{IM_2{}^{O_2},BP_6} = k_{IM_2{}^{O_2},BP_6}[O_2][H^+][IM_2{}^{O_2}]$	$r_{IM_2{}^{N_2},BP_5} = k_{IM_2{}^{N_2},BP_5}[H^+][IM_2{}^{N_2}]$

artemisinin and the lumped byproduct species BP_6. The first model does not allow any formation of BP_4. In the absence of oxygen, the second model describes the conversion of the byproduct to BP_4 and a further lumped byproduct species BP_5. The rate equations of the proposed models for the acid-catalyzed sequence are given in Tab. 7.8.

The distinction between the sub-models corresponds to a reaction mechanism where the accumulating intermediate species differs depending on the composition of the gas phase. Therefore, the accumulating intermediate species is redefined as $IM_2{}^{O_2}$ and $IM_2{}^{N_2}$ in pure oxygen and an oxygen-free atmosphere, respectively. The kinetic parameters obtained by fitting the two joint models to the batch and the continuous data are listed in Tab. 7.9. The corresponding parity plots are shown in Fig. 7.16.

Comparing the results from the base model in Fig. 7.12 and the final model in Fig. 7.16 shows that the changes in the model structure achieved a strongly improved fit between measured and simulated data. The final model reproduces the conversion of PO_1, the formation of BP_3, and high concentrations of artemisinin at the end

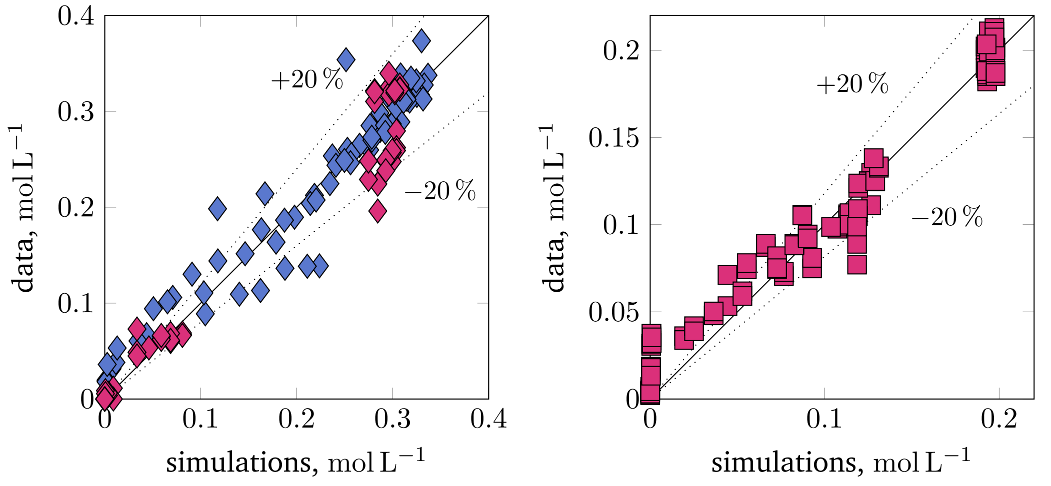

(a) PO_1 **(b)** Artemisinin

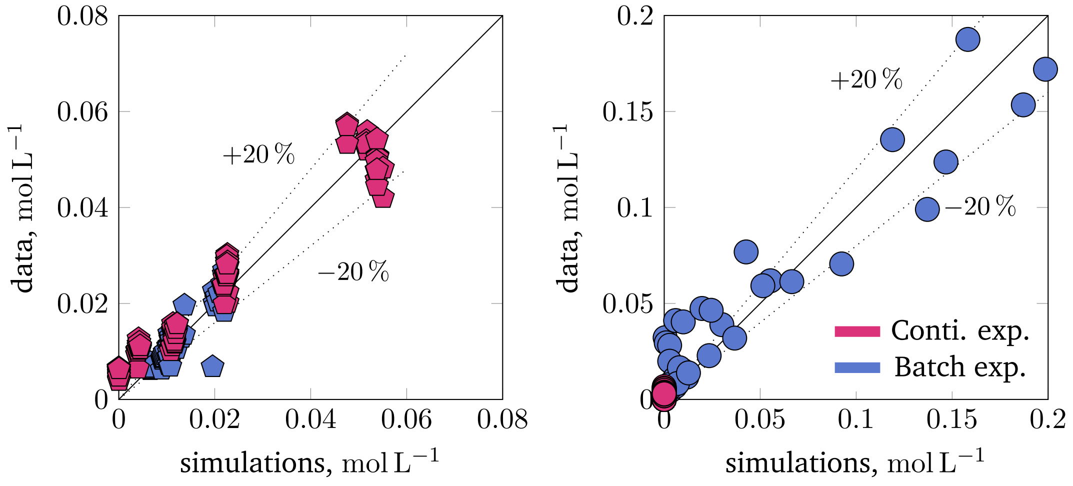

(c) BP_3 **(d)** BP_4

Fig. 7.16: Goodness of the model-data fit of the proposed kinetic model introduced in Fig. 7.15 and Tab. 7.8 describing the acid-catalyzed reaction sequence. The blue and red points indicate data from the batch and continuous experiments, respectively.

of the reaction. Applying the two separate sub-models instead of one joint model enabled a good description of the observed wide spread in BP_4 formation between continuous and batch experiments.

However, the model underestimates the artemisinin formation at the beginning of the reaction. The mean relative deviation between the experimental data and simulated artemisinin concentrations differing from zero is 14 %.

In model candidates with a joint description of artemisinin and BP_4 formation, the kinetic parameters for the distinction between the two paths approached the set upper bound for the corresponding parameter and thus were practically non-identifiable. By fitting two separate models instead, a complete set of eight identifiable parameters

Tab. 7.9: Kinetic parameters identified for the acid-catalyzed reaction sequence described by the equations in Tab. 7.8. The first subscript states the reactant and the second the product of the corresponding reaction. The parameters for the photooxygenation and reactor model are taken from Tab. 7.2.

model-data fit					
Symbol	unit	value	description		
SSE	$\mathrm{mol}^2/\mathrm{L}^2$	0.1600	sum of squared errors		
SSE_{conti}	$\mathrm{mol}^2/\mathrm{L}^2$	0.0748	SSE for continuous exp.		
SSE_{batch}	$\mathrm{mol}^2/\mathrm{L}^2$	0.0853	SSE for batch exp.		
$\hat{\sigma}^2$	$\mathrm{mol}^2/\mathrm{L}^2$	$2.66e-4$	measurement error variance		
	%	13.97	averaged relative deviation for Arte ([Arte]$>0.01\,\mathrm{M}$) †		
estimated parameters					
Symbol	unit	value	COD	CI_{95}^{-}	CI_{95}^{+}
$k_{\mathrm{PO_x}}$	$1/\mathrm{min}$	0.0105	0.161	0.0096	0.0113
n	-	2.646	0.013	2.629	2.664
$k_{\mathrm{PO_1,BP_3}}$	$(\mathrm{L\,mol^{-1}})^{n+1}\ \mathrm{min}^{-1}$	424.2	0.245	373.0	477.1
$k_{\mathrm{PO_1,IM_2}}$	$(\mathrm{L\,mol^{-1}})^{n}\ \mathrm{min}^{-1}$	880.3	0.112	833.2	931.6
$k_{\mathrm{IM_2{}^{N_2},BP_5}}$	$\mathrm{L\,mol^{-1}\,min^{-1}}$	0.0	-	-	-
$k_{\mathrm{IM_2{}^{O_2},BP_6}}$	$\mathrm{L\,mol^{-1}\,min^{-1}}$	0.682	0.206	0.614	0.755
$k_{\mathrm{IM_2{}^{N_2},BP_4}}$	$\mathrm{L\,mol^{-1}\,min^{-1}}$	0.887	0.290	0.770	1.026
$k_{\mathrm{IM_2{}^{O_2},Arte}}$	$(\mathrm{L\,mol^{-1}})^{2}\ \mathrm{min}^{-1}$	30.07	0.138	28.07	32.24
fixed parameters					
Symbol	unit	value	reference		
$\widetilde{k_l a}$	$\sqrt{1/\mathrm{cm\,min}}$	1.094	fixed to estimated value in the photoreactor		

†: $\left(\sum_i^{n_{\mathrm{PO_1}}} \left|(y_{\mathrm{PO_1},i}^{\mathrm{data}} - y_{\mathrm{PO_1},i})\right| / y_{\mathrm{PO_1},i}\right) / n_{\mathrm{PO_1}}$

COD: coefficient of dispersion, $COD = (CI_{95}^{+} - CI_{95}^{-})/\hat{\theta}$, $\hat{\theta}$: estimated value

$CI_{95}^{+/-}$: ±95 % confidence interval

is obtained (Tab. 7.9). The description of BP_4 formation in the batch experiments does not require the formation of a byproduct species. Thus, the number of kinetic parameters can be further reduced to seven. The good description of the reaction progress is based on reaction orders of TFA of 2.65 and 3.65 in the conversion of PO_1 to IM_2 and BP_3, respectively (Tab. 7.9). These large values emphasize that a linear dependence of the overall reaction rate on the acid concentration is unsuitable for describing the experimental data. Due to the incompletely elucidated product spectrum, empirical tools, such as the introduction of lumped species, fitted reaction orders, and the split into submodels specific to the experimental conditions, were

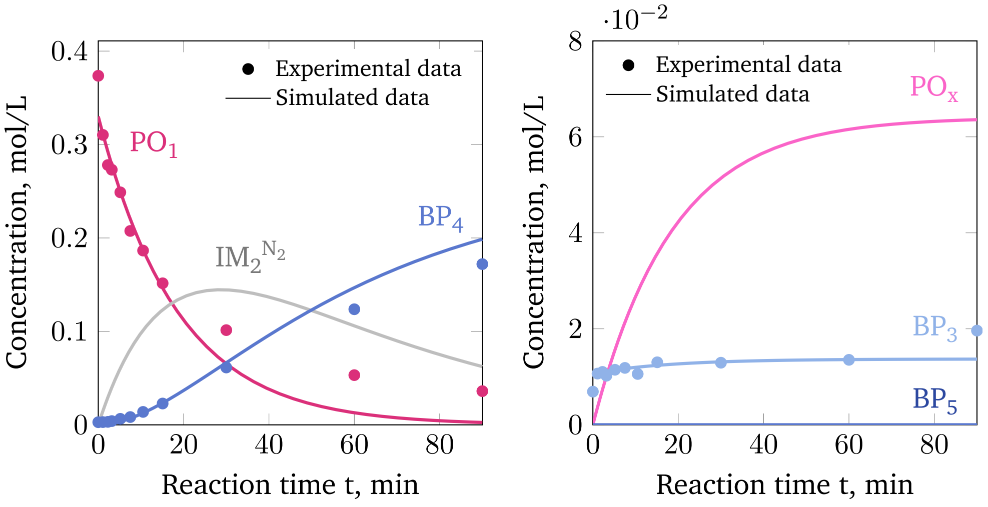

(a) Main species

(b) Byproducts

Fig. 7.17: Simulated concentration profiles of (a) the main species and (b) the byproducts of the acid-catalyzed reaction sequence described by the equations in Tab. 7.8. The reaction progress is shown after addition of $0.024\,\mathrm{M}$ TFA to a PO_1 containing solution in a batch experiment in nitrogen atmosphere.

required to describe the reaction kinetics. As a result of this semi-mechanistic approach, the final model describes experimental data exclusively within the tested set of conditions. The model should not be applied to settings varying from toluene as solvent, TFA as acidic catalyst, and gas phase compositions differing from either $x_{O_2} = 1$ or $x_{O_2} = 0$. For more details on the identifiability of the obtained parameters and a global sensitivity analysis of the overall model, the reader is referred to the thesis of Moritz Schulze [360].

The behavior of the acid-catalyzed reaction sequence predicted by the model is exemplified on a batch experiment and several continuous experiments in Figs. 7.17 and 7.18. The continuous data were obtained at a 10-fold increased TFA concentration in comparison to the batch data. Please note that Fig. 7.18 includes data in steady-state conditions at the reactor outlet depending on the theoretical residence time in the acid-catalyzed section. The discontinuities between the simulated data points arise from differences in the experimental conditions for each steady-state experiment, e.g. a varied residence time in the photoreactor.

In N_2 atmosphere, the hydroperoxide PO_1 reacts to $IM_2^{N_2}$, which is further converted to BP_4 as the main species (Fig. 7.17a). The only byproduct measured is BP_3, which is well described by the simulated data. According to the developed model, the main byproduct is PO_x which incorporates all unknown species formed directly from PO_1. Due to the considerable formation of PO_x, introducing a second byproduct species, BP_5, is not required to describe the BP_3 formation.

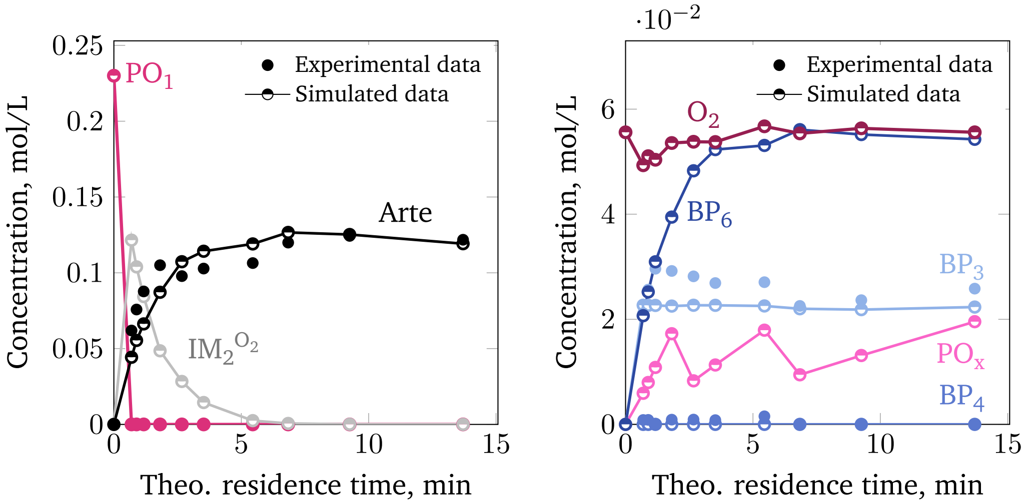

(a) Main species

(b) Byproducts

Fig. 7.18: Comparison of simulations and experimental results for continuous experiments with $0.25\,\mathrm{M}$ TFA in dependence on the set residence time in the acid-catalyzed reactor section. The data points plotted represent concentrations at the reactor outlet in steady state. Conditions: $[\mathrm{DHAA}]^0 = 0.25\,\mathrm{M}$, $p_{O_2} = 7\,\mathrm{bar}$, $T_{photo} = -20\,°\mathrm{C}$, $T_{2nd} = 20\,°\mathrm{C}$.

The PO_1 conversion is well matched at the beginning but is too fast in the late stage of the reaction. This overestimation of the reaction rate appears in all batch experiments. It arises from the large difference in the reaction rates observed with high and low TFA concentrations.

At the 10-fold acid concentration in the continuous experiments (Fig. 7.18), PO_1 is entirely converted in the acid-catalyzed section within one minute of residence time, which the model reproduces. Due to the fast PO_1 conversion, the byproduct PO_x is formed to a lesser extent depending mainly on the residence time in the upstream photoreactor.

Since oxygen is present in the continuous experiments, $IM_2^{O_2}$ accumulates and is converted to artemisinin as the main product. The reaction is not significantly limited by oxygen mass transfer from the gas to the liquid phase in these conditions (Fig. 7.18b). The model matches the artemisinin concentrations at the end of the reaction well but underestimates the rate of formation at the reaction start.

In the presence of oxygen, BP_4 formation is neglected by the model as observed in the experimental data (Fig. 7.18b). The main byproducts formed are BP_3 and BP_6, which was introduced to fill the discrepancy between the measured artemisinin, BP_3 and BP_4 concentrations and the initial PO_1 concentration.

In summary, the developed and parametrized model (Tabs. 7.8 and 7.9) can reproduce main characteristics of converting PO_1 into the known product species artemisinin, BP_3, and BP_4. However, the simulated data show significant deviations from the measured data, especially for small artemisinin concentrations and the PO_1 conversion at low acid concentrations. Improving the model-data fit requires further analytic insight into the reaction mechanism and elucidation of the formed intermediate species.

Before proposing further steps to obtain a more detailed kinetic model, a showcase is presented below, illustrating how the developed model can be used for reactor and experimental design.

7.3 Utilization of the model to identify mass transfer limited regimes

A kinetic model can aid in predicting suitable process conditions and reactor settings for the artemisinin partial synthesis. Limitation in the availability of oxygen, which results from high light intensity and slow mass transfer rates, can lead to reduced productivity of the reaction step.

These mass-transfer limited operation regimes can be predicted independent of the experimental setup based on the Hatta number Ha (Sec. 3.2.3), which relates the rate of chemical reaction in the liquid phase to the diffusion rate across the phase boundary [256, 321]. Increasing Hatta numbers represent higher reaction rates in comparison to diffusion, so that the chemical reaction takes place solely at the phase boundary. The Hatta number for the analysis of the partial synthesis is formulated based on the photooxygenation kinetics, since this reaction steps exhibits the higher reaction rates than the acid-catalyzed reaction sequence. Accordingly, the Hatta number is defined as

$$Ha = \frac{1}{k_\mathrm{l}} \sqrt{D_{\mathrm{O_2}} L_\mathrm{p}^\mathrm{a} \frac{1}{k_\mathrm{l1}[\mathrm{O_2}] + k_\mathrm{l2}} \frac{(\tilde{k}_{\mathrm{PO_1}} + \tilde{k}_{\mathrm{PO_y}})[\mathrm{DHAA}]}{1 + (\tilde{k}_{\mathrm{PO_1}} + \tilde{k}_{\mathrm{PO_y}})[\mathrm{DHAA}]}}. \tag{7.35}$$

The diffusion coefficient of oxygen in toluene is reported to be $2.4860 \times 10^{-9}\,\mathrm{m^2\,s^{-1}}$ at $-20\,^\circ\mathrm{C}$ [408]. The complete derivation of Eq. (7.35) is included in [387]. The limits of the Hatta regimes are drawn as contours in Fig. 7.19. As observed in Sec. 7.1.5, the conducted experiments, visualized as the grey rectangle, lie in intersection of the kinetic and partially mass transfer limited regime. This analyses aids in future kinetic studies to ensure experimental conditions were mass transfer limitation is excluded. For industrial reactor design this classification is essential in adjusting the irradiation conditions together with the flow pattern so that the reactor reaches optimal performance.

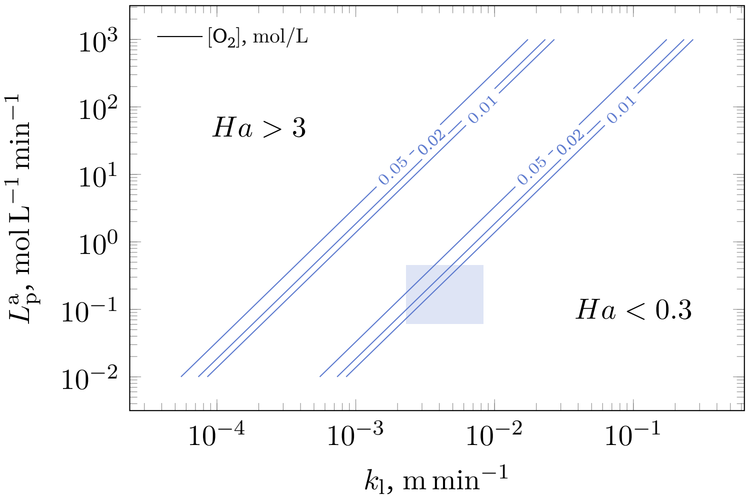

Fig. 7.19: Mass-transfer limited regimes for the partial synthesis of artemisinin starting from DHAA based on the Hatta number. Ha is estimated in dependence on the provided volumetric rate of photon absorption L_p and the mass transfer for different O_2 concentrations (contour lines, in $\mathrm{mol\,L^{-1}}$) and for DHAA $= 0.5\,\mathrm{mol\,L^{-1}}$. The blue rectangle approximates the experimental space investigated in this kinetic study.

7.4 Limitations, extensions, and transferability of the developed model

The developed model is based on several simplifications justified only for the chosen system of purified dihydroartemisinic acid in toluene catalyzed by 9,10-dicyanoanthracene and trifluoroacetic acid. The model is only valid at a temperature of $-20\,°\mathrm{C}$ and $20\,°\mathrm{C}$ in the photooxygenation and the acid-catalyzed reaction sequence, respectively. Application of the model for the acid-catalyzed reaction sequence is further limited to either a gas phase composition of pure oxygen or pure nitrogen.

To increase the predictive capability of the developed model, future investigations are required, especially for the acid-catalyzed reaction step. A complete elucidation of all reaction products and intermediates is crucial to achieve a widely applicable kinetic model. A second important step is the quantification of the water formation and phase separation during the reaction. When the underlying reaction mechanism is better understood, the model can be extended to include the temperature dependency. The reaction temperature influences all aspects of the process from transfer phenomena, flow conditions, and reaction kinetics. The challenge is to identify the quantities most affected by temperature to limit the number of parameters to be estimated.

When applied to the partial synthesis in crude extract, the model needs to be adjusted considering chlorophyll as photosensitizer and the presence of other co-extracts during the partial synthesis. Since the photosensitizer solely affects the formation of singlet oxygen and light absorption, only the quantum yield relation and the absorption coefficient need to be substituted. The absorption coefficients of the chlorophyll species in toluene are included in App. B.3. The singlet oxygen quantum yield of chlorophyll in toluene and benzene was reported to be in the range of 0.5 to 0.6 [409, 410]. When irradiated, however, chlorophyll undergoes significant photobleaching. Thus, including catalyst deactivation into the model is crucial to describe the overall photooxygenation behavior in the extract.

The impurities in the extract can affect both the photooxygenation and the acid-catalyzed sequence. At high DHAA concentrations, the effect on the reaction performance is negligible, as shown in Sec. 5.1. With decreasing DHAA initial concentration, the other components in the extract have an increasingly adverse effect on the observed artemisinin yield (Sec 6.4). Since the main species interfering with the partial synthesis are unknown and hard to identify, a first-principle-based approach to describe this effect is difficult. Alternatively, the decrease in selectivity can be related directly to the total solid content of the extract. However, this approach is limited to a specific extract source and requires reparametrization once the leaf source or the extraction conditions change.

7.5 Conclusion

Designing and optimizing the integration of the artemisinin partial synthesis into the overall process chain for both the semi-synthetic or extraction-based production requires a simple but sufficiently accurate kinetic model to facilitate model-based process optimization. The development of a widely applicable model, however, is especially difficult for the artemisinin partial synthesis due to the limitation by photon and oxygen supply and a not completely elucidated product spectrum. Decoupling of the photooxygenation and the acid-catalyzed sequence enabled a separated analysis of the different facets of complexity.

The photooxygenation model achieves a good fit between the model outputs and the experimental results from steady-state experiments for a wide range of different critical process parameters. The formation of the main intermediate PO_1 could be reproduced with a mean relative deviation of $7.6\,\%$. The made assumptions and the simplifications, including the two-fluid model, provide a suitable description for the main process characteristics of the photooxygenation. Nevertheless, assuming a spatially independent rate of photon absorption within the reactor is a strong simplification of the reaction system applied, considering its geometrical complexity and the large value obtained for the average path length. By analyzing the process behavior, different regimes of operation were identified where the process is limited by either the absorbed photon flux, substrate concentration, or mass transfer.

The model developed for the photooxygenation was used as a fixed building block in studying the acid-catalyzed sequence yielding artemisinin. Depending on the reaction progress, $24\,\%$ to $76\,\%$ of the reaction products formed in this step could be quantified. The analysis of the different postulated reaction networks showed that a purely linear dependence of the reaction rates on the present acid concentration is not sufficient to describe the experimental data. Only models could reproduce the measured concentration profiles, which contained either higher reaction orders regarding TFA or included reaction pathways with temporary H^+ consumption.

The model with the best model-data fit includes reaction orders higher than two regarding TFA and considers separate intermediates for the artemisinin formation in the presence of oxygen and the BP_4 formation in the absence of O_2. The parametrized model represents a good semi-mechanistic description of the acid-catalyzed reaction sequence in toluene at $20\,°C$ with a mean relative deviation for artemisinin of $14\,\%$. Due to its potential to describe the main process characteristics, the developed model and its estimated parameters are seen as an essential building block in optimizing the whole process chain from extraction to artemisinin purification.

8

Economic evaluation of integrating the partial synthesis in plant-based artemisinin production

In the previous chapters, it was demonstrated that co-extracted dihydroartemisinic acid can be converted easily to artemisinin by treating the crude extract at ambient temperature with intensive blue light, trifluoroacetic acid, and pressurized air. The process is technologically simple but consumes trifluoroacetic acid as catalyst, a base as quenching agent, and electrical power for operating the LED lamps and pumps. The added value of synthesized artemisinin needs to exceed the operating costs so that the reaction step improves the cost-efficiency of the overall plant-based artemisinin production. This question will be addressed by identifying the main cost driver and defining a feasibility region with a minimal DHAA content and a minimal artemisinin price.

The cost estimation described in this chapter focuses on the operating costs related to the reaction step. Capital investment costs and the operating costs of the upstream extraction and downstream purification unit are not included in the analysis. The calculations are based on the assumption that the reaction step neither affects the extraction nor the purification of artemisinin. The cost estimation involves the streams specific to the reaction step, e.g., TFA streams, but excludes components intrinsic to the overall process as the feed streams for toluene and *A. annua* leaves. The solvent removal after the extraction was not attributed to the reaction step since it is required for the final purification and split only into two parts by integrating the reaction step. Fig. 8.1 summarizes the boundaries set and the assumptions made.

The cost estimation was performed for the lab-scale process and did not cover scale-up related uncertainties regarding energy consumption. Photoreactions are often scaled up by numbering up parallel reactor channels and increasing the required lighting power [241, 244, 261]. Thus, the relation between costs due to chemical and power consumption does not tend to change significantly with scale for this type of reaction. Since the applied reactor setup (Sec. 4.1) is not optimized for energy-efficiency, the estimated costs for power consumption pose an upper estimate

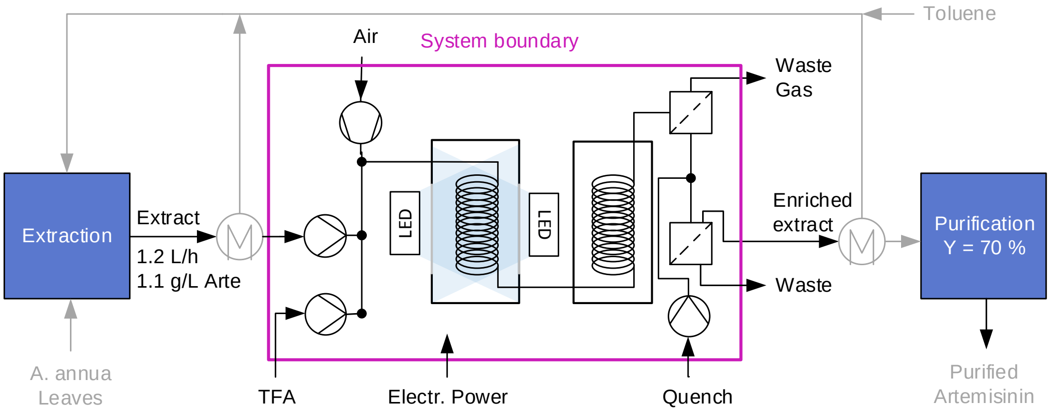

Fig. 8.1: Streams and components included in the cost estimation to analyze the economic viability of the artemisinin partial synthesis as an additional unit between extraction and purification.

for the operating costs of an industrial process at a larger scale.

In accordance with the experimental conditions, the calculations are based on a specific extract stream of $1.2\,\mathrm{L\,h^{-1}}$ exiting the extraction unit, the maximum amount processable with the existing lab setup (Sec. 6.5). The artemisinin concentration in the extract was set constant to $1.1\,\mathrm{g\,L^{-1}}$, while the DHAA concentration was varied up to the previously set boundary of $2\,\mathrm{g\,L^{-1}}$.

The economic feasibility of a process can be assessed by the net economic potential (NEP) [411]. The NEP is calculated by balancing the gross economic potential (GEP) with the operating costs C_{OPEX}.

$$NEP = GEP - C_{OPEX} \tag{8.1}$$

The GEP of the process extension is equal to the value of purified artemisinin additionally gained by converting co-extracted DHAA. The GEP depends primarily on the DHAA content in the extract and the price artemisinin is sold at. The DHAA initial concentration affects both the absolute amount of artemisinin obtainable and the partial synthesis artemisinin yield (Sec. 6.4).The yield of purifying artemisinin from the extract $\mathrm{Y_{pur}}$ was set to $70\,\%$, corresponding to a conventional multi-step purification by adsorption and crystallization [25].

The operating costs comprise the costs for TFA addition, quenching, and electrical power consumption for operating the pumps, the compressor, and LED modules. Details on the calculations, the power consumption of the applied equipment, the set concentrations, and the prices for chemicals and electricity are given in App. H. The NEP, the GEP, and the operating cost are related to the volume of extract treated. The lab-scale reactor equipment used in this work can process $9648\,\mathrm{L}$ of crude extract per year, assuming an 8040-hour-working year. Purification of the extracted

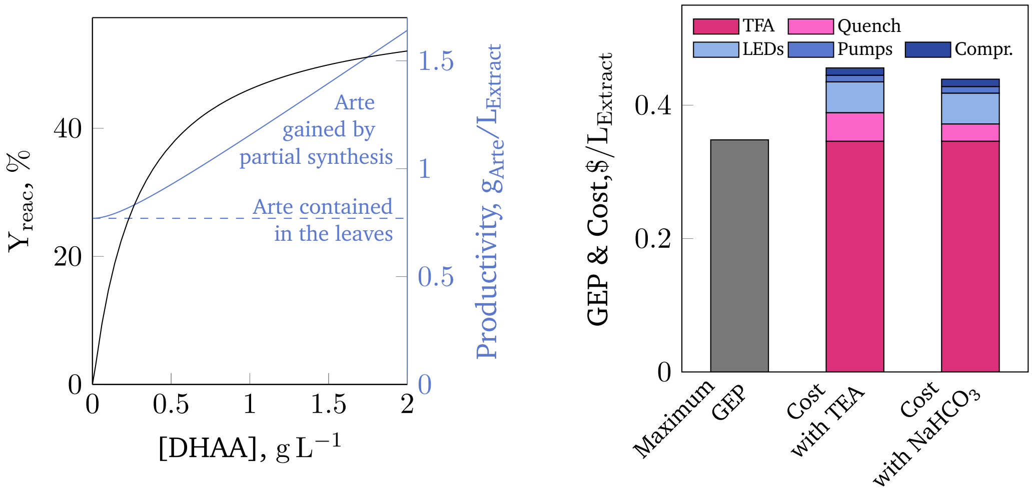

(a) Yield and artemisinin amount gained from the partial synthesis

(b) GEP and operational costs

Fig. 8.2: Comparison of the artemisinin amount gained by coupling the partial synthesis with the extraction and the additional costs related to the reaction step: a) Effect of the initial DHAA concentration in the crude extract on the partial synthesis yield and the resulting artemisinin amount obtained per liter extract after purification, b) Break down of the operating costs related to power consumption, TFA consumption, and quenching by triethylamine (TEA) or aq. NaHCO$_3$ compared to the maximum gross economic potential (Arte Price:$400\,\$/\mathrm{kg}$, [DHAA]^0= $2\,\mathrm{g}/\mathrm{L}_{\mathrm{Extract}}$, Assumed electricity price: $0.1\,\$/\mathrm{kWh}$).

artemisinin without partial synthesis results in an annual artemisinin production of $7.4\,\mathrm{kg}$, equal to $0.77\,\mathrm{g}/\mathrm{L}_{\mathrm{Extract}}$. Fig. 8.2a shows how this productivity of purified artemisinin can be increased by integrating the partial synthesis in the process. At a DHAA concentration in the extract of $1\,\mathrm{g}/\mathrm{L}_{\mathrm{Extract}}$, the obtained artemisinin amount can be enhanced by $50\,\%$. The increase is more than twofold for a DHAA content of $1.8\,\mathrm{g}/\mathrm{L}_{\mathrm{Extract}}$. At low DHAA concentrations in the extract, the partial synthesis achieves only a minor improvement in productivity due to the reduced yield in the synthesis.

For an artemisinin price of $400\,\$/\mathrm{kg}$ [31], the additionally synthesized amount of artemisinin results in a gross economic potential of $0.35\,\$/\mathrm{L}_{\mathrm{Extract}}$. Fig. 8.2b compares this maximum GEP with the operating costs when using triethylamine (TEA) or NaHCO$_3$ as quenching agent. It is shown that aqueous sodium bicarbonate is more cost-efficient than TEA. However, the main cost driver is the consumption of TFA, accounting for more than $76\,\%$ of the overall operational costs, while the accumulated power consumption makes up $15\,\%$. The estimated operating costs exceed the GEP by at least $20\,\%$.

Therefore, the costs caused by the acid consumption need to be drastically reduced to achieve an economically feasible process. The simplest option is to lower the dosed TFA concentration and compensate for the decreased reaction rate with more residence time and, thus, reactor volume. The next step is to recycle TFA after the reaction step without prior quenching, e.g., by distillation of TFA from the toluene-based extract. The recycling requires additional energy consumption and processing of highly concentrated and corrosive acid.

Alternatively, TFA can be substituted by cheaper acids or heterogeneous acidic catalysts, as discussed in Sec. 5.3. The application of solid acids eliminates the costs for homogeneous acids and reduces the challenges related to corrosion and acidic waste treatment. However, the heterogeneous catalyst needs to be replaced or regenerated regularly, generating additional costs.

The economic feasibility of all these proposed alternatives depends on the specific acidic material used, the method of recycling or regeneration, and the produced waste streams. Estimating these operating costs need further experimental studies, especially on the deactivation and regeneration of potential heterogeneous acidic catalysts.

Neglecting the costs for the acidic catalyst, including quenching, poses an upper bound of the economic feasibility. This scenario corresponds to applying a heterogeneous acidic catalyst that does not undergo any deactivation. The energy required to power the pumps, compressor, and LEDs is the only operating cost driver remaining. In this case, the economic feasibility is determined mainly by the price for electrical power P_{Elec} and the expected GEP, specifically the initial DHAA concentration in the extract and the artemisinin price. In Fig. 8.3, each line marks the limit of the economic feasibility with $NEP = 0$ at a specific price for electricity. At an average electricity price for industry in Germany of $0.10\,\$/\mathrm{kWh}$ in 2021 [412], a minimum DHAA content in the extract of $0.5\,\mathrm{g}/\mathrm{L}_{\mathrm{Extract}}$ is required to balance the operational costs. For the target price of artemisinin of $100\,\$/\mathrm{kg}$ [24, 31], the extract must contain a DHAA concentration of at least $1.45\,\mathrm{g}/\mathrm{L}_{\mathrm{extract}}$ to obtain a feasible process. With the immense increase electricity prices in 2022 in Germany up to $0.58\,\$/\mathrm{kWh}$ [413], feasible operation of the partial synthesis is not anymore possible.

Operating the LED modules contributes to $67\,\%$ of the costs for electrical power. The current cost evaluation is performed for a lab-scale setup, which is not optimized regarding energy-efficiency. Therefore, improving the illumination within the reactor is crucial to broaden the economically feasible range of the partial synthesis. Two feasible approaches are the improvement of the photonic efficiency [222, 263] in the reactor and the use of solar light instead of LEDs [247, 414, 415]. Due to the pre-optimized absorption of chlorophyll in the visible spectrum, solar light is best suited to initiate the partial synthesis. However, the reactor concept needs to be adapted to the low and variable intensity of natural light [247, 416–418].

The operating cost estimation presented here shows that the acidic catalyst is the

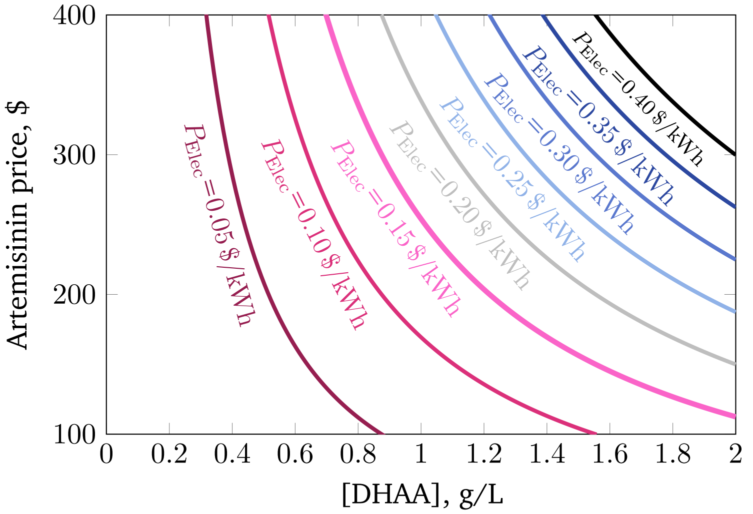

Fig. 8.3: Feasibility range of integrating the partial synthesis in the extraction-based production in dependence on the artemisinin price, DHAA content in the extract, and the price for electricity $\mathrm{P_{elec}}$. Each line indicates the boundary of feasible operation with $NEP = 0$ (Eq. (8.1)). No cost is attributed to adding and quenching the acidic catalyst.

main cost driver in integrating the partial synthesis in the extract-based production of artemisinin. An economically feasible process can only be achieved if TFA is either fully recovered or substituted by cheaper alternatives, e.g., by applying heterogeneous catalysts. Under this condition, the power consumption by the light source is the next limiting factor.

9

Conclusion

To ensure the constant availability of the currently most-active anti-malaria medications, a cost-efficient and simple production process for the base compound artemisinin is crucial. This natural product is primarily produced by extraction from its natural source, the plant *Artemisia annua L.*. Utilization of the late-stage precursor dihydroartemisinic acid (DHAA) is a promising option to increase the amount of artemisinin obtained by plant-based artemisinin production. *A.annua* can accumulate DHAA in up to the doubled concentration compared to artemisinin. In the presence of singlet oxygen and acid, DHAA reacts stereoselectively to artemisinin in high yields. The conversion of DHAA requires a photosensitizer for singlet oxygen formation, a strong acid, e.g., trifluoroacetic acid, intense reactions conditions with sufficient oxygen supply, strong irradiation, and low temperatures during the initial photooxygenation to ensure selective artemisinin formation. In previous investigations, this partial synthesis was well-established with highly concentrated, purified reagents for semi-synthetic artemisinin production.

In this thesis, a process was developed to convert DHAA co-extracted from the plant to additional artemisinin using directly the plant extract as the feed.

The extract differs from the reaction media used in the previous studies of the semi-synthetic artemisinin production mainly by the 50-fold reduced DHAA initial concentration and the presence of other co-extracted metabolites exceeding the amount of DHAA at least two-fold. Among the co-extracted impurities, chlorophylls are present and act as potent photosensitizers that enable similar photooxygenation performance as purified reagents. This activity eliminates the need for additional photosensitizers and, thus, increases the safety, viability and sustainability of the overall process. It should be noted that crude chlorophyll, a widely available, non-toxic, and highly reactive dye with strong and broad absorption in the visible range, is an attractive photosensitizer for other reactions as well.

Heterogenous acids showed great potential to substitute trifluoroacetic acid as acidic catalyst for the final conversion of the formed intermediate hydroperoxide to artemisinin. From the set of commercially available solid acids, an H-β-zeolite (Si/Al=360:1) and DOWEX 50-WX8 were identified as the best candidates. However, the spacial decoupling of both reaction steps using a photoreactor connected with a downstream packed-bed reactor led to an overall reduced selectivity to artemisinin.

For the conditions tested, the solid acids considered did not achieve a comparable reaction performance as TFA. For detailed studies, co-extracted chlorophyll and TFA were chosen as catalysts for the conversion of co-extracted DHAA in the extract.

The reaction step could be further simplified by switching to milder reaction conditions and lower acid concentrations. In the final process, co-extracted DHAA is converted to artemisinin by processing the crude plant extract at ambient temperature with pressurized air, visible light, and $0.0625\,\mathrm{M}$ trifluoroacetic acid. A total residence time of $6.5\,\mathrm{min}$ was sufficient to achieve a final artemisinin yield of $40\,\%$ to $50\,\%$ when starting from the upper limit for the DHAA concentration in the extract. The artemisinin yield decreases with a decreasing DHAA initial concentration and an increasing amount of byproducts present. The developed process is robust to changes in the leaf source and compatible with advanced continuous counter-current extraction. With the existing reactor setup, the process was upscaled to process $1.2\,\mathrm{L\,h^{-1}}$ of extract by optimizing the extract pretreatment and the flow composition. Due to the simplicity and robustness of the process, the reaction step can be well integrated into extraction-based processes without requiring major adjustments of the extraction or the purification steps.

To facilitate model-based optimization of the whole process chain, a semi-mechanistic model for the partial synthesis of artemisinin was developed in collaboration with Moritz Schulze from TU Braunschweig based on experiments with purified reagents. The developed set of model-equations considers mass transfer, photon transfer, the flow conditions, and the reaction kinetics based on simplified approaches. The parameterized model for the photooxygenation and the photon flow reactor describes the formation of the intermediate PO_1 with a deviation of $7.5\,\%$.

It could be shown that the description of the acid-catalyzed reaction sequence requires a model structure with a non-linear dependence on the acid concentration with different intermediates accumulating in the presence and the absence of oxygen. The best model candidate identified includes variable reaction orders for TFA and the formation of a lumped byproduct species after the second oxidation. These structural features resulted in a good model-data fit with a mean deviation of $14\,\%$ for artemisinin concentrations higher than $0.01\,\mathrm{M}$. However, systematic deviations were observed for the midsection of the reaction, with almost complete conversion of PO_1 but low formation of the main products artemisinin and BP_4.

In summary, coupling the extraction of *Artemisia annua* leaves with the artemisinin partial synthesis can increase the artemisinin amount obtained from the plant up to two-fold simply by treating the extract with acid, air, and visible light. The developed kinetic model serves as a valuable tool in optimizing the whole process chain for plant-based and also for semi-synthetic artemisinin production.

Outlook

10

Successful industrial application of integrating the artemisinin partial synthesis in the extraction-based production process benefits from further research in three main directions: Improving the understanding of the reaction mechanism, optimizing the reaction step regarding acid utilization, and coupling of extraction and partial synthesis with the purification.

A better insight into the reaction mechanism is essential to identify bottlenecks in the formation of artemisinin. Most importantly, the formed unknown intermediates and byproducts need to be identified. This challenge necessitates studying the reaction *in situ* with advanced analytical methods to exclude effects of sample workup and quenching on the product solution. In addition, the water concentration during the synthesis needs to be quantified to describe the effect of water on the reaction behavior. Once the product solution is entirely characterized, the kinetic model developed in this work can be adjusted and extended to cover a broader range of reaction conditions, e.g., higher reaction temperatures and the presence of impurities. Developing a more detailed reaction mechanism will be also beneficial in optimizing the acid concentration to achieve a high artemisinin selectivity.

The addition of the acidic catalyst was identified as a major cost driver for the production process. In the case of applying trifluoroacetic acid, a process for TFA recycling needs to be developed to make the process economically feasible. Alternatively, heterogeneous acids can be applied, which do not need an additional separation step after the reaction. To obtain comparable results with the homogenous case, the immobilization of the acidic material in the reaction line needs to be optimized together with the flow pattern to avoid by mass transfer limitation.

The extract can be contacted with the heterogeneous acid within the photoreactor by applying reactor designs well-known in heterogeneous photocatalysis. Alternatively, the extract can enter illuminated and acid-catalyzed sections alternately so that the intermediate hydroperoxide does not accumulate while at the same time using established reactor designs. The optimal design of such reactors requires a better understanding of adsorption processes occurring within the reactor, the effect of the solid acid's surface properties on the reaction mechanism, and the deactivation of the catalyst. The chosen catalyst and reactor design must be robust regarding the observed formation of gel-like films during irradiation.

If solid acids are not applicable for processing the extract, TFA can be potentially substituted with cheaper homogeneous alternatives, e.g., inorganic acids. This option requires also a change in the process solvent from toluene to a polar solvent as ethanol [208].

The optimized reaction step needs to be coupled with both the extraction and the downstream purification to demonstrate that the integration in extraction facilities is feasible. A preliminary study showed that the crystallization of artemisinin in the extract-based effluent of the partial synthesis is not affected by the reaction byproducts when starting with high DHAA initial concentrations [215]. Further investigations need to prove that this crystallization process is applicable for the 50-fold lower natural DHAA content in the extract.

Finally, the feasibility of the coupled process from extraction, partial synthesis, and purification needs to be confirmed for different leaf sources. The previous analysis revealed that the integration of the partial synthesis in the extraction-based processing is only viable for leaves with a high DHAA content, e.g., specific *A. annua* strains and fresh or freeze-dried leaves. The different metabolite profiles in the leaves and the changes caused by the drying process might result in a promoted extraction of other metabolites affecting the performance in all process units.

Bibliography

[1] David J. Newman and Gordon M. Cragg. “Natural Products as Sources of New Drugs over the Nearly Four Decades from 01/1981 to 09/2019”. In: *Journal of Natural Products* 83.3 (2020), pp. 770–803. DOI: `10.1021/acs.jnatprod.9b01285`.

[2] Benjamin J. Huffman and Ryan A. Shenvi. “Natural Products in the "Marketplace": Interfacing Synthesis and Biology”. In: *Journal of the American Chemical Society* 141.8 (2019), pp. 3332–3346.

[3] Atanas G. Atanasov, Birgit Waltenberger, Eva-Maria Pferschy-Wenzig, Thomas Linder, Christoph Wawrosch, et al. “Discovery and resupply of pharmacologically active plant-derived natural products: A review”. In: *Biotechnology Advances* 33.8 (2015), pp. 1582–1614. DOI: `10.1016/j.biotechadv.2015.08.001`.

[4] Youyou Tu. “The discovery of artemisinin (qinghaosu) and gifts from Chinese medicine”. In: *Nature Medicine* 17.10 (2011), pp. 1217–1220. DOI: `10.1038/nm.2471`.

[5] Youyou Tu. “Artemisinin - A Gift from Traditional Chinese Medicine to the World (Nobel Lecture)”. In: *Angewandte Chemie (Int. ed.)* 55.35 (2016), pp. 10210–10226. DOI: `10.1002/anie.201601967`.

[6] Youyou Tu. *From Artemisia annua L. to Artemisinins: The discovery and development of Artemisinins and antimalarial agents*. London: Academic Press, 2017. ISBN: 9780128116562.

[7] Guoqiao Li, Ying Li, Zelin Li, and Meiyi Zeng, eds. *Artemisinin-Based and Other Antimalarials: Detailed Account of Studies by Chinese Scientists Who Discovered and Developed Them*. San Diego: Elsevier Science & Technology, 2017. ISBN: 9780128131336.

[8] Liwang Cui and Xin-zhuan Su. “Discovery, mechanisms of action and combination therapy of artemisinin”. In: *Expert Review of Anti-infective Therapy* 7.8 (2009), pp. 999–1013. DOI: `10.1586/eri.09.68`.

[9] Global Malaria Programme. “World malaria report 2021”. In: *World Health Organization* (6/12/2021). URL: `https://www.who.int/publications/i/item/9789240040496` (visited on Dec. 21, 2021).

[10] WHO Global Malaria Programme. “WHO Guidelines for malaria”. In: *World Health Organization* (13/07/2021). URL: `https://www.who.int/publications/i/item/guidelines-for-malaria` (visited on Dec. 22, 2021).

[11] Mohit K. Tiwari and Sandeep Chaudhary. “Artemisinin-derived antimalarial endoperoxides from bench-side to bed-side: Chronological advancements and future challenges”. In: *Medicinal research reviews* 40.4 (2020), pp. 1220–1275.

[12] Thomas Efferth. “Molecular pharmacology and pharmacogenomics of artemisinin and its derivatives in cancer cells”. In: *Current drug targets* 7.4 (2006), pp. 407–421. DOI: `10.2174/138945006776359412`.

[13] Henry C. Lai, Narendra P. Singh, and Tomikazu Sasaki. “Development of artemisinin compounds for cancer treatment”. In: *Investigational new drugs* 31.1 (2013), pp. 230–246. DOI: `10.1007/s10637-012-9873-z`.

[14] Bushra Hafeez Kiani, Waqas Khan Kayani, Asma Umer Khayam, Erum Dilshad, Hammad Ismail, et al. “Artemisinin and its derivatives: a promising cancer therapy”. In: *Molecular biology reports* 47.8 (2020), pp. 6321–6336. DOI: `10.1007/s11033-020-05669-z`.

[15] Pitambar Khanal. “Antimalarial and anticancer properties of artesunate and other artemisinins: current development”. In: *Monatshefte für Chemie* (2021), pp. 1–14. DOI: `10.1007/s00706-021-02759-x`.

[16] Thomas Efferth, Marta R. Romero, Dana G. Wolf, Thomas Stamminger, Jose J. G. Marin, et al. “The antiviral activities of artemisinin and artesunate”. In: *Clinical infectious diseases* 47.6 (2008), pp. 804–811. DOI: `10.1086/591195`.

[17] Mathieu Gendrot, Isabelle Duflot, Manon Boxberger, Océane Delandre, Priscilla Jardot, et al. “Antimalarial artemisinin-based combination therapies (ACT) and COVID-19 in Africa: In vitro inhibition of SARS-CoV-2 replication by mefloquine-artesunate”. In: *International journal of infectious diseases* 99 (2020), pp. 437–440. DOI: `10.1016/j.ijid.2020.08.032`.

[18] Yuyong Zhou, Kerry Gilmore, Santseharay Ramirez, Eva Settels, Karen A. Gammeltoft, et al. “In vitro efficacy of artemisinin-based treatments against SARS-CoV-2”. In: *Scientific Reports* 11.1 (2021). DOI: `10.1038/s41598-021-93361-y`.

[19] Chuanxiong Nie, Jakob Trimpert, Sooyeon Moon, Rainer Haag, Kerry Gilmore, et al. “In vitro efficacy of Artemisia extracts against SARS-CoV-2”. In: *Virology Journal* 18.1 (2021). DOI: `10.1186/s12985-021-01651-8`.

[20] J. Utzinger, X. Shu-Hua, M. Tanner, and J. Keiser. “Artemisinins for schistosomiasis and beyond”. In: *Current Opinion in Investigational Drugs* 8.2 (2007), pp. 105–116.

[21] Sanjeev Krishna, Leyla Bustamante, Richard K. Haynes, and Henry M. Staines. “Artemisinins: their growing importance in medicine”. In: *Trends in pharmacological sciences* 29.10 (2008), pp. 520–527. DOI: `10.1016/j.tips.2008.07.004`.

[22] Seokjoon Lee. “Artemisinin, promising lead natural product for various drug developments”. In: *Mini reviews in medicinal chemistry* 7.4 (2007), pp. 411–422. DOI: `10.2174/138955707780363837`.

[23] Hikaru G. Jolliffe and Dimitrios I. Gerogiorgis. “Process modelling and simulation for continuous pharmaceutical manufacturing of artemisinin”. In: *Chemical Engineering Research and Design* 112 (2016), pp. 310–325. DOI: `10.1016/j.cherd.2016.02.017`.

[24] Burak Kazaz, Scott Webster, and Prashant Yadav. “Interventions for an Artemisinin-Based Malaria Medicine Supply Chain”. In: *Production and Operations Management* 25.9 (2016), pp. 1576–1600. DOI: `10.1111/poms.12574`.

[25] Alexei Lapkin, Eba Adou, Benhilda N. Mlambo, Smain Chemat, John Suberu, et al. “Integrating medicinal plants extraction into a high-value biorefinery: An example of Artemisia annua L”. In: *Comptes Rendus Chimie* 17.3 (2014), pp. 232–241. DOI: `10.1016/j.crci.2013.10.023`.

[26] Mark Peplow. “Synthetic biology’s first malaria drug meets market resistance”. In: *Nature* 530.7591 (2016), pp. 389–390. DOI: `10.1038/530390a`.

[27] Dae-Kyun Ro, Eric M. Paradise, Mario Ouellet, Karl J. Fisher, Karyn L. Newman, et al. “Production of the Antimalarial Drug Precursor Artemisinic Acid in Engineered Yeast”. In: *Nature* 440.7086 (2006), pp. 940–943. DOI: `10.1038/nature04640`.

[28] C. J. Paddon, P. J. Westfall, D. J. Pitera, K. Benjamin, K. Fisher, et al. “High-level semi-synthetic production of the potent antimalarial artemisinin”. In: *Nature* 496.7446 (2013), pp. 528–532. DOI: `10.1038/nature12051`.

[29] Joël Turconi, Frédéric Griolet, Ronan Guevel, Gilles Oddon, Roberto Villa, et al. “Semisynthetic Artemisinin, the Chemical Path to Industrial Production”. In: *Organic Process Research & Development* 18.3 (2014), pp. 417–422. DOI: `10.1021/op4003196`.

[30] Andreas Burgard, Tile Gieshoff, Alexander Peschl, Dirk Hörstermann, Claus Keleschovsky, et al. “Optimisation of the photochemical oxidation step in the industrial synthesis of artemisinin”. In: *Chemical Engineering Journal* 294 (2016), pp. 83–96. DOI: `10.1016/j.cej.2016.02.085`.

[31] Mark Peplow. “Looking for Cheaper Routes to Malaria Medicines”. In: *Chemical & Engineering News* (2018). URL: `https://cen.acs.org/articles/96/i11/Looking-cheaper-routes-malaria-medicines.html` (visited on Dec. 22, 2021).

[32] Jorge F. S. Ferreira, Vagner A. Benedito, Devinder Sandhu, José A. Marchese, and Shuoqian Liu. “Seasonal and Differential Sesquiterpene Accumulation in Artemisia annua Suggest Selection Based on Both Artemisinin and Dihydroartemisinic Acid may Increase Artemisinin in planta”. In: *Frontiers in Plant Science* 9 (2018), p. 1096. DOI: `10.3389/fpls.2018.01096`.

[33] Merlin Willcox, Gerard Bodeker, Geneviève Bourdy, Vikas Dhigra, Jacques Falquet, et al. “Artemisia annua as a Traditional Herbal Antimalarial”. In: *Traditional medicinal plants and malaria*. Ed. by Gerard Bodeker, Merlin Willcox, and Philippe Rasanavo. Traditional herbal medicines for modern times. Boca Raton: CRC Press, 2004, pp. 43–59. ISBN: 0415301122.

[34] J. C. Laughlin. “Post-Harvest Drying Treatment Effects on Antimalarial Constituents of Artemisia Annua L”. In: *Acta Horticulturae* 576 (2002), pp. 315–320. DOI: `10.17660/ActaHortic.2002.576.47`.

[35] Stephen O. Duke and Rex N. Paul. “Development and Fine Structure of the Glandular Trichomes of Artemisia annua L”. In: *International Journal of Plant Sciences* 154.1 (1993), pp. 107–118. DOI: `10.1086/297096`.

[36] Mary V. Duke, Rex N. Paul, Hala N. ElSohly, George Sturtz, and Stephen O. Duke. “Localization of Artemisinin and Artemisitene in Foliar Tissues of Glanded and Glandless Biotypes of Artemisia annua L”. In: *International Journal of Plant Sciences* 155.3 (1994), pp. 365–372. DOI: `10.1086/297173`.

[37] Rika Judd, M. Caleb Bagley, Mingzhuo Li, Yue Zhu, Caiyan Lei, et al. “Artemisinin Biosynthesis in Non-glandular Trichome Cells of Artemisia annua”. In: *Molecular Plant* 12.5 (2019), pp. 704–714. DOI: `10.1016/j.molp.2019.02.011`.

[38] Jorge F. S. Ferreira, James E. Simon, and Jules Janick. “Artemisia annua : Botany, Horticulture, Pharmacology”. In: ed. by Jules Janick. Horticultural reviews. New York: John Wiley & Sons Inc, 1997, pp. 319–371. ISBN: 9780470650622.

[39] Richard K. Haynes. “From artemisinin to new artemisinin antimalarials: biosynthesis, extraction, old and new derivatives, stereochemistry and medicinal chemistry requirements”. In: *Current Topics in Medicinal Chemistry* 6.5 (2006), pp. 509–537. DOI: `10.2174/156802606776743129`.

[40] J.F.S. Ferreira and Jules Janick. “Distribution of artemisinin in Artemisia annua”. In: *Progress in new crops*. Ed. by Jules Janick. Arlington Press, 1996, pp. 579–584.

[41] R. Liersch, H. Soicke, C. Stehr, and H. U. Tüllner. “Formation of Artemisinin in Artemisia annua during One Vegetation Period”. In: *Planta Medica* 52.5 (1986), pp. 387–390. DOI: `10.1055/s-2007-969193`.

[42] Colin W. Wright. *Artemisia*. CRC Press, 2001. ISBN: 9780203303061.

[43] J.F.S. Ferreira, J. C. Laughlin, N. Delabays, and P. M. de Magalhães. “Cultivation and genetics of Artemisia annua L. for increased production of the antimalarial artemisinin”. In: *Plant Genetic Resources* 3.2 (2005), pp. 206–229. DOI: `10.1079/PGR200585`.

[44] J. F. Ferreira. *Picture of Artemisia annua L.* URL: `https://commons.wikimedia.org/wiki/File:Artemisia_annua.jpg` (visited on Dec. 24, 2021).

[45] S. Bharel, A. Gulati, M. Z. Abdin, P. S. Srivastava, and S. K. Jain. “Structure, biosynthesis and functions of artemisinin”. In: *Fitoterapia* 67.5 (1996), pp. 387–402.

[46] Liu Chunzhao, Wang Yuchun, Ouyang Fan, Ye Hechun, and Li Guofeng. “Advance in artemisinin biosynthesis research”. In: *Natural Product Research and Development* 12.1 (2000), pp. 83–86.

[47] Pamela J. Weathers, Shereen Elkholy, and Kristin K. Wobbe. “Artemisinin: The biosynthetic pathway and its regulation in Artemisia annua, a terpenoid-rich species”. In: *In Vitro Cellular & Developmental Biology - Plant* 42.4 (2006), pp. 309–317. DOI: `10.1079/IVP2006782`.

[48] Anna-Margareta Rydén and Oliver Kayser. “Chemistry, Biosynthesis and Biological Activity of Artemisinin and Related Natural Peroxides”. In: *Bioactive heterocycles III*. Ed. by Mahmud Tareq Hassan Khan and M. Alamgir. Topics in heterocyclic chemistry. Berlin: Springer, 2007, pp. 1–31. ISBN: 978-3-540-73402-4. DOI: `10.1007/7081_2007_085`.

[49] Patrick S. Covello, Keat H. Teoh, Devin R. Polichuk, Darwin W. Reed, and Goska Nowak. “Functional genomics and the biosynthesis of artemisinin”. In: *Phytochemistry* 68.14 (2007), pp. 1864–1871. DOI: `10.1016/j.phytochem.2007.02.016`.

[50] Geoffrey D. Brown. “The biosynthesis of artemisinin (Qinghaosu) and the phytochemistry of Artemisia annua L. (Qinghao)”. In: *Molecules (Basel, Switzerland)* 15.11 (2010), pp. 7603–7698. DOI: `10.3390/molecules15117603`.

[51] De-Yu Xie, Dong-Ming Ma, Rika Judd, and Ashley Loray Jones. “Artemisinin biosynthesis in Artemisia annua and metabolic engineering: questions, challenges, and perspectives”. In: *Phytochemistry Reviews* 15.6 (2016), pp. 1093–1114. DOI: `10.1007/s11101-016-9480-2`.

[52] Nur K. B. K. Ikram and Henrik T. Simonsen. “A Review of Biotechnological Artemisinin Production in Plants”. In: *Frontiers in Plant Science* 8 (2017), p. 1966. DOI: `10.3389/fpls.2017.01966`.

[53] Yansheng Zhang, Keat H. Teoh, Darwin W. Reed, Lies Maes, Alain Goossens, et al. “The molecular cloning of artemisinic aldehyde reductase and its role in glandular trichome-dependent biosynthesis of artemisinin in Artemisia annua”. In: *Journal of Biological Chemistry* 283.31 (2008), pp. 21501–21508. DOI: `10.1074/jbc.M803090200`.

[54] Keat H. Teoh, Devin R. Polichuk, Darwin W. Reed, and Patrick S. Covello. “Molecular cloning of an aldehyde dehydrogenase implicated in artemisinin biosynthesis in Artemisia annua”. In: *Botany* 87.6 (2009), pp. 635–642. DOI: `10.1139/B09-032`.

[55] T. E. Wallaart, N. Pras, A. C. Beekman, and W. J. Quax. “Seasonal variation of artemisinin and its biosynthetic precursors in plants of Artemisia annua of different geographical origin: proof for the existence of chemotypes”. In: *Planta Medica* 66.1 (2000), pp. 57–62. DOI: `10.1055/s-2000-11115`.

[56] Jorge F. S. Ferreira. “Nutrient deficiency in the production of artemisinin, dihydroartemisinic acid, and artemisinic acid in Artemisia annua L”. In: *Journal of Agricultural and Food Chemistry* 55.5 (2007), pp. 1686–1694. DOI: `10.1021/jf063017v`.

[57] Jorge F. S. Ferreira and Devanand L. Luthria. “Drying affects artemisinin, dihydroartemisinic acid, artemisinic acid, and the antioxidant capacity of Artemisia annua L. leaves”. In: *Journal of Agricultural and Food Chemistry* 58.3 (2010), pp. 1691–1698. DOI: `10.1021/jf903222j`.

[58] Harro J. Bouwmeester, T.Eelco Wallaart, Michiel H.A. Janssen, Bert van Loo, Ben J.M. Jansen, et al. “Amorpha-4,11-diene synthase catalyses the first probable step in artemisinin biosynthesis”. In: *Phytochemistry* 52.5 (1999), pp. 843–854. DOI: `10.1016/S0031-9422(99)00206-X`.

[59] Keat H. Teoh, Devin R. Polichuk, Darwin W. Reed, Goska Nowak, and Patrick S. Covello. “Artemisia annua L. (Asteraceae) trichome-specific cDNAs reveal CYP71AV1, a cytochrome P450 with a key role in the biosynthesis of the antimalarial sesquiterpene lactone artemisinin”. In: *FEBS Letters* 580.5 (2006), pp. 1411–1416. DOI: `10.1016/j.febslet.2006.01.065`.

[60] Yansheng Zhang, Goska Nowak, Darwin W. Reed, and Patrick S. Covello. “The production of artemisinin precursors in tobacco”. In: *Plant Biotechnology Journal* 9.4 (2011), pp. 445–454. DOI: `10.1111/j.1467-7652.2010.00556.x`.

[61] Nam-Cheol Kim, Jeong-Gu Kim, Hyung-Joon Lim, Tae-Ryong Hahn, and Soo-Un Kim. "Production of secondary metabolites by tissue culture of Artemisia annua L". In: *Applied Biological Chemistry* 35.2 (1992), pp. 99–105.

[62] T. Eelco Wallaart, Wim van Uden, Heidi G. M. Lubberink, Herman J. Woerdenbag, Niesko Pras, et al. "Isolation and Identification of Dihydroartemisinic Acid from Artemisia Annua and Its Possible Role in the Biosynthesis of Artemisinin". In: *Journal of natural products* 62.3 (1999), pp. 430–433. DOI: `10.1021/np980370p`.

[63] John Suberu, Piotr S. Gromski, Alison Nordon, and Alexei Lapkin. "Multivariate data analysis and metabolic profiling of artemisinin and related compounds in high yielding varieties of Artemisia annua field-grown in Madagascar". In: *Journal of Pharmaceutical and Biomedical Analysis* 117 (2016), pp. 522–531. DOI: `10.1016/j.jpba.2015.10.003`.

[64] Tomasz Czechowski, Tony R. Larson, Theresa M. Catania, David Harvey, Cenxi Wei, et al. "Detailed Phytochemical Analysis of High- and Low Artemisinin-Producing Chemotypes of Artemisia annua". In: *Frontiers in Plant Science* 9 (2018), p. 641. DOI: `10.3389/fpls.2018.00641`.

[65] Geoffrey D. Brown and Lai-King Sy. "In vivo transformations of artemisinic acid in Artemisia annua plants". In: *Tetrahedron* 63.38 (2007), pp. 9548–9566. DOI: `10.1016/j.tet.2007.06.062`.

[66] Geoffrey D. Brown and Lai-King Sy. "In vivo transformations of dihydroartemisinic acid in Artemisia annua plants". In: *Tetrahedron* 60.5 (2004), pp. 1139–1159. DOI: `10.1016/j.tet.2003.11.070`.

[67] Y. S. Zhang, B. Y. Liu, Z. Q. Li, H. C. Ye, H. Wang, et al. "Molecular cloning of a classical plant peiroxidase firom Artemisia annua and its effect on the biosynthesis of artemisinin in vitro". In: *ACTA BOTANICA SINICA* 46.11 (2004), pp. 1338–1346.

[68] Jianhua Zhu, Jiazeng Yang, Zihan Zeng, Wenjin Zhang, Liyan Song, et al. "Inducing effect of dihydroartemisinic acid in the biosynthesis of artemisinins with cultured cells of Artemisia annua by enhancing the expression of genes". In: *The Scientific World Journal* 2014 (2014), p. 293190. DOI: `10.1155/2014/293190`.

[69] Laura Bryant, Brian Flatley, Chhaya Patole, Geoffrey D. Brown, and Rainer Cramer. "Proteomic analysis of Artemisia annua–towards elucidating the biosynthetic pathways of the antimalarial pro-drug artemisinin". In: *BMC Plant Biology* 15.1 (2015), p. 175. DOI: `10.1186/s12870-015-0565-7`.

[70] Lai-King Sy and Geoffrey D. Brown. "The mechanism of the spontaneous autoxidation of dihydroartemisinic acid". In: *Tetrahedron* 58.5 (2002), pp. 897–908. DOI: `10.1016/S0040-4020(01)01193-0`.

[71] Wallaart, Pras, and Quax. "Isolation and identification of dihydroartemisinic acid hydroperoxide from artemisia annua: A novel biosynthetic precursor of artemisinin". In: *Journal of Natural Products* 62.8 (1999), pp. 1160–1162. DOI: `10.1021/np9900122`.

[72] Jean-Marie Kindermans, Jacques Pilloy, Piero Olliaro, and Melba Gomes. "Ensuring sustained ACT production and reliable artemisinin supply". In: *Malaria journal* 6.1 (2007), p. 125. DOI: `10.1186/1475-2875-6-125`.

[73] Fangyu Ding, Tian Ma, Mengmeng Hao, Qian Wang, Shuai Chen, et al. “Mapping Worldwide Environmental Suitability for Artemisia annua L”. In: *Sustainability* 12.4 (2020), p. 1309. DOI: `10.3390/su12041309`.

[74] Sushil Kumar, S.K Gupta, Poorinima Singh, Pratima Bajpai, M.M Gupta, et al. “High yields of artemisinin by multi-harvest of Artemisia annua crops”. In: *Industrial Crops and Products* 19.1 (2004), pp. 77–90. DOI: `10.1016/j.indcrop.2003.07.003`.

[75] H. J. Woerdenbag, N. Pras, N. G. Chan, B. T. Bang, R. Bos, et al. “Artemisinin, Related Sesquiterpenes, and Essential Oil in Artemisia annua During a Vegetation Period in Vietnam”. In: *Planta Medica* 60.3 (1994), pp. 272–275. DOI: `10.1055/s-2006-959474`.

[76] Willemien J. M. Lommen, Sytze Elzinga, Francel W. A. Verstappen, and Harro J. Bouwmeester. “Artemisinin and sesquiterpene precursors in dead and green leaves of Artemisia annua L. crops”. In: *Planta Medica* 73.10 (2007), pp. 1133–1139. DOI: `10.1055/s-2007-981567`.

[77] José A. Marchese, Jorge F.S. Ferreira, Vera L.G. Rehder, and Osmar Rodrigues. “Water deficit effect on the accumulation of biomass and artemisinin in annual wormwood(Artemisia annua L., Asteraceae)”. In: *Brazilian Journal of Plant Physiology* 22.1 (2010), pp. 1–9. DOI: `10.1590/S1677-04202010000100001`.

[78] Li-Ling Feng, Rui-Yi Yang, Xue-Qin Yang, Xiao-Mei Zeng, Wen-Jie Lu, et al. “Synergistic re-channeling of mevalonate pathway for enhanced artemisinin production in transgenic Artemisia annua”. In: *Plant Science* 177.1 (2009), pp. 57–67. DOI: `10.1016/j.plantsci.2009.03.014`.

[79] M. Irfan Qureshi, M. Israr, M. Z. Abdin, and M. IQBAL. “Responses of L. to lead and salt-induced oxidative stress”. In: *Environmental and Experimental Botany* 53.2 (2005), pp. 185–193. DOI: `10.1016/j.envexpbot.2004.03.014`.

[80] Ritesh Kumar Yadav, Rajender Singh Sangwan, Avadesh K. Srivastava, and Neelam S. Sangwan. “Prolonged exposure to salt stress affects specialized metabolites-artemisinin and essential oil accumulation in Artemisia annua L.” In: *Protoplasma* 254.1 (2017), pp. 505–522. DOI: `10.1007/s00709-016-0971-1`.

[81] Yuchun Wang, Haoxian Zhang, Bing Zhao, and Xiaofan Yuan. “Improved growth of Artemisia annua L hairy roots and artemisinin production under red light conditions”. In: *Biotechnology Letters* 23 (2001), pp. 1971–1973. DOI: `10.1023/A:1013786332363`.

[82] Chun-zhao Liu, Chen Guo, Yu-chun Wang, and Fan Ouyang. “Effect of light irradiation on hairy root growth and artemisinin biosynthesis of Artemisia annua L”. In: *Process Biochemistry* 38.4 (2002), pp. 581–585. DOI: `10.1016/S0032-9592(02)00165-6`.

[83] M. E. Poulson and T. Thai. “Effect of high light intensity on photoinhibition, oxyradicals and artemisinin content in Artemisia annua L”. In: *Photosynthetica* 53.3 (2015), pp. 403–409. DOI: `10.1007/s11099-015-0130-5`.

[84] Melissa Yit Yee Kam and Winnie Soo Ping Yap. “An oxidatively stressful situation: a case of Artemisia annua L”. In: *Biotechnology & genetic engineering reviews* 36.1 (2020), pp. 1–31. DOI: `10.1080/02648725.2020.1749818`.

[85] Kaiser Iqbal Wani, Sadaf Choudhary, Andleeb Zehra, M. Naeem, Pamela Weathers, et al. “Enhancing artemisinin content in and delivery from Artemisia annua: a review of alternative, classical, and transgenic approaches”. In: *Planta* 254.2 (2021), p. 29. DOI: `10.1007/s00425-021-03676-3`.

[86] N. Delabays, X. Simonnet, and M. Gaudin. “The genetics of artemisinin content in Artemisia annua L. and the breeding of high yielding cultivars”. In: *Current Medicinal Chemistry* 8.15 (2001), pp. 1795–1801. DOI: `10.2174/0929867013371635`.

[87] J. F.S. Ferreira. “Seasonal and Post-harvest Accumulation of Artemisinin, Artemisinic Acid, and Dihydroartemisinic Acid in Three Accessions of Artemisia annua Cultivated in West Virginia, USA”. In: *Planta Medica* 74.03 (2008). DOI: `10.1055/s-2008-1075155`.

[88] Tony R. Larson, Caroline Branigan, David Harvey, Teresa Penfield, Dianna Bowles, et al. “A survey of artemisinic and dihydroartemisinic acid contents in glasshouse and global field-grown populations of the artemisinin-producing plant Artemisia annua L”. In: *Industrial Crops and Products* 45 (2013), pp. 1–6. DOI: `10.1016/j.indcrop.2012.12.004`.

[89] X. Simonnet. “Le fanage au champ d’Artemisia annua L.: elever la teneur en artemisinine et abaisser les couts de production”. In: *Revue suisse de viticulture, arboriculture et horticulture* 33.5 (2001), pp. 263–272.

[90] Pamela J. Weathers and Melissa J. Towler. “Changes in key constituents of clonally propagated Artemisia annua L. during preparation of compressed leaf tablets for possible therapeutic use”. In: *Industrial Crops and Products* 62 (2014), pp. 173–178. DOI: `10.1016/j.indcrop.2014.08.033`.

[91] Anders Kjær, Francel Verstappen, Harro Bouwmeester, Elise Ivarsen, Xavier Fretté, et al. “Artemisinin production and precursor ratio in full grown Artemisia annua L. plants subjected to external stress”. In: *Planta* 237.4 (2013), pp. 955–966. DOI: `10.1007/s00425-012-1811-y`.

[92] John Suberu, Peyman Yamin, Robert Cornell, Arya Sam, and Alexei Lapkin. “Feasibility of Using 2,3,3,3-Tetrafluoropropene (R1234yf) as a Solvent for Solid–Liquid Extraction of Biopharmaceuticals”. In: *ACS Sustainable Chemistry & Engineering* 4.5 (2016), pp. 2559–2568. DOI: `10.1021/acssuschemeng.5b01721`.

[93] R. S. Bhakuni, D. C. Jain, R. P. Sharma, and S. Kumar. “Secondary metabolites of Artemisia annua and their biological activity”. In: *Current Science* 80.1 (2001), pp. 35–48.

[94] Jorge F. S. Ferreira, Devanand L. Luthria, Tomikazu Sasaki, and Arne Heyerick. “Flavonoids from Artemisia annua L. as antioxidants and their potential synergism with artemisinin against malaria and cancer”. In: *Molecules (Basel, Switzerland)* 15.5 (2010), pp. 3135–3170. DOI: `10.3390/molecules15053135`.

[95] A. R. Bilia, P. Melillo de Malgalhaes, M. C. Bergonzi, and F. F. Vincieri. “Simultaneous analysis of artemisinin and flavonoids of several extracts of Artemisia annua L. obtained from a commercial sample and a selected cultivar”. In: *Phytomedicine* 13.7 (2006), pp. 487–493. DOI: `10.1016/j.phymed.2006.01.008`.

[96] Rita Baraldi, Benedetta Isacchi, Stefano Predieri, Giancarlo Marconi, Franco Francesco Vincieri, et al. “Distribution of artemisinin and bioactive flavonoids from Artemisia annua L. during plant growth”. In: *Biochemical Systematics and Ecology* 36.5-6 (2008), pp. 340–348. DOI: `10.1016/j.bse.2007.11.002`.

[97] Barry C. Elford, Margaret F. Roberts, J.David Phillipson, and Robert J.M. Wilson. “Potentiation of the antimalarial activity of qinghaosu by methoxylated flavones”. In: *Transactions of the Royal Society of Tropical Medicine and Hygiene* 81.3 (1987), pp. 434–436. DOI: `10.1016/0035-9203(87)90161-1`.

[98] K. C. Liu, S. L. Yang, M. F. Roberts, B. C. Elford, and J. D. Phillipson. “Antimalarial activity of Artemisia annua flavonoids from whole plants and cell cultures”. In: *Plant Cell Reports* 11.12 (1992), pp. 637–640. DOI: `10.1007/BF00236389`.

[99] Tomasz Czechowski, Mauro A. Rinaldi, Mufuliat Toyin Famodimu, Maria van Veelen, Tony R. Larson, et al. “Flavonoid Versus Artemisinin Anti-malarial Activity in Artemisia annua Whole-Leaf Extracts”. In: *Frontiers in Plant Science* 10 (2019), p. 984. DOI: `10.3389/fpls.2019.00984`.

[100] John O. Suberu, Peyman Yamin, Kai Leonhard, Lijiang Song, Smain Chemat, et al. “The effect of O-methylated flavonoids and other co-metabolites on the crystallization and purification of artemisinin”. In: *Journal of Biotechnology* 171 (2014), pp. 25–33. DOI: `10.1016/j.jbiotec.2013.11.024`.

[101] Shahid Iqbal, Umer Younas, Kim Wei Chan, Muhammad Zia-Ul-Haq, and Maznah Ismail. “Chemical composition of Artemisia annua L. leaves and antioxidant potential of extracts as a function of extraction solvents”. In: *Molecules (Basel, Switzerland)* 17.5 (2012). DOI: `10.3390/molecules17056020`.

[102] Hala N. ElSohly, Edward M. Croom, Farouk S. El-Feraly, and Moshera M. El-Sherei. “A Large-Scale Extraction Technique of Artemisinin from Artemisia annua”. In: *Journal of Natural Products* 53.6 (1990), pp. 1560–1564. DOI: `10.1021/np50072a026`.

[103] Alexei A. Lapkin, Pawel K. Plucinski, and Malcolm Cutler. “Comparative Assessment of Technologies for Extraction of Artemisinin”. In: *Journal of natural products* 69.11 (2006), pp. 1653–1664. DOI: `10.1021/np060375j`.

[104] Alexei A. Lapkin. “Green Extraction of Artemisinin from Artemisia annua L”. In: *Green extraction of natural products*. Ed. by Farid Chemat and Jochen Strube. Weinheim: Wiley-VCH, 2015, pp. 333–356. ISBN: 9783527676828.

[105] Lutfun Nahar, Mingquan Guo, and Satyajit D. Sarker. “A review on the latest advances in extraction and analysis of artemisinin”. In: *Phytochemical analysis : PCA* 31.1 (2020), pp. 5–14. DOI: `10.1002/pca.2873`.

[106] Alexei A. Lapkin, Martina Peters, Lasse Greiner, Smain Chemat, Kai Leonhard, et al. “Screening of new solvents for artemisinin extraction process using ab initio methodology”. In: *Green Chemistry* 12.2 (2010), pp. 241–251. DOI: `10.1039/B922001A`.

[107] Souhila Laboukhi-Khorsi, Kamel Daoud, and Smain Chemat. “Efficient Solvent Selection Approach for High Solubility of Active Phytochemicals: Application for the Extraction of an Antimalarial Compound from Medicinal Plants”. In: *ACS Sustainable Chemistry & Engineering* 5.5 (2017), pp. 4332–4339. DOI: `10.1021/acssuschemeng.7b00384`.

[108] Maximilian Sixt and Jochen Strube. “Systematic and Model-Assisted Evaluation of Solvent Based- or Pressurized Hot Water Extraction for the Extraction of Artemisinin from Artemisia annua L”. In: *Processes* 5.4 (2017), p. 86. DOI: `10.3390/pr5040086`.

[109] Yongqiang Zhang, Phongphat Prawang, Chunshan Li, Xiangzhan Meng, Yu Zhao, et al. “Ultrasonic assisted extraction of artemisinin from Artemisia Annua L. using monoether-based solvents”. In: *Green Chemistry* 20.3 (2018), pp. 713–723. DOI: `10.1039/C7GC03191B`.

[110] Nancy Acton, Daniel L. Klayman, Irvin J. Rollman, and Jaroslav F. Novotny. “Isolation of artemisinin (qinghaosu) and its separation from artemisitene using the ito multilayer coil separator-extractor and isolation of arteannuin B”. In: *Journal of Chromatography A* 355 (1986), pp. 448–450. DOI: `10.1016/S0021-9673(01)97352-2`.

[111] Marcel Kohler, Werner Haerdi, Philippe Christen, and Jean-Luc Veuthey. “Extraction of artemisinin and artemisinic acid from Artemisia annua L. using supercritical carbon dioxide”. In: *Journal of Chromatography A* 785.1-2 (1997), pp. 353–360. DOI: `10.1016/S0021-9673(97)00403-2`.

[112] Marcel Kohler, Werner Haerdi, Philippe Christen, and Jean-Luc Veuthey. “Supercritical fluid extraction and chromatography of artemisinin and artemisinic acid. An improved method for the analysis ofArtemisia annua samples”. In: *Phytochemical Analysis* 8.5 (1997), pp. 223–227.

[113] Sócrates Quispe-Condori, Deny Sánchez, Mary A. Foglio, Paulo T.V. Rosa, Carsten Zetzl, et al. “Global yield isotherms and kinetic of artemisinin extraction from Artemisia annua L leaves using supercritical carbon dioxide”. In: *The Journal of Supercritical Fluids* 36.1 (2005), pp. 40–48. DOI: `10.1016/j.supflu.2005.03.003`.

[114] Patrícia Coimbra, Miguel R. Blanco, Hélio S. R. Costa Silva, Maria H. Gil, and Hermínio C. de Sousa. “Experimental Determination and Correlation of Artemisinin’s Solubility in Supercritical Carbon Dioxide”. In: *Journal of Chemical & Engineering Data* 51.3 (2006), pp. 1097–1104. DOI: `10.1021/je060015y`.

[115] Xiao-Yan Gong and Xue-Jun Cao. “Measurement and correlation of solubility of artemisinin in supercritical carbon dioxide”. In: *Fluid Phase Equilibria* 284.1 (2009), pp. 26–30. DOI: `10.1016/j.fluid.2009.05.018`.

[116] Hugo A. Martinez-Correa, Raphaela G. Bitencourt, Ana Carolina A.V. Kayano, Pedro M. Magalhães, Fabio T.M. Costa, et al. “Integrated extraction process to obtain bioactive extracts of Artemisia annua L. leaves using supercritical CO2, ethanol and water”. In: *Industrial Crops and Products* 95 (2017), pp. 535–542. DOI: `10.1016/j.indcrop.2016.11.007`.

[117] Michelle F.F. Rodrigues, Ilza M.O. Sousa, Renata Vardanega, Gislaine C. Nogueira, M. Angela A. Meireles, et al. “Techno-economic evaluation of artemisinin extraction from Artemisia annua L. using supercritical carbon dioxide”. In: *Industrial Crops and Products* 132 (2019), pp. 336–343. DOI: `10.1016/j.indcrop.2019.02.049`.

[118] Lucia Baldino, Ernesto Reverchon, and Giovanna Della Porta. “An optimized process for SC-CO 2 extraction of antimalarial compounds from Artemisia annua L”. In: *The Journal of Supercritical Fluids* 128 (2017), pp. 89–93. DOI: `10.1016/j.supflu.2017.05.018`.

[119] Ozan Nazim Ciftci, Jessica Cahyadi, Selma E. Guigard, and Marleny D. A. Saldaña. “Optimization of artemisinin extraction from Artemisia annua L. with supercritical carbon dioxide + ethanol using response surface methodology”. In: *ELECTROPHORESIS* 39.15 (2018), pp. 1926–1933. DOI: `10.1002/elps.201800084`.

[120] T. TZENG, Y. LIN, T. JONG, and C. CHANG. “Ethanol modified supercritical fluids extraction of scopoletin and artemisinin from Artemisia annua L”. In: *Separation and Purification Technology* 56.1 (2007), pp. 18–24. DOI: `10.1016/j.seppur.2007.01.010`.

[121] Jiaqin Wang, Yanying Zhou, Man Wang, Wentao Bi, Hongli Li, et al. “High-Throughput Analysis for Artemisinins with Deep Eutectic Solvents Mechanochemical Extraction and Direct Analysis in Real Time Mass Spectrometry”. In: *Analytical chemistry* 90.5 (2018), pp. 3109–3117. DOI: `10.1021/acs.analchem.7b04060`.

[122] Zuchen Pan, Yiyang Bo, Yihong Liang, Beibei Lu, Jingbo Zhan, et al. “Intermolecular interactions in natural deep eutectic solvents and their effects on the ultrasound-assisted extraction of artemisinin from Artemisia annua”. In: *Journal of Molecular Liquids* 326 (2021), p. 115283. DOI: `10.1016/j.molliq.2021.115283`.

[123] Yingying Cao, Zhixing Wu, Ying Zhang, Yanrong Liu, and Hui Wang. “Screening of alternative solvent ionic liquids for artemisinin: COSMO-RS prediction and experimental verification”. In: *Journal of Molecular Liquids* 338 (2021), p. 116778. DOI: `10.1016/j.molliq.2021.116778`.

[124] Bioniqs Limited, ed. *Extraction of Artemisinin Using Ionic Liquids: BIONIQS Project report*. 2008. URL: `https://www.mmv.org/newsroom/publications/extraction-artemisinin-using-ionic-liquids` (visited on Sept. 9, 2021).

[125] Marc W. Sanders, Lawrence Wright, Lauren Tate, Gayle Fairless, Lorna Crowhurst, et al. “Unexpected preferential dehydration of artemisinin in ionic liquids”. In: *The Journal of Physical Chemistry A* 113.38 (2009), pp. 10143–10145. DOI: `10.1021/jp906436e`.

[126] Phongphat Prawang, Yongqiang Zhang, Ying Zhang, and Hui Wang. “Ultrasonic Assisted Extraction of Artemisinin from Artemisia annua L. Using Poly(Ethylene Glycol): Toward a Greener Process”. In: *Industrial & Engineering Chemistry Research* 58.39 (2019), pp. 18320–18328. DOI: `10.1021/acs.iecr.9b03305`.

[127] P. Christen and J. L. Veuthey. “New trends in extraction, identification and quantification of artemisinin and its derivatives”. In: *Current Medicinal Chemistry* 8.15 (2001), pp. 1827–1839. DOI: `10.2174/0929867013371563`.

[128] Jorge F.S. Ferreira, Valtcho D. Zheljazkov, and Javier M. Gonzalez. “Artemisinin concentration and antioxidant capacity of Artemisia annua distillation byproduct”. In: *Industrial Crops and Products* 41 (2013), pp. 294–298. DOI: `10.1016/j.indcrop.2012.05.005`.

[129] Shuoqian Liu, Jorge Freire Silva Da Ferreira, Liping Liu, Yuwei Tang, Dongming Tian, et al. “Isolation of Dihydroartemisinic Acid from Artemisia annua L. By-Product by Combining Ultrasound-Assisted Extraction with Response Surface Methodology”. In: *CHEMICAL & PHARMACEUTICAL BULLETIN* 65.8 (2017), pp. 746–753. DOI: `10.1248/cpb.c17-00192`.

[130] Haihui Zhang, Li Zhang, Xigui Hu, Yonghong Zhou, Chunbang Ding, et al. “Optimization of Ultrasound-Assisted Extraction of Artemisinin from Artemisia annua L. by Response Surface Methodology”. In: *Separation Science and Technology* 49.5 (2014), pp. 673–681. DOI: `10.1080/01496395.2013.862545`.

[131] Jin-yu Hao, Wei Han, Shun-de Huang, Bo-yong Xue, and Xiu Deng. “Microwave-assisted extraction of artemisinin from Artemisia annua L”. In: *Separation and Purification Technology* 28.3 (2002), pp. 191–196. DOI: `10.1016/S1383-5866(02)00043-6`.

[132] Rhianna Briars and Larysa Paniwnyk. “Examining the extraction of artemisinin from artemisia annua using ultrasound”. In: AIP Conference Proceedings. AIP, 2012, pp. 581–585. DOI: `10.1063/1.3703254`.

[133] Rhianna Briars and Larysa Paniwnyk. “Effect of ultrasound on the extraction of artemisinin from Artemisia annua”. In: *Industrial Crops and Products* 42 (2013), pp. 595–600. DOI: `10.1016/j.indcrop.2012.06.043`.

[134] Nigist Asfaw, Peter Licence, Alexander A. Novitskii, and Martyn Poliakoff. “Green Chemistry in Ethiopia: the cleaner extraction of essential oils from Artemisia afra: a comparison of clean technology with conventional methodology”. In: *Green Chemistry* 7.5 (2005), p. 352. DOI: `10.1039/b417961g`.

[135] Maximilian Sixt, Axel Schmidt, Fabian Mestmäcker, Maximilian Huter, Lukas Uhlenbrock, et al. “Systematic and Model-Assisted Process Design for the Extraction and Purification of Artemisinin from Artemisia annua L.—Part I: Conceptual Process Design and Cost Estimation”. In: *Processes* 6.9 (2018), p. 161. DOI: `10.3390/pr6090161`.

[136] Stephan Münzberg, Truong Giang Vu, and Andreas Seidel-Morgenstern. “Generalizing Countercurrent Processes: Distillation and Beyond”. In: *Chemie Ingenieur Technik* 90.11 (2018), pp. 1769–1781. DOI: `10.1002/cite.201800132`.

[137] Truong Giang Vu and Andreas Seidel-Morgenstern. “Development from batch to continuous Solid Liquid Extraction - Artemisinin extraction from Artemisia Annua leaves”. In: AIChE Annual Meeting 2020.

[138] Heike Lorenz and Andreas Seidel-Morgenstern. “Separation Processes to Provide Pure Enantiomers and Plant Ingredients”. In: *Annual Review of Chemical and Biomolecular Engineering* 11.1 (2020), pp. 469–502. DOI: `10.1146/annurev-chembioeng-100419-103732`.

[139] Axel Schmidt, Maximilian Sixt, Maximilian Huter, Fabian Mestmäcker, and Jochen Strube. “Systematic and Model-Assisted Process Design for the Extraction and Purification of Artemisinin from Artemisia annua L.—Part II: Model-Based Design of Agitated and Packed Columns for Multistage Extraction and Scrubbing”. In: *Processes* 6.10 (2018), p. 179. DOI: `10.3390/pr6100179`.

[140] Elena V. Piletska, Kal Karim, Malcolm Cutler, and Sergey A. Piletsky. “Development of the protocol for purification of artemisinin based on combination of commercial and computationally designed adsorbents”. In: *Journal of Separation Science* 36.2 (2013), pp. 400–406. DOI: `10.1002/jssc.201200520`.

[141] E. Weiss, H. Ziffer, and Y. Ito. “USE OF COUNTERCURRENT CHROMATOGRAPHY (CCC) TO SEPARATE MIXTURES OF ARTEMISININ, ARTEMISITENE, AND ARTEANNUIN B”. In: *Journal of Liquid Chromatography & Related Technologies* 23.6 (2000), pp. 909–913. DOI: `10.1081/JLC-100101497`.

[142] Jindi Xu, Jianguang Luo, and Lingyi Kong. “Single-Step Preparative Extraction of Artemisinin from Artemisia annua by Charcoal Column Chromatography”. In: *Chromatographia* 74.5-6 (2011), pp. 471–475. DOI: `10.1007/s10337-011-2075-6`.

[143] Na Tian, Juan Li, Shuoqian Liu, Jianan Huang, Xun Li, et al. “Simultaneous isolation of artemisinin and its precursors from Artemisia annua L. by preparative RP-HPLC”. In: *Biomedical Chromatography* 26.6 (2012), pp. 708–713. DOI: `10.1002/bmc.1719`.

[144] Baojun Yang and Xuejun Cao. “Synthesis of the artemisinin-imprinting polymers on silica surface and its adsorption behavior in supercritical CO2 fluid”. In: *AIChE Journal* 57.12 (2011), pp. 3514–3521. DOI: `10.1002/aic.12547`.

[145] Ning Qing Liu, Wolfgang Schuehly, Michaela von Freyhold, and Frank van der Kooy. “A novel purification method of artemisinin from Artemisia annua”. In: *Industrial Crops and Products* 34.1 (2011), pp. 1084–1088. DOI: `10.1016/j.indcrop.2011.03.023`.

[146] Haiyan Qu, Kathrine B. Christensen, Xavier C. Fretté, Fang Tian, Jukka Rantanen, et al. “A Novel Hybrid Chromatography−Crystallization Process for the Isolation and Purification of a Natural Pharmaceutical Ingredient from a Medicinal Herb”. In: *Organic Process Research & Development* 14.3 (2010), pp. 585–591. DOI: `10.1021/op1000176`.

[147] Chandrakant Ramkrishna Malwade, Hannes Buchholz, Ben-Guang Rong, Haiyan Qu, Lars Porskjær Christensen, et al. “Crystallization of Artemisinin from Chromatography Fractions of Artemisia annua Extract”. In: *Organic Process Research & Development* 20.3 (2016), pp. 646–652. DOI: `10.1021/acs.oprd.5b00399`.

[148] Fabian Mestmäcker, Axel Schmidt, Maximilian Huter, Maximilian Sixt, and Jochen Strube. “Systematic and Model-Assisted Process Design for the Extraction and Purification of Artemisinin from Artemisia annua L.—Part III: Chromatographic Purification”. In: *Processes* 6.10 (2018), p. 180. DOI: `10.3390/pr6100180`.

[149] Maximilian Huter, Axel Schmidt, Fabian Mestmäcker, Maximilian Sixt, and Jochen Strube. "Systematic and Model-Assisted Process Design for the Extraction and Purification of Artemisinin from Artemisia annua L.—Part IV: Crystallization". In: *Processes* 6.10 (2018), p. 181. DOI: `10.3390/pr6100181`.

[150] Rodger W. Stringham, Gary L. Moore, David S. Teager, and Tai-Yuen Yue. "Analysis and Isolation of Potential Artemisinin Precursors from Waste Streams of Artemisia Annua Extraction". In: *ACS omega* 3.7 (2018), pp. 7803–7808. DOI: `10.1021/acsomega.8b00974`.

[151] J.-M. Liu, M.-Y. Ni, J.-F. Fan, Y.-Y. Tu, Z.-H. Wu, et al. "Structure and reaction of arteannuin." In: *Huaxue Xuebao* 37.2 (1979), pp. 129–143.

[152] G. Schmid and W. Hofheinz. "Total synthesis of qinghaosu". In: *Journal of the American Chemical Society* 105.3 (1983), pp. 624–625.

[153] W.-S. Zhou. "Total synthesis of arteannuin (Quinghaosu) and related compounds". In: *Pure and Applied Chemistry* 58.5 (1986), pp. 817–824. DOI: `10.1351/pac198658050817`.

[154] Xu Xing-Xiang, Zhu Jie, Huang Da-Zhong, and Zhou Wei-Shan. "Total synthesis of arteannuin and deoxyarteannuin". In: *Tetrahedron* 42.3 (1986), pp. 819–828. DOI: `10.1016/S0040-4020(01)87487-1`.

[155] Mitchell A. Avery, Clive Jennings-White, and Wesley K.M. Chong. "The Total synthesis of (+)-artemisinin and (+)-9-desmethyltemesinin". In: *Tetrahedron Letters* 28.40 (1987), pp. 4629–4632. DOI: `10.1016/S0040-4039(00)96582-1`.

[156] T. Ravindranathan, M. Anil Kumar, Rani B. Menon, and S. V. Hiremath. "Stereoselective synthesis of artemisinin". In: *Tetrahedron Letters* 31.5 (1990), pp. 755–758. DOI: `10.1016/S0040-4039(00)94621-5`.

[157] Mitchell A. Avery, Wesley K. M. Chong, and Clive Jennings-White. "Stereoselective total synthesis of (+)-artemisinin, the antimalarial constituent of Artemisia annua L". In: *Journal of the American Chemical Society* 114.3 (1992), pp. 974–979. DOI: `10.1021/ja00029a028`.

[158] Liu Hsing-Jang, Yeh Wen-Lung, and Yeu Chew Sew. "A total synthesis of the antimarial natural product (+)-qinghaosu". In: *Tetrahedron Letters* 34.28 (1993), pp. 4435–4438. DOI: `10.1016/0040-4039(93)88052-K`.

[159] Mauricio Gomes Constantino, Milton Beltrame, Gil Valdo José da Silva, and Julio Zukerman-Schpector. "A Novel Asymmetric Total Synthesis of (+)-Artemisinin". In: *Synthetic Communications* 26.2 (1996), pp. 321–329. DOI: `10.1080/00397919608003621`.

[160] J. S. Yadav, B. Thirupathaiah, and P. Srihari. "A concise stereoselective total synthesis of (+)-artemisinin". In: *Tetrahedron* 66.11 (2010), pp. 2005–2009.

[161] Johannes Krieger, Toni Smeilus, Marcel Kaiser, Ean-Jeong Seo, Thomas Efferth, et al. "Total Synthesis and Biological Investigation of (-)-Artemisinin: The Antimalarial Activity of Artemisinin Is not Stereospecific". In: *Angewandte Chemie (Int. ed.)* 57.27 (2018), pp. 8293–8296.

[162] Chunyin Zhu and Silas P. Cook. "A concise synthesis of (+)-artemisinin". In: *Journal of the American Chemical Society* 134.33 (2012), pp. 13577–13579.

[163] Bernd Schäfer. “Artemisinin”. In: *Chemie in unserer Zeit* 48.3 (2014), pp. 216–225. DOI: `10.1002/ciuz.201400652`.

[164] Silas Cook. “Artemisinin: A Case Study in the Evolution of Synthetic Strategy”. In: *Synlett* 25.06 (2014), pp. 751–759. DOI: `10.1055/s-0033-1340627`.

[165] Xiaoping Tang, Melodi Demiray, Thomas Wirth, and Rudolf K. Allemann. “Concise synthesis of artemisinin from a farnesyl diphosphate analogue”. In: *Bioorganic & medicinal chemistry* 26.7 (2018), pp. 1314–1319. DOI: `10.1016/j.bmc.2017.03.068`.

[166] Geoffrey Schwertz, Andrea Zanetti, Marllon Nascimento de Oliveira, Mario Andrés Gomez Fernandez, Zacharias Amara, et al. “Chemo- and Diastereoselective Hydrosilylation of Amorphadiene toward the Synthesis of Artemisinin”. In: *The Journal of organic chemistry* 85.15 (2020), pp. 9607–9613. DOI: `10.1021/acs.joc.0c00617`.

[167] Mario Andrés Gomez Fernandez, Marllon Nascimento de Oliveira, Andrea Zanetti, Geoffrey Schwertz, Janine Cossy, et al. “Photochemical Hydrothiolation of Amorphadiene and Formal Synthesis of Artemisinin via a Pummerer Rearrangement”. In: *Organic Letters* 23.15 (2021), pp. 5593–5598. DOI: `10.1021/acs.orglett.1c00636`.

[168] Patrick J. Westfall, Douglas J. Pitera, Jacob R. Lenihan, Diana Eng, Frank X. Woolard, et al. “Production of amorphadiene in yeast, and its conversion to dihydroartemisinic acid, precursor to the antimalarial agent artemisinin”. In: *Proceedings of the National Academy of Sciences* 109.3 (2012), E111–8. DOI: `10.1073/pnas.1110740109`.

[169] K. Boehme and H. D. Brauer. “Generation of singlet oxygen from hydrogen peroxide disproportionation catalyzed by molybdate ions”. In: *Inorganic Chemistry* 31.16 (1992), pp. 3468–3471. DOI: `10.1021/ic00042a024`.

[170] Paul L. Alsters, Walther Jary, Véronique Nardello-Rataj, and Jean-Marie Aubry. ““Dark” Singlet Oxygenation of β-Citronellol: A Key Step in the Manufacture of Rose Oxide”. In: *Organic Process Research & Development* 14.1 (2010), pp. 259–262. DOI: `10.1021/op900076g`.

[171] Véronique Nardello-Rataj, Paul L. Alsters, and Jean-Marie Aubry. “Industrial Prospects for the Chemical and Photochemical Singlet Oxygenation of Organic Compounds”. In: *Liquid Phase Aerobic Oxidation Catalysis*. Ed. by Paul L. Alsters and Shannon S. Stahl. Wiley-VCH, 2016, pp. 369–395. ISBN: 9783527337811.

[172] Michael A. Corsello and Neil K. Garg. “Synthetic chemistry fuels interdisciplinary approaches to the production of artemisinin”. In: *Natural product reports* 32.3 (2015), pp. 359–366. DOI: `10.1039/c4np00113c`.

[173] Marco Montalti, Alberto Credi, Luca Prodi, M. Teresa Gandolfi, Josef Michl, et al. *Handbook of photochemistry*. Third edition. Boca Raton: CRC/Taylor & Francis, 2020. ISBN: 9780367577902.

[174] Francis Wilkinson, W. Phillip Helman, and Alberta B. Ross. “Quantum Yields for the Photosensitized Formation of the Lowest Electronically Excited Singlet State of Molecular Oxygen in Solution”. In: *Journal of Physical and Chemical Reference Data* 22.1 (1993), pp. 113–262. DOI: `10.1063/1.555934`.

[175] Rodrigo Costa e Silva, Luely Da Oliveira Silva, Aloisio de Andrade Bartolomeu, Timothy John Brocksom, and Kleber Thiago de Oliveira. “Recent applications of porphyrins as photocatalysts in organic synthesis: batch and continuous flow approaches”. In: *Beilstein Journal of Organic Chemistry* 16 (2020), pp. 917–955. DOI: `10.3762/bjoc.16.83`.

[176] Diane C. Dobrowolski, Peter R. Ogilby, and Christopher S. Foote. “Chemistry of singlet oxygen. 39. 9,10-Dicyanoanthracene-sensitized formation of singlet oxygen”. In: *The Journal of Physical Chemistry* 87.13 (1983), pp. 2261–2263. DOI: `10.1021/j100236a001`.

[177] F. Wilkinson, D. J. McGarvey, and A. F. Olea. “Factors governing the efficiency of singlet oxygen production during oxygen quenching of singlet and triplet states of anthracene derivatives in cyclohexane solution”. In: *Journal of the American Chemical Society* 115.25 (1993), pp. 12144–12151. DOI: `10.1021/ja00078a062`.

[178] A. F. Olea and F. Wilkinson. “Singlet Oxygen Production from Excited Singlet and Triplet States of Anthracene Derivatives in Acetonitrile”. In: *The Journal of Physical Chemistry* 99.13 (1995), pp. 4518–4524. DOI: `10.1021/j100013a022`.

[179] D. Kopetzki, F. Lévesque, and Peter H. Seeberger. “A continuous-flow process for the synthesis of artemisinin”. In: *Chemistry* 19.17 (2013), pp. 5450–5456. DOI: `10.1002/chem.201204558`.

[180] Alison Telfer. “Singlet Oxygen Production by PSII Under Light Stress: Mechanism, Detection and the Protective role of β-Carotene”. In: *Plant and Cell Physiology* 55.7 (2014), pp. 1216–1223. DOI: `10.1093/pcp/pcu040`.

[181] Anja Krieger-Liszkay. “Singlet oxygen production in photosynthesis”. In: *Journal of Experimental Botany* 56.411 (2005), pp. 337–346. DOI: `10.1093/jxb/erh237`.

[182] Christian Triantaphylidès and Michel Havaux. “Singlet oxygen in plants: production, detoxification and signaling”. In: *Trends in Plant Science* 14.4 (2009), pp. 219–228. DOI: `10.1016/j.tplants.2009.01.008`.

[183] Ieva Ruks Politzer, Gary W. Griffin, and John L. Laseter. “Singlet oxygen and biological systems”. In: *Chemico-Biological Interactions* 3.2 (1971), pp. 73–93. DOI: `10.1016/0009-2797(71)90088-3`.

[184] Yasuhiko Araki, Diane C. Dobrowolski, Thomas E. Goyne, Douglas C. Hanson, Zhi Qin Jiang, et al. “Chemistry of Singlet Oxygen. 47. 9,10-Dicyanoanthracene-Sensitized Photooxygenation of Alkyl-Substituted Olefins”. In: *Journal of the American Chemical Society* 106.16 (1984), pp. 4570–4575. DOI: `10.1021/ja00328a045`.

[185] Richard C. Kanner and Christopher S. Foote. “Singlet oxygen production from singlet and triplet states of 9,10-dicyanoanthracene”. In: *Journal of the American Chemical Society* 114.2 (1992), pp. 678–681. DOI: `10.1021/ja00028a040`.

[186] Rodger D. Scurlock and Peter R. Ogilby. “Production of singlet oxygen by 9,10-dicyanoanthracene and acridine: quantum yields in acetonitrile”. In: *Journal of Photochemistry and Photobiology A: Chemistry* 72.1 (1993), pp. 1–7. DOI: `10.1016/1010-6030(93)85077-L`.

[187] F. Wilkinson, D. J. McGarvey, and A. Olea. “Factors which determine the efficiency of sensitized singlet oxygen production”. In: *Journal of Chemical Sciences* 105.6 (1993), pp. 685–694. DOI: `10.1007/BF03040842`.

[188] Andres F. Olea, David R. Worrall, Frank Wilkinson, Sian L. Williams, and Ayman A. Abdel-Shafi. “Solvent effects on the photophysical properties of 9,10-dicyanoanthracene”. In: *Physical Chemistry Chemical Physics* 4.2 (2002), pp. 161–167. DOI: `10.1039/b104806f`.

[189] Lewis E. Manring, Chee Liang Gu, and C. S. Foote. “Chemistry of singlet oxygen. 40. Enhanced molecular oxygen 1O2 formation in cyanoaromatic-sensitized photooxidations by substrate-enhanced intersystem crossing”. In: *The Journal of Physical Chemistry* 87.1 (1983), pp. 40–44. DOI: `10.1021/j100224a012`.

[190] Hendrik Küpper, Roman D*v*edic, Antonin Svoboda, Jan Hála, and Peter M.H Kroneck. “Kinetics and efficiency of excitation energy transfer from chlorophylls, their heavy metal-substituted derivatives, and pheophytins to singlet oxygen”. In: *Biochimica et Biophysica Acta (BBA) - General Subjects* 1572.1 (2002). DOI: `10.1016/s0304-4165(02)00284-2`.

[191] A. V. Lobanov, G. I. Kobzev, K. S. Davydov, and G. G. Komissarov. “Generation of reactive oxygen species under singlet oxygen photosensitivity by chlorophyll and its analogs”. In: *Russian Journal of Physical Chemistry B* 8.3 (2014), pp. 277–283. DOI: `10.1134/S1990793114030221`.

[192] Mikkel Bregnhøj, Michael Westberg, Frank Jensen, and Peter R. Ogilby. “Solvent-dependent singlet oxygen lifetimes: temperature effects implicate tunneling and charge-transfer interactions”. In: *Physical Chemistry Chemical Physics* 18.33 (2016), pp. 22946–22961. DOI: `10.1039/c6cp01635a`.

[193] D. R. Adams and F. Wilkinson. “Lifetime of singlet oxygen in liquid solution”. In: *Journal of the Chemical Society, Faraday Transactions 2* 68 (1972), p. 586. DOI: `10.1039/f29726800586`.

[194] Francis Wilkinson, W. Phillip Helman, and Alberta B. Ross. “Rate Constants for the Decay and Reactions of the Lowest Electronically Excited Singlet State of Molecular Oxygen in Solution. An Expanded and Revised Compilation”. In: *Journal of Physical and Chemical Reference Data* 24.2 (1995), pp. 663–677. DOI: `10.1063/1.555965`.

[195] Günther O. Schenck, Klaus G. Kinkel, and Hans-Joachim Mertens. “Photochemische Reaktionen I. Über die Photosynthese des Askaridols und verwandter Endoperoxyde”. In: *Justus Liebigs Annalen der Chemie* 584.1 (1953), pp. 125–155. DOI: `10.1002/jlac.19535840110`.

[196] Günther O. Schenck, O.-Albrecht Neumüller, and Wolfgang Eisfeld. “Zur photosensibilisierten Autoxydation der Steroide: Δ5-Steroid-7α-hydroperoxyde und -7-ketone durch Allylumlagerung von Δ6-Steroid-5α-hydroperoxyden”. In: *Justus Liebigs Annalen der Chemie* 618.1 (1958), pp. 202–210. DOI: `10.1002/jlac.19586180123`.

[197] Lai-King Sy, Geoffrey D. Brown, and Richard Haynes. “A novel endoperoxide and related sesquiterpenes from Artemisia annua which are possibly derived from allylic hydroperoxides”. In: *Tetrahedron* 54.17 (1998), pp. 4345–4356. DOI: `10.1016/S0040-4020(98)00148-3`.

[198] Lai-King Sy, Koon-Sin Ngo, and Geoffrey D. Brown. “Biomimetic synthesis of arteannuin h and the 3,2-rearrangement of allylic hydroperoxides”. In: *Tetrahedron* 55.52 (1999), pp. 15127–15140. DOI: `10.1016/S0040-4020(99)00987-4`.

[199] Nancy Acton and Ronald J. Roth. “On the conversion of dihydroartemisinic acid into artemisinin”. In: *The Journal of Organic Chemistry* 57.13 (1992), pp. 3610–3614. DOI: `10.1021/jo00039a020`.

[200] R. J. Roth and N. Acton. “A simple conversion of artemisinic acid into artemisinin”. In: *Journal of natural products* 52.5 (1989), pp. 1183–1185. DOI: `10.1021/np50065a050`.

[201] Ronald J. Roth and Nancy Acton. “A facile semisynthesis of the antimalarial drug Qinghaosu”. In: *Journal of Chemical Education* 68.7 (1991), p. 612. DOI: `10.1021/ed068p612`.

[202] Richard K. Haynes and Simone C. Vonwiller. “Catalysed oxygenation of allylic hydroperoxides derived from qinghao (artemisinic) acid. Conversion of qinghao acid into dehydroginghaosu (artemisitene) and qinghaosu (artemisinin)”. In: *Journal of the Chemical Society, Chemical Communications* 6 (1990), p. 451. DOI: `10.1039/c39900000451`.

[203] Simone C. Vonwiller, Jacqueline A. Warner, Simon T. Mann, and Richard K. Haynes. “Copper(II) Trifluoromethanesulfonate-Induced Cleavage Oxygenation of Allylic Hydroperoxides Derived from Qinghao Acid in the Synthesis of Qinghaosu Derivatives: Evidence for the Intermediacy of Enols”. In: *Journal of the American Chemical Society* 117.45 (1995), pp. 11098–11105. DOI: `10.1021/ja00150a009`.

[204] Richard K. Haynes and Simone C. Vonwiller. “From Qinghao, Marvelous Herb of Antiquity, to the Antimalarial Trioxane Qinghaosuand Some Remarkable New Chemistry”. In: *Accounts of Chemical Research* 30.2 (1997), pp. 73–79. DOI: `10.1021/ar950058w`.

[205] Kaitlyn Varela, Hadi D. Arman, and Francis K. Yoshimoto. “Synthesis of 3,3-2H2-Dihydroartemisinic Acid to Measure the Rate of Nonenzymatic Conversion of Dihydroartemisinic Acid to Artemisinin”. In: *Journal of natural products* 83.1 (2020), pp. 66–78. DOI: `10.1021/acs.jnatprod.9b00686`.

[206] Kaitlyn Varela, Hadi D. Arman, and Francis K. Yoshimoto. “Synthesis of 15,15,15-2H3-Dihydroartemisinic Acid and Isotope Studies Support a Mixed Mechanism in the Endoperoxide Formation to Artemisinin”. In: *Journal of Natural Products* 84.7 (2021), pp. 1967–1984. DOI: `10.1021/acs.jnatprod.1c00246`.

[207] Zerong Wang. “Hock Rearrangement”. In: *Comprehensive Organic Name Reactions and Reagents*. American Cancer Society, 2010, pp. 1438–1442. DOI: `10.1002/9780470638859.conrr321`.

[208] Zacharias Amara, Jessica F. B. Bellamy, Raphael Horvath, Samuel J. Miller, Andrew Beeby, et al. “Applying green chemistry to the photochemical route to artemisinin”. In: *Nature Chemistry* 7.6 (2015), pp. 489–495. DOI: `10.1038/nchem.2261`.

[209] Shi-Man Hui, Koon-Sin Ngo, and Geoffrey D. Brown. “Epimerization in acid degradation products of artemisinin”. In: *Journal of the Chemical Society, Perkin Transactions 1* 22 (1997), pp. 3435–3442. DOI: `10.1039/A702714A`.

[210] Darren S. Lee, Zacharias Amara, Charlotte A. Clark, Zeyuan Xu, Bruce Kakimpa, et al. “Continuous Photo-Oxidation in a Vortex Reactor: Efficient Operations Using Air Drawn from the Laboratory”. In: *Organic Process Research & Development* 21.7 (2017), pp. 1042–1050. DOI: `10.1021/acs.oprd.7b00153`.

[211] François Lévesque and Peter H. Seeberger. “Continuous-flow synthesis of the anti-malaria drug artemisinin”. In: *Angewandte Chemie (Int. ed.)* 51.7 (2012), pp. 1706–1709. DOI: `10.1002/anie.201107446`.

[212] Liang Feng, Ying Wang, Shuai Yuan, Kun-Yu Wang, Jia-Luo Li, et al. “Porphyrinic Metal–Organic Frameworks Installed with Brønsted Acid Sites for Efficient Tandem Semisynthesis of Artemisinin”. In: *ACS Catalysis* 9.6 (2019), pp. 5111–5118. DOI: `10.1021/acscatal.8b04960`.

[213] Stephanie H. Kung, Sean Lund, Abhishek Murarka, Derek McPhee, and Chris J. Paddon. “Approaches and Recent Developments for the Commercial Production of Semi-synthetic Artemisinin”. In: *Frontiers in Plant Science* 9 (2018), p. 87. DOI: `10.3389/fpls.2018.00087`.

[214] Zoltán Horváth, Elena Horosanskaia, Ju Weon Lee, Heike Lorenz, Kerry Gilmore, et al. “Recovery of Artemisinin from a Complex Reaction Mixture Using Continuous Chromatography and Crystallization”. In: *Organic Process Research & Development* 19.6 (2015), pp. 624–634. DOI: `10.1021/acs.oprd.5b00048`.

[215] Elena Horosanskaia, Susann Triemer, Andreas Seidel-Morgenstern, and Heike Lorenz. “Purification of Artemisinin from the Product Solution of a Semisynthetic Reaction within a Single Crystallization Step”. In: *Organic Process Research & Development* 23.9 (2019), pp. 2074–2079. DOI: `10.1021/acs.oprd.9b00175`.

[216] Lingqiao Wu, Bruna L. Abreu, Alexander J. Blake, Laurence J. Taylor, William Lewis, et al. “Multigram Synthesis of Trioxanes Enabled by a Supercritical CO2 Integrated Flow Process”. In: *Organic Process Research & Development* 25.8 (2021), pp. 1873–1881. DOI: `10.1021/acs.oprd.1c00111`.

[217] Caleb J. Kong, Daniel Fisher, Bimbisar K. Desai, Yuan Yang, Saeed Ahmad, et al. “High throughput photo-oxidations in a packed bed reactor system”. In: *Bioorganic & medicinal chemistry* 25.23 (2017), pp. 6203–6208. DOI: `10.1016/j.bmc.2017.07.004`.

[218] Mohsen Tamtaji, Mohammad Kazemeini, Abhishek Tyagi, and Alexander Perez Roxas. “Selective Photooxygenation of Dihydroartemisinic Acid in a Reusable Microreactor with Physically Immobilized Photocatalysts”. In: *Materials Research Bulletin* 145 (2022), p. 111540. DOI: `10.1016/j.materresbull.2021.111540`.

[219] Christopher G. Thomson, Ai-Lan Lee, and Filipe Vilela. “Heterogeneous photocatalysis in flow chemical reactors”. In: *Beilstein Journal of Organic Chemistry* 16 (2020), pp. 1495–1549. DOI: `10.3762/bjoc.16.125`.

[220] Robin Smith. *Chemical Process: Design and Integration*. First. Wiley, 2014. ISBN: 978-1-119-09441-8.

[221] Tom van Gerven, Guido Mul, Jacob Moulijn, and Andrzej Stankiewicz. “A review of intensification of photocatalytic processes”. In: *Chemical Engineering and Processing: Process Intensification* 46.9 (2007), pp. 781–789. DOI: `10.1016/j.cep.2007.05.012`.

[222] Emine Kayahan, Mathias Jacobs, Leen Braeken, Leen Cj Thomassen, Simon Kuhn, et al. “Dawn of a new era in industrial photochemistry: the scale-up of micro- and mesostructured photoreactors”. In: *Beilstein Journal of Organic Chemistry* 16 (2020), pp. 2484–2504. DOI: `10.3762/bjoc.16.202`.

[223] K. Jähnisch and U. Dingerdissen. “Photochemical Generation and [4+2]-Cycloaddition of Singlet Oxygen in a Falling-Film Micro Reactor”. In: *Chemical Engineering & Technology* 28.4 (2005), pp. 426–427. DOI: `10.1002/ceat.200407139`.

[224] Ma’moun Al-Rawashdeh, Alberto Cantu-Perez, Dirk Ziegenbalg, Patrick Löb, Asterios Gavriilidis, et al. “Microstructure-based intensification of a falling film microreactor through optimal film setting with realistic profiles and in-channel induced mixing”. In: *Chemical Engineering Journal* 179 (2012), pp. 318–329. DOI: `10.1016/j.cej.2011.11.014`.

[225] Oksana Shvydkiv, Carolin Limburg, Kieran Nolan, and Michael Oelgemöller. “Synthesis of Juglone (5-Hydroxy-1,4-Naphthoquinone) in a Falling Film Microreactor”. In: *Journal of Flow Chemistry* 2.2 (2012), pp. 52–55. DOI: `10.1556/jfchem.2012.00022`.

[226] Charlotte A. Clark, Darren S. Lee, Stephen J. Pickering, Martyn Poliakoff, and Michael W. George. “A Simple and Versatile Reactor for Photochemistry”. In: *Organic Process Research & Development* 20.10 (2016), pp. 1792–1798. DOI: `10.1021/acs.oprd.6b00257`.

[227] Alexander Yavorskyy, Oksana Shvydkiv, Carolin Limburg, Kieran Nolan, Yan M. C. Delauré, et al. “Photooxygenations in a bubble column reactor”. In: *Green Chemistry* 14.4 (2012), p. 888. DOI: `10.1039/c2gc16439f`.

[228] B. O. Burek, A. Sutor, D. W. Bahnemann, and J. Z. Bloh. “Completely integrated wirelessly-powered photocatalyst-coated spheres as a novel means to perform heterogeneous photocatalytic reactions”. In: *Catalysis Science & Technology* 7.21 (2017), pp. 4977–4983. DOI: `10.1039/C7CY01537B`.

[229] Michael N. Gandy, Colin L. Raston, and Keith A. Stubbs. “Photoredox catalysis under shear using thin film vortex microfluidics”. In: *Chemical communications (Cambridge, England)* 51.55 (2015), pp. 11041–11044. DOI: `10.1039/c5cc02153g`.

[230] Martin Obst and Burkhard König. “Solvent-free, visible-light photocatalytic alcohol oxidations applying an organic photocatalyst”. In: *Beilstein journal of organic chemistry* 12 (2016), pp. 2358–2363. DOI: `10.3762/bjoc.12.229`.

[231] Darren S. Lee, Medhat Sharabi, Richard Jefferson-Loveday, Stephen J. Pickering, Martyn Poliakoff, et al. “Scalable Continuous Vortex Reactor for Gram to Kilo Scale for UV and Visible Photochemistry”. In: *Organic Process Research & Development* 24.2 (2020), pp. 201–206. DOI: `10.1021/acs.oprd.9b00475`.

[232] K. Barberis and C. R. Howarth. “Reactivity Studies In The Ozonolysis Of Pollutants Using A Perforated Spinning Disc Reactor To Enhance Mass Transfer”. In: *Ozone: Science & Engineering* 13.5 (1991), pp. 501–519. DOI: `10.1080/01919512.1991.10555698`.

[233] D. Dionysiou. “Rotating disk photocatalytic reactor: development, characterization, and evaluation for the destruction of organic pollutants in water”. In: *Water Research* 34.11 (2000), pp. 2927–2940. DOI: `10.1016/S0043-1354(00)00022-1`.

[234] Erica N. DeLaney, Darren S. Lee, Luke D. Elliott, Jing Jin, Kevin I. Booker-Milburn, et al. “A laboratory-scale annular continuous flow reactor for UV photochemistry using excimer lamps for discrete wavelength excitation and its use in a wavelength study of a photodecarboxlyative cyclisation”. In: *Green Chemistry* 19.6 (2017), pp. 1431–1438. DOI: `10.1039/C6GC02888H`.

[235] Georgios I. Ioannou, Tamsyn Montagnon, Dimitris Kalaitzakis, Spiros A. Pergantis, and Georgios Vassilikogiannakis. “A Novel Nebulizer-Based Continuous Flow Reactor: Introducing the Use of Pneumatically Generated Aerosols for Highly Productive Photooxidations”. In: *ChemPhotoChem* 1.5 (2017), pp. 173–177. DOI: `10.1002/cptc.201600054`.

[236] Gaowei Wu, Enhong Cao, Peter Ellis, Achilleas Constantinou, Simon Kuhn, et al. “Development of a flat membrane microchannel packed-bed reactor for scalable aerobic oxidation of benzyl alcohol in flow”. In: *Chemical Engineering Journal* 377 (2019), p. 120086. DOI: `10.1016/j.cej.2018.10.023`.

[237] François Lévesque, Michael J. Di Maso, Karthik Narsimhan, Michael K. Wismer, and John R. Naber. “Design of a Kilogram Scale, Plug Flow Photoreactor Enabled by High Power LEDs”. In: *Organic Process Research & Development* 24.12 (2020), pp. 2935–2940. DOI: `10.1021/acs.oprd.0c00373`.

[238] Dario Cambié, Cecilia Bottecchia, Natan J. W. Straathof, Volker Hessel, and Timothy Noël. “Applications of Continuous-Flow Photochemistry in Organic Synthesis, Material Science, and Water Treatment”. In: *Chemical Reviews* 116.17 (2016), pp. 10276–10341. DOI: `10.1021/acs.chemrev.5b00707`.

[239] M. Poliakoff and M. W. George. “Manufacturing chemicals with light: any role in the circular economy?” In: *Philosophical Transactions of the Royal Society A: Mathematical, Physical and Engineering Sciences* 378.2176 (2020), p. 20190260. DOI: `10.1098/rsta.2019.0260`.

[240] Christian G. Bochet. “On the Sustainability of Photochemical Reactions”. In: *CHIMIA International Journal for Chemistry* 73.9 (2019), pp. 720–723. DOI: `10.2533/chimia.2019.720`.

[241] Laura Buglioni, Fabian Raymenants, Aidan Slattery, Stefan D. A. Zondag, and Timothy Noël. “Technological Innovations in Photochemistry for Organic Synthesis: Flow Chemistry, High-Throughput Experimentation, Scale-up, and Photoelectrochemistry”. In: *Chemical Reviews* (2021). DOI: `10.1021/acs.chemrev.1c00332`.

[242] Arlene Bonner, Aisling Loftus, Alex C. Padgham, and Marcus Baumann. “Forgotten and forbidden chemical reactions revitalised through continuous flow technology”. In: *Organic & Biomolecular Chemistry* 19.36 (2021), pp. 7737–7753. DOI: `10.1039/D1OB01452H`.

[243] Marcus Baumann and Ian R. Baxendale. “The synthesis of active pharmaceutical ingredients (APIs) using continuous flow chemistry”. In: *Beilstein journal of organic chemistry* 11 (2015), pp. 1194–1219. DOI: `10.3762/bjoc.11.134`.

[244] Mateo Berton, Juliana M. de Souza, Irini Abdiaj, D. Tyler McQuade, and David R. Snead. “Scaling continuous API synthesis from milligram to kilogram: extending the enabling benefits of micro to the plant”. In: *Journal of Flow Chemistry* 10.1 (2020), pp. 73–92. DOI: `10.1007/s41981-019-00060-x`.

[245] Christopher A. Hone, Dominique M. Roberge, and C. Oliver Kappe. “The Use of Molecular Oxygen in Pharmaceutical Manufacturing: Is Flow the Way to Go?” In: *ChemSusChem* 10.1 (2017), pp. 32–41. DOI: `10.1002/cssc.201601321`.

[246] Andrea Basso and Pietro Capurro. “3 Recent applications of photochemistry on large-scale synthesis (2015–2019)”. In: *Photochemistry*. Ed. by Stefano Protti and Carlotta Raviola. Vol. 48. Photochemistry. Cambridge: Royal Society of Chemistry, 2020, pp. 293–321. ISBN: 978-1-83916-140-7. DOI: `10.1039/9781839162114-00293`.

[247] Jayson S. Wau, Mark J. Robertson, and Michael Oelgemöller. “Solar Photooxygenations for the Manufacturing of Fine Chemicals-Technologies and Applications”. In: *Molecules* 26.6 (2021), p. 1685. DOI: `10.3390/molecules26061685`.

[248] Matthew B. Plutschack, Bartholomäus Pieber, Kerry Gilmore, and Peter H. Seeberger. “The Hitchhiker’s Guide to Flow Chemistry”. In: *Chemical Reviews* 117.18 (2017), pp. 11796–11893. DOI: `10.1021/acs.chemrev.7b00183`.

[249] Timothy Noël, ed. *Photochemical processes in continuous-flow reactors: From engineering principles to chemical applications*. World Scientific, 2017. ISBN: 978-1-78634-218-8. DOI: `10.1142/q0065`.

[250] Mara Guidi, Peter H. Seeberger, and Kerry Gilmore. “How to approach flow chemistry”. In: *Chemical Society Reviews* 49.24 (2020), pp. 8910–8932. DOI: `10.1039/C9CS00832B`.

[251] Christopher A. Hone and C. Oliver Kappe. “Towards the Standardization of Flow Chemistry Protocols for Organic Reactions”. In: *Chemistry - Methods* (2021). DOI: `10.1002/cmtd.202100059`.

[252] Julio C. Pastre, Duncan L. Browne, and Steven V. Ley. “Flow chemistry syntheses of natural products”. In: *Chemical Society Reviews* 42.23 (2013), pp. 8849–8869. DOI: `10.1039/c3cs60246j`.

[253] Fabrizio Politano and Gabriela Oksdath-Mansilla. “Light on the Horizon: Current Research and Future Perspectives in Flow Photochemistry”. In: *Organic Process Research & Development* 22.9 (2018), pp. 1045–1062. DOI: `10.1021/acs.oprd.8b00213`.

[254] Thomas H. Rehm. “Flow Photochemistry as a Tool in Organic Synthesis”. In: *Chemistry – A European Journal* 26.71 (2020), pp. 16952–16974. DOI: `10.1002/chem.202000381`.

[255] Volker Hessel, Dana Kralisch, Norbert Kockmann, Timothy Noël, and Qi Wang. “Novel process windows for enabling, accelerating, and uplifting flow chemistry”. In: *ChemSusChem* 6.5 (2013), pp. 746–789. DOI: `10.1002/cssc.201200766`.

[256] Yuanhai Su, Natan J. W. Straathof, Volker Hessel, and Timothy Noël. “Photochemical transformations accelerated in continuous-flow reactors: basic concepts and applications”. In: *Chemistry* 20.34 (2014), pp. 10562–10589. DOI: `10.1002/chem.201400283`.

[257] Karine Loubière, Michael Oelgemöller, Tristan Aillet, Odile Dechy-Cabaret, and Laurent Prat. “Continuous-flow photochemistry: A need for chemical engineering”. In: *Chemical Engineering and Processing: Process Intensification* 104 (2016), pp. 120–132. DOI: `10.1016/j.cep.2016.02.008`.

[258] Nicole C. Neyt and Darren L. Riley. “Application of reactor engineering concepts in continuous flow chemistry: a review”. In: *Reaction Chemistry & Engineering* 6.8 (2021), pp. 1295–1326. DOI: `10.1039/D1RE00004G`.

[259] Carlo Sambiagio and Timothy Noël. “Flow Photochemistry: Shine Some Light on Those Tubes!” In: *Trends in Chemistry* 2.2 (2020), pp. 92–106. DOI: `10.1016/j.trechm.2019.09.003`.

[260] Zhengbiao Peng, Guichao Wang, Behdad Moghtaderi, and Elham Doroodchi. “A review of microreactors based on slurry Taylor (segmented) flow”. In: *Chemical Engineering Science* 247 (2022), p. 117040. DOI: `10.1016/j.ces.2021.117040`.

[261] Zhengya Dong, Zhenghui Wen, Fang Zhao, Simon Kuhn, and Timothy Noël. “Scale-up of micro- and milli-reactors: An overview of strategies, design principles and applications”. In: *Chemical Engineering Science: X* 10 (2021), p. 100097. DOI: `10.1016/j.cesx.2021.100097`.

[262] Tristan Aillet, Karine Loubiere, Odile Dechy-Cabaret, and Laurent Prat. “Accurate Measurement of the Photon Flux Received Inside Two Continuous Flow Microphotoreactors by Actinometry”. In: *International Journal of Chemical Reactor Engineering* 12.1 (2014), pp. 257–269. DOI: `10.1515/ijcre-2013-0121`.

[263] Dirk Ziegenbalg, Benjamin Wriedt, Günter Kreisel, and Dana Kralisch. “Investigation of Photon Fluxes within Microstructured Photoreactors Revealing Great Optimization Potentials”. In: *Chemical Engineering & Technology* 39.1 (2016), pp. 123–134. DOI: `10.1002/ceat.201500498`.

[264] Claes Joris, Brabants Bert, Kuhn Simon, Thomassen Leen, and Leblebici Mumin Enis. “Comparative Study of Convective and Radiative Heat Transfer in Milliflow Reactors”. In: *Chemical Engineering Transactions* 74 (2019), pp. 1333–1338. DOI: `10.3303/CET1974223`.

[265] Hannes P. L. Gemoets, Yuanhai Su, Minjing Shang, Volker Hessel, Rafael Luque, et al. “Liquid phase oxidation chemistry in continuous-flow microreactors”. In: *Chemical Society Reviews* 45.1 (2016), pp. 83–117. DOI: `10.1039/C5CS00447K`.

[266] C. Liebner, J. Fischer, S. Heinrich, T. Lange, H. Hieronymus, et al. “Are micro reactors inherently safe? An investigation of gas phase explosion propagation limits on ethene mixtures”. In: *Process Safety and Environmental Protection* 90.2 (2012), pp. 77–82. DOI: `10.1016/j.psep.2011.08.006`.

[267] Hartmut Hieronymus, Johannes Fischer, Sebastian Heinrich, Christian Liebner, Thomas Lange, et al. “Sicherheitstechnische Untersuchungen zum Betrieb von Mikroreaktoren im Explosionsbereich”. In: *Chemie Ingenieur Technik* 83.10 (2011), pp. 1742–1747. DOI: `10.1002/cite.201100112`.

[268] Stefan Haase, Dmitry Yu. Murzin, and Tapio Salmi. “Review on Hydrodynamics and Mass Transfer in Minichannel Wall Reactors with GasTaylor Flow”. In: *Chemical Engineering Research and Design* 113 (2016), pp. 304–329. DOI: `10.1016/j.cherd.2016.06.017`.

[269] Rufat Abiev, Stanislav Svetlov, and Stefan Haase. “Hydrodynamics and Mass Transfer of Gas-Liquid and Liquid-Liquid Taylor Flow in Microchannels”. In: *Chemical Engineering & Technology* 40.11 (2017), pp. 1985–1998. DOI: `10.1002/ceat.201700041`.

[270] P. Sobieszuk, J. Aubin, and R. Pohorecki. “Hydrodynamics and Mass Transfer in Gas-Liquid Flows in Microreactors”. In: *Chemical Engineering & Technology* 35.8 (2012), pp. 1346–1358. DOI: `10.1002/ceat.201100643`.

[271] Axel Günther, Manish Jhunjhunwala, Martina Thalmann, Martin A. Schmidt, and Klavs F. Jensen. “Micromixing of miscible liquids in segmented gas-liquid flow”. In: *Langmuir : the ACS journal of surfaces and colloids* 21.4 (2005), pp. 1547–1555. DOI: `10.1021/la0482406`.

[272] P. Angeli and A. Gavriilidis. “Hydrodynamics of Taylor Flow in Small Channels: A Review”. In: *Proceedings of the Institution of Mechanical Engineers, Part C: Journal of Mechanical Engineering Science* 222.5 (2008), pp. 737–751. DOI: `10.1243/09544062JMES776`.

[273] Yuanhai Su. “A Geeral Introduction to Transport Phenomena in Continuous-Flow Microreactors for Photochemical Transformations”. In: *Photochemical processes in continuous-flow reactors*. Ed. by Timothy Noël. New Jersey, London, and Singapore: World Scientific, 2017, pp. 37–68. ISBN: 978-1-78634-218-8.

[274] Madhvanand N. Kashid, Albert Renken, and Lioubov Kiwi-Minsker. “Gas–liquid and liquid–liquid mass transfer in microstructured reactors”. In: *Chemical Engineering Science* 66.17 (2011), pp. 3876–3897. DOI: `10.1016/j.ces.2011.05.015`.

[275] Carl J. Mallia and Ian R. Baxendale. “The Use of Gases in Flow Synthesis”. In: *Organic Process Research & Development* 20.2 (2016), pp. 327–360. DOI: `10.1021/acs.oprd.5b00222`.

[276] Senne Fransen and Simon Kuhn. “A model-based technique for the determination of interfacial fluxes in gas–liquid flows in capillaries”. In: *Reaction Chemistry & Engineering* 1.3 (2016), pp. 288–299. DOI: `10.1039/C5RE00053J`.

[277] Axel Günther, Saif A. Khan, Martina Thalmann, Franz Trachsel, and Klavs F. Jensen. “Transport and reaction in microscale segmented gas-liquid flow”. In: *Lab on a chip* 4.4 (2004), pp. 278–286. DOI: `10.1039/b403982c`.

[278] Anca Roibu, Tom van Gerven, and Simon Kuhn. “Photon Transport and Hydrodynamics in Gas–Liquid Flows Part 1: Characterization of Taylor Flow in a Photo Microreactor”. In: *ChemPhotoChem* 4.10 (2020), pp. 5181–5192. DOI: `10.1002/cptc.202000065`.

[279] Fabian Guba, Ümit Tastan, Katrin Gugeler, Melanie Buntrock, Tobias Rommel, et al. “Rapid Prototyping for Photochemical Reaction Engineering”. In: *Chemie Ingenieur Technik* (2018). DOI: `10.1002/cite.201800035`.

[280] Cesar Parra-Cabrera, Clement Achille, Simon Kuhn, and Rob Ameloot. “3D printing in chemical engineering and catalytic technology: structured catalysts, mixers and reactors”. In: *Chemical Society Reviews* 47.1 (2018), pp. 209–230. DOI: `10.1039/C7CS00631D`.

[281] Jochen M. Neumaier, Amiera Madani, Thomas Klein, and Thomas Ziegler. “Low-budget 3D-printed equipment for continuous flow reactions”. In: *Beilstein journal of organic chemistry* 15.1 (2019). DOI: `10.3762/bjoc.15.50`.

[282] Matthew R. Hartings and Zeeshan Ahmed. “Chemistry from 3D printed objects”. In: *Nature Reviews Chemistry* 3.5 (2019), pp. 305–314. DOI: `10.1038/s41570-019-0097-z`.

[283] Matthew J. Harding, Sarah Brady, Heather O’Connor, Rafael Lopez-Rodriguez, Matthew D. Edwards, et al. “3D printing of PEEK reactors for flow chemistry and continuous chemical processing”. In: *Reaction Chemistry & Engineering* 5.4 (2020), pp. 728–735. DOI: `10.1039/C9RE00408D`.

[284] Victor Sans. “Emerging trends in flow chemistry enabled by 3D printing: Robust reactors, biocatalysis and electrochemistry”. In: *Current Opinion in Green and Sustainable Chemistry* 25 (2020), p. 100367. DOI: `10.1016/j.cogsc.2020.100367`.

[285] Sourav Chatterjee, Mara Guidi, Peter H. Seeberger, and Kerry Gilmore. “Automated radial synthesis of organic molecules”. In: *Nature* 579.7799 (2020), pp. 379–384. DOI: `10.1038/s41586-020-2083-5`.

[286] Momoe Nakano, Yasuhiro Nishiyama, Hiroki Tanimoto, Tsumoru Morimoto, and Kiyomi Kakiuchi. “Remarkable Improvement of Organic Photoreaction Efficiency in the Flow Microreactor by the Slug Flow Condition Using Water”. In: *Organic Process Research & Development* 20.9 (2016), pp. 1626–1632. DOI: `10.1021/acs.oprd.6b00181`.

[287] Yuanhai Su, Volker Hessel, and Timothy Noël. “A compact photomicroreactor design for kinetic studies of gas-liquid photocatalytic transformations”. In: *AIChE Journal* 61.7 (2015), pp. 2215–2227. DOI: `10.1002/aic.14813`.

[288] Tristan Aillet, Karine Loubière, Odile Dechy-Cabaret, and Laurent Prat. “Microreactors as a Tool for Acquiring Kinetic Data on Photochemical Reactions”. In: *Chemical Engineering & Technology* 39.1 (2016), pp. 115–122. DOI: `10.1002/ceat.201500163`.

[289] Chong Shen, Minjing Shang, Hong Zhang, and Yuanhai Su. “A UV–LEDs based photomicroreactor for mechanistic insights and kinetic studies in the norbornadiene photoisomerization”. In: *AIChE Journal* 66.2 (2020). DOI: `10.1002/aic.16841`.

[290] Robbie Radjagobalou, Jean-François Blanco, Luca Petrizza, Mickael Le Bechec, Odile Dechy-Cabaret, et al. “Efficient Photooxygenation Process of Biosourced α-Terpinene by Combining Controlled LED-Driven Flow Photochemistry and Rose Bengal-Anchored Polymer Colloids”. In: *ACS Sustainable Chemistry & Engineering* 8.50 (2020), pp. 18568–18576. DOI: `10.1021/acssuschemeng.0c06627`.

[291] Connor J. Taylor, Jamie A. Manson, Graeme Clemens, Brian A. Taylor, Thomas W. Chamberlain, et al. “Modern advancements in continuous-flow aided kinetic analysis”. In: *Reaction Chemistry & Engineering* 7 (5 2022), pp. 1037–1046. DOI: `10.1039/D1RE00467K`.

[292] Konstantin N. Loponov, Joao Lopes, Maciej Barlog, Ekaterina V. Astrova, Andrei V. Malkov, et al. “Optimization of a Scalable Photochemical Reactor for Reactions with Singlet Oxygen”. In: *Organic Process Research & Development* 18.11 (2014), pp. 1443–1454. DOI: `10.1021/op500181z`.

[293] Octave Levenspiel. *Chemical Reaction Engineering*. 3rd ed. New York: Wiley, 1999. ISBN: 978-0-471-25424-9.

[294] Manfred Baerns, Arno Behr, Axel Brehm, Jürgen Gmehling, Kai-Olaf Hinrichsen, et al. *Technische Chemie*. Zweite, erweiterte Auflage. Weinheim: Wiley-VCH, 2013. ISBN: 3527330720.

[295] Orlando M. Alfano, Roberto L. Romero, and Alberto E. Cassano. *Modelling of Radiation Transport and Energy Absorption in Photoreactors*. Vol. 4. Advances in Transport Processes. 1986.

[296] Jonathan Z. Bloh. “A Holistic Approach to Model the Kinetics of Photocatalytic Reactions”. In: *Frontiers in Chemistry* 7 (2019), p. 128. DOI: `10.3389/fchem.2019.00128`.

[297] M. F. Modest. *Radiative Heat Transfer*. third. New York: Academic Press, 2013. ISBN: 978-0-12-386944-9.

[298] Alberto E. Cassano, Carlos A. Martin, Rodolfo J. Brandi, and Orlando M. Alfano. “Photoreactor Analysis and Design: Fundamentals and Applications”. In: *Industrial & Engineering Chemistry Research* 34.7 (1995), pp. 2155–2201. DOI: `10.1021/ie00046a001`.

[299] Mario J. Muñoz-Batista, María M. Ballari, Anna Kubacka, Orlando M. Alfano, and Marcos Fernández-García. “Braiding Kinetics and Spectroscopy in Photo-Catalysis: The Spectro-Kinetic Approach”. In: *Chemical Society Reviews* 48.2 (2019), pp. 637–682. DOI: `10.1039/C8CS00108A`.

[300] Anca Roibu and Simon Kuhn. “Modeling of Photochemical Processes in Continuous-Flow Reactors”. In: *Photochemical processes in continuous-flow reactors*. Ed. by Timothy Noël. World Scientific, 2017, pp. 69–96. ISBN: 978-1-78634-218-8.

[301] Orlando Mario Alfano, María Lucila Satuf, and Agustina Manassero. “Photon Transport Phenomena: Radiation Absorption and Scattering Effects on Photoreactors”. In: *Photochemical processes in continuous-flow reactors*. Ed. by Timothy Noël. World Scientific, 2017, pp. 97–122. ISBN: 978-1-78634-218-8.

[302] John R. Howell, Robert Siegel, and M. Pinar Mengüç. *Thermal radiation heat transfer*. 5th ed. CRC Press and Francis & Taylor, 2011. ISBN: 9781439805336.

[303] Orlando M. Alfano, Roberto L. Romero, and Alberto E. Cassano. “Radiation field modelling in photoreactors—I. homogeneous media”. In: *Chemical Engineering Science* 41.3 (1986), pp. 421–444. DOI: `10.1016/0009-2509(86)87025-7`.

[304] A. Gianetto and P. L. Silveston. *Multiphase chemical reactors:Theory, design, scale-up*. Hemisphere Publishing,New York, NY, 1986.

[305] Hugo A. Jakobsen. *Chemical Reactor Modeling: Multiphase Reactive Flows*. Berlin, Heidelberg: Springer Berlin Heidelberg, 2008. ISBN: 9783540686224.

[306] Said Irandoust, Sylvie Ertlé, and Bengt Andersson. “Gas-liquid mass transfer in taylor flow through a capillary”. In: *The Canadian Journal of Chemical Engineering* 70.1 (1992), pp. 115–119. DOI: `10.1002/cjce.5450700116`.

[307] C. O. Vandu, H. Liu, and R. Krishna. “Mass transfer from Taylor bubbles rising in single capillaries”. In: *Chemical Engineering Science* 60.22 (2005), pp. 6430–6437. DOI: `10.1016/j.ces.2005.01.037`.

[308] C. O. Vandu, J. Ellenberger, and R. Krishna. “Hydrodynamics and mass transfer in an upflow monolith loop reactor”. In: *Chemical Engineering and Processing: Process Intensification* 44.3 (2005), pp. 363–374. DOI: `10.1016/j.cep.2004.05.011`.

[309] Bercić. “The role of gas bubbles and liquid slug lengths on mass transport in the Taylor flow through capillaries”. In: *Chem. Eng. Sci.* 52.(21–22) (1997), p. 3709.

[310] Johan J. Heiszwolf, Michiel T. Kreutzer, Menno G. van den Eijnden, Freek Kapteijn, and Jacob A. Moulijn. “Gas–liquid mass transfer of aqueous Taylor flow in monoliths”. In: *Catalysis Today* 69.1-4 (2001), pp. 51–55. DOI: `10.1016/S0920-5861(01)00354-6`.

[311] J. M. van Baten and R. Krishna. “CFD simulations of mass transfer from Taylor bubbles rising in circular capillaries”. In: *Chemical Engineering Science* 59.12 (2004), pp. 2535–2545. DOI: `10.1016/j.ces.2004.03.010`.

[312] Jun Yue, Guangwen Chen, Quan Yuan, Lingai Luo, and Yves Gonthier. “Hydrodynamics and mass transfer characteristics in gas–liquid flow through a rectangular microchannel”. In: *Chemical Engineering Science* 62.7 (2007), pp. 2096–2108. DOI: `10.1016/j.ces.2006.12.057`.

[313] Jun Yue, Lingai Luo, Yves Gonthier, Guangwen Chen, and Quan Yuan. “An experimental study of air–water Taylor flow and mass transfer inside square microchannels”. In: *Chemical Engineering Science* 64.16 (2009), pp. 3697–3708. DOI: `10.1016/j.ces.2009.05.026`.

[314] PaweŁ Sobieszuk. “Determination of the Interfacial Area and Mass Transfer Coefficients in the Taylor Gas Liquid Flow in a Microchannel”. In: *Chemical Engineering Science* (2011), p. 9.

[315] Dingsheng Liu and Shudong Wang. “Gas–Liquid Mass Transfer in Taylor Flow through Circular Capillaries”. In: *Industrial & Engineering Chemistry Research* 50.4 (2011), pp. 2323–2330. DOI: `10.1021/ie902055p`.

[316] Simon Kuhn and Klavs F. Jensen. “A pH-Sensitive Laser-Induced Fluorescence Technique To Monitor Mass Transfer in Multiphase Flows in Microfluidic Devices”. In: *Industrial & Engineering Chemistry Research* 51.26 (2012), pp. 8999–9006. DOI: `10.1021/ie300978n`.

[317] R.Sh. Abiev. “Bubbles velocity, Taylor circulation rate and mass transfer model for slug flow in milli- and microchannels”. In: *Chemical Engineering Journal* 227 (2013), pp. 66–79. DOI: `10.1016/j.cej.2012.10.009`.

[318] Chaoqun Yao, Zhengya Dong, Yuchao Zhao, and Guangwen Chen. “The effect of system pressure on gas-liquid slug flow in a microchannel”. In: *AIChE Journal* 60.3 (2014), pp. 1132–1142. DOI: `10.1002/aic.14306`.

[319] Milad Abolhasani, Eugenia Kumacheva, and Axel Günther. “Peclet Number Dependence of Mass Transfer in Microscale Segmented Gas–Liquid Flow”. In: *Industrial & Engineering Chemistry Research* 54.36 (2015), pp. 9046–9051. DOI: `10.1021/acs.iecr.5b01991`.

[320] Raghvendra Gupta, David F. Fletcher, and Brian S. Haynes. “On the CFD Modelling of Taylor Flow in Microchannels”. In: *Chemical Engineering Science* 64.12 (2009), pp. 2941–2950. DOI: `10.1016/j.ces.2009.03.018`.

[321] John R. Bourne. “Mixing and the Selectivity of Chemical Reactions”. In: *Organic Process Research & Development* 7.4 (2003), pp. 471–508. DOI: `10.1021/op020074q`.

[322] Ignasi Salvadó-Estivill, Alberto Brucato, and Gianluca Li Puma. “Two-Dimensional Modeling of a Flat-Plate Photocatalytic Reactor for Oxidation of Indoor Air Pollutants”. In: *Industrial & Engineering Chemistry Research* 46.23 (2007), pp. 7489–7496. DOI: `10.1021/ie070391r`.

[323] Tristan Aillet, Karine Loubière, Laurent Prat, and Odile Dechy-Cabaret. “Impact of the diffusion limitation in microphotoreactors”. In: *AIChE Journal* 61.4 (2015), pp. 1284–1299. DOI: `10.1002/aic.14718`.

[324] Kjell H. Bendiksen, Dag Maines, Randi Moe, and Sven Nuland. “The Dynamic Two-Fluid Model OLGA: Theory and Application”. In: *SPE Production Engineering* 6.02 (1991), pp. 171–180. DOI: `10.2118/19451-PA`.

[325] M. Ishii and Takashi Hibiki. *Thermo-Fluid Dynamics of Two-Phase Flow*. New York, N.Y: Springer Science+Business Media, 2006. ISBN: 978-0-387-28321-0 978-0-387-29187-1.

[326] Michiel T. Kreutzer, Freek Kapteijn, and Jacob A. Moulijn. “Fast Gas: A Case Study of Nitro-Aromatic Hydrogenation”. In: *Catalysis Today* (2005), p. 8.

[327] Bin Cao and Lingai Luo. “Modeling of Gas Liquid Taylor Flow in Capillaries by Using a Two Fluid Model”. In: *Industrial & Engineering Chemistry Research* (2012), p. 8.

[328] R. A. Peixoto and C. W. Bullard. “A Simulation and Design Model for Capillary Tube - Suction Line Heat Exchangers”. In: *International Refigeration and Air Conditioning Conference*. 1994, p. 7.

[329] B. Xu and P.K Bansal. “Non-Adiabatic Capillary Tube Flow: A Homogeneous Model and Process Description”. In: *Applied Thermal Engineering* 22.16 (2002), pp. 1801–1819. DOI: `10.1016/S1359-4311(02)00110-2`.

[330] Masoud Zareh, Morteza Khayat, and Hamed Fouladi. “Numerical Simulation of Two Phase Refrigerant Flow through Non-Adiabatic Capillary Tubes Using Drift Flux Model”. In: *Journal of Mechanical Science and Technology* 32.1 (2018), pp. 381–389. DOI: `10.1007/s12206-017-1238-2`.

[331] R. Gupta, D. F. Fletcher, and B. S. Haynes. “Taylor Flow in Microchannels: A Review of Experimental and Computational Work”. In: *The Journal of Computational Multiphase Flows* 2.1 (2010), pp. 1–31. DOI: `10.1260/1757-482X.2.1.1`.

[332] Martin Wörner. “Numerical Modeling of Multiphase Flows in Microfluidics and Micro Process Engineering: A Review of Methods and Applications”. In: *Microfluidics and Nanofluidics* 12.6 (2012), pp. 841–886. DOI: `10.1007/s10404-012-0940-8`.

[333] N. Zuber and J. A. Findlay. “Average Volumetric Concentration in Two-Phase Flow Systems”. In: *Journal of Heat Transfer* 87.4 (1965), pp. 453–468. DOI: `10.1115/1.3689137`.

[334] K. Mishima and T. Hibiki. “Some characteristics of air-water two-phase flow in small diameter vertical tubes”. In: *International Journal of Multiphase Flow* 22.4 (1996), pp. 703–712. DOI: `10.1016/0301-9322(96)00010-9`.

[335] Cristina S. Zalazar, Marisol D. Labas, Carlos A. Martín, Rodolfo J. Brandi, Orlando M. Alfano, et al. “The extended use of actinometry in the interpretation of photochemical reaction engineering data”. In: *Chemical Engineering Journal* 109.1-3 (2005), pp. 67–81. DOI: `10.1016/j.cej.2005.03.011`.

[336] H. J. Kuhn, S. E. Braslavsky, and R. Schmidt. “Chemical Actinometry (IUPAC Technical Report)”. In: *Pure and Applied Chemistry* 76.12 (2004), pp. 2105–2146. DOI: `10.1351/pac200476122105`.

[337] Benjamin Wriedt and Dirk Ziegenbalg. “Common Pitfalls in Chemical Actinometry”. In: *Journal of Flow Chemistry* 10.1 (2020), pp. 295–306. DOI: `10.1007/s41981-019-00072-7`.

[338] C. G. Hatchard and C. A. Parker. “A New Sensitive Chemical Actinometer - II. Potassium Ferrioxalate as a Standard Chemical Actinometer”. In: *Proceedings of the Royal Society of London. Series A. Mathematical and Physical Sciences* 235.1203 (1956), pp. 518–536. DOI: `10.1098/rspa.1956.0102`.

[339] John Lee and H. H. Seliger. “Quantum Yield of the Ferrioxalate Actinometer”. In: *The Journal of Chemical Physics* 40.2 (1964), pp. 519–523. DOI: `10.1063/1.1725147`.

[340] J. N. Demas, W. D. Bowman, E. F. Zalewski, and R. A. Velapoldi. “Determination of the Quantum Yield of the Ferrioxalate Actinometer with Electrically Calibrated Radiometers”. In: *The Journal of Physical Chemistry* 85.19 (1981), pp. 2766–2771. DOI: `10.1021/j150619a015`.

[341] Sara Goldstein and Joseph Rabani. “The ferrioxalate and iodide–iodate actinometers in the UV region”. In: *Journal of Photochemistry and Photobiology A: Chemistry* 193.1 (2008), pp. 50–55. DOI: `10.1016/j.jphotochem.2007.06.006`.

[342] Tímea Lehóczki, Éva Józsa, and Katalin Osz. “Ferrioxalate actinometry with online spectrophotometric detection”. In: *Journal of Photochemistry and Photobiology A: Chemistry* 251 (2013), pp. 63–68. DOI: `10.1016/j.jphotochem.2012.10.005`.

[343] Christian Weller, Sabrina Horn, and Hartmut Herrmann. “Effects of Fe(III)-Concentration, Speciation, Excitation-Wavelength and Light Intensity on the Quantum Yield of Iron(III)-Oxalato Complex Photolysis”. In: *Journal of Photochemistry and Photobiology A: Chemistry* 255 (2013), pp. 41–49. DOI: `10.1016/j.jphotochem.2013.01.014`.

[344] Benjamin Wriedt, Daniel Kowalczyk, and Dirk Ziegenbalg. “Experimental Determination of Photon Fluxes in Multilayer Capillary Photoreactors”. In: *ChemPhotoChem* 2.10 (2018), pp. 913–921. DOI: `10.1002/cptc.201800106`.

[345] Steffen Straub, Paul Brünker, Jörg Lindner, and Peter Vöhringer. “Femtosecond infrared spectroscopy reveals the primary events of the ferrioxalate actinometer”. In: *Physical Chemistry Chemical Physics* 20.33 (2018), pp. 21390–21403. DOI: `10.1039/c8cp03824d`.

[346] Steffen Straub, Paul Brünker, Jörg Lindner, and Peter Vöhringer. “An Iron Complex with a Bent, O-Coordinated CO2 Ligand Discovered by Femtosecond Mid-Infrared Spectroscopy”. In: *Angewandte Chemie (Int. ed.)* 57.18 (2018), pp. 5000–5005. DOI: `10.1002/anie.201800672`.

[347] Frank Hendrik Pilz, Jörg Lindner, and Peter Vöhringer. “Time-resolved Fourier-transform infrared spectroscopy reveals the hidden bimolecular process of the ferrioxalate actinometer”. In: *Physical Chemistry Chemical Physics* 21.43 (2019), pp. 23803–23807. DOI: `10.1039/c9cp05233j`.

[348] W. D. Bowman and J. N. Demas. “Ferrioxalate actinometry. A warning on its correct use”. In: *The Journal of Physical Chemistry* 80.21 (1976), pp. 2434–2435. DOI: `10.1021/j100562a025`.

[349] A. D. Kirk and C. Namasivayam. “Errors in ferrioxalate actinometry”. In: *Analytical Chemistry* 55.14 (1983), pp. 2428–2429. DOI: `10.1021/ac00264a053`.

[350] László Vincze, Terence J. Kemp, and Patrick R. Unwin. “Flow actinometry in a thin film reactor: modeling and measurements”. In: *Journal of Photochemistry and Photobiology A: Chemistry* 123.1-3 (1999), pp. 7–13. DOI: `10.1016/S1010-6030(99)00048-9`.

[351] Benjamin Wriedt and Dirk Ziegenbalg. “Application Limits of the Ferrioxalate Actinometer”. In: *ChemPhotoChem* 5.10 (2021), pp. 947–956. DOI: `10.1002/cptc.202100122`.

[352] Anca Roibu, Senne Fransen, M. Enis Leblebici, Glen Meir, Tom van Gerven, et al. “An Accessible Visible-Light Actinometer for the Determination of Photon Flux and Optical Pathlength in Flow Photo Microreactors”. In: *Scientific Reports* 8.1 (2018), p. 5421. DOI: `10.1038/s41598-018-23735-2`.

[353] Shin Aida, Kimitada Terao, Yasuhiro Nishiyama, Kiyomi Kakiuchi, and Michael Oelgemöller. “Microflow photochemistry—a reactor comparison study using the photochemical synthesis of terebic acid as a model reaction”. In: *Tetrahedron Letters* 53.42 (2012), pp. 5578–5581. DOI: `10.1016/j.tetlet.2012.07.143`.

[354] Matiss Reinfelds, Volker Hermanns, Thomas Halbritter, Josef Wachtveitl, Markus Braun, et al. “A Robust, Broadly Absorbing Fulgide Derivative as a Universal Chemical Actinometer for the UV to NIR Region”. In: *ChemPhotoChem* 3.6 (2019), pp. 441–449. DOI: `10.1002/cptc.201900010`.

[355] Mélanie Roseau, Vincent de Waele, Xavier Trivelli, Francois Xavier Cantrelle, Maël Penhoat, et al. “Azobenzene: a Visible–Light Chemical Actinometer for the Characterization of Fluidic Photosystems”. In: *Helvetica Chimica Acta* 104.7 (2021). DOI: `10.1002/hlca.202100071`.

[356] Xiangzhong Xie, René Schenkendorf, and Ulrike Krewer. “Efficient sensitivity analysis and interpretation of parameter correlations in chemical engineering”. In: *Reliability Engineering & System Safety* 187 (2019), pp. 159–173. DOI: `10.1016/j.ress.2018.06.010`.

[357] Xiangzhong Xie, René Schenkendorf, and Ulrike Krewer. “The Effect of Correlated Kinetic Parameters on (Bio)Chemical Reaction Networks”. In: *Chemie Ingenieur Technik* 91.5 (2019), pp. 632–636. DOI: `10.1002/cite.201800201`.

[358] Gaia Franceschini and Sandro Macchietto. “Model-Based Design of Experiments for Parameter Precision: State of the Art”. In: *Chemical Engineering Science* 63.19 (2008), pp. 4846–4872. DOI: `10.1016/j.ces.2007.11.034`.

[359] Krist V. Gernaey and Rafiqul Gani. “A Model-Based Systems Approach to Pharmaceutical Product-Process Design and Analysis”. In: *Chemical Engineering Science* 65.21 (2010), pp. 5757–5769. DOI: `10.1016/j.ces.2010.05.003`.

[360] Moritz Schulze. “Model identification and model-based analysis of the partial synthesis of artemisinin”. PhD Thesis. Karlsruhe: Karlsruher Institute for Technology, 2022.

[361] E. Walter and Luc Pronzato. *Identification of Parametric Models from Experimental Data*. Communications and Control Engineering. London: Springer, 1997. ISBN: 978-3-540-76119-8.

[362] Yonathan Bard. *Nonlinear Parameter Estimation*. New York: Academic Press, 1974. ISBN: 978-0-12-078250-5.

[363] Peter Englezos. *Applied Parameter Estimation for Chemical Engineers*. 1st ed. Chemical Industries Ser. Baton Rouge: Chapman and Hall/CRC, 2000. ISBN: 0-8247-9561-X.

[364] Oliver Nelles. *Nonlinear system identification: From classical approaches to neural networks and fuzzy models*. Engineering online library. Berlin and Heidelberg: Springer, 2001. ISBN: 3-540-67369-5.

[365] Vincent Laue, Fridolin Röder, and Ulrike Krewer. “Practical identifiability of electrochemical P2D models for lithium-ion batteries”. In: *Journal of Applied Electrochemistry* 51.9 (2021), pp. 1253–1265. DOI: `10.1007/s10800-021-01579-5`.

[366] David L. I. Janzén, Linnéa Bergenholm, Mats Jirstrand, Joanna Parkinson, James Yates, et al. “Parameter Identifiability of Fundamental Pharmacodynamic Models”. In: *Frontiers in Physiology* 7 (2016). DOI: `10.3389/fphys.2016.00590`.

[367] A. Raue, C. Kreutz, T. Maiwald, J. Bachmann, M. Schilling, et al. “Structural and Practical Identifiability Analysis of Partially Observed Dynamical Models by Exploiting the Profile Likelihood”. In: *Bioinformatics* 25.15 (2009), pp. 1923–1929. DOI: `10.1093/bioinformatics/btp358`.

[368] William C. Rooney and Lorenz T. Biegler. “Design for Model Parameter Uncertainty Using Nonlinear Confidence Regions”. In: *AIChE Journal* 47.8 (2001), pp. 1794–1804. DOI: `10.1002/aic.690470811`.

[369] William Q. Meeker and Luis A. Escobar. “Teaching about Approximate Confidence Regions Based on Maximum Likelihood Estimation”. In: 49.1 (1995), p. 7.

[370] Hirotogu Akaike. “Information Theory and an Extension of the Maximum Likelihood Principle”. In: *Selected Papers of Hirotugu Akaike*. Ed. by Kunio Tanabe, Genshiro Kitagawa, and Emanuel Parzen. Springer eBook Collection Mathematics and Statistics. New York: Springer, 1998, pp. 199–213. ISBN: 978-1-4612-7248-9.

[371] Kenneth P. Burnham, David Ray Anderson, and David Raymond Anderson. *Model selection and multimodel inference: A practical information-theoretic approach*. 2. ed. New York, Berlin, and Heidelberg: Springer, 2002. ISBN: 0-387-95364-7.

[372] Nariaki Sugiura. “Further analysts of the data by akaike’ s information criterion and the finite corrections”. In: *Communications in Statistics - Theory and Methods* 7.1 (1978), pp. 13–26. DOI: `10.1080/03610927808827599`.

[373] R. J. Flassig and K. Sundmacher. “Optimal Design of Stimulus Experiments for Robust Discrimination of Biochemical Reaction Networks”. In: *Bioinformatics* 28.23 (2012), pp. 3089–3096. DOI: `10.1093/bioinformatics/bts585`.

[374] Federico Galvanin, Carlo C. Ballan, Massimiliano Barolo, and Fabrizio Bezzo. “A General Model-Based Design of Experiments Approach to Achieve Practical Identifiability of Pharmacokinetic and Pharmacodynamic Models”. In: *Journal of Pharmacokinetics and Pharmacodynamics* 40.4 (2013), pp. 451–467. DOI: `10.1007/s10928-013-9321-5`.

[375] Vinzenz Abt, Tilman Barz, Mariano Nicolas Cruz-Bournazou, Christoph Herwig, Paul Kroll, et al. “Model-Based Tools for Optimal Experiments in Bioprocess Engineering”. In: *Current Opinion in Chemical Engineering* 22 (2018), pp. 244–252. DOI: `10.1016/j.coche.2018.11.007`.

[376] Moritz Schulze and René Schenkendorf. “Robust Model Selection: Flatness-Based Optimal Experimental Design for a Biocatalytic Reaction”. In: *Processes* 8.2 (2020), p. 190. DOI: `10.3390/pr8020190`.

[377] Steven M. Kay. *Fundamentals of statistical signal processing*. 20. pr. Upper Saddle River, NJ: Prentice Hall PTR, 2013. ISBN: 0133457117.

[378] Moritz Schulze and René Schenkendorf. “Flatness-Based Design of Experiments for Model Selection”. In: *IFAC-PapersOnLine* 51.15 (2018), pp. 233–238. DOI: `10.1016/j.ifacol.2018.09.140`.

[379] Luc Pronzato. “Optimal Experimental Design and Some Related Control Problems”. In: *Automatica* 44.2 (2008), pp. 303–325.

[380] Conor Waldron, Arun Pankajakshan, Marco Quaglio, Enhong Cao, Federico Galvanin, et al. “Model-based design of transient flow experiments for the identification of kinetic parameters”. In: *Reaction Chemistry & Engineering* 5.1 (2020), pp. 112–123. DOI: `10.1039/C9RE00342H`.

[381] Susann Triemer, Kerry Gilmore, Giang T. Vu, Peter H. Seeberger, and Andreas Seidel-Morgenstern. “Literally Green Chemical Synthesis of Artemisinin from Plant Extracts”. In: *Angewandte Chemie (Int. ed.)* 57.19 (2018), pp. 5525–5528. DOI: `10.1002/anie.201801424`.

[382] Truong Giang Vu. *Particle size dristribution of ground plant material of A. annua*. private communication.

[383] H. K. Lichtenthaler and C. Buschmann. “Chlorophylls and Carotenoids: Measurement And Characterization by UV-VIS Spectroscopy”. In: *Handbook of food analytical chemistry*. Ed. by Ronald E. Wrolstad. Hoboken, NJ: Wiley-Interscience, 2005, pp. 171–178. ISBN: 9780471709084.

[384] C. Tanielian and C. Wolff. “Mechanism of Physical Quenching of Singlet Molecular Oxygen by Chlorophylls and Related Compounds of Biological Interest”. In: *Photochemistry and Photobiology* 48.3 (1988), pp. 277–280. DOI: `10.1111/j.1751-1097.1988.tb02821.x`.

[385] Günther, O. Schenck, and K. Ziegler. “Die Synthese des Ascaridols”. In: *Naturwissenschaften* 32.14-26 (1944), p. 157. DOI: `10.1007/BF01467891`.

[386] Günther O. Schenck, Klaus G. Kinkel, and Hans-Joachim Mertens. “Photochemische Reaktionen I. Über die Photosynthese des Askaridols und verwandter Endoperoxyde”. In: *Justus Liebigs Annalen der Chemie* 584.1 (1953), pp. 125–155. DOI: `10.1002/jlac.19535840110`.

[387] S. Triemer, M. Schulze, B. Wriedt, R. Schenkendorf, D. Ziegenbalg, et al. “Kinetic analysis of the partial synthesis of artemisinin: Photooxygenation to the intermediate hydroperoxide”. In: *Journal of Flow Chemistry* 11.3 (2021), pp. 641–659. DOI: `10.1007/s41981-021-00181-2`.

[388] GESTIS-Stoffdatenbank. *Toluene*. Ed. by Institut für Arbeitsschutz der Deutschen Gesetzlichen Unfallversicherung. URL: `https://gestis.dguv.de/data?name=010070&lang=en` (visited on Nov. 9, 2021).

[389] Denis Prat, John Hayler, and Andy Wells. “A survey of solvent selection guides”. In: *Green Chemistry* 16.10 (2014), pp. 4546–4551. DOI: `10.1039/C4GC01149J`.

[390] Denis Prat, Andy Wells, John Hayler, Helen Sneddon, C. Robert McElroy, et al. “CHEM21 selection guide of classical- and less classical-solvents”. In: *Green Chemistry* 18.1 (2016), pp. 288–296. DOI: `10.1039/C5GC01008J`.

[391] GESTIS-Stoffdatenbank. *Anisol*. Ed. by Institut für Arbeitsschutz der Deutschen Gesetzlichen Unfallversicherung. URL: `https://gestis.dguv.de/data?name=021890` (visited on Dec. 16, 2021).

[392] Richard K. Henderson, Concepción Jiménez-González, David J. C. Constable, Sarah R. Alston, Graham G. A. Inglis, et al. "Expanding GSK's solvent selection guide – embedding sustainability into solvent selection starting at medicinal chemistry". In: *Green Chemistry* 13.4 (2011), p. 854. DOI: `10.1039/c0gc00918k`.

[393] Paul T. Anastas and John Charles Warner. *Green chemistry: Theory and practice*. 1. paperback. Oxford: Oxford University Press, 2000. ISBN: 0198502346.

[394] Hideshi Hattori and Yoshio Ono. *Solid acid catalysis: From fundamentals to applications*. CRC Press, 2015. ISBN: 9780429076367. DOI: `10.1201/b15665`.

[395] Kerry Gilmore. *Leaf material supplied by ArtemiFlow*. private communication.

[396] Steffi Wünsche, Karyna Oliynyk, Andreas Seidel-Morgenstern, and Heike Lorenz. "Purification of the Antimalarial Artemisinin from Crude Plant Extract Using a Combination of Adsorption and Antisolvent Cooling Crystallization". In: 27th International Workshop on Industrial Crystallization BIWIC 2022.

[397] René Schenkendorf, Dimitrios Gerogiorgis, Seyed Mansouri, and Krist Gernaey. "Model-Based Tools for Pharmaceutical Manufacturing Processes". In: *Processes* 8.1 (2020), p. 49. DOI: `10.3390/pr8010049`.

[398] Xian-wang Zhang, Xuan Zhao, Kun-hui Liu, and Hong-mei Sub. "Kinetics Study on Reaction between Dihydroartemisinic Acid and Singlet Oxygen: An Essential Step to Photochemical Synthesis of Artemisinin". In: *Chinese Journal of Chemical Physics* 33.2 (2020), pp. 145–150. DOI: `10.1063/1674-0068/cjcp2002021`.

[399] René Schenkendorf, Xiangzhong Xie, Moritz Rehbein, Stephan Scholl, and Ulrike Krewer. "The Impact of Global Sensitivities and Design Measures in Model-Based Optimal Experimental Design". In: *Processes* 6.4 (2018), p. 27. DOI: `10.3390/pr6040027`.

[400] Stanley I. Sandler. *Chemical, Biochemical, and Engineering Thermodynamics*. 4th ed. Hoboken, N.J: John Wiley, 2006. ISBN: 978-0-471-66174-0.

[401] Glen Meir, Mumin E. Leblebici, Senne Fransen, Simon Kuhn, and Tom van Gerven. "Principles of Co-axial Illumination for Photochemical Reactions: Part 1. Model Development". In: *Journal of Advanced Manufacturing and Processing* 2.2 (2020). DOI: `10.1002/amp2.10044`.

[402] Xiankun Wu, Zilei Deng, Jiujuan Yan, Zhongyang Zhang, Feng Zhang, et al. "Experimental Investigation on the Solubility of Oxygen in Toluene and Acetic Acid". In: *Industrial & Engineering Chemistry Research* 53.23 (2014), pp. 9932–9937. DOI: `10.1021/ie5014772`.

[403] J. M. van Baten and R. Krishna. "CFD Simulations of Mass Transfer from Taylor Bubbles Rising in Circular Capillaries". In: *Chemical Engineering Science* 59.12 (2004), pp. 2535–2545. DOI: `10.1016/j.ces.2004.03.010`.

[404] C. O. Vandu, H. Liu, and R. Krishna. “Mass Transfer from Taylor Bubbles Rising in Single Capillaries”. In: *Chemical Engineering Science* 60.22 (2005), pp. 6430–6437. DOI: `10.1016/j.ces.2005.01.037`.

[405] Axel G. Griesbeck, Waldemar Adam, Anna Bartoschek, and Tamer T. El-Idreesy. “Photooxygenation of Allylic Alcohols: Kinetic Comparison of Unfunctionalized Alkenes with Prenol-Type Allylic Alcohols, Ethers and Acetates”. In: *Photochem. Photobiol. Sci.* 2.8 (2003), pp. 877–881. DOI: `10.1039/B302255B`.

[406] W. Zhang, T. Hibiki, and K. Mishima. “Correlations of two-phase frictional pressure drop and void fraction in mini-channel”. In: *International Journal of Heat and Mass Transfer* 53.1-3 (2010), pp. 453–465. DOI: `10.1016/j.ijheatmasstransfer.2009.09.011`.

[407] Matthias Beller, Albert Renken, and Rutger A. van Santen, eds. *Catalysis: From principles to applications*. Weinheim: Wiley-VCH-Verlag GmbH & Co. KGaA, 2012. ISBN: 352732349X.

[408] Adrian Schumpe and Petra Luehring. “Oxygen Diffusivities in Organic Liquids at 293.2 K”. In: *Journal of Chemical & Engineering Data* 35.1 (1990), pp. 24–25. DOI: `10.1021/je00059a007`.

[409] C. Tanielian, L. Golder, and C. Wolff. “Production and quenching of singlet oxygen by the sensitizer in dye-sensitized photo-oxygenations”. In: *Journal of Photochemistry* 25.2-4 (1984), pp. 117–125. DOI: `10.1016/0047-2670(84)87016-1`.

[410] Charles Tanielian and Christian Wolff. “Determination of the Parameters Controlling Singlet Oxygen Production via Oxygen and Heavy-Atom Enhancement of Triplet Yields”. In: *The Journal of Physical Chemistry* 99.24 (1995), pp. 9831–9837. DOI: `10.1021/j100024a026`.

[411] Don W. Green and Marylee Z. Southard. *Perry’s Chemical Engineers’ Handbook, 9th Edition*. 9th edition. New York, N.Y.: McGraw-Hill Education and McGraw Hill, 2019. ISBN: 9780071834094.

[412] Statista. *Strompreis für die Industrie in Deutschland | Statista*. 20/03/2022. URL: `https://de.statista.com/statistik/daten/studie/155964/umfrage/entwicklung-der-industriestrompreise-in-deutschland-seit-1995/` (visited on Mar. 20, 2022).

[413] Bundesnetzagentur. *Stromgroßhandelspreise in Deutschland, 01.01.2022-01.09.2022*, ed. by SMARD-Strommarktdaten. 2022. (Visited on Sept. 10, 2022).

[414] Dario Cambié and Timothy Noël. “Solar Photochemistry in Flow”. In: *Topics in current chemistry (Cham)* 376.6 (2018), p. 45. DOI: `10.1007/s41061-018-0223-2`.

[415] Tom M. Masson, Stefan D. A. Zondag, Koen P. L. Kuijpers, Dario Cambié, Michael G. Debije, et al. “Development of an Off-Grid Solar-Powered Autonomous Chemical Mini-Plant for Producing Fine Chemicals”. In: *ChemSusChem* 14.24 (2021), pp. 5417–5423. DOI: `10.1002/cssc.202102011`.

[416] Dario Cambié, Fang Zhao, Volker Hessel, Michael G. Debije, and Timothy Noël. “A Leaf-Inspired Luminescent Solar Concentrator for Energy-Efficient Continuous-Flow Photochemistry”. In: *Angewandte Chemie (Int. ed.)* 56.4 (2017), pp. 1050–1054. DOI: `10.1002/anie.201611101`.

[417] Fang Zhao, Dario Cambié, Volker Hessel, Michael G. Debije, and Timothy Noël. “Real-time reaction control for solar production of chemicals under fluctuating irradiance”. In: *Green Chemistry* 20.11 (2018), pp. 2459–2464. DOI: `10.1039/C8GC00613J`.

[418] Dario Cambié, Jeroen Dobbelaar, Paola Riente, Jochen Vanderspikken, Chong Shen, et al. “Energy-Efficient Solar Photochemistry with Luminescent Solar Concentrator Based Photomicroreactors”. In: *Angewandte Chemie (Int. ed.)* 58.40 (2019), pp. 14374–14378. DOI: `10.1002/anie.201908553`.

[419] Gábor Blaskó, Geoffrey A. Cordell, and David C. Lankin. “Definitive 1 H- and 13 C-Nmr Assignments of Artemisinin (Qinghaosu)”. In: *Journal of natural products* 51.6 (1988), pp. 1273–1276. DOI: `10.1021/np50060a040`.

[420] GESTIS-Stoffdatenbank, ed. *Natriumhydrogencarbonat*. 5/04/2022. URL: `https://gestis.dguv.de/data?name=002440` (visited on Apr. 19, 2022).

[421] Alfa Aesar, ed. *Price of trifluoroacetic acid*. URL: `https://www.alfa.com/en/catalog/A12198/` (visited on Mar. 19, 2022).

[422] Alfa Aesar, ed. *Price of triethylamine*. URL: `https://www.alfa.com/en/catalog/A12646/` (visited on Mar. 19, 2022).

[423] Alfa Aesar, ed. *Price of Sodium hydrogen carbonate*. URL: `https://www.alfa.com/en/catalog/014707/` (visited on Mar. 9, 2022).

[424] Statista. *Wasserpreise im Ländervergleich 2011 | Statista*. 20/03/2022. URL: `https://de.statista.com/statistik/daten/studie/1538/umfrage/wasserpreise-weltweit/` (visited on Mar. 20, 2022).

Appendix

Contents

Experimental setup

A

A.1 Components of the photoreactor system

This section complements the description of the applied photoflow reactor system given in Sec. 4.1. The custom-made parts are listed in Tab. A.1 and shown Fig. A.1. Tab. A.2 specifies all other components. The LED modules are described in the next section.

Tab. A.1: Dimensions of the custom made reactors for the photooxygenation and the second residence time unit.

Type	Material	Dimension
Photoreactor		
Casing	Stainless steel	240 x 220 x 70 mm
	with polystyrol windows	170 x 180 mm
Frame	Stainless steel and polystyrol	150 x 140 mm
	wrapped with FEP tubing	1/16" & 1/8", 1 m to 20 m
2nd Reactor		
Casing	Stainless steel	210 x 210 x 210 mm
Frame	Stainless steel	150 x 150 x 140 mm
	wrapped with FEP tubing	1/8", 2 m to 16 m

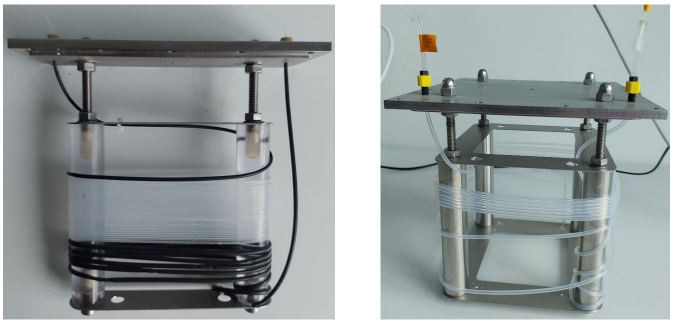

(a) Frame integrated in the photoreactor

(b) Frame integrated in the second reactor

Fig. A.1: Pictures of the reaction lines used for the photooxygenation (a) and the acid-catalyed reaction sequence as residence time module (b).

Tab. A.2: Specifications of the components of the reactor system applied.

Type	Manufacturer	Model specification
LED Modules	OSA Opto Light	OLM-018 B $\lambda = 417\,\mathrm{nm}$ & $\lambda = 666\,\mathrm{nm}$
Liquid dosing	Hitec Zang	Syrdos 2
	Knauer	Azura P4.1S
Acidic dosing	Landgraf Laborsysteme	LA 30
Gas dosing	Bronkhorst	EL-Flow Select
Temperature Control	LAUDA	PRO RP 245 E
Pressure sensors	FirstSensor	Type: CTE
Temperature sensors	TC-Mess- und Regeltechnik	thermo couple type 12
6-way valve	VALCO	C22-3716EUHC
T-mixer	VICI-Jour	PEEK 1/8"
Glass column	YMC	ECO SR, ID: $1.5\,\mathrm{cm}$
UV/Vis spectrometer	Ocean Optics	FLAME-T-XR1-ES with fiber probe
Gas-liquid-separator	Zaiput	Sep-10
Gas flow sensor	Bronkhorst	EL-Flow Select
Back pressure regulator		
Gas side	VICI-Jour	JR-BPR1
Liquid side	Equilibar	U3L0SVN8
Connectors	Upchurch	PEEK - 1/16" & 1/8"
Tubing	Bohlender	FEP 1/16" & 1/8"
Photoreactor		
Casing	In-house	Stainless steel casing with polystyrol windows (170 x 180 mm)
Frame	In-house	Stainless steel and polystyrol (150 x 140 mm)
2nd Reactor		
Casing	In-house	Stainless steel casing (210 x 210 x 210 mm)
Frame	In-house	Stainless steel (150 x x 150 x 140 mm)

A.2 Specification of the applied light sources

The photoreactor is irradiated from two sides by two LED modules with an equal emission spectrum. The emitted light was either in the red or blue region of the visible light spectrum. The applied LED modules are specified in Tab. A.3. The emitted spectra are shown together with the absorption spectrum of 9,10-dicyanoanthracene and the extract in toluene in Fig. A.2.

Tab. A.3: Specification of the used LED modules.

	LED module	
	Blue	Red
Supplier	OSA Opto Light	
Type	OLM-018 Silent Air	
Emission window	25 x 25 mm	
Emission angle, °	120	
Peak wavelength, nm	417	658
Optical Power, W	26.3	19.6

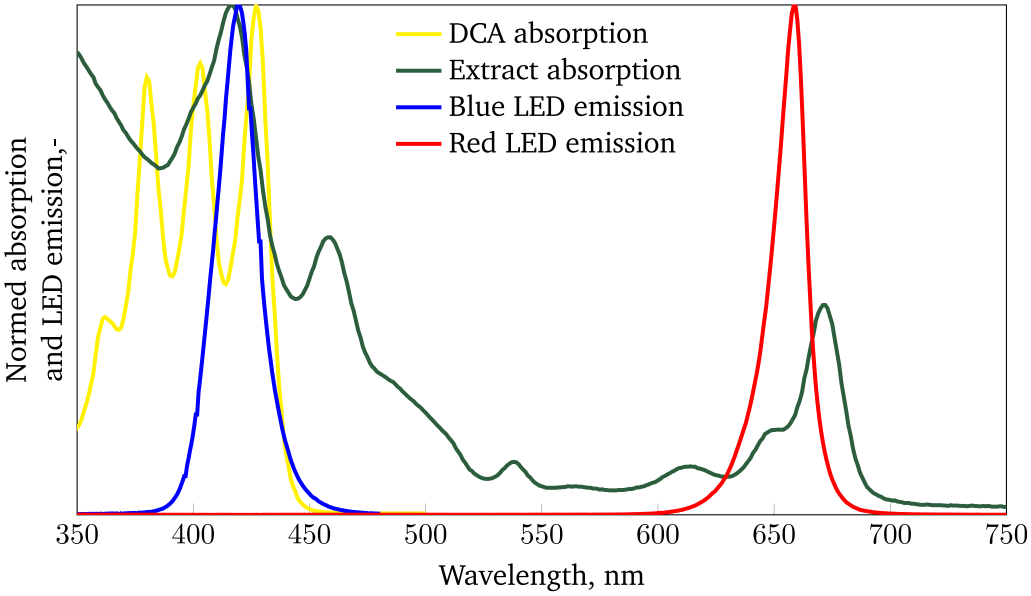

Fig. A.2: Emission spectra of the avaiblable red and blue LED modules versus the absorption spectra of the applied photosensitizers 9,10-dicyanoantracene (DCA) and chlorophyll contained in the crude extract of *A.annua* in toluene.

A.3 Materials

The suppliers of the used chemicals for the partial synthesis and actinometric experiments are listed in Tab. A.4. All chemicals were used without further purification.

Tab. A.4: List of chemicals used for the partial synthesis and actinometric experiments including sample workup for NMR analysis.

Substance	Purity, %	Supplier
Dihydroartemisinic acid	98	CfM Tropitzsch
Artemisinin	98	Carbosynth
Artemisinic Acid	98	Cayman Chemical
9,10-Dicyanoanthracene	98	TCI
Chlorophyll A	85	Sigma-Aldrich
Chlorophyll B	95	Sigma-Aldrich
Trifluoroacetic acid	99.8	VWR Chemicals
Triethylamine	99.6	VWR Chemicals
Sodium bicarbonate decahydrate	99	Merck
Anisol	99	Alfa Aesar
1-Butanol	98.5	VWR Chemicals
Cumene	98	Sigma-Aldrich
p-Cymene	97	Alfa Aesar
Ethanol absolute	99.7	VWR Chemicals
Ethyl methyl ketone	99.5	Merck
Toluene	HPLC grade	VWR Chemicals
Iron(III) chloride	98	Alfa Aesar
di-Potassium oxalate monohydrate	99	Merck
Sodium acetate trihydrate	99.5	AppliChem
1,10-Phenanthroline	99	Alfa Aesar
0.05 M Sulfuric acid		Merck
Acetonitril	99.9	VWR Chemicals
Water		Milli-Q System
Acetic acid	99.7	Fisher Scientific
Dimethylterephthalate	Standard for quant. NMR	Sigma-Aldrich
Chloroform-D1	99.8	Merck

B

Analytical tools to investigate the partial synthesis of artemisinin

This section complements the description of applied HPLC and NMR methods given in Sec. 4.4. Both methods were applied to quantify the reaction products of the partial synthesis and in the extract.

B.1 HPLC analysis for the quantification of artemisinin and DHAA

The artemisinin and DHAA concentration in the samples were quantified by HPLC using a gradient method which is summarized in Tab. B.1. Before analysis, the sample is diluted in ACN/water = 0.8/0.2 (v/v) to precipitate nonpolar substances and filtered with a $0.2\,\mu\mathrm{m}$ syringe filter. The samples are prepared for analysis on the day of the experiment and stored at $4\,^{\circ}\mathrm{C}$ until measurement.

B.2 Identification and quantification of reaction products by NMR

Quantitative NMR was used to quantify reaction products, where the pure species was not available as calibration standard. The following section describes the sample preparation, quantification and shows exemplary $^{1}\mathrm{H-NMR}$ spectra of the product solution.

B.2.1 Sample workup for NMR analysis

For quantification, mesitylene and dimethylterephthalate (DMT) were used as internal standards. In the case of dimethylterephthalate, a standard solution of DMT in toluene was added to $0.8\,\mathrm{mL}$ of the sample. The mixture is evaporated in a rotation

Tab. B.1: Specification of the gradient method for analysis of the extract with high performance liquid chromatography (HPLC) using an evaporative light scattering detector (ELSD) for quantification.

Sample preparation			
1)	Dilution of $50\,\mu\mathrm{L}$ sample with $950\,\mu\mathrm{L}$ mobile phase (ACN/Water = 20/80 (v/v))		
2)	Filtration with $0.2\,\mu\mathrm{m}$ cellulose filter		
Mobile Phase			
Flow rate	$1\,\mathrm{mL\,min^{-1}}$		
Eluent A	Acetonitrile		
Eluent B	Water + $0.1\,\mathrm{vol\%}$ Acetic Acid		
Gradient profile	time, min	A, vol-%	B, vol-%
	0	50	50
	5	100	0
	15	100	0
	20	50	50
	25	50	50
Injection volume	$100\,\mu\mathrm{L}$		
Column			
Specification	Phenomenex Kinetex C18 ($150 \times 4.6\,\mathrm{mm}$, $2.6\,\mu\mathrm{m}$)		
Temperature	$25\,^{\circ}\mathrm{C}$		
ELSD Settings			
Evaporator temperature	$40\,^{\circ}\mathrm{C}$		
Nebulizer temperature	$40\,^{\circ}\mathrm{C}$		
Gas flow rate	$1.60\,\mathrm{L\,min^{-1}}$		

evaporator at ambient temperature close to dryness and entirely dissolved in deuterated chloroform. In the case of mesitylene as internal standard, $0.8\,\mathrm{mL}$ of the sample were first evaporated and dissolved in $CDCl_3$ before adding $0.4\,\mathrm{mL}$ of a standard solution of mesitylene in chloroform. The concentration of the standard solution was chosen so that the amount of reference is in the same order of magnitude as the expected amount of reaction products. The obtained samples were analyzed in the NMR laboratory of the *Otto-von-Guericke university*. To prevent the semi-stable hydroperoxide species from degradation, the sample preparation and analysis of the photooxygenation experiments were performed on the day of the experiment.

B.2.2 Quantification

The signals within the region of $4.5\,\mathrm{ppm}$ to $6.5\,\mathrm{ppm}$ were used to quantify the reaction products. Tab. B.2 lists the characteristic signals of the main products from the conversion of DHAA to artemisinin. Based on the known added mass of the reference, m_{ref}, the concentration of the unknown analyte, c_{i}, is calculated as

$$c_{\mathrm{i}} = \frac{m_{\mathrm{sample}}}{\delta_{\mathrm{sample}}} \frac{m_{\mathrm{ref}}}{M_{\mathrm{ref}}} \frac{y_{\mathrm{ref}}}{y_{\mathrm{i}}} \frac{S_{\mathrm{i}}}{S_{\mathrm{ref}}} \tag{B.1}$$

with δ_{sample} and m_{sample} being the density and mass of the sample i, y_i as the number of protons and S the integral of the considered signal.

Tab. B.2: ^{1}H-NMR-signals used for quantification of the main products and intermediates of the partial synthesis to artemisinin.

Species	δ, ppm	Number of protons	Multiplicity	Ref.
Dimethyl terephthalate	8.1	4	s	-
Mesitylene	6.8	3	s	-
DHAA	5.11	1	s	[197]
PO_1	5.23	1	s	[197]
PO_2	4.73	1	d	[198]
PO_3	5.69	1	s	[198]
BP_3	5.64	1	s	[197]
BP_4	6.07	1	s	[70]
ArteH	4.84	1	s	[197]
Artemisinin	5.85	1	s	[419]

B.2.3 $^1\mathrm{H-NMR}$ spectra of the reactor feed and the reactor outlet after photooxygenation and the acid catalyzed sequence

The following section gives examples on typical $^1\mathrm{H-NMR}$ spectrum of the reactor outlet. For comparison with the pure substances, Figs. B.1 and B.2 show the $^1\mathrm{H-NMR}$ of the DHAA and artemisinin, respectively. Figs. B.1 and B.2 show the $^1\mathrm{H-NMR}$ of the pure substances DHAA and artemisinin, respectively.

The spectrum of the product from photooxygenation without acid present is included in Fig. B.3. Fig. B.4 contains $^1\mathrm{H-NMR}$ spectra of the product solution at the start of the acid-catalyzed reaction sequence and after completion of the complete pathway.

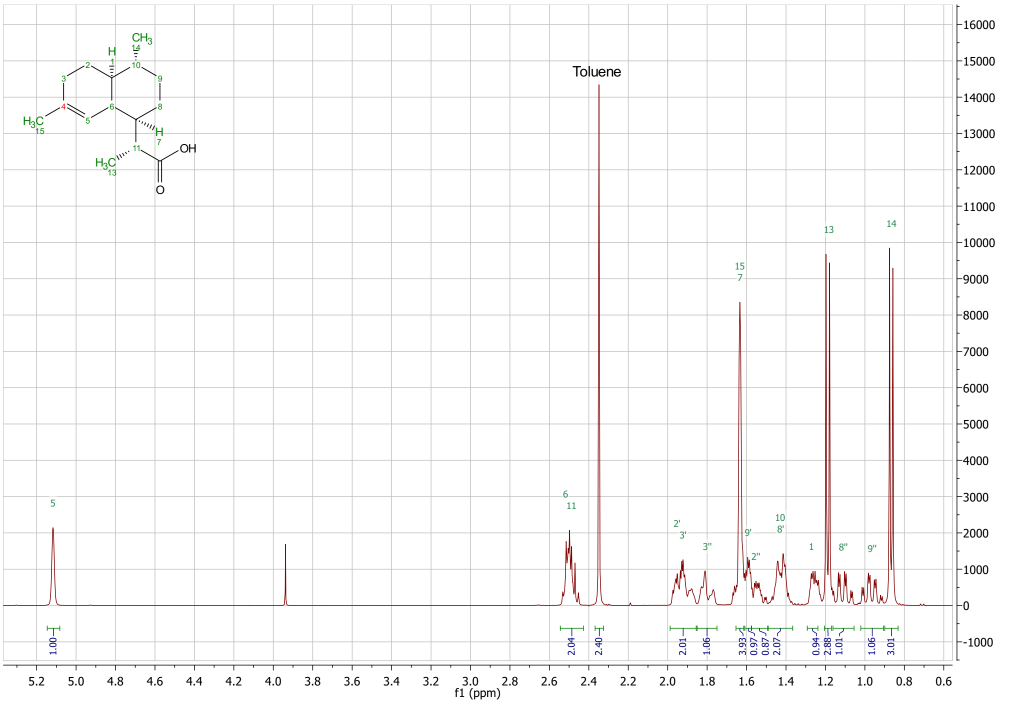

Fig. B.1: ^{1}H–NMR signals assigned to the structure of dihydroartemisinic acid (DHAA) according to [197]. Solvent: $CDCl_3$

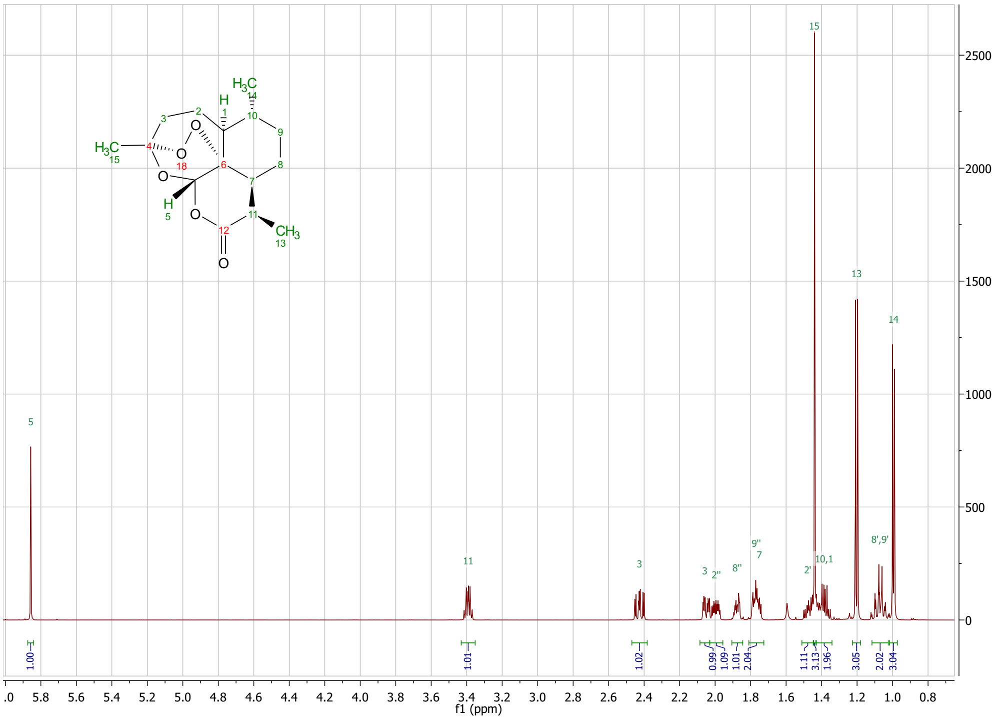

Fig. B.2: ^{1}H–NMR spectrum assigned to the structure of artemisinin according to [419]. Solvent: $CDCl_3$

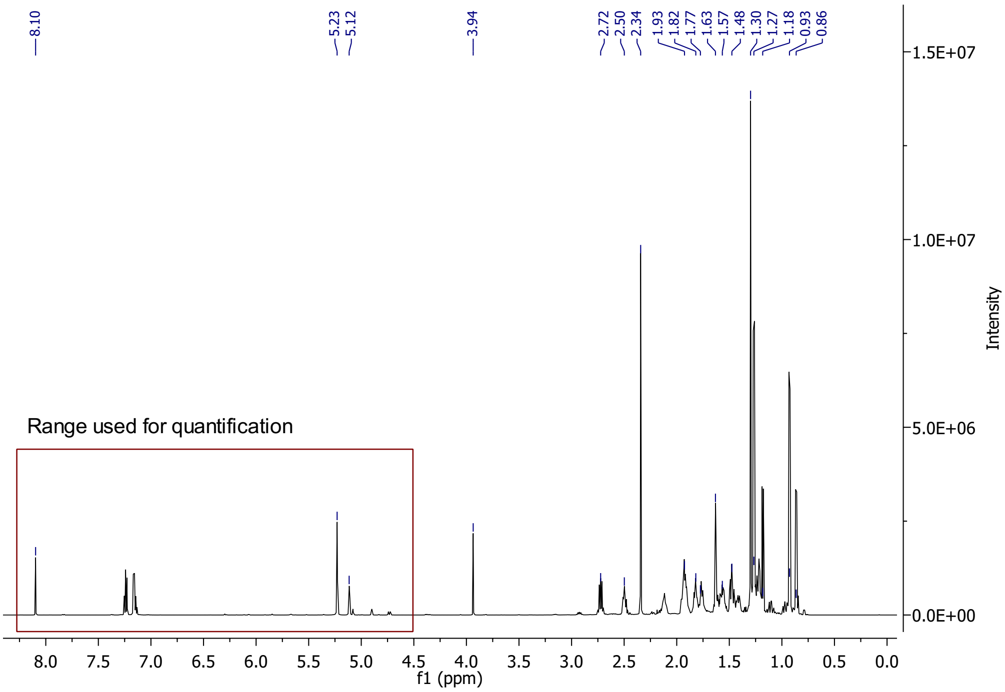

(a) Complete spectrum

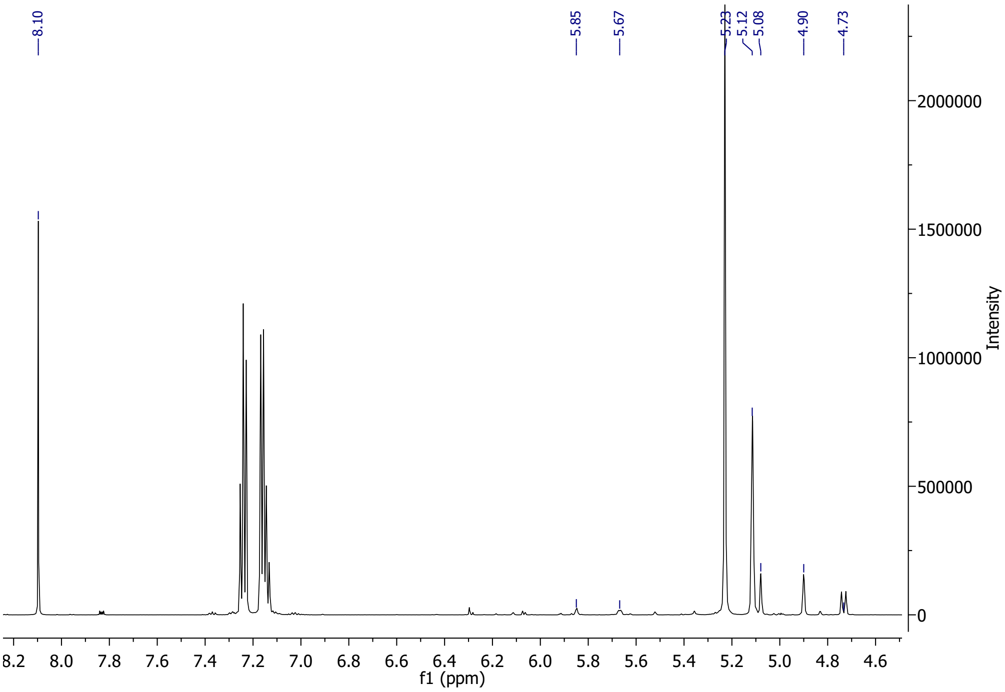

(b) Range used for quantification

Fig. B.3: ^{1}H-NMR spectrum of the product solution of the photooxygenation. The range used for quantification is shown in the second graph. (NMR sample solvent: $CDCl_3$)

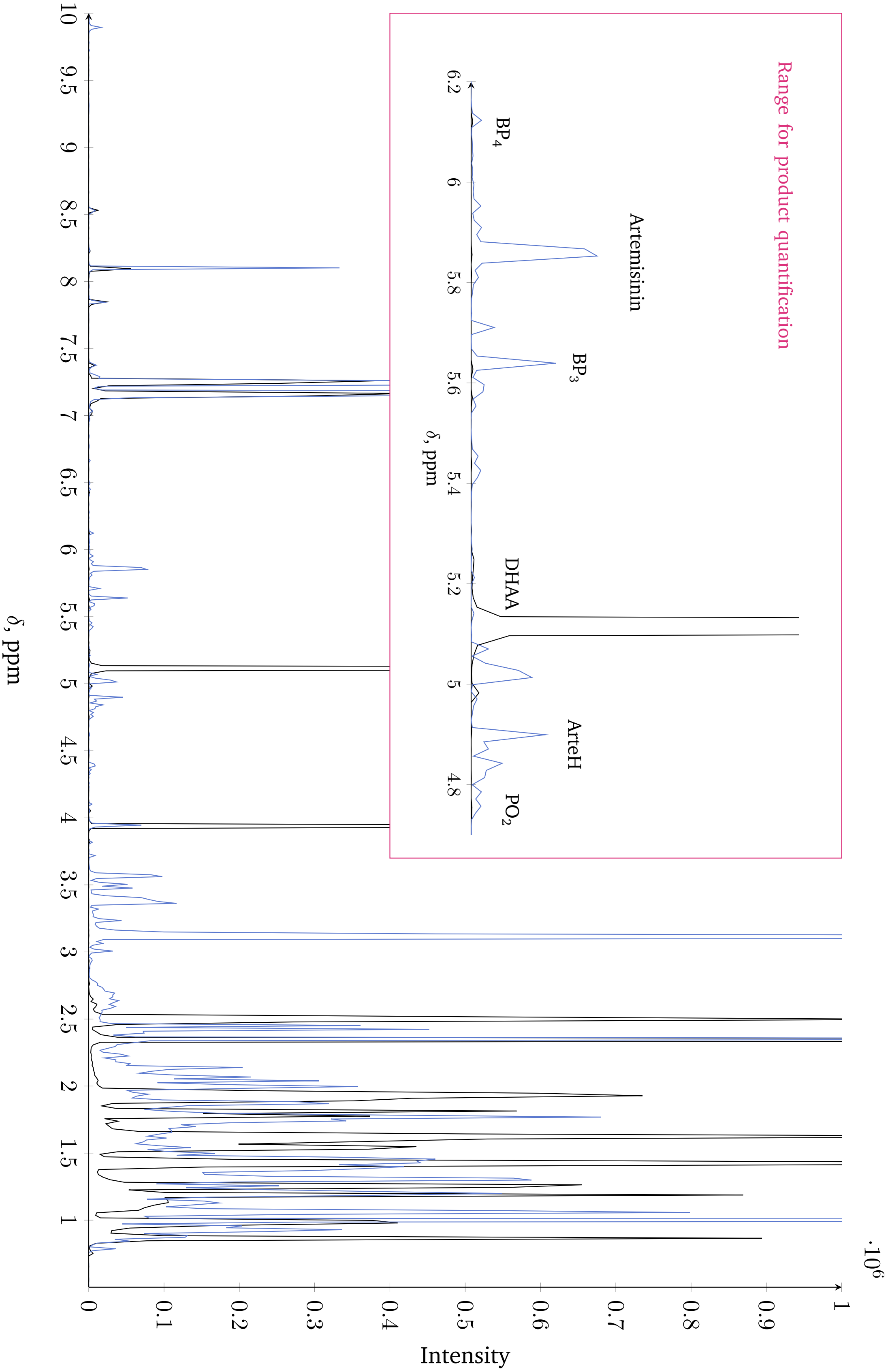

Fig. B.4: ^{1}H-NMR spectrum of a sample taken from the reactor effluent after photooxygenation and TFA addition. The black color shows the spectrum right after acid addition. The spectrum in blue is obtained after completion of the acid-catalyzed reaction sequence. (NMR sample solvent: $CDCl_3$)

B.3 Measurement of absorption coefficients

The absorption coefficients were required to quantify the chlorophyll amount in the extract (Sec. 4.4.3) and to assess the photon absorption in the reactor for 9,10-dicyanoanthracene (DCA) (Sec. 3.2).

B.3.1 Absorption coefficient of 9,10-dicyanoanthracene in toluene

The absorbance A_λ of standard DCA solutions in toluene were analyzed at $417\,\mathrm{nm}$ with a UV/Vis spectrometer (Genesys 6, Thermo Fisher) using glas cuvettes (d=$1\,\mathrm{cm}$) (Fig. B.5). The measured absorbance is defined based on the decadic logarithm of the ratio between residual and initial light intensity I. The naperian absorption coefficient κ was obtained by correcting the decadic absorption coefficient ε according to Eq. (B.2) and Eq. (B.3),

$$A_\lambda = lg\left(\frac{I}{I_0}\right) = \varepsilon \cdot [\mathrm{DCA}] \cdot d \tag{B.2}$$

$$\kappa = \ln(10) \cdot \varepsilon = 12841.98 \frac{\mathrm{L}}{\mathrm{mol\,cm}}. \tag{B.3}$$

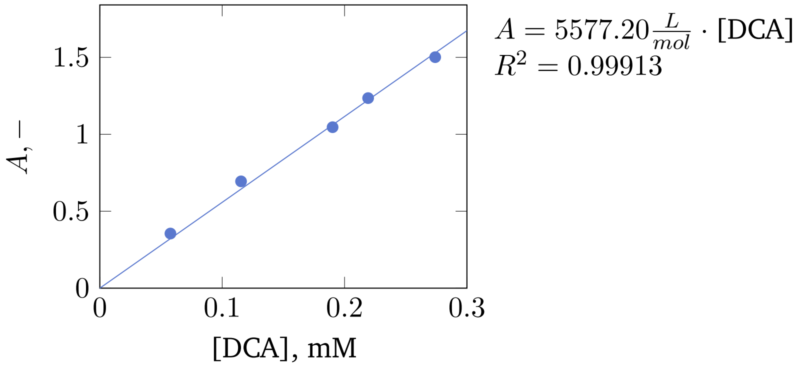

Fig. B.5: Absorption of 9,10-dicyanoanthracene (DCA) solutions in toluene at $417\,\mathrm{nm}$.

B.3.2 Absorption coefficients of chlorophyll A, B, and pheophytin A

The method of Lichtenthaler et al. [383] was used to quantify the concentration of three chlorophyll species in the extract chlorophyll A (ChlA), chlorophyll B (ChlB), and pheophytin (PheoA). The decadic absorption coefficients ϵ_{max} at the absorption maxima of the different chlorophyll species were determined with the pure pigments dissolved in the corresponding solvent. Pheophytin A was obtained by adding $2\,\mu\mathrm{L}$

of formic acid to 6 mL of a ChlA standard solution and keeping the mixture for 24 h at −15 °C. The measured absorbances are shown examplarily for toluene in Fig. B.6. The absorption coefficients of the present chlorophyll species in toluene, ethanol, butanol, and cyclohexanone are given in Tab. B.3. Pheophytin A was only quantified in toluene as a separate species. The absorption coefficients of the chlorophylls in acetone were taken from [383].

For extract analysis, the absorption spectrum of the extract is assessed at the absorption maxima A_{max} of the three chlorophylls. The concentration of the three species is obtained by solving the following linear system of equations numerically,

$$A_{max_{\text{ChlB}}} = \left(\epsilon_{max_{\text{ChlB}},\text{ChlA}} \cdot c_{\text{ChlA}} + \epsilon_{max_{\text{ChlB}},\text{ChlB}} \cdot c_{\text{ChlB}} + \epsilon_{max_{\text{ChlB}},\text{PheoA}} \cdot c_{\text{PheoA}}\right) \cdot d \tag{B.4}$$

$$A_{max_{\text{ChlA}}} = \left(\epsilon_{max_{\text{ChlA}},\text{ChlA}} \cdot c_{\text{ChlA}} + \epsilon_{max_{\text{ChlA}},\text{ChlB}} \cdot c_{\text{ChlB}} + \epsilon_{max_{\text{ChlA}},\text{PheoA}} \cdot c_{\text{PheoA}}\right) \cdot d \tag{B.5}$$

$$A_{max_{\text{PheoA}}} = \left(\epsilon_{max_{\text{PheoA}},\text{ChlA}} \cdot c_{\text{ChlA}} + \epsilon_{max_{\text{PheoA}},\text{ChlB}} \cdot c_{\text{ChlB}} + \epsilon_{max_{\text{PheoA}},\text{PheoA}} \cdot c_{\text{PheoA}}\right) \cdot d. \tag{B.6}$$

Tab. B.3: Absorption coefficients of chlorophyll A and B in ethanol, butanol and cyclohexanone at the distinct absorption maxima of each species.

ϵ, L/(mol cm)		Chlorophyll A	Chlorophyll B	Pheophytin A
Toluene	A_{max}, nm	666	648	672
	At 648 nm	12311.9	46604.2	7074.7
	At 666 nm	64759.6	3834.8	35928.1
	At 672 nm	51594.6	0	47130.1
Ethanol	A_{max}, nm	666	650	-
	At 651 nm	27903	31608	-
	At 667 nm	89012	12692	-
Butanol	A_{max}, nm	667	651	-
	At 651 nm	20151	34634	-
	At 667 nm	68956	13427	-
Cyclohexanone	A_{max}, nm	666	648	-
	At 648 nm	19954	41544	-
	At 666 nm	95774	5403	-

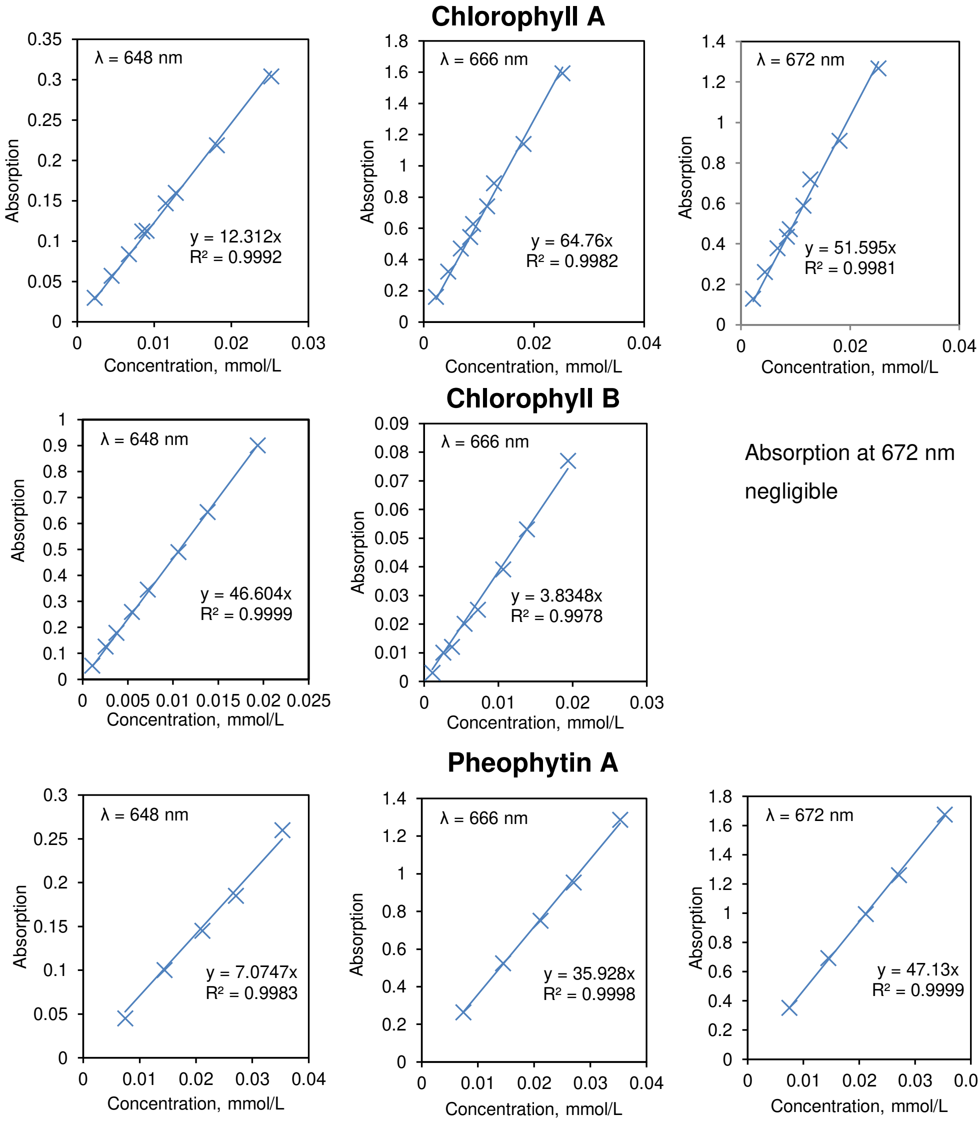

Fig. B.6: Absorption coefficients of the main chlorophyll species contained in the extract of *A. annua* (chlorophyll A, B and pheophytin A) at the corresponding wavelengths with maximum absorption 648 nm (ChlB), 666 nm (ChlA), 672 nm (PheoA).

C

Effect of the solvent, the temperature, and the acid concentration on the partial synthesis in plant extract

Utilizing chlorophyll as photosensitzer in Sec. 5.1 and the extract as reaction medium in Sec. 6 required optimization of all reaction conditions. This section gives further information regarding the effect of temperature and the solvent on the photoxygenation behavior. Finally, the reactor length and the acid concentration are investigated to utilize DHAA contained in the plant extract as artemisinin source.

C.1 Effect of temperature on the photooxygenation selectivity

These results complement the data given on optimizing the photooxygenation performance using chlorophyll as photosensitizer in Section 5.1.2. Tab. C.1 shows the effect of the temperature in the photooxygenation reactor on the obtained yield of the main intermediate PO_1. The experiments were performed with a high initial DHAA concentration of $0.5\,\mathrm{M}$.

Tab. C.1: Effect of increasing the photoreactor temperature on the yield of the desired hydroperoxide PO_1 ([DHAA]=$0.5\,\mathrm{M}$,g/l=4/1 (v/v), p_{O_2}=$7\,\mathrm{bar}$).

	T	λ	τ^{s}_{photo}	X, %	Y, %	
	°C	nm	min	DHAA	PO_1	PO_y
$2.5\,\mathrm{mM}$ DCA in toluene	-20	420	2	98	91	9
Extract	-20	420	5	100	89	10
Extract	25	420	5	100	**81**	11
Extract	-20	660	4	100	89	8
Extract	25	660	4	100	**83**	12

C.2 Optimization of the acid concentration and the reactor length for the use of crude extract as reaction medium

After suitable photooxygenation conditions were found (Sec. 5.1.2), the complete partial synthesis to artemisinin using the plant extract was optimized by variation of the acid concentration and the reactor length after the photoreactor. The results of this optimization are shown in Fig. C.1. The optimal conditions were an additional residence time of $10\,\mathrm{min}$ after the photooxygenation and a TFA concentration of $0.375\,\mathrm{M}$. With these settings, the experimental results on the comparison of pure toluene with DCA and crude extract as reaction medium shown in Sec. 5.1.3 were obtained.

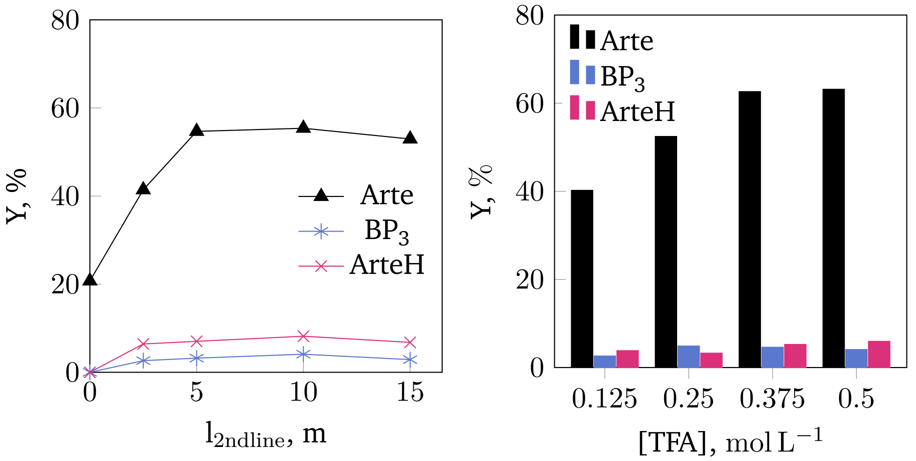

(a) Yield over the length of the added reaction line (ID: $1.6\,\mathrm{mm}$, $[\mathrm{TFA}] = 0.25\,\mathrm{M}$)

(b) Yield over the TFA concentration in the reactor feed ($l_{2\mathrm{nd\,line}} = 5\,\mathrm{m}$)

Fig. C.1: Optimization of the partial synthesis performed in crude extract regarding the reactor volume and the TFA concentration ($[\mathrm{DHAA}]=0.5\,\mathrm{M}$, g/l=4/1 (v/v), $\dot{V}_{\mathrm{tot}}=1\,\mathrm{mL\,min^{-1}}$,$p_{O_2}=7\,\mathrm{bar}$, TEA as quenching agent) .

C.3 Effect of the solvent on the extraction of chlorophyll and the photooxygenation

Seven different solvents were tested as alternatives to toluene, as introduced in Sec. 5.2. Before applying them in the partial synthesis, the extraction of chlorophyll from *A. annua* was investigated. All solvents extracted the plant dye from the leaves.

Tab. C.2: Conditions applied to extract chlorophyll from *A. annua* with various solvents. The stated chlorophyll concentration is the sum of the observed concentrations for chlorophyll A, chlorophyll B, and pheophytin A.

Solvent	Extraction conditions		[Chl],
	T, °C	t, min	mmol L^{-1}
Toluene	50	10	0.33
Ethanol	50	60	0.31
Butanol	50	30	0.34
Cyclohexanone	50	60	0.25
Acetone	25	180	0.13
Anisol	50	60	0.24
Butanone	50	60	0.25
Cumene	60	60	0.24
p-Cymene	50	60	0.16

The aim was to obtain extraction conditions which yield comparable chlorophyll concentrations in all tested solvents. Due to the different vapor pressure and polarity of the solvents, the applicable extraction temperatures and required extraction durations varied strongly. Tab. C.2 lists the final extraction conditions for each solvent used to obtain extract as feed for the later synthesis experiments.

In the next step, the photooxygenation was investigated in the different solvent candidates. Fig. C.2 shows the conversion of DHAA and the resulting yield of PO_1 in dependence on the solvent. In all solvents, DHAA was completely converted after 10 min residence time in the photoreactor. PO_1 yields were obtained in the range of 63 % to 74 % differing only to a minor extend between the solvents. Thus, the distinct spread in performance of the solvents observed for the complete conversion to artemisinin (Sec. 5.2) is mainly attributed to a strong solvent dependence of the acid-catalyzed reaction sequence.

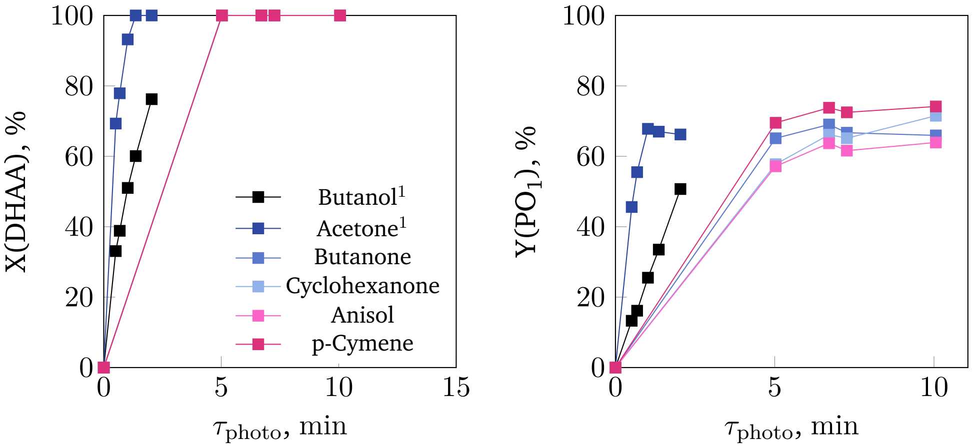

(a) Conversion of DHAA **(b)** Yield of artemisinin

Fig. C.2: Effect of the reaction solvent on the formation of artemisinin, the intermediate PO_1 and its main byproduct BP_3 in the partial synthesis. The reactor feed consisted either of the pure solvent with DCA as photocatalyst ($0.3\,\mathrm{mM}$) or (^{1}) the extract obtained by contacting *A. annua* with the corresponding solvent. Reaction conditions: $T_{photo}=-10\,°C$, β = 0.8, $p_{O_2}=7\,\mathrm{bar}$, TEA as quench, Pure conditions: [DHAA] = $0.01\,\mathrm{M}$, [TFA] = $0.09\,\mathrm{M}$, Extract-based feed source: [DHAA] = $0.05\,\mathrm{M}$, [TFA] = $0.35\,\mathrm{M}$.

Application of solid acids

D

This section concerns the use of solid acidic materials as catalysts for the conversion of PO_1 to artemisinin (Sec. 5.3). In the following, details are given on the materials tested as catalysts, the applied packed-bed reactors, and experimental results of the initial screening for applicable heterogeneous catalysts (Sec. 5.3.1).

D.1 Specification of the tested solid acids and the applied packed-bed reactors

Tab. D.2 specifies all acidic materials which were tested in the initial batch experiments (Sec. 4.3.4). Depending on the material, the acids were pretreated at varied temperatures and pressures before using them in the experiments as catalyst.
After the initial screening, the four best performing candidates were tested in continuous mode as packed beds. Tab. D.1 lists the dimensions, the composition, and the pretreatment of the specific packed-bed reactors.

Tab. D.1: Specifications of the applied packed beds for continuous experiments using solid acids including the diameter, d, and the length, l, of the catalyst bed, the composition of the bed, and the pretreatment of the solid acid.

Solid acid	Reactor type	Bed dimensions		Mass, g		Pretreatment		
		l, cm	d, cm	Acid	Seasand	T, °C	t, h	p, mbar
Amberlyst 36	Column	20	1.5	27.2	0	70	24	< 100
	Tubing	500	0.16	9.7	0	70	24	< 100
	Tubing	1000	0.16	19.4	0	70	24	< 100
DOWEX 50WX8	Column	20	1.5	27.98	0	30	24	< 100
	Column	20	1.5	27.1	0	30	24	< 100
	Column	20	1.5	28.1	0	30	24	< 100
H-β (Si/Al=360)	Column	15	1.5	6.3	24.1	500	2	ambient
	Column	7.5	1.5	4	13.5	500	2	ambient
	Column	7.5	1.5	4	13.5	500	2	ambient
Sulf. ZrO_2	Column	20	1.5	54.7	0	500	2	ambient

Tab. D.2: Solid acidic materials tested as catalysts for the conversion of PO_1 to artemisinin

Solid material	Specification	Appearance	Surface area $m^2\,g^{-1}$	Supplier	Thermal Pre-treatment T, °C	t, h	p, mbar
Amberlyst 15	H^+-form	Pellets		Alfa Aesar	70	12	< 100
Amberlyst 36	H^+-form	Pellets		Sigma-Aldrich	70	12	< 100
DOWEX50-WX2	H^+-form	Pellets		Alfa Aesar	25	12	< 100
DOWEX50-WX8	H^+-form	Powder, 0.09-0.25 mm		Merck	25	12	< 100
Nafion	NR50	Pellets		Alfa Aesar	25	12	< 100
Nafion	POWDion	Powder, -40+60 mesh		Ion Power	25	12	< 100
NH_4-ZSM5[1]	Si/Al =30	Powder	400	Alfa Aesar	500	5	ambient
NH_4-ZSM5[1]	Si/Al =200	Powder	400	Alfa Aesar	500	5	ambient
NH_4-Y[1]	Si/Al =5	Powder	660	Alfa Aesar	500	5	ambient
H-Y	Si/Al =30	Powder	780	Alfa Aesar	500	5	ambient
H-Y	Si/Al =80	Powder	780	Alfa Aesar	500	5	ambient
$NH_4-\beta$[1]	Si/Al = 25	Powder	680	Alfa Aesar	500	5	ambient
$H-\beta$	Si/Al = 360	Powder	620	Alfa Aesar	500	2-5	ambient
H-SAPO34		Powder	≥ 550	ACS Materials	500	5	ambient
Montmorrilonite K30		Powder	330	Sigma-Aldrich			
$Zr(HPO_4)_2$		Powder		Sigma-Aldrich	200	2	< 100
$\gamma - Al_2O_3$		Powder	90 - 170	Sigma-Aldrich	500	5	ambient
		50-200 μm					ambient
Sulfated ZrO_2		Pellets,		Alfa Aesar	500	24	ambient
		3 mm		Alfa Aesar	500	24	ambient
Functionalized Carbon	Norit Cap Super	Powder		Cabot	70	2	ambient
12-Molybdophosphoric acid hydrate		Powder		Alfa Aesar	none		
Tungstophosphoric acid hydrate		Powder		VWR Chemicals	none		

[1] Zeolite was stirred in 1 M NH_4Cl solution before thermal pretreatment

D.2 Conversion of PO_1 to Arte using solid acids in batch experiments

The scanning for suitable solid acidic materials was performed in batch operation (Sec. 4.3.4). The endpoints after $90\,\mathrm{min}$ reaction time were shown for all tested materials in Sec. 5.3.1 together with the reaction profiles for the best-performing candidates Amberlyst 15, Amberlyst 36, DOWEX-WX8, H-β (Si/Al:360), and sulfated zirconia. Figs. D.1 - D.3 complement this illustration with the time-resolved conversion of PO_1 and the yield of artemisinin for the other tested solid acids.

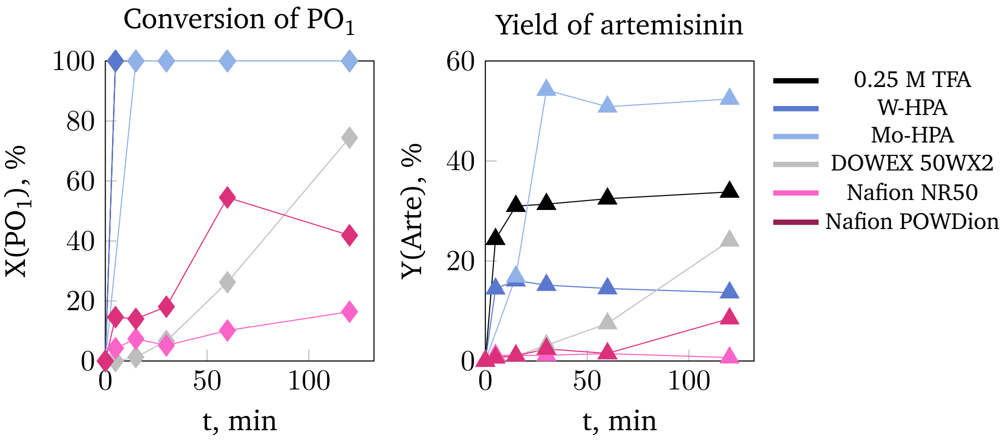

(a) Conversion of PO_1 **(b)** Yield of artemisinin

Fig. D.1: Performance of phosphotungstic acid (W-HPA), phosphomolybdic acid (Mo-HPA), DOWEX 50WX2, and Nafion as acidic catalysts in cleaving PO_1. TFA serves as reference for the homogeneous catalyzed reaction. Conditions: Batch operation, $[PO_1] = 0.3\,\mathrm{M}$, $V_{acid}/V_{liq} = 1:10$, $p_{O_2} = 1\,\mathrm{bara}$, $T = 25\,°\mathrm{C}$.

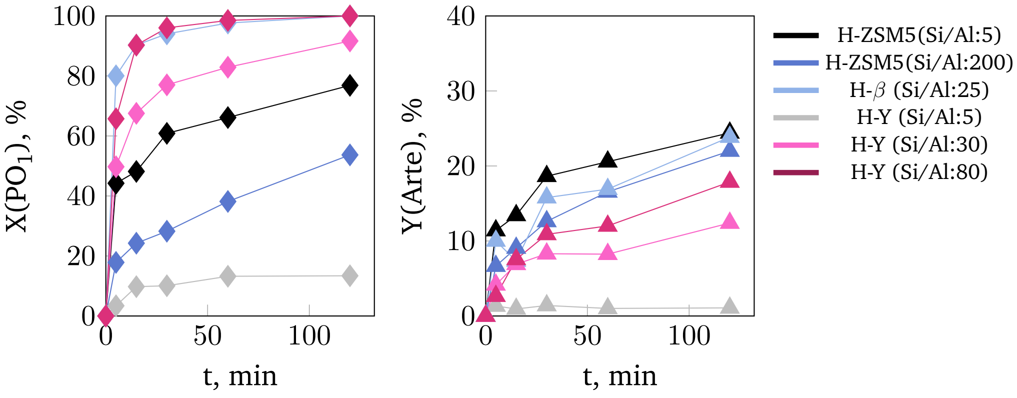

(a) Conversion of PO_1 **(b)** Yield of artemisinin

Fig. D.2: Performance of six zeolites with varied silica to alumina ratios as acidic catalysts in cleaving PO_1. Conditions: Batch operation, $[PO_1] = 0.3\,\mathrm{M}$, $V_{acid}/V_{liq} = 1:10$, $p_{O_2} = 1\,\mathrm{bara}$, $T = 25\,°\mathrm{C}$.

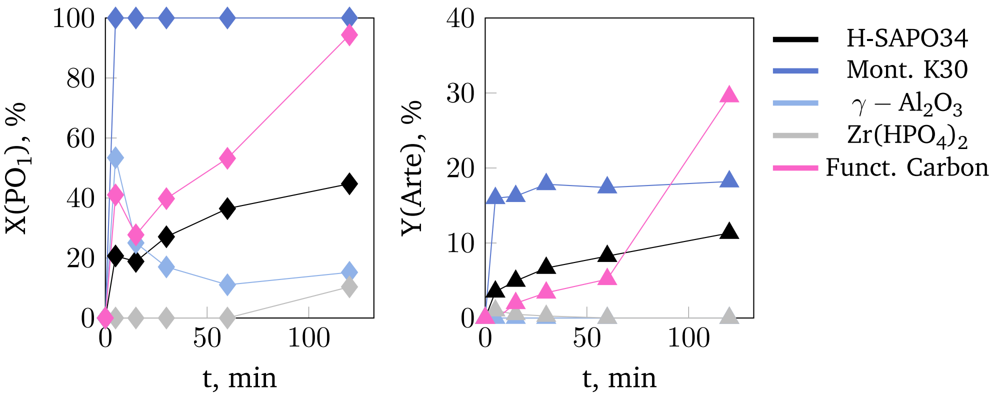

(a) Conversion of PO_1 **(b)** Yield of artemisinin

Fig. D.3: Performance of H-SAPO34, montmorillonite K30, γ-alumina, $Zr(HPO_4)_2$, and carbon with acidic functionality as acidic catalysts in cleaving PO_1. Conditions: Batch operation, $[PO_1] = 0.3\,\mathrm{M}$, $V_{\mathrm{acid}}/V_{\mathrm{liq}} = 1:10$, $p_{O_2} = 1\,\mathrm{bara}$, T$= 25\,°\mathrm{C}$.

E

Determination of the distribution factor C_0

The distribution factor is a crucial parameter to link the liquid with the gas flow. It was determined by residence time measurements of the liquid phase after tracer injection (Sec. 4.2.1). The gas fraction was determined based on the measured mean residence time $\bar{\tau}$ according to Eq. (7.15) as

$$\alpha = 1 - \frac{\dot{V}_1}{A l_r}\bar{\tau} = 1 - \frac{\dot{V}_1}{V}\bar{\tau}. \tag{E.1}$$

The obtained results are plotted in dependence on the known dosed gas holdup in Fig. E.1. The determined value for the distribution factor is

$$C_0 = 1.02 \pm 0.025. \tag{E.2}$$

The value determined for C_0 is close to the ideal case of $C_0 = 1$, meaning that both phases move with almost equal velocity through the channel. Thus, only a very thin liquid film forms around the moving gas bubbles in the investigated range of relatively small flow rates.

However, the residence time measurements can only give an estimate for the distribution factor due to uncertainties arising from tracer injection and detecting. More precise data can be obtained by applying high speed camera equipment.

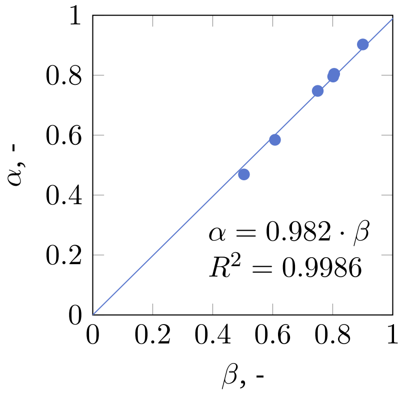

Fig. E.1: Determination of the distribution factor C_0: The gas fractions α were obtained from residence measurements of the liquid phase varied dosed gas holdups β

F

Procedure and validation of the actinometric measurements

Chemical actinometry with potassium ferrioxalate was applied to quantify the photon flux incident to the reaction line. Before performing actinometric experiments, the procedure of preparing the actinometer solution, performing the measurement, and analyzing the samples was validated. In addition, the range of process conditions where the actinometric measurements yield reproducible and reliable results was determined. In the following, details on the experimental procedure and results of this validation process are given, complementing Sec. 4.2.2 and Sec. 7.1.2.

F.1 Calibration of Fe(II)

The basis for applying actinometric measurements with ferrioxalate is the quantification of the red Fe(II)-phenanthrolin complex by UV/Vis spectroscopy. The applied UV/Vis spectrometer was calibrated with iron(II) sulfate standard solutions following the procedure in [338] using the absorption signal at $510\,\mathrm{nm}$. The obtained calibration curve is depicted in Fig. F.1.

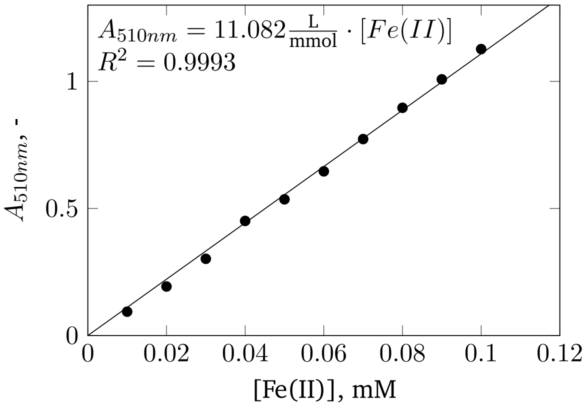

Fig. F.1: Calibration curve for the quantification of the Fe(II) concentration based on the measured absorption at $510\,\mathrm{nm}$.

F.2 Reference measurement for quality control of the actinometer solution

Before each measurement sequence, the freshly prepared actinometer was checked on reproducible ferrioxalate conversion with a reference irradiation stand (Fig. F.2). $3\,\mathrm{mL}$ of the actinometer solution were filled in a standard glass cuvette for UV/Vis spectroscopy (d $= 1\,\mathrm{cm}$) and placed within the reference device. After $120\,\mathrm{s}$ of irradiation from a LED strip (VARDAflex Para, rutec Licht GmbH & Co. KG, λ=$397\,\mathrm{nm}$, l=$3\,\mathrm{cm}$), the converted actinometer solution was stirred and sampled. This sample was processed according to the procedure described in Sec. 4.2.2. If the measured absorption at $510\,\mathrm{nm}$ was within 0.42 to 0.46 the actinometer solution could be used for the measurements. Otherwise reproducible measurements could not be ensured. The solution was discarded and and a new one was prepared and checked.

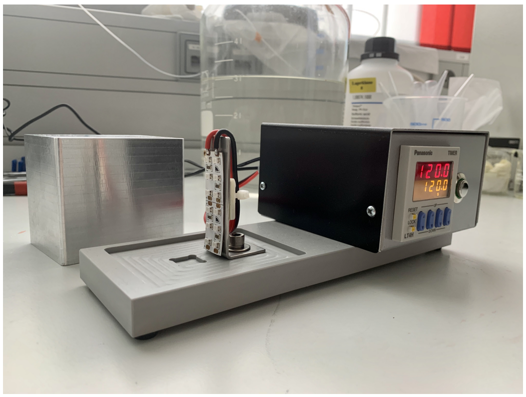

Fig. F.2: Reference setup to check the freshly prepared actinometer solution before using it for measurement of the photon flux.

F.3 Sample workup and data analysis

After irradiation of the actinometer, the collected sample required dilution and addition of phenanthrolin to form the red complex, which was used for quantification. For this sample workup, $1\,\mathrm{mL}$ (V_1) of the collected sample of the reactor effluent was added to $24\,\mathrm{mL}$ (V_2) of $0.05\,\mathrm{M}$ sulfuric acid. After that, $5\,\mathrm{mL}$ (V_3) of the diluted sample were combined with $20\,\mathrm{mL}$ (V_4) of a buffer solution ($0.1\,\%$ phenanthroline solution in $0.05\,\mathrm{M}$ sulfuric acid with $0.06\,\mathrm{M}$ sodium acetate). The mixture was kept for $30\,\mathrm{min}$ in a dark room. Finally, the absorption of the sample was measured at $510\,\mathrm{nm}$ with a UV/Vis spectrometer (Genesys 6, Thermo Fisher). If required, the sample for UV/Vis analysis (V_5) was diluted with $0.05\,\mathrm{M}$ sulfuric acid (V_6) so that the measured absorption signal did not exceed 1.2 .

The Fe(II) concentration in the diluted sample was determined based on the calibration shown in F.1. The obtained concentration was corrected by the dilution steps during sample work up as shown in Eq. (F.1). k is the calibration factor from Fig. F.1.

$$[Fe^{II}_{sample}] = \frac{A_{510nm}}{k}\frac{V_1+V_2}{V_1}\frac{V_3+V_4}{V_3}\frac{V_5+V_6}{V_5} \tag{F.1}$$

F.4 Validation of the actinometric method and the measurement conditions

The validation of the actinometric method included four steps: First, the reproducibility of the experimental procedure was optimized. Second, the effect of the flow conditions was tested. Third, the reaction lines with varied lengths were checked on their equality regarding the present irradiation conditions. Finally, the feasible set of flow conditions, reactor length, and irradiation span was defined.

The ferrioxalate actinometer is very sensitive to the quality of the reagent and small deviations in irradiation time. Automated switching of the LED modules and checking of the actinometer solution in a reference irradiation stand (App. F.2) achieved reproducible actinometer conversions with less than $5\,\%$ deviation.

Three tubing lines with lengths of $2\,\mathrm{m}$, $4\,\mathrm{m}$, and $10\,\mathrm{m}$ were used as photoreactor line in the photooxygenation experiments to cover a broad residence time range. In the next validation step, these different reaction lines were compared in respect to the irradiation intensity based on the actinometer conversion after $8\,\mathrm{s}$ irradiation (Fig. F.3a). The actinometric measurements were performed in discontinuous mode with no flow during irradiation (Sec. 4.2.2). All three reactors showed equal conversions and conclusively were exposed to comparable photon fluxes relative to the reactor volume. Thus, the part of the photorreactor casing where the tubing is positioned is evenly illuminated by the two light sources.

To check on the effect of the flow conditions, the actinometric experiments in discontinuous mode were adapted by continuously pumping the actinometer solution either in single or two-phase flow (g/l = 4/1 (v/v)) through the channel during irradiation. The results are shown in Fig. F.3b in dependence on the set LED power and the irradiation duration, which was equal to the residence time in irradiated photoreactor section for the continuous measurements.

In all three investigated LED power settings, the two-phase flow mode resulted in the highest actinometer conversions. Theoretically, the use of single-phase flow and the discontinuous should give similar results, since the channel is completely filled in both cases and thus the irradiation conditions are equal. The observed $15\,\%$ lower conversion in the discontinuous mode results from the diffusion-limited mixing in

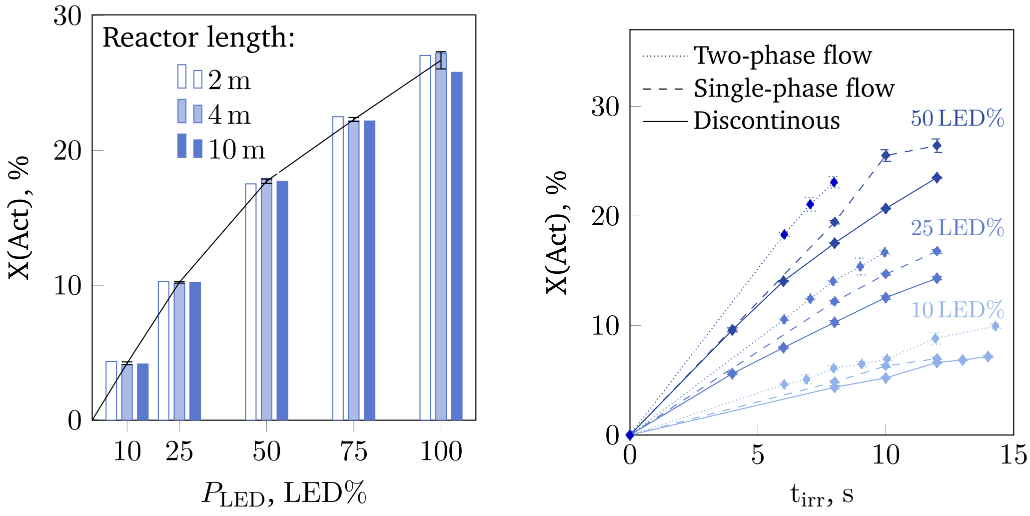

(a)

(b)

Fig. F.3: Identification of a feasible operation window for characterizing the irradiation conditions in the photoreactor with the ferrioxalate actinometer: a) Effect of the reactor length integrated in the photoreactor on the actinometer conversion measured after 8 s irradiation in the discontinuous mode, b) Effect of the flow conditions on the actinometer conversion (2 m reactor length).

the channel, shifting the reaction mechanism of the ferrioxalate photolysis and lowering the effective quantum yield [351]. This effect explains also the non-linearity regarding the LED power setting observed for the discontinuous measurements (Fig. F.3a). Thus, the discontinuous mode is only suitable for qualitative comparison but not to quantify the photon flux in the available reactor setup.

The change from single phase flow to two-phase flow (v/l=4/1 (v/v)) leads to a further increase in actinometer conversion by 20 %. The enhanced photon absorption is attributed to the thin film surrounding the gas bubbles in Taylor flow resulting in overall shorter optical path lengths than in single phase flow [278]. In addition, the operation in the Taylor flow regime ensures high mixing rates during irradiation. Thus, operation in two-phase flow is best suitable to quantify the incident photon flux for the photooxygenation experiments performed at equal flow conditions.

A practical limitation of ferrioxalate arises from the precipitation of Fe(II) at conversions exceeding 25 % [351]. In two-phase flow, this boundary is already reached within a few seconds. These short residence times can only be obtained in the shortest reactor of 2 m length due to the pump's limited capacity. At LED-power settings of ≥50 % precipitation was observed in all samples - even for very short residence times. Therefore, the experimental conditions for determining the photon flux were limited to two-phase flow operation using a reactor length of 2 m, LED powers of up to 25 % and residence times of up to 14 s.

F.5 Results with varied initial actinometer concentration

The standard concentration of ferrioxalate in the actinometer solution was $0.15\,\mathrm{M}$. To determine the optical pathlength, actinometric measurements were performed at varied initial concentrations in the range of $0.075\,\mathrm{mol\,L^{-1}}$ to $0.15\,\mathrm{mol\,L^{-1}}$ following the procedure of Roibu et al. [278]. The measured concentrations of Fe(II) formed while passing the irradiated photoreactor are depicted in Fig. F.4.

Due to reduced light absorption, the formation of Fe(II) was expected to be slower at lower initial concentration in comparison to higher concentrated solutions. However, this is trend was not distinctly observed in the actinometric measurements. Even though the initial concentration was changed by $100\,\%$, the concentration of Fe(II) formed at equal irradiation times did not vary significantly. The effect of changing the initial concentration is masked by the measurement error observed in the scattering of the data points obtained at equal irradiation times. This is why no unique parameter set of the optical pathlength and the incident photon flux could be fitted to the data.

One possible reason for the observed behaviour is a long optical pathlength ($l_{\mathrm{opt}} \geq 1.5\,\mathrm{mm}$) resulting in irradiation conditions close to total absorption. In this case, changing the concentration of the absorbing substance would have only a minor effect on the absorption factor. Another explanation might be that the ferrioxalate actinometer behaves differently at lower concentrations resulting in a change of the effective quantum yield.

In conclusion, it was not possible to quantify the optical pathlength by variation of the ferrioxalate initial concentration in the used concentration range and the applied experimental setup.

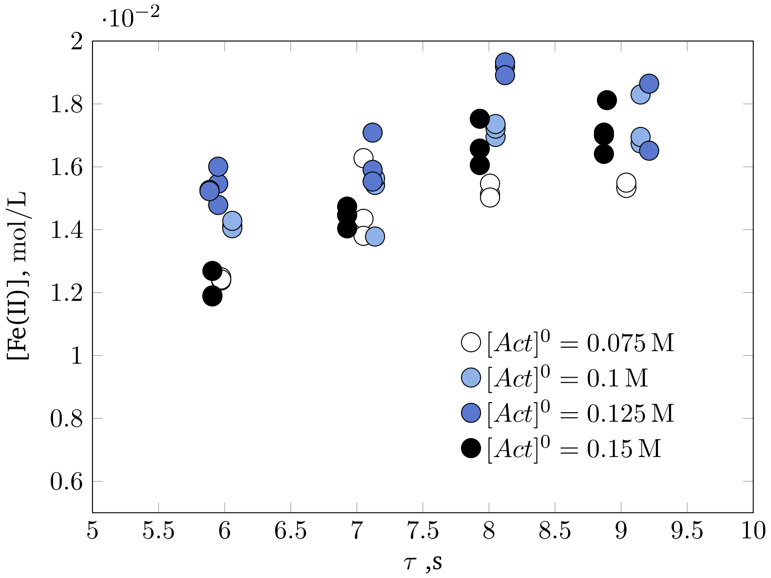

Fig. F.4: Actinometric measurements with ferrioxalate at varied initial concentration to determine the optical pathlength: Formation of Fe(II) in dependence on the residence time in the irradiated section of the photoreactor and the initial concentration of ferrioxalate $[\mathrm{Act}]^0$.

.

Kinetic investigation of the partial synthesis

G

In Chapter 7, a semi-mechanistic model was developed for the reaction kinetics of the initial photooxygenation of DHAA and the subsequent acid-catalyzed conversion of PO_1 to artemisinin. The following section complements the previously shown model development by assessing further the model-data fit for the photooxygenation model, analysing 2D-NMR data on the product spectrum of the acid-catalyzed sequence, comparing experimental data obtained in batch and continuous mode and giving additional details on crucial model candidates, which facilitated the developement of the final kinetic model.

G.1 Goodness of the model-data fit for the photooxygenation in dependence on the reaction conditions

The photooxygenation was investigated by varying five different process parameters: the residence time τ, the DHAA initial concentration, the set LED power P_{LED} relative to the maximum, the concentration of the catalyst DCA, and the oxygen concentration in the gas phase x_{O_2}. Fig. G.1 illustrates the fit quality of the identified photooxygenation model in dependence on these main process parameters. The corresponding ranges are listed in the table below the figure. All boxes accumulate around the zero deviation line across the whole parameter range, except for the thin box for the residence time in the last section. There is no distinct trend towards a lower or upper bound of any of the investigated parameters noticeable. The accumulation around zero suggests that the existent deviations of the data obtained with the photooxygenation model and the experimental data are mainly caused by measurement noise and errors that inherently occur during the measurement procedure but not by systematic model discrepancy.

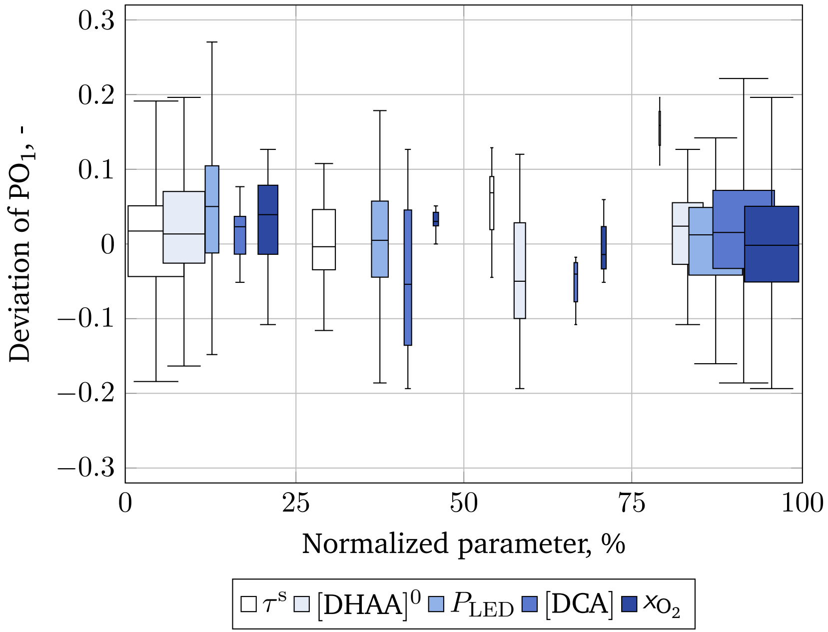

Symbol	Unit	Description	Lower bound	Upper bound
τ^s	min	Theoretical residence time	0.439	5.931
$[DHAA]^0$	$mol\,L^{-1}$	Initial concentration of DHAA	0.231	0.491
P_{LED}	%LED	LED light power	50	100
[DCA]	$mmol\,L^{-1}$	Concentration of photosensitizer DCA	0.117	0.850
x_{O_2}	$mol\,mol^{-1}$	Molar fraction of oxygen in gas phase	0.41	1.00

Fig. G.1: Relative deviation between the simulation with the photooxygenation model (Sec. 7.1.4) and the experimental data $(y^{data} - y)/y$ for PO_1, depicted over the investigated range of process parameter values. The widths of the boxes reflect the number of samples in each of the four sections. (The whiskers are based on 1.5 times the interquartile range. Outliers are not shown.)

G.2 NMR studies on the acid-catalyzed reaction sequence performed in $CDCl_3$

In the acid-catalyzed reaction sequence, PO_1 is converted to a wide spectrum of intermediates and reaction products [70]. As shown in Sec. 7.2.1.1, not all reaction products formed after PO_1 cleavage could be identified. To elucidate the product spectrum further, the reaction solution was analyzed with 2D-NMR techniques.

The kinetic experiments were performed in toluene as solvent, which needed to be evaporated from the sample prior to NMR analysis. To reduce the effect of sample workup, the experiment for providing the product solution for 2D NMR analysis was performed with $CDCl_3$ as reaction solvent. The solution was prepared with the continuous reaction setup (Sec. 4.1) following the procedure introduced in Sec. 4.3.3. The reactor feed contained $0.37\,\mathrm{M}$ DHAA, $2\,\mathrm{mM}$ DCA, and $0.06\,\mathrm{M}$ TFA in $CDCl_3$. Thus, the acid-catalyzed reaction sequence started directly after PO_1 formation in the photoreactor. The residence times in the photoreactor and the acid-catalyzed reaction were $5\,\mathrm{min}$ and $1\,\mathrm{min}$, respectively. This setting ensured complete conversion of DHAA and almost complete conversion of PO_1 but no significant formation of artemisinin. In this way, the unknown intermediate species are highly concenctrated in the reaction solution. The photoreactor was operated at $-20\,°\mathrm{C}$ and irradiated by $420\,\mathrm{nm}$ LED light at $100\,\%$ intensity. The acid-catalyzed section was at room temperature. After reaching steady-state, a sample was collected from the reactor effluent and immediately quenched with TEA to stop the reaction. The sample was directly subjected to NMR analysis in the NMR lab at the *Otto-von-Guericke University*.

The obtained spectra are depicted in Figs. G.2 - G.7. The $^1\mathrm{H-NMR}$ spectrum in Fig. G.2 shows that only traces of PO_1 (δ=$5.23\,\mathrm{ppm}$) are remaining after the experiment. Apart from artemisinin (δ=$5.85\,\mathrm{ppm}$), BP_3 (δ=$5.64\,\mathrm{ppm}$) and PO_2 (δ=$4.82\,\mathrm{ppm}$), no other formed products show significant signals in the range of $4\,\mathrm{ppm}$ to $7\,\mathrm{ppm}$. The majority of the $^1\mathrm{H-NMR}$ signals appear in the region of $0.5\,\mathrm{ppm}$ to $3\,\mathrm{ppm}$.

The 2D-NMR spectra in Figs. G.5, G.6, and G.7 show many couplings in this region, which can not be clearly distinguished. The large number of couplings indicates that PO_1 is not converted to a few number of main intermediates but to a wide spectrum of different species, which later in the reaction pathway react to the main reaction products artemisinin and BP_4. Structural elucidation of these intermediate species requires separation of each compound from the reaction solution. With the set of analytical tools available in this study, the formed intermediate species could not be identified nor quantified. Thus, simplified reaction networks were proposed, which group the formed intermediates in several lumped species (Sec. 7.2.2.1).

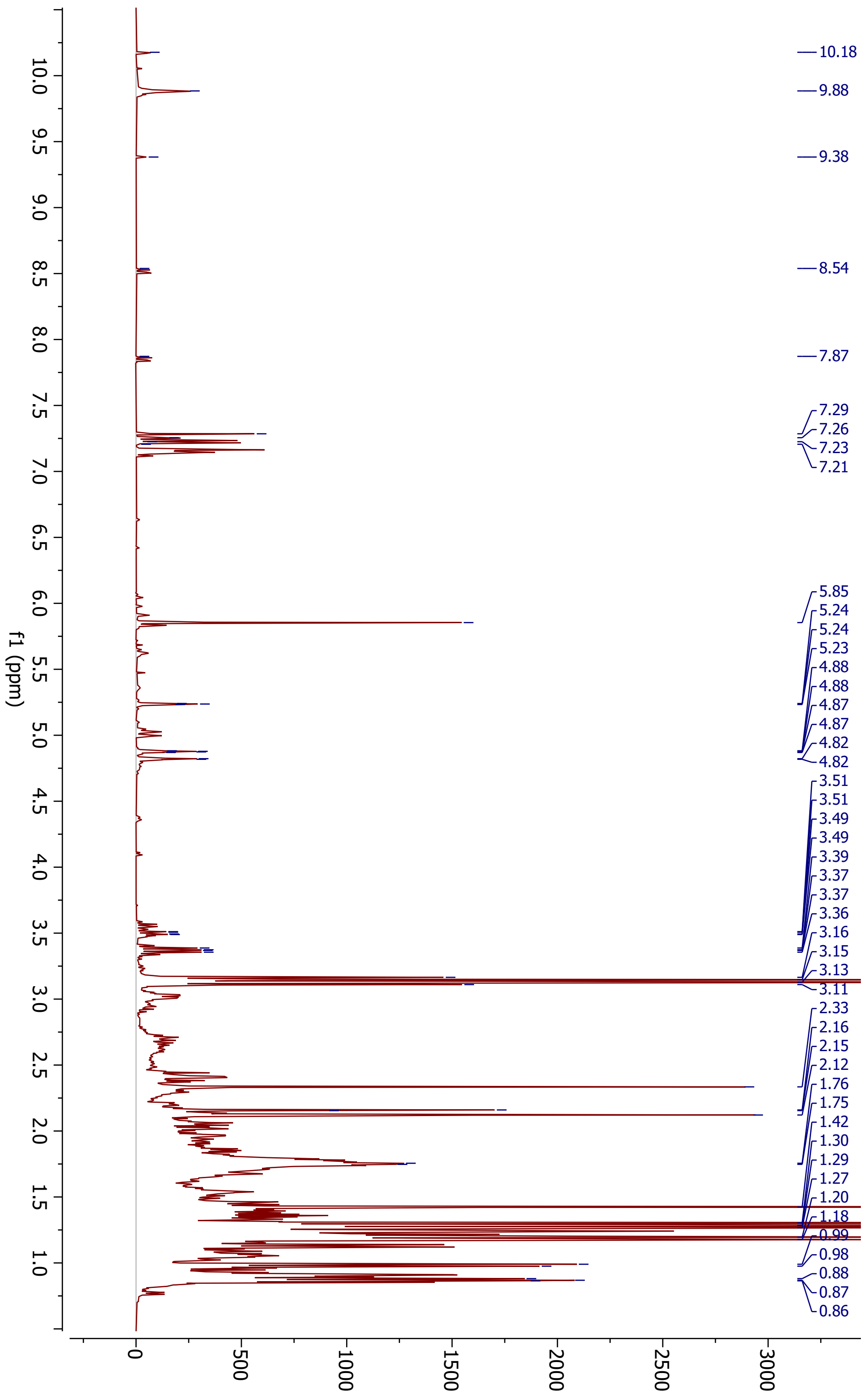

Fig. G.2: ^{1}H−NMR-spectrum of a reaction solution of the acid-catalyzed cleavage of PO_1. The reaction was performed in $CDCl_3$ as solvent with DCA as photocatalyst, and TFA as acidic catalyst. The solution was quenched with TEA directly after exiting the reactor.

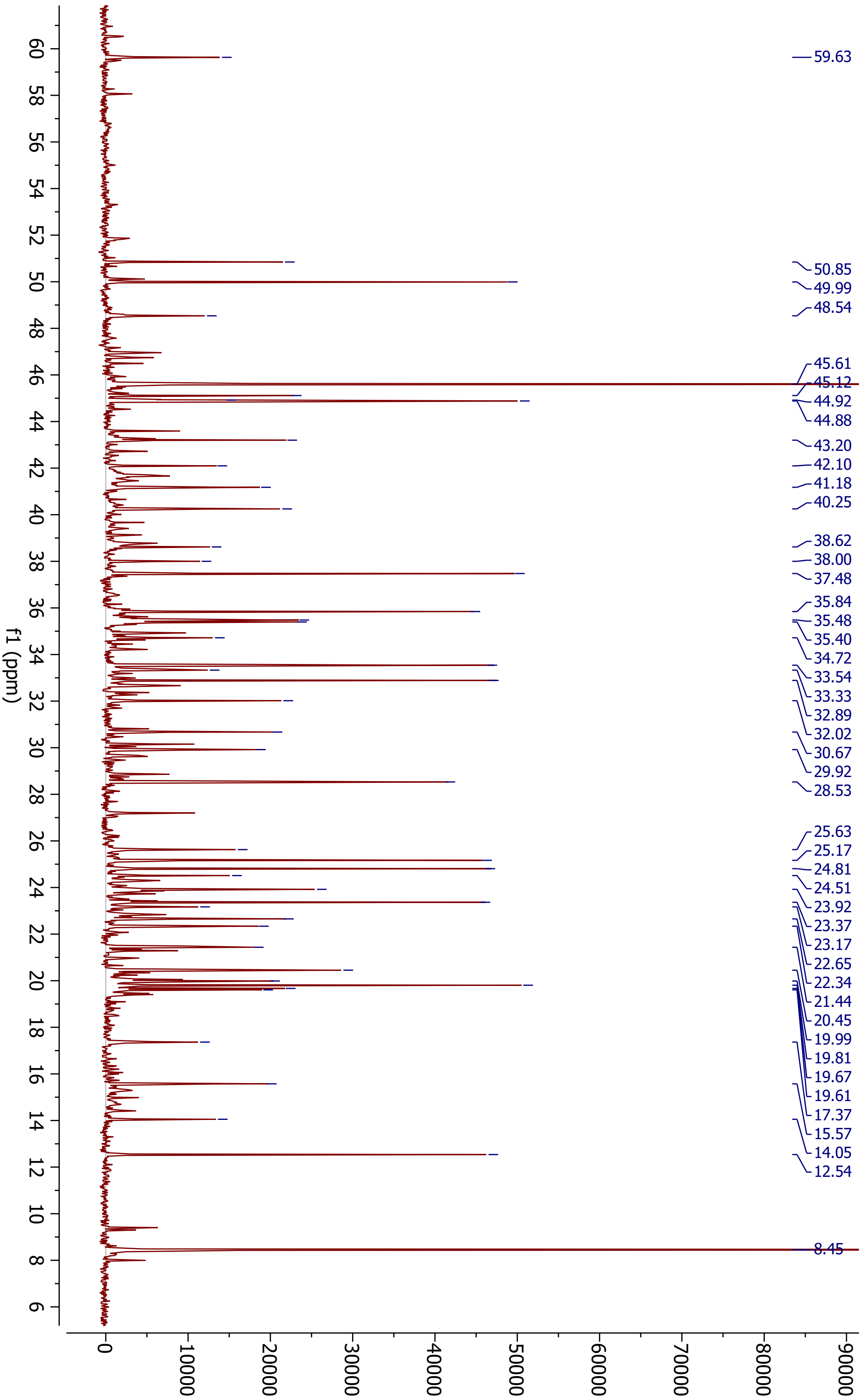

Fig. G.3: ^{13}C NMR spectrum of a reaction solution of the acid-catalyzed cleavage of PO_1. The reaction was performed in $CDCl_3$ as solvent with DCA as photocatalyst, and TFA as acidic catalyst. The solution was quenched with TEA directly after exiting the reactor.

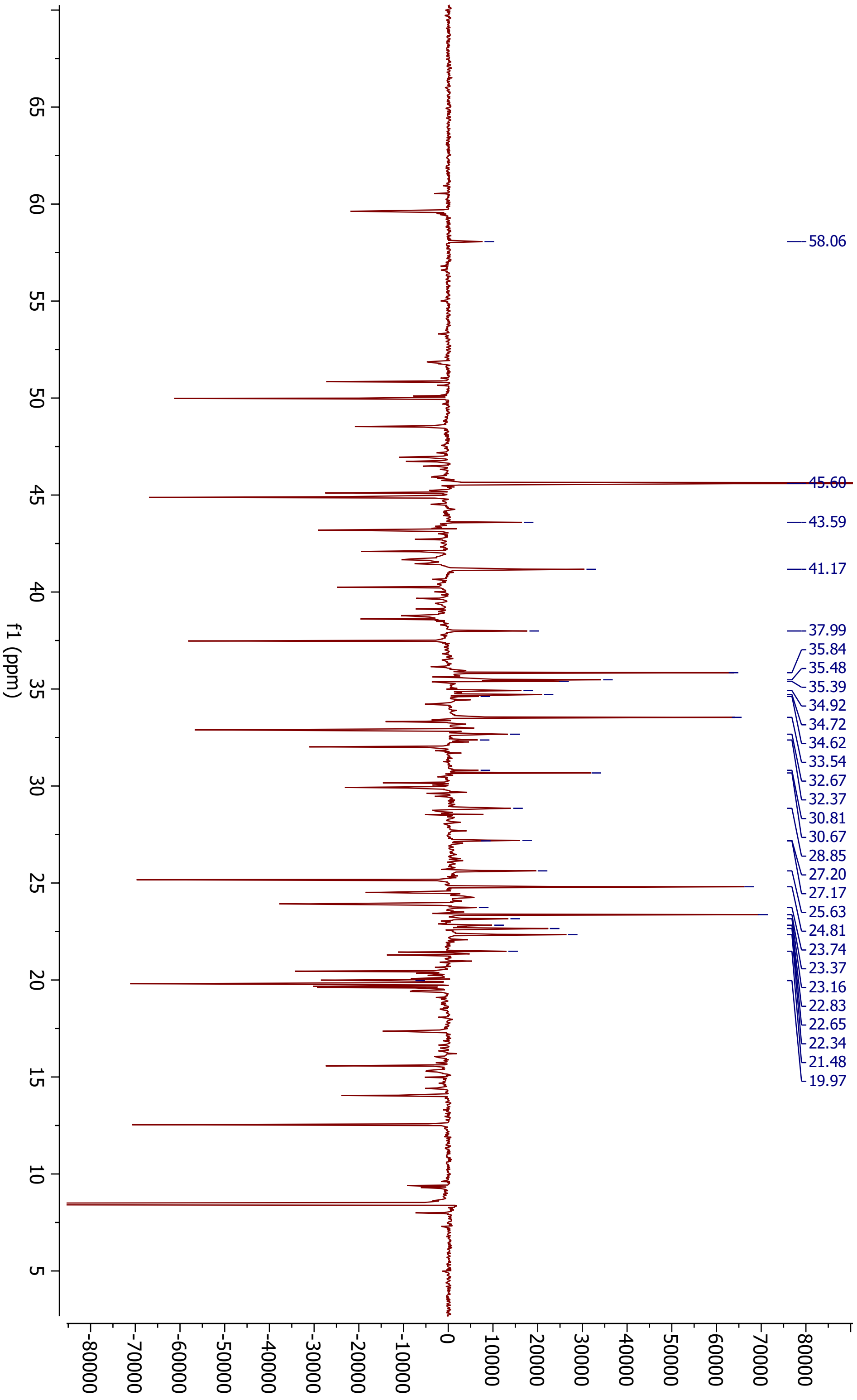

Fig. G.4: ^{13}C-DEPT NMR-spectrum of a reaction solution of the acid-catalyzed cleavage of PO_1. The reaction was performed in $CDCl_3$ as solvent with DCA as photocatalyst, and TFA as acidic catalyst. The solution was quenched with TEA directly after exiting the reactor.

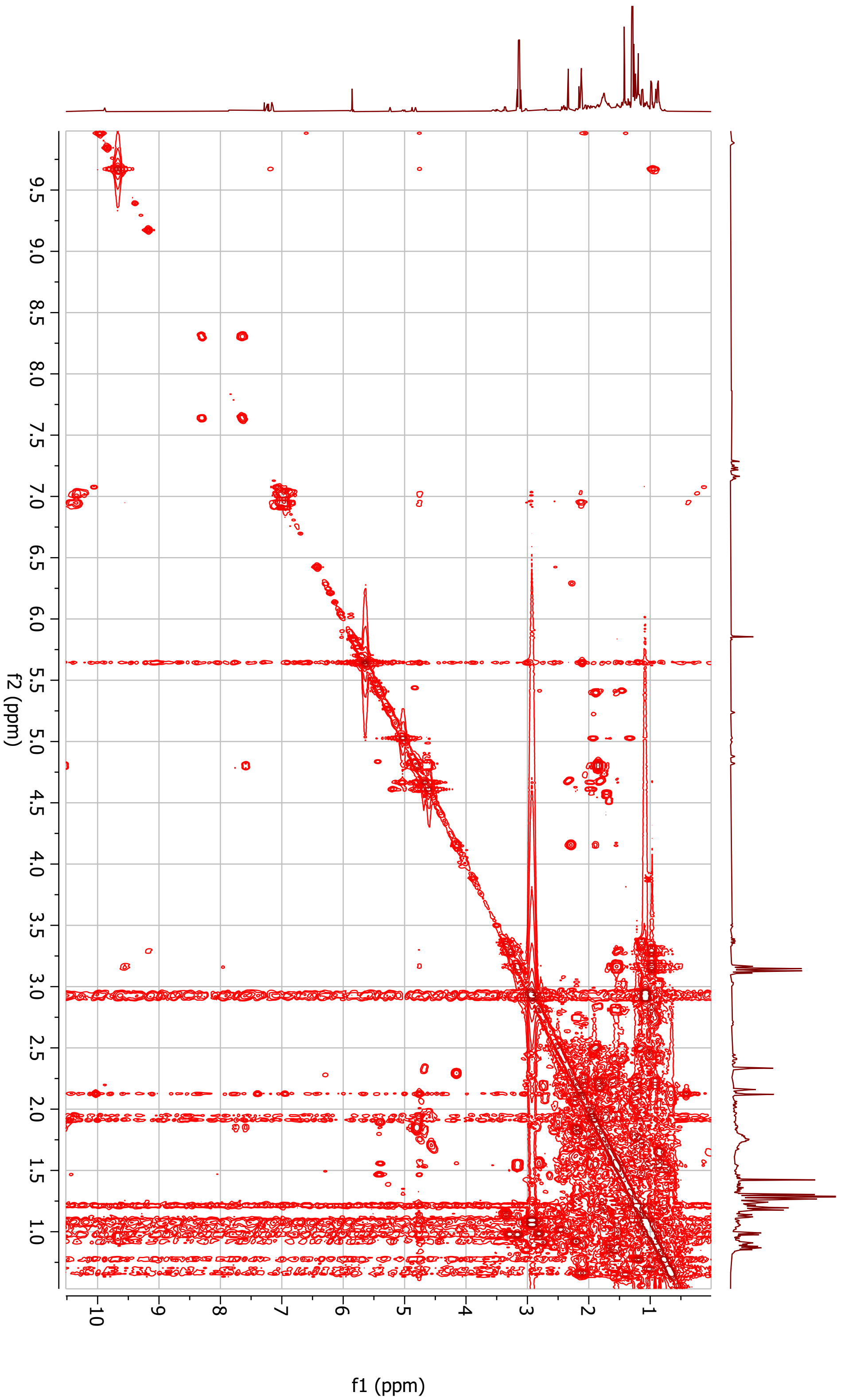

Fig. G.5: ^{1}H,^{1}H-COSY spectrum of a reaction solution of the acid-catalyzed cleavage of PO_1. The reaction was performed in $CDCl_3$ as solvent with DCA as photocatalyst, and TFA as acidic catalyst. The solution was quenched with TEA directly after exiting the reactor.

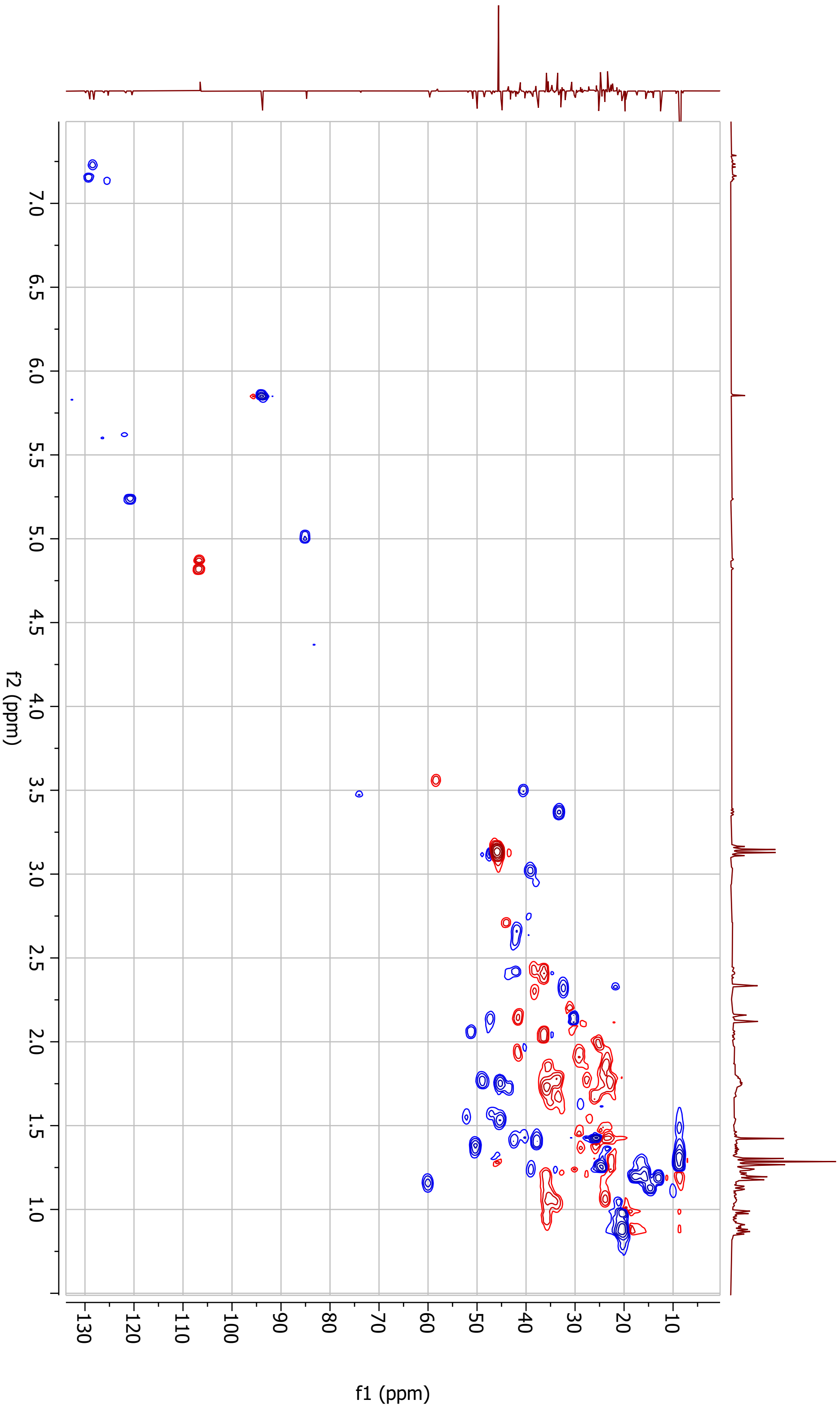

Fig. G.6: $^{1}H,^{13}C$-HSQC NMR spectrum of a reaction solution of the acid-catalyzed cleavage of PO_1. The reaction was performed in $CDCl_3$ as solvent with DCA as photocatalyst, and TFA as acidic catalyst. The solution was quenched with TEA directly after exiting the reactor.

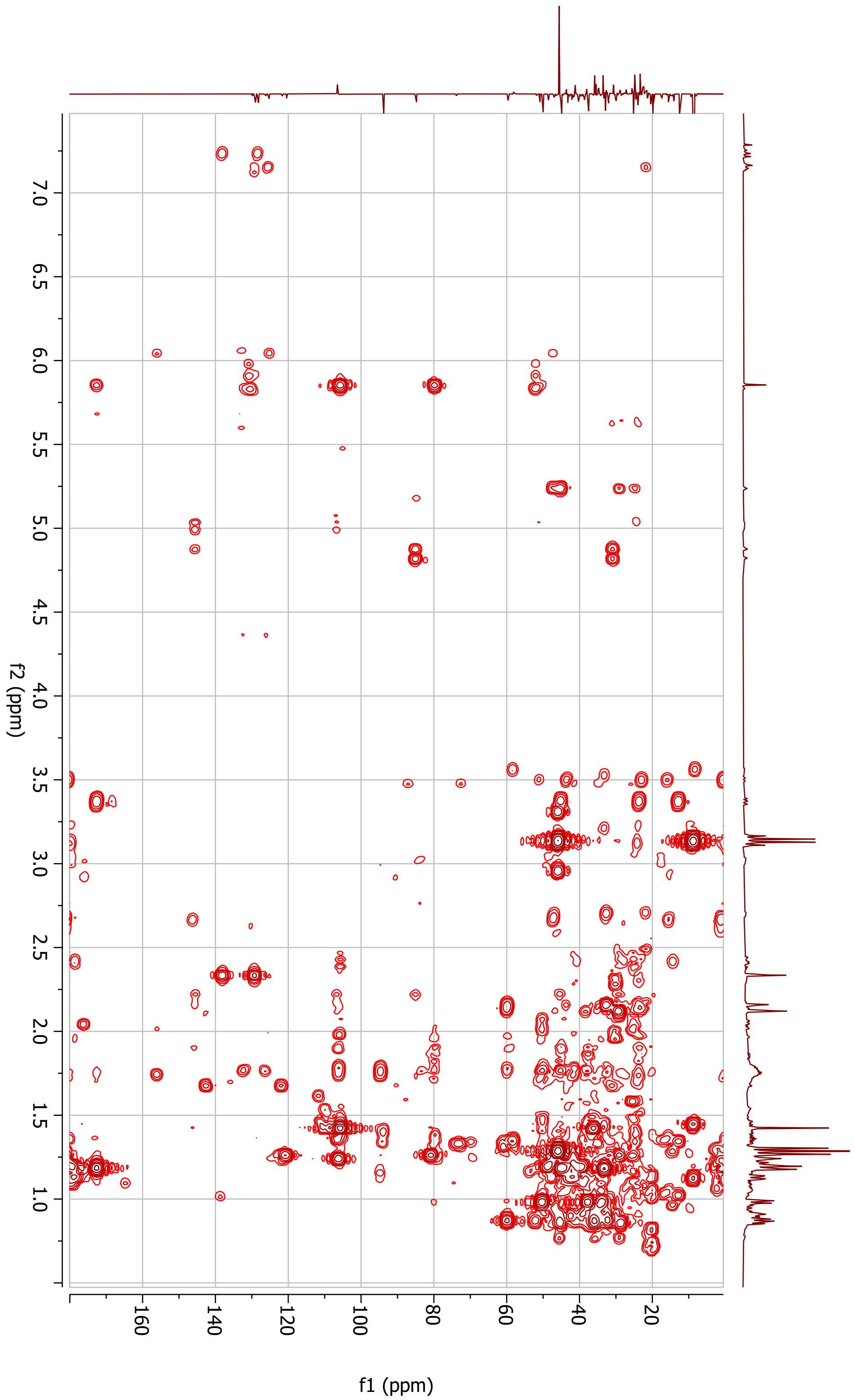

Fig. G.7: ^{1}H,^{13}C-HMBC NMR spectrum of a reaction solution of the acid-catalyzed cleavage of PO$_1$. The reaction was performed in CDCl$_3$ as solvent with DCA as photocatalyst, and TFA as acidic catalyst. The solution was quenched with TEA directly after exiting the reactor.

G.3 Comparison of batch and continuous experiments to study the acid-catalyzed reaction sequence

The acid-catalyzed reaction sequence from PO_1 to artemisinin was investigated by continuous experiments in the presence of oxygen and batch experiments in the absence of oxygen (Sec. 4.3.4). Batch experiments are particularly suitable to gather several kinetic data points with one experiment, while each continuous experiment in steady-state represented a single data point. Due to the limited residence time in the continuous reactor, batch experiments were utilized to investigate lower acid concentrations requiring longer experimental time.

Fig. G.8 compares experimental data of batch and continuous experiments at comparable TFA concentrations. The experimental modes were compared based on the PO_1 concentration and the concentration of the byproduct BP_3. According to the reaction mechanism (Sec. 2.3.1), the conversion of PO_1 and the formation of BP_3 are independent of the oxygen concentration present.

The similar results after equal residence times in the continous mode and experimental time in batch mode show that both experimental settings yield comparable results for PO_1 and BP_3 despite the different flow conditions.

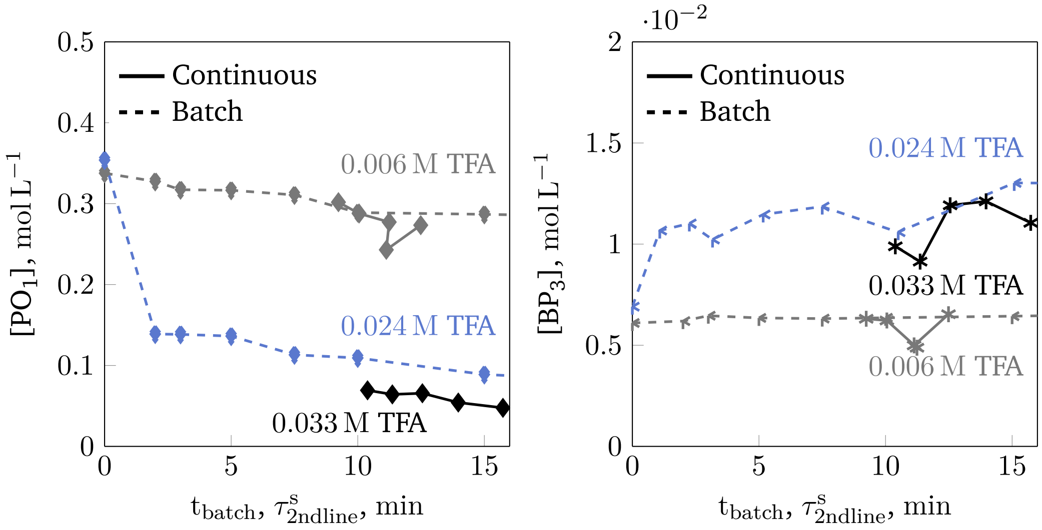

(a) PO_1 **(b)** BP_3

Fig. G.8: Comparison of experimental data on the acid-catalyzed reaction sequence obtained in continuous operation in the presence of oxygen and in batch operation in nitrogen atmosphere ($[DHAA]^0 = 0.5\,M$, $T_{photo} = -20\,°C$, $\tau_{photo} = 5$ minute, $[DCA] = 2.5\,mM$, $x_{O_2} = 1$, $P_{LED} = 100\,\%$): a) Cleavage of PO_1 b) Formation of BP_3.

G.4 Details on the tested model candidates for the acid-catalyzed reaction sequence

In Sec. 7.2.2 several model candidates differing in the regarded reaction network were introduced. The following section supports the previous analysis of essential features in the kinetic model by giving additional information on the kinetic equations and the obtained model-data fit of selected model candidates, which were crucial in developing the final kinetic model for the acid-catalyzed reaction sequence introduced in Sec. 7.2.3.

G.4.1 Kinetic equations of the base model

The base model served as a starting point in the model development. The model structure and the obtained model-data fit were shown Fig. 7.11 and Fig. 7.12, respectivly. The rate equations of the base model are given in Eqs. (G.1) - (G.8).

$$\mathrm{PO_1} \xrightarrow{\quad} \mathrm{PO_x} \qquad r_{\mathrm{PO_x}} = k_{\mathrm{PO_x}}[\mathrm{PO_1}] \tag{G.1}$$

$$\mathrm{PO_1} \xrightarrow{\mathrm{H+}} \mathrm{IM_2} \qquad r_{\mathrm{PO_1,IM_2}} = k_{\mathrm{PO_1,IM_2}}[\mathrm{H^+}][\mathrm{PO_1}] \tag{G.2}$$

$$\mathrm{PO_1} \xrightarrow{\mathrm{H+}} \mathrm{BP_3} \qquad r_{\mathrm{PO_1,BP_3}} = k_{\mathrm{PO_1,BP_3}}[\mathrm{H^+}][\mathrm{PO_1}] \tag{G.3}$$

$$\mathrm{IM_2} + \mathrm{O_2} \xrightarrow{\quad} \mathrm{IM_3} \qquad r_{\mathrm{IM_2,IM_3}} = k_{\mathrm{IM_2,IM_3}}[\mathrm{O_2}][\mathrm{IM_2}] \tag{G.4}$$

$$\mathrm{IM_2} \xrightarrow{\mathrm{H+}} \mathrm{BP_4} \qquad r_{\mathrm{IM_2,BP_4}} = k_{\mathrm{IM_2,BP_4}}[\mathrm{H^+}][\mathrm{IM_2}] \tag{G.5}$$

$$\mathrm{IM_3} \xrightarrow{\mathrm{H+}} \mathrm{Arte} \qquad r_{\mathrm{IM_3,Arte}} = k_{\mathrm{IM_3,Arte}}[\mathrm{H^+}][\mathrm{IM_3}] \tag{G.6}$$

$$\mathrm{IM_2} \xrightarrow{\mathrm{H+}} \mathrm{BP_5} \qquad r_{\mathrm{IM_2,BP_5}} = k_{\mathrm{IM_2,BP_5}}[\mathrm{H^+}][\mathrm{IM_3}] \tag{G.7}$$

$$[\mathrm{H^+}] = [\mathrm{TFA}]^0 \tag{G.8}$$

G.4.2 Model-data fit for selected model candidates extending the base model

This section gives additional information on four model candidates, Models 6, 7, 13 and 21, introduced in Sec. 7.2.2.3. The model ID is equal to the number given in Tab. 7.6. The abbreviations of the different model features were given in Fig. 7.11, Tab. 7.4, and Tab. 7.5. Further information on the other tested model candidates can be found in [360].

G.4.2.1 Model 6 - Base-A-IV

Model 6 is similar to the base network in the regarded reaction pathways but includes a variable reaction order for TFA in the initial PO_1 conversion. The TFA reaction orders n in the formation of IM_2 and in the formation of BP_3 are directly coupled. The resulting kinetic equations are:

$$\mathrm{PO_1} \xrightarrow{\quad\quad} \mathrm{PO_x} \qquad r_{\mathrm{PO_x}} = k_{\mathrm{PO_x}}[\mathrm{PO_1}] \tag{G.9}$$

$$\mathrm{PO_1} \xrightarrow{\mathrm{H+}} \mathrm{IM_2} \qquad r_{\mathrm{PO_1,IM_2}} = k_{\mathrm{PO_1,IM_2}}[\mathrm{H^+}]^{n_{\mathrm{IM_2}}}[\mathrm{PO_1}] \tag{G.10}$$

$$\mathrm{PO_1} \xrightarrow{\mathrm{H+}} \mathrm{BP_3} \qquad r_{\mathrm{PO_1,BP_3}} = k_{\mathrm{PO_1,BP_3}}[\mathrm{H^+}]^{n_{\mathrm{IM_2}}+1}[\mathrm{PO_1}] \tag{G.11}$$

$$\mathrm{IM_2} + \mathrm{O_2} \xrightarrow{\quad\quad} \mathrm{IM_3} \qquad r_{\mathrm{IM_2,IM_3}} = k_{\mathrm{IM_2,IM_3}}[\mathrm{O_2}][\mathrm{IM_2}] \tag{G.12}$$

$$\mathrm{IM_2} \xrightarrow{\mathrm{H+}} \mathrm{BP_4} \qquad r_{\mathrm{IM_2,BP_4}} = k_{\mathrm{IM_2,BP_4}}[\mathrm{H^+}][\mathrm{IM_2}] \tag{G.13}$$

$$\mathrm{IM_3} \xrightarrow{\mathrm{H+}} \mathrm{Arte} \qquad r_{\mathrm{IM_3,Arte}} = k_{\mathrm{IM_3,Arte}}[\mathrm{H^+}][\mathrm{IM_3}] \tag{G.14}$$

$$\mathrm{IM_2} \xrightarrow{\mathrm{H+}} \mathrm{BP_5} \qquad r_{\mathrm{IM_2,BP_5}} = k_{\mathrm{IM_2,BP_5}}[\mathrm{H^+}][\mathrm{IM_2}] \tag{G.15}$$

$$[\mathrm{H^+}] = [\mathrm{TFA}]^0. \tag{G.16}$$

The introduction of a variable reaction order resulted in a significantly improved model-data fit as shown in the parity plots given in Fig. G.9. The identified model parameters are listed in Tab. G.1.

Tab. G.1: Kinetic parameters identified for Model 6 (Eqs. (G.9) - (G.16)).

Model-data fit of Model 6			
Symbol	unit	value	description
SSE	$\mathrm{mol^2/L^2}$	0.2074	sum of squared errors
SSE_{conti}	$\mathrm{mol^2/L^2}$	0.1214	SSE for continuous exp.
SSE_{batch}	$\mathrm{mol^2/L^2}$	0.0860	SSE for batch exp.
estimated parameters			
Symbol	unit	value	
$k_{\mathrm{PO_x}}$	$\mathrm{min^{-1}}$	0.0107	
$n_{\mathrm{IM_2}}$	-	2.674	
$k_{\mathrm{PO_1,BP_3}}$	$(\mathrm{L\,mol^{-1}})^{n+1}\ \mathrm{min^{-1}}$	634.2	
$k_{\mathrm{PO_1,IM_2}}$	$(\mathrm{L\,mol^{-1}})^{n}\ \mathrm{min^{-1}}$	985.2	
$k_{\mathrm{IM_2,BP_5}}$	$\mathrm{L\,mol^{-1}\,min^{-1}}$	0	
$k_{\mathrm{IM_2,BP_4}}$	$\mathrm{L\,mol^{-1}\,min^{-1}}$	0.8582	
$k_{\mathrm{IM_2,IM_3}}$	$\mathrm{L\,mol^{-1}\,min^{-1}}$	$5000^{\dagger}$	
$k_{\mathrm{IM_3,Arte}}$	$\mathrm{L\,mol^{-1}\,min^{-1}}$	0.7864	

†: Upper boundary of the set parameter range

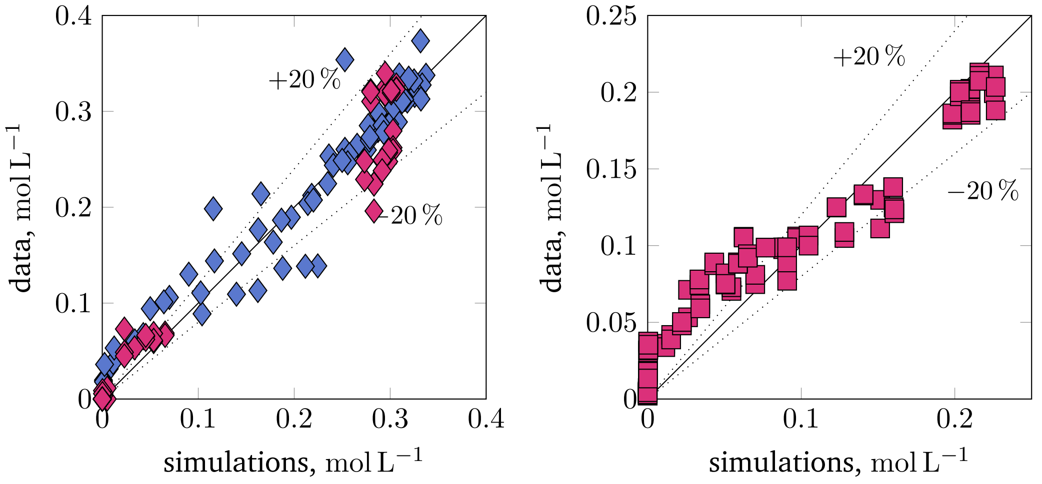

(a) PO_1 **(b)** Artemisinin

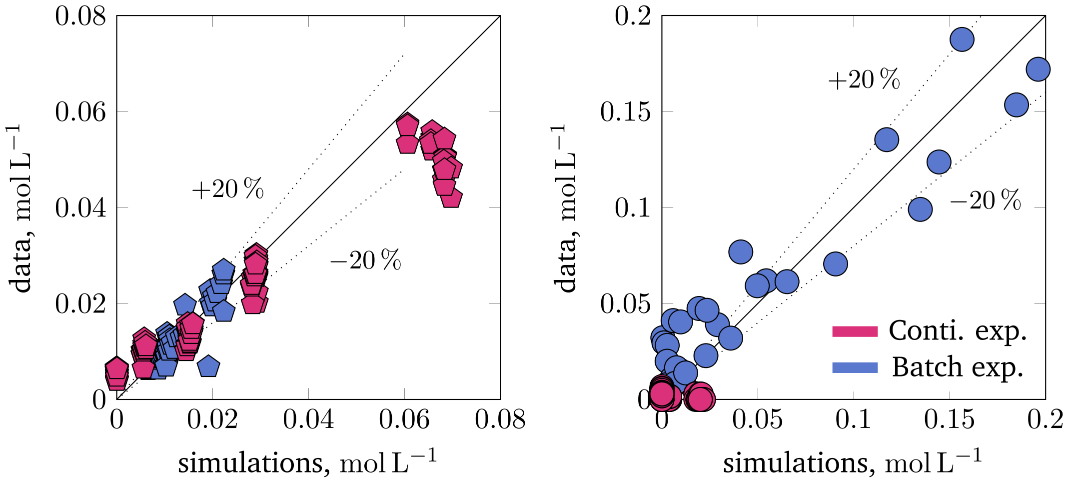

(c) BP_3 **(d)** BP_4

Fig. G.9: Fit between the simulated results obtained with Model 6 and the experimental data of the acid-catalyzed reaction sequence. Blue and red points indicate data from the batch and continuous experiments, respectively.

G.4.2.2 Model 7 - Base-A-V

Model 7 differs from Model 6 by decoupling both TFA reaction orders, $n_{\mathrm{IM_2}}$ and $n_{\mathrm{BP_3}}$. The rate equations of Model 7 are given in Eqs. (G.17) - (G.24).

$$\mathrm{PO_1} \xrightarrow{\quad} \mathrm{PO_x} \qquad r_{\mathrm{PO_x}} = k_{\mathrm{PO_x}}[\mathrm{PO_1}] \tag{G.17}$$

$$\mathrm{PO_1} \xrightarrow{\mathrm{H+}} \mathrm{IM_2} \qquad r_{\mathrm{PO_1,IM_2}} = k_{\mathrm{PO_1,IM_2}}[\mathrm{H^+}]^{n_{\mathrm{IM_2}}}[\mathrm{PO_1}] \tag{G.18}$$

$$\mathrm{PO_1} \xrightarrow{\mathrm{H+}} \mathrm{BP_3} \qquad r_{\mathrm{PO_1,BP_3}} = k_{\mathrm{PO_1,BP_3}}[\mathrm{H^+}]^{n_{\mathrm{BP_3}}}[\mathrm{PO_1}] \tag{G.19}$$

$$\mathrm{IM_2} + \mathrm{O_2} \xrightarrow{\quad} \mathrm{IM_3} \qquad r_{\mathrm{IM_2,IM_3}} = k_{\mathrm{IM_2,IM_3}}[\mathrm{O_2}][\mathrm{IM_2}] \tag{G.20}$$

$$\mathrm{IM_2} \xrightarrow{\mathrm{H+}} \mathrm{BP_4} \qquad r_{\mathrm{IM_2,BP_4}} = k_{\mathrm{IM_2,BP_4}}[\mathrm{H^+}][\mathrm{IM_2}] \tag{G.21}$$

$$\mathrm{IM_3} \xrightarrow{\mathrm{H+}} \mathrm{Arte} \qquad r_{\mathrm{IM_3,Arte}} = k_{\mathrm{IM_3,Arte}}[\mathrm{H^+}][\mathrm{IM_3}] \tag{G.22}$$

$$\mathrm{IM_2} \xrightarrow{\mathrm{H+}} \mathrm{BP_5} \qquad r_{\mathrm{IM_2,BP_5}} = k_{\mathrm{IM_2,BP_5}}[\mathrm{H^+}][\mathrm{IM_2}] \tag{G.23}$$

$$[\mathrm{H^+}] = [\mathrm{TFA}]^0 \tag{G.24}$$

The additional model parameter does not facilitate a further improved model-data fit in comparison to Model 6. The parity plots for Model 7 are shown in Fig. G.10. The obtained model parameters are given in Tab. G.2.

Tab. G.2: Kinetic parameters identified for Model 7 (Eqs. (G.17) - (G.24)) describing the acid-catalyzed reaction sequence starting from $\mathrm{PO_1}$ to artemisinin.

Model-data fit of Model 7			
Symbol	unit	value	description
SSE	$\mathrm{mol^2/L^2}$	0.2074	sum of squared errors
SSE_{conti}	$\mathrm{mol^2/L^2}$	0.1214	SSE for continuous exp.
SSE_{batch}	$\mathrm{mol^2/L^2}$	0.0860	SSE for batch exp.
estimated parameters			
Symbol	unit	value	
$k_{\mathrm{PO_x}}$	$\mathrm{min^{-1}}$	0.0107	
$n_{\mathrm{IM_2}}$	-	2.674	
$n_{\mathrm{BP_3}}$	-	3.684	
$k_{\mathrm{PO_1,BP_3}}$	$(\mathrm{L\,mol^{-1}})^{n_{\mathrm{BP_3}}}\,\mathrm{min^{-1}}$	641.4	
$k_{\mathrm{PO_1,IM_2}}$	$(\mathrm{L\,mol^{-1}})^{n_{\mathrm{IM_2}}}\,\mathrm{min^{-1}}$	985.8	
$k_{\mathrm{IM_2,BP_5}}$	$\mathrm{L\,mol^{-1}\,min^{-1}}$	0	
$k_{\mathrm{IM_2,BP_4}}$	$\mathrm{L\,mol^{-1}\,min^{-1}}$	0.8576	
$k_{\mathrm{IM_2,IM_3}}$	$\mathrm{L\,mol^{-1}\,min^{-1}}$	5000†	
$k_{\mathrm{IM_3,Arte}}$	$\mathrm{L\,mol^{-1}\,min^{-1}}$	0.7862	

†: Upper boundary of the set parameter range

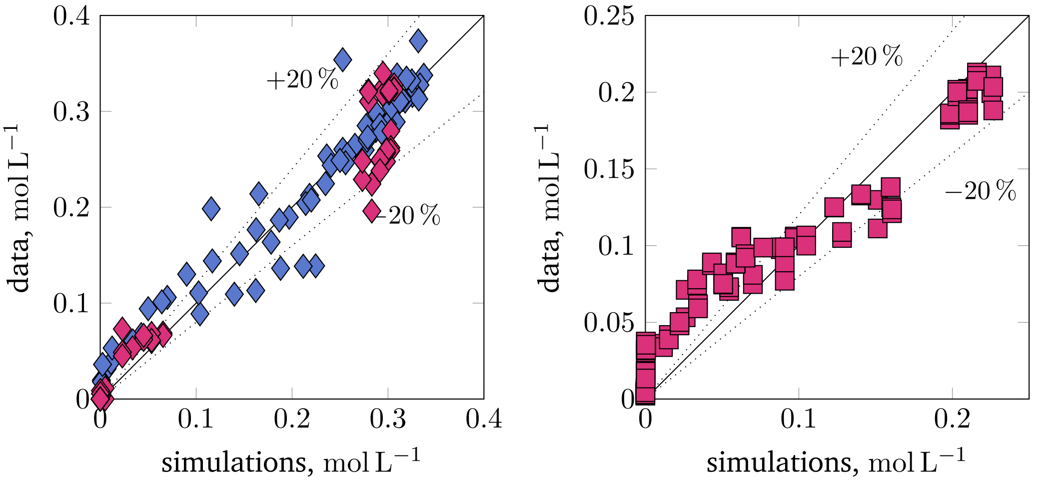

(a) PO_1 **(b)** Artemisinin

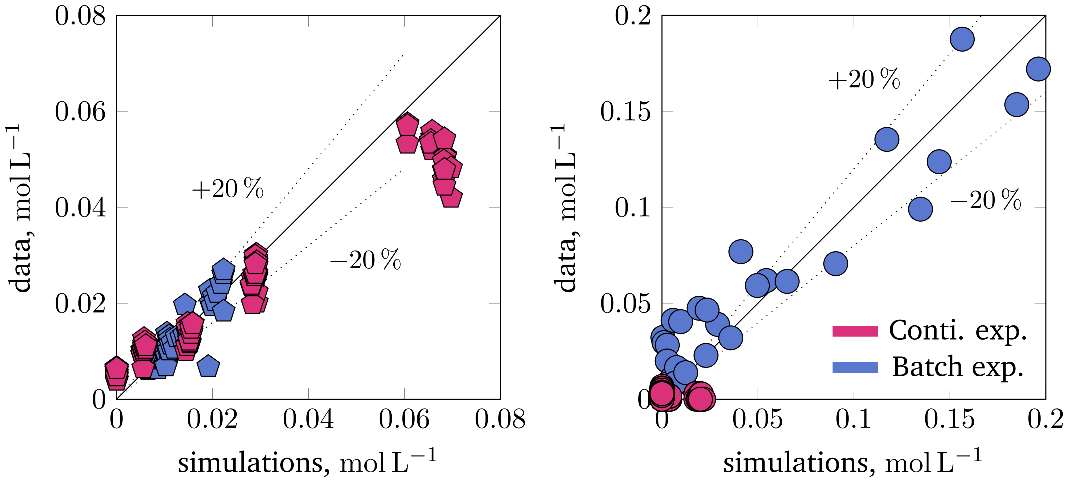

(c) BP_3 **(d)** BP_4

Fig. G.10: Fit between the simulated results obtained with Model 7 and the experimental data of the acid-catalyzed reaction sequence. Blue and red points indicate data from the batch and continuous experiments, respectively.

G.4.2.3 Model 13 - Base-A-I +Prot + Hyd

Model 13 includes the protonation and the hydration extension introduced in Fig. 7.11. The protonation extension was tested as alternative to variable TFA reaction orders. The corresponding kinetic equations of Model 13 are:

$$\mathrm{PO_1} \longrightarrow \mathrm{PO_x} \qquad r_{\mathrm{PO_x}} = k_{\mathrm{PO_x}}[\mathrm{PO_1}] \tag{G.25}$$

$$\mathrm{PO_1} + \mathrm{H^+} \longrightarrow \mathrm{PO_1H^+} \qquad r_{\mathrm{PO_1,PO_1H^+}} = k^{+}_{\mathrm{PO_1,PO_1H^+}}[\mathrm{H^+}][\mathrm{PO_1}] \tag{G.26}$$

$$\mathrm{PO_1H^+} \longrightarrow \mathrm{PO_1} + \mathrm{H^+} \qquad r_{\mathrm{PO_1H^+,PO_1}} = k^{-}_{\mathrm{PO_1,PO_1H^+}}[\mathrm{PO_1H^+}] \tag{G.27}$$

$$\mathrm{PO_1H^+} \longrightarrow \mathrm{IM_2} + \mathrm{H^+} \qquad r_{\mathrm{PO_1H^+,IM_2}} = k_{\mathrm{PO_1H^+,IM_2}}[\mathrm{PO_1H^+}] \tag{G.28}$$

$$\mathrm{PO_1} + \mathrm{H^+} \longrightarrow {}^{\mathrm{T}}\mathrm{PO_1H^+} \qquad r_{\mathrm{PO_1},{}^{T}\mathrm{POH^+}} = k^{+}_{\mathrm{PO_1},{}^{T}\mathrm{POH^+}}[\mathrm{H^+}][\mathrm{PO_1}] \tag{G.29}$$

$${}^{\mathrm{T}}\mathrm{PO_1H} \longrightarrow \mathrm{PO_1} + \mathrm{H^+} \qquad r_{{}^{T}\mathrm{POH^+},\mathrm{PO_1}} = k^{-}_{\mathrm{PO_1},{}^{T}\mathrm{POH^+}}[{}^{T}\mathrm{POH^+}] \tag{G.30}$$

$${}^{\mathrm{T}}\mathrm{PO_1H^+} \longrightarrow \mathrm{IM_2} + \mathrm{H^+} \qquad r_{{}^{T}\mathrm{POH^+},\mathrm{IM_2}} = k_{{}^{T}\mathrm{POH^+},\mathrm{IM_2}}[{}^{T}\mathrm{POH^+}] \tag{G.31}$$

$$\mathrm{IM_2} + \mathrm{O_2} \longrightarrow \mathrm{IM_3} \qquad r_{\mathrm{IM_2,IM_3}} = k_{\mathrm{IM_2,IM_3}}[\mathrm{O_2}][\mathrm{IM_2}] \tag{G.32}$$

$$\mathrm{IM_2} \xrightarrow{\mathrm{H+}} \mathrm{BP_4} \qquad r_{\mathrm{IM_2,BP_4}} = k_{\mathrm{IM_2,BP_4}}[\mathrm{H^+}][\mathrm{IM_2}] \tag{G.33}$$

$$\mathrm{IM_2} \xrightarrow{\mathrm{H+}} \mathrm{BP_5} \qquad r_{\mathrm{IM_2,BP_5}} = k_{\mathrm{IM_2,BP_5}}[\mathrm{H^+}][\mathrm{IM_2}] \tag{G.34}$$

$$\mathrm{IM_2} + \mathrm{H_2O} \longrightarrow \mathrm{IM_2{-}hyd} \qquad r_{\mathrm{IM_2,IM_2-hyd}} = k^{+}_{\mathrm{IM_2,IM_2-hyd}}[\mathrm{H_2O}][\mathrm{IM_2}] \tag{G.35}$$

$$\mathrm{IM_2{-}hyd} \longrightarrow \mathrm{IM_2} + \mathrm{H_2O} \qquad r_{\mathrm{IM_2-hyd,IM_2}} = k^{-}_{\mathrm{IM_2,IM_2-hyd}}[\mathrm{IM_2{-}hyd}] \tag{G.36}$$

$$\mathrm{IM_3} \xrightarrow{\mathrm{H+}} \mathrm{Arte} \qquad r_{\mathrm{IM_3,Arte}} = k_{\mathrm{IM_3,Arte}}[\mathrm{H^+}][\mathrm{IM_3}] \tag{G.37}$$

$$[\mathrm{H^+}] = [\mathrm{TFA}]^0 \tag{G.38}$$

The obtained model-data fit (Fig. G.11) is better than obtained with the base network but worse than achieved by Model 6 and 7. The identified kinetic parameters for Model 13 are summarized in Tab. G.3. The resulting concentration profiles at high acid concentrations in continuous mode and low acid concentrations in batch mode are exemplified in Fig. G.13 and Fig. G.4, respectively.

The protonation extension enables a precise description of the PO_1 conversion and artemisinin formation. There are no systematic deviations except for concentrations close to zero. However, the model does not match the BP_3 formation at the widely differing acid concentrations in batch and continuous experiments.

At the low acid concentration in batch experiments (Fig. G.4), the temporary binding of H^+ leads to a total depletion of H^+. In the continuous experiments with the higher initial TFA concentration, the drop in acid concentration is negligible. The fast formation of artemisinin causes a rapid release of water which reversibly hydrates IM_2. In the batch experiments, the combination of protonation and reversible IM_2 hydration results in equal formation rates of BP_4 and $\mathrm{IM_2{-}hyd}$. Despite the large number of parameters and extensions in the reaction network, Model 13 could not reproduce the complete experimental data set.

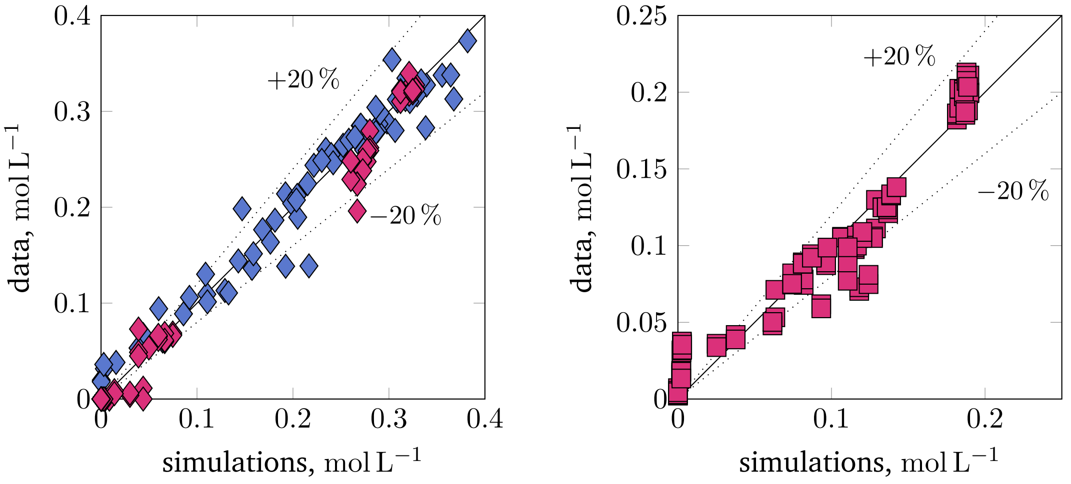

(a) PO_1 **(b)** Artemisinin

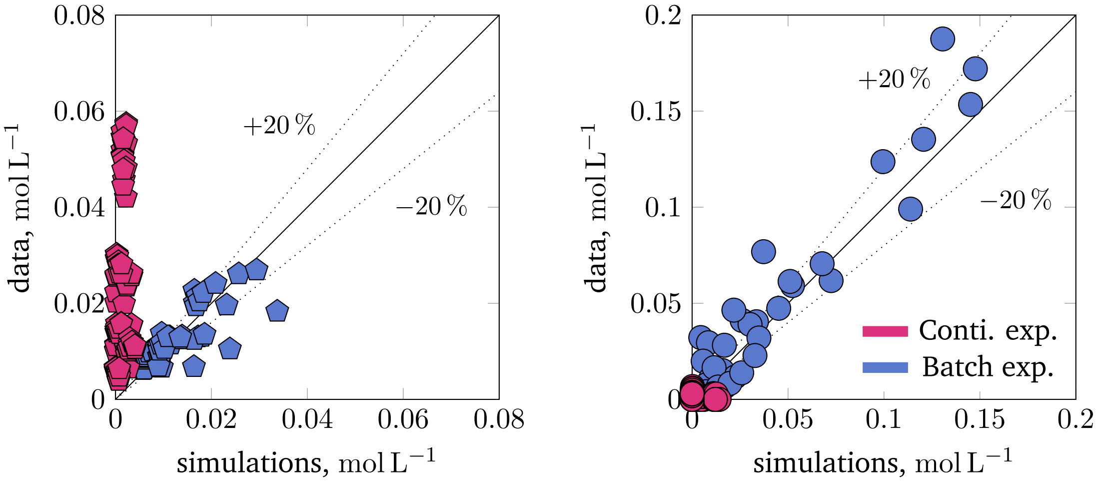

(c) BP_3 **(d)** BP_4

Fig. G.11: Fit between the experimental data of the acid-catalyzed reaction sequence and the simulated results obtained with Model 13 (Eqs. (G.25)-(G.38)). Blue and red points indicate data from the batch and continuous experiments, respectively.

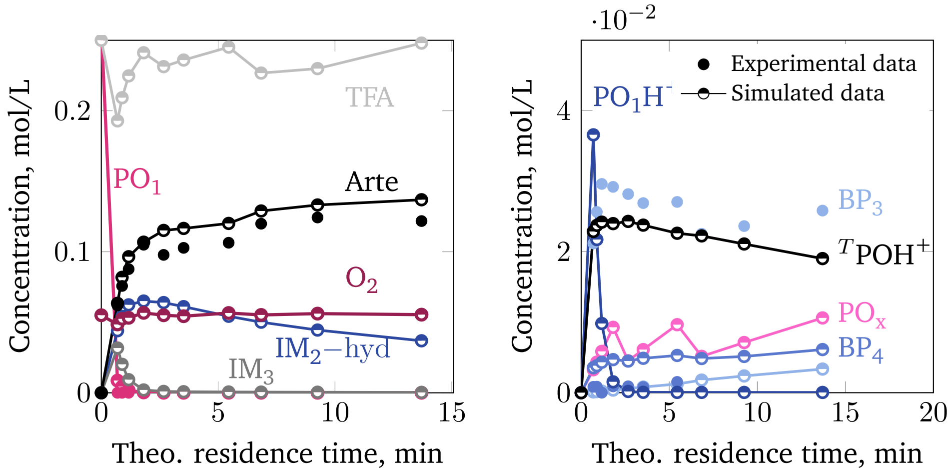

(a) Main species **(b)** Byproducts

Fig. G.13: Comparison of simulation with Model 13 and experimental results for continuous experiments with 0.25 M TFA. Conditions: $[DHAA]^0 = 0.25\,M$, $p_{O_2} = 7\,bar$, $T_{photo} = -20\,°C$, $T_{2nd} = 20\,°C$.

Tab. G.3: Kinetic parameters identified for Model 13 (Eqs. (G.25) - (G.38)) describing the acid-catalyzed reaction sequence to artemisinin.

Model-data fit of Model 13

Symbol	unit	value	description
SSE	$\mathrm{mol^2/L^2}$	0.1985	sum of squared errors
SSE_{conti}	$\mathrm{mol^2/L^2}$	0.1229	SSE for continuous exp.
SSE_{batch}	$\mathrm{mol^2/L^2}$	0.0756	SSE for batch exp.

estimated parameters

Symbol	unit	value
$k_{\mathrm{PO_x}}$	$\mathrm{min^{-1}}$	0.0054
$k^+_{\mathrm{PO_1,PO_1H^+}}$	$\mathrm{L\,mol^{-1}\,min^{-1}}$	35.69
$k^-_{\mathrm{PO_1,PO_1H^+}}$	$1/\mathrm{min}$	1.1381
$k_{\mathrm{PO_1H^+,IM_2}}$	$1/\mathrm{min}$	2.4714
$k^+_{\mathrm{PO_1},{}^T\mathrm{POH^+}}$	$\mathrm{L\,mol^{-1}\,min^{-1}}$	3.3477
$k^-_{\mathrm{PO_1},{}^T\mathrm{POH^+}}$	$1/\mathrm{min}$	0.0054
$k_{{}^T\mathrm{POH^+},\mathrm{BP_3}}$	$1/\mathrm{min}$	0.0078
$k_{\mathrm{IM_2,BP_5}}$	$\mathrm{L\,mol^{-1}\,min^{-1}}$	0
$k_{\mathrm{IM_2,BP_4}}$	$\mathrm{L\,mol^{-1}\,min^{-1}}$	15.10
$k_{\mathrm{IM_2,IM_3}}$	$\mathrm{L\,mol^{-1}\,min^{-1}}$	1568.1
$k^+_{\mathrm{IM_2,IM_2-hyd}}$	$\mathrm{L\,mol^{-1}\,min^{-1}}$	$5000^\dagger$
$k^-_{\mathrm{IM_2,IM_2-hyd}}$	$1/\mathrm{min}$	0.1834
$k_{\mathrm{IM_3,Arte}}$	$\mathrm{L\,mol^{-1}\,min^{-1}}$	14.20

†: Upper boundary of the set parameter range

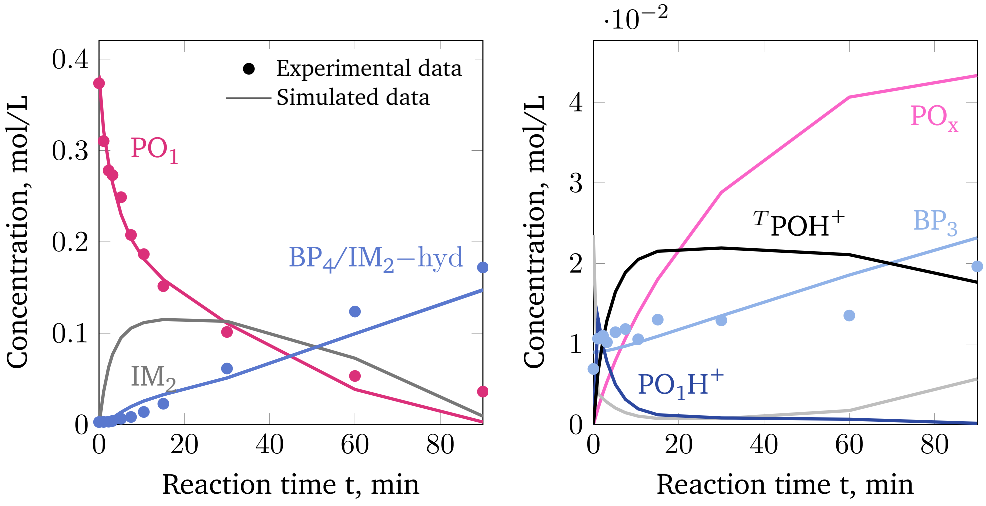

(a) Main species

(b) Byproducts

Tab. G.4: Concentration profiles simulated with Model 13 for the acid-catalyzed reaction sequence after addition of $0.024\,\mathrm{M}$ TFA to a $\mathrm{PO_1}$ containing solution in nitrogen atmosphere in batch mode.

G.4.2.4 Model 21 - Base-A-IV + BP_6

The structure of Model 21 is similar to the initial base model in Fig. 7.11 but differs in two aspects. First, it includes variable reaction orders for TFA in the initial conversion of PO_1. Second, the lumped byproduct species BP_6 is formed after the oxidation starting from IM_3. The rate equations of Model 21 for the acid-catalyzed sequence are given in Eqs. (G.39) - (G.46).

$$\mathrm{PO_1} \xrightarrow{} \mathrm{PO_x} \qquad r_{\mathrm{PO_x}} = k_{\mathrm{PO_x}}[\mathrm{PO_1}] \tag{G.39}$$

$$\mathrm{PO_1} \xrightarrow{\mathrm{H+}} \mathrm{IM_2} \qquad r_{\mathrm{PO_1,IM_2}} = k_{\mathrm{PO_1,IM_2}}[\mathrm{H^+}]^{n_{\mathrm{IM_2}}}[\mathrm{PO_1}] \tag{G.40}$$

$$\mathrm{PO_1} \xrightarrow{\mathrm{H+}} \mathrm{BP_3} \qquad r_{\mathrm{PO_1,BP_3}} = k_{\mathrm{PO_1,BP_3}}[\mathrm{H^+}]^{n_{\mathrm{IM_2}}+1}[\mathrm{PO_1}] \tag{G.41}$$

$$\mathrm{IM_2} + \mathrm{O_2} \xrightarrow{} \mathrm{IM_3} \qquad r_{\mathrm{IM_2,IM_3}} = k_{\mathrm{IM_2,IM_3}}[\mathrm{O_2}][\mathrm{IM_2}] \tag{G.42}$$

$$\mathrm{IM_2} \xrightarrow{\mathrm{H+}} \mathrm{BP_4} \qquad r_{\mathrm{IM_2,BP_4}} = k_{\mathrm{IM_2,BP_4}}[\mathrm{H^+}][\mathrm{IM_2}] \tag{G.43}$$

$$\mathrm{IM_3} \xrightarrow{\mathrm{H+}} \mathrm{Arte} \qquad r_{\mathrm{IM_3,Arte}} = k_{\mathrm{IM_3,Arte}}[\mathrm{H^+}][\mathrm{IM_3}] \tag{G.44}$$

$$\mathrm{IM_3} \xrightarrow{\mathrm{H+}} \mathrm{BP_6} \qquad r_{\mathrm{IM_2,BP_6}} = k_{\mathrm{IM_2,BP_6}}[\mathrm{H^+}][\mathrm{IM_3}] \tag{G.45}$$

$$[\mathrm{H^+}] = [\mathrm{TFA}]^0 \tag{G.46}$$

The kinetic parameters obtained by fitting Model 21 to the batch and the continuous data are listed in Tab. G.5. The corresponding parity plots are shown in Fig. G.14. Model 21 shows a similarly good model-data fit as the final model introduced in Sec. 7.2.3. However, the rate constant for the oxidation of IM_2 to IM_3 is estimated at the upper boundary of the set parameter range. This parameter is the only model parameter which is practically non-identifiable with the given experimental data set. In the current model, the rate equation for IM_3 works as a switch. In the presence of oxygen, IM_2 reacts directly to IM_3.

The resulting simulated process behavior is shown on the example of a batch experiment and several continuous experiments in Fig. G.16 and Fig. G.15. In N_2 atmosphere, the hydroperoxide PO_1 reacts to IM_2, which is further converted to BP_4 as the main species (Fig. 7.17). IM_3, BP_5, and artemisinin are not formed due to the lack of oxygen. In the continuous experiments (Fig. G.15), the conversion of IM_2 to IM_3 is fast so that IM_2 does not accumulate to a significant extent in the presence of oxygen. IM_3 reacts to artemisinin slower than its formation and thus accumulates as the main intermediate according to the model. Therefore, the formation of artemisinin in the continuous experiments proceeds via a different late-stage precursor than the formation of BP_4 in nitrogen atmosphere in batch experiments. This insight led to splitting the reaction pathways to artemisinin and BP_4 directly after the PO_1 conversion, which resulted in a fully identifiable parameter set and a further improved model-data fit (Sec. 7.2.3).

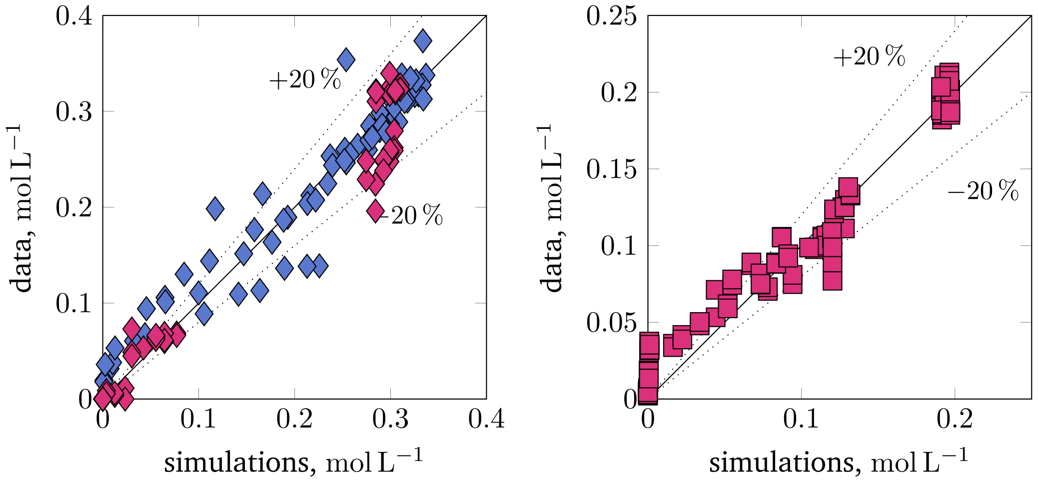

(a) PO_1 **(b)** Artemisinin

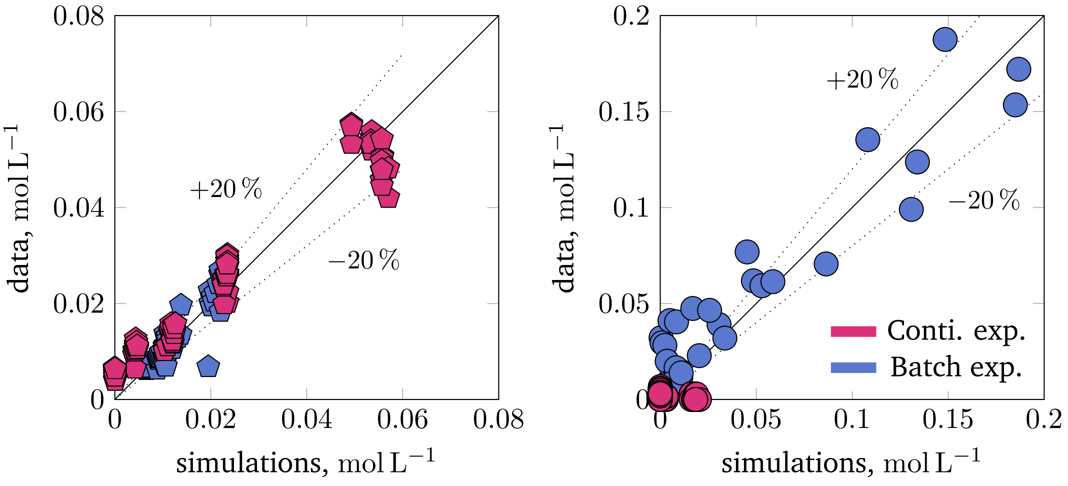

(c) BP_3 **(d)** BP_4

Fig. G.14: Fit between the experimental data of the acid-catalyzed reaction sequence and the simulated results obtained with Model 21 (Eqs. (G.39) - (G.46)). Blue and red points indicate data from the batch and continuous experiments, respectively.

Tab. G.5: Kinetic parameters identified for Model 21 (Eqs. (G.39) - (G.46)) describing the acid-catalyzed reaction sequence starting from PO_1 to artemisinin.

Model-data fit of Model 21			
Symbol	unit	value	description
SSE	mol^2/L^2	0.2074	sum of squared errors
SSE_{conti}	mol^2/L^2	0.1214	SSE for continuous exp.
SSE_{batch}	mol^2/L^2	0.0860	SSE for batch exp.
estimated parameters			
Symbol	unit	value	
k_{PO_x}	min^{-1}	0.0099	
n_{IM_2}	-	2.369	
k_{PO_1,BP_3}	$(L\,mol^{-1})^{n+1}\ min^{-1}$	159.2	
k_{PO_1,IM_2}	$(L\,mol^{-1})^{n}\ min^{-1}$	318.0	
k_{IM_2,BP_4}	$L\,mol^{-1}\ min^{-1}$	0.7325	
k_{IM_2,IM_3}	$L\,mol^{-1}\ min^{-1}$	5000†	
$k_{IM_3,Arte}$	$L\,mol^{-1}\ min^{-1}$	0.7864	
k_{IM_3,BP_6}	$L\,mol^{-1}\ min^{-1}$	0.5899	
fixed parameters			
Symbol	unit	value	reference
$\widetilde{k_l a}$	$\sqrt{1/cm\,min}$	1.094	fixed to estimated value in the photoreactor

†: Upper boundary of the set parameter range

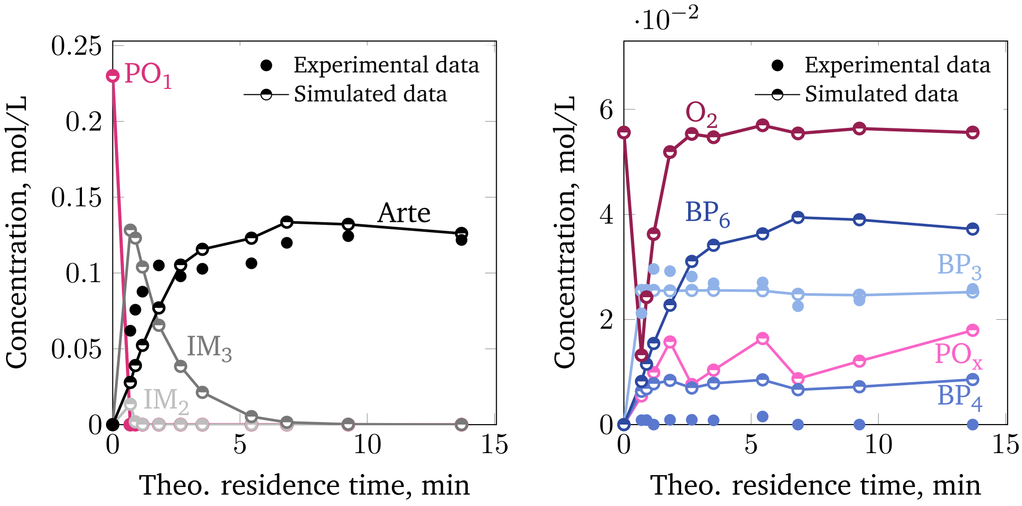

(a) Main species **(b)** Byproducts

Fig. G.15: Simulated reaction behaviour obtained with Model 21 in comparison with measured data from continuous experiments with 0.25 M TFA. Conditions: $[DHAA]^0 = 0.25\,M$, $p_{O_2} = 7\,bar$, $T_{photo} = -20\,°C$, $T_{2nd} = 20\,°C$.

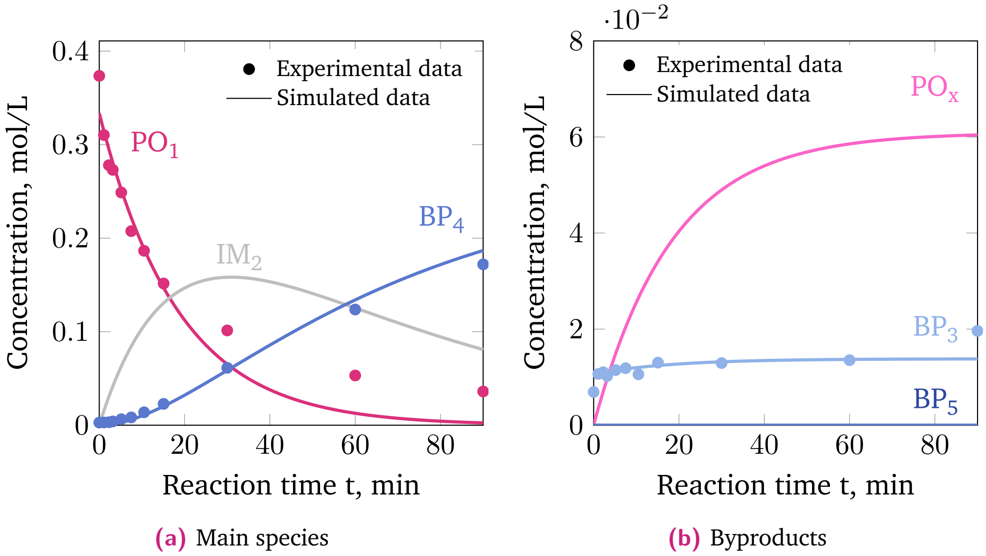

(a) Main species **(b)** Byproducts

Fig. G.16: Concentration profiles in batch mode in nitrogen atmosphere obtained with Model 21 ($0.024\,\mathrm{M}$ TFA).

H

Basis of the cost estimation

The feasibility study on the partial synthesis as extension of the plant-based artemisinin production was introduced in Chapter 8. The economic analysis is based on balancing the operating costs of the reaction with the added value of the reaction products. The value of the synthesized artemisinin after purification represents the gross economic potential (GEP) of implementing the partial synthesis. The economic feasibility is expressed as the net economic potential NEP, which is the difference of operating costs C_{OPEX} and the GEP [411].

$$NEP = GEP - C_{OPEX} \tag{H.1}$$

All three quantities are related to the volume of extract being processed. The cost estimation was performed for the photoreactor system introduced in Sec. 4.1 with a maximum throughput of $1.2\,\mathrm{L\,h^{-1}}$ extract.

The GEP depends on the DHAA content in the extract, the yield of converting DHAA to artemisinin, $\mathrm{Y_{Reac}}$, and the price artemisinin is sold, $\mathrm{Pr_{Arte}}$.

$$GEP = Pr_{Arte} \cdot Y_{pur} \cdot Y_{Reac} \cdot [\mathrm{DHAA}]^0 \cdot M_{Arte} \tag{H.2}$$

with M as the molar mass. The artemisinin yield obtained from the partial synthesis is affected by the DHAA concentration in the extract (Sec. 6.4). To include this dependence in the cost estimation, an empirical relation is fit to the experimental data (Fig. H.1). Please note, that the given empirical equation relates the yield with the DHAA concentration after four-fold concentration by solvent removal prior to the reaction step:

$$[\mathrm{DHAA}]^0_{reac} = F_{conc} \cdot [\mathrm{DHAA}]^0 \tag{H.3}$$

with $F_{conc} = 4$.

The operating costs include costs for chemical consumption for TFA, the quenching agent and the electrical power consumption for operating the pumps, compressor and the LED modules.

$$\begin{aligned} C_{OPEX} = {} & Pr_{Elec} \cdot \frac{P^C_{Pumps} + P^C_{LED}}{\dot{V}_{Ext}} + Pr_{Elec} \cdot \frac{P^C_{Compressor} \cdot p \cdot \beta}{F_{conc}} \\ & + 0.9 \cdot Pr_{TFA} \cdot \frac{[\mathrm{TFA}]}{F_{conc}} \cdot M_{TFA} + 0.9 \cdot Pr_{Quench} \cdot \frac{[\mathrm{Quench}]}{F_{conc}} \cdot M_{Quench} \end{aligned} \tag{H.4}$$

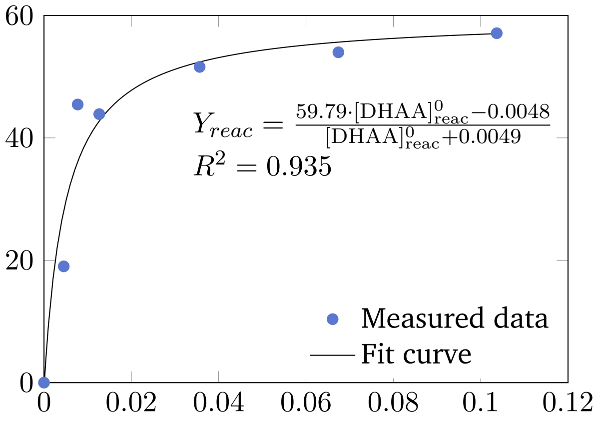

Fig. H.1: Empirical relation to describe the dependence of the artemisinin yield of the partial synthesis and the initial DHAA concentration in the extract after extraction and partial solvent removal. The experimental data was given in Sec. 6.4.

The factor of 0.9 reduces the chemical prices taken from chemical suppliers to consider bulk prices [23]. The concentration of TFA, the quenchers triethylamine (TEA) and saturated $NaHCO_3$ are listed in Tab. H.1. The power consumption P^C of the applied equipment is given in Tab. H.2 and the prices for electricity and chemicals in Tab. H.3. The chemical and electricity prices were assumed to be constant. The cost for treating the quenched TFA stream after the reaction step were not considered.

Tab. H.1: Process conditions and concentrations set for estimating the operating costs.

Quantity	Value	Reference
Extract throughput	$1.2\,\mathrm{L\,h^{-1}}$	Sec. 6.5
$[\mathrm{TFA}]$ in concentrated extract	$0.065\,\mathrm{M}$	Sec. 6.2.2
System pressure p	$7\,\mathrm{bar}$	Sec. 6.5
Optimized gas holdup β	0.43	Sec. 6.5
Molar ratio of quenching agent and TFA	1	Sec. 4.3.3
Solubility of $NaHCO_3$ in H_2O	$93\,\mathrm{g\,L^{-1}}$	[420]

Tab. H.2: Power consumption of the equipment integrated in the investigated lab-scale photoreactor system (Sec. A.1) with the number of installed units.

Device	Type	No.	Electrical Power, W
LED modules	OSA Opto Light OLM-018 Silent Air	2	280 W
Pumps	Knauer Azura P4.1S	3	40 W
Compressor	Stanley DN200/10/5	1	$102\,\mathrm{W/NL}$

Tab. H.3: Prices for used chemicals and electricity. The prices for TFA, TEA, and $NaHCO_3$ were taken from chemical suppliers. Prices in euro were converted into dollar by the conversion factor of 1.1 as of 19.03.2022.

Quantity	Value	Reference
Artemisinin	100 - 400 \$/kg	[24, 31]
Trifluoroacetic acid (TFA)	207.7 \$/kg	[421]
Triethylamine (TEA)	30.8 \$/kg	[422]
Sodium bicarbonate	21.0 \$/kg	[423]
Water	6.36 $\$/\mathrm{m}^3$	[424]
Electricity	0.10 \$/kWh	[412]

Bibliography

[23] Hikaru G. Jolliffe and Dimitrios I. Gerogiorgis. “Process modelling and simulation for continuous pharmaceutical manufacturing of artemisinin”. In: *Chemical Engineering Research and Design* 112 (2016), pp. 310–325. DOI: `10.1016/j.cherd.2016.02.017`.

[24] Burak Kazaz, Scott Webster, and Prashant Yadav. “Interventions for an Artemisinin-Based Malaria Medicine Supply Chain”. In: *Production and Operations Management* 25.9 (2016), pp. 1576–1600. DOI: `10.1111/poms.12574`.

[31] Mark Peplow. “Looking for Cheaper Routes to Malaria Medicines”. In: *Chemical & Engineering News* (2018). URL: `https://cen.acs.org/articles/96/i11/Looking-cheaper-routes-malaria-medicines.html` (visited on Dec. 22, 2021).

[412] Statista. *Strompreis für die Industrie in Deutschland | Statista*. 20/03/2022. URL: `https://de.statista.com/statistik/daten/studie/155964/umfrage/entwicklung-der-industriestrompreise-in-deutschland-seit-1995/` (visited on Mar. 20, 2022).

[420] GESTIS-Stoffdatenbank, ed. *Natriumhydrogencarbonat*. 5/04/2022. URL: `https://gestis.dguv.de/data?name=002440` (visited on Apr. 19, 2022).

[421] Alfa Aesar, ed. *Price of trifluoroacetic acid*. URL: `https://www.alfa.com/en/catalog/A12198/` (visited on Mar. 19, 2022).

[422] Alfa Aesar, ed. *Price of triethylamine*. URL: `https://www.alfa.com/en/catalog/A12646/` (visited on Mar. 19, 2022).

[423] Alfa Aesar, ed. *Price of Sodium hydrogen carbonate*. URL: `https://www.alfa.com/en/catalog/014707/` (visited on Mar. 9, 2022).

[424] Statista. *Wasserpreise im Ländervergleich 2011 | Statista*. 20/03/2022. URL: `https://de.statista.com/statistik/daten/studie/1538/umfrage/wasserpreise-weltweit/` (visited on Mar. 20, 2022).